Mechanical Characterization of Nanoporous Thin Films by Nanoindentation and Laser-induced Surface Acoustic Waves

Gabriel Chow

A dissertation
submitted in partial fulfillment of the
requirements for the degree of

Doctor of Philosophy

University of Washington

2014

Reading Committee:

Junlan Wang (Chair)
Vipin Kumar
Amy Shen
Guozhong Cao

Program Authorized to Offer Degree:

Mechanical Engineering

University of Washington

Abstract

Mechanical Characterization of Nanoporous Thin Films by Nanoindentation and Laser-induced Surface Acoustic Waves

Gabriel Chow

Chair of the Supervisory Committee:
Professor Junlan Wang
Department of Mechanical Engineering

Thin films represent a critical sector of modern engineering that strives to produce functional coatings at the smallest possible length scales. They appear most commonly in semiconductors where they form the foundation of all electronic circuits, but exist in many other areas to provide mechanical, electrical, chemical, and optical properties. The mechanical characterization of thin films has been a continued challenge due foremost to the length scales involved. However, emerging thin films focusing on materials with significant porosity, complex morphologies, and nanostructured surfaces produce additional difficulties towards mechanical analysis.

Nanoindentation has been the dominant thin film mechanical characterization technique for the last decade because of the quick results, wide range of sample applicability, and ease of sample

preparation. However, the traditional nanoindentation technique encounters difficulties for thin porous films. For such materials, alternative means of analysis are desirable and the lesser known laser-induced surface acoustic wave technique (LiSAW) shows great potential in this area. This dissertation focuses on studying thin, porous, and nanostructured films by nanoindentation and LiSAW techniques in an effort to directly correlate the two methodologies and to test the limits and applicabilities of each technique on challenging media.

The LiSAW technique is particularly useful for thin porous films because unlike indentation, the substrate is properly accounted for in the wave motion analysis and no plastic deformation is necessary. Additionally, the use of lasers for surface acoustic wave generation and detection allows the technique to be fully non-contact. This is desirable in the measurement of thin, delicate, and porous films where physical sample probing may not be feasible. The LiSAW technique is also valuable in overcoming nanoscale roughness, particularly for films that cannot be mechanically polished, since typical SAW wavelengths are micrometers in scale whereas indentation depths are usually confined to the nanometer scale. This dissertation demonstrates the effectiveness of LiSAW on both thin porous layers and rough surfaces and shows the challenges faced by nanoindentation on the same films.

Zeolite thin films are studied extensively in this work as a model system because of their porous crystalline framework and enormous economic market. Many types of zeolite exist and their widely varying structures and levels of porosity present a unique opportunity for mechanical characterization. For a fully dense ZSM-5 type zeolite with wear and corrosion resistance properties, nanoindentation was used to compare its mechanical properties to industrial chromium and cadmium films. Through tribological and indentation tests, it was shown that the zeolite film possesses exceptional resilience and hardness therefore demonstrating superior wear resistance to chromium and cadmium. This also highlighted the quality of nanoindentation measurements on thick dense layers where traditional nanoindentation excels.

Nanoindentation was then performed on porous and non-porous MFI zeolite films with low-k (low dielectric constant) properties. These films were softer and much thinner than the ZSM-5 coatings resulting in significant substrate effects, evidenced by inflation of the measurements from the hard silicon substrate, during indentation. Such effects were avoided with the LiSAW technique on the same films where properties were readily extracted without complications. An alternative indentation analysis method was demonstrated to produce accurate mechanical measurements in line with the LiSAW results, but the non-traditional technique requires substantial computational intensity. Thus LiSAW was proven to be an accurate and efficient means of mechanical characterization for thin porous layers.

The case for LiSAW was further supported by utilizing the technique on a porous nanostructured V_2O_5 electrode film. The surface roughness, on the same scale as indentation depths, created difficulty in obtaining consistent nanoindentation results. Since the film was too delicate for mechanical polishing, the nanoindentation results possessed a high level of uncertainty. It was demonstrated that the LiSAW technique could extract the mechanical properties from such layers without substrate effects and with higher accuracy than nanoindentation.

The research in this dissertation directly demonstrates the areas where nanoindentation excels and the areas where it encounters difficulty. It is shown how the LiSAW technique can be an efficient alternative in the challenging areas through its dependence on bulk dispersive wave motion rather than localized deformation. Thus, LiSAW opens up many avenues towards the mechanical characterization of thin, porous, soft, or rough films. Nanoindentation remains an extremely useful technique for thin film characterization, especially with the alternative analysis adaptation. However, as films continue trending towards smaller length scales, more complex porous morphologies, and engineered nanoscale surfaces, LiSAW may well become an equally valuable and indispensable technique.

Table of Contents

List of Tables

List of Figures

ACKNOWLEDGEMENTS

My deepest and sincerest gratitude goes to my advisor, Professor Junlan Wang. In the many years we have worked together, she has provided me with an immeasurable amount of guidance and feedback. There are few people in this world who exhibit her level of care towards her students' well-being in an academic, professional, and personal sense and I have been continually impressed by her commitment to teaching and mentorship, even in the busiest of times.

I wish to thank all of my lab mates for their intellectual support and companionship during my time at UW and UC Riverside. Phil, Wu-feng, Jane, Frank, Elias, Joe, Mark, and Melicent, I will carry fond memories of my time with each of you for the rest of my life. I also wish to acknowledge a few students from other labs who were great collaborators. Raj, Jennie, Frank, Chris, and Evan, I thank you all for your support and patience in introducing me to your respective research fields. I have special thanks for Professor Yushan Yan, my co-advisor at UC Riverside, who taught me so much about zeolites and who continued to support my zeolite work throughout my time at UW.

Words cannot describe the amount of support that my family has given me throughout my graduate career and my entire lifetime. They have been instrumental in giving me the confidence to tackle my academic and professional endeavors and I am forever thankful for their patience and unconditional love. Lastly, I have very special thanks for Trinh. She has been an amazing companion throughout all the ups and downs of my university studies and has been an endless source of support and inspiration. She brightens up every day of my life, which is especially appreciated on those gloomy Seattle days, and I look forward to overcoming all of life's challenges together with her.

DEDICATION

To my grandmother, who cherished every educational milestone.

Chapter 1 Introduction

1.1 Background of thin film technology

Thin film technology has evolved and advanced greatly in the past fifty years to become an integral part of many engineering applications. With the ongoing expansion of nanotechnology, the demand for functional films at decreasing length scales is growing rapidly with new and novel applications seeing substantial research investment. At the core, thin films are typically used for several general functions: to provide electrical and magnetic properties in microelectronic devices, to provide a layer with desirable optical properties, to supplement or provide necessary mechanical properties, and as a shielding layer to protect components from various environmental factors. Thin films are often designed to provide many subsets of the above categories simultaneously, thus their structure and geometry can vary greatly. There are no strictly defined conditions for materials to be considered a thin film. The general requirement is that the length in one dimension should be significantly lower than the length in the other two dimensions and that the properties of the layer are different from the substrate. The film thickness can range from a single atom of material to many microns with no set upper limit, however "thin" films are typically regarded as those in the range of several microns and below. (Freund and Suresh, 2003)

There are several popular methods to attain thin films with each procedure being a balance of cost, complexity, film quality (surface and microstructure), and quickness. They can be grouped into the following main categories: physical vapor deposition (PVD) such as in evaporation and sputtering, chemical vapor deposition (CVD) typically as thermal CVD or plasma enhanced

CVD, electrochemical deposition such as in electroplating and chemical deposition, thermal spray, and plating through casting and mechanical action. It can be seen that the majority of techniques rely on either the physical transfer of material, whether it is through an atomistic vapor or a stream of larger particles, or a chemical reaction in a controlled environment. Continuous improvements to deposition technology have led to a greater understanding of film growth for many materials allowing for ever more complex films to be created and tailored for specific applications.

There are many areas of engineering which utilize thin film technology, but the semiconductor industry in particular represents a significant fraction of the field. The fabrication of microelectronic devices is fully reliant on the ability to successively deposit thin films of various materials to tightly controlled specifications. The functions of each material can vary greatly from copper electrical leads to silicon oxide insulating layers and together, many layers form the basic integrated circuit components such as diodes and transistors. These can then combine to form the backbone of all modern functional electronic devices. The continuous miniaturization of electronics is thus dependent on the ability to produce thin films at shrinking scale factors, but requiring the same level of control on film structure and properties. Therefore, accurate measurement of film parameters at each step is highly important for quality control. This is also very true for thin films outside the semiconductor industry as precise measurement of thin film properties is usually necessary in order to validate their functional performance.

In other areas of industry, thin films are typically employed as a means to supplement or provide desired mechanical, tribological, or optical properties to materials lacking such qualities. One major segment of this application is in the coating of structural materials for performance in adverse environments. A popular example of this is in the electroplating of steels for corrosion resistance in marine environments. However, the same idea can be applied in much different areas like biotechnology where implants can be coated with biocompatible layers or in optics where films can provide selective reflectance of light for smart windows. In all of these cases, the trend is that a relatively inexpensive substrate material with long established qualities is significantly enhanced by the addition of a thin film making it possible to operate outside of its traditional limits. The engineering marvel is that the volume of material necessary for the layer can be very small while still attaining a large difference in performance. This fact reduces the need for tailoring exotic materials in the bulk in favor of thin films which can provide the same properties at a fraction of the cost. Thus thin film technology is a vital part of engineering today and will continue to grow as new and more complex films come to fruition for an ever increasing list of applications.

1.2 Overview of mechanical characterization challenges and techniques

While the deposition of thin films is typically not done for structural reasons, accurate mechanical characterization of the film is often desired since the layer becomes the point of physical contact to the outside environment. Whether or not the mechanical properties serve a functional purpose comes secondary to the fact that the mechanical behavior will govern how reliable the film is in service. For example, in the semiconductor industry, the mechanical property of films may not influence their electrical performance. However, a degree of mechanical reliability is typically necessary in order to withstand polishing and packaging steps during fabrication. Thus, an accurate mechanical measurement of the as-deposited layers in each step is needed for developing processing parameters for the following stages and to ensure lasting functionality of the final product.

The main challenge to the mechanical characterization of thin films is the scale at which the test must be performed. At the micrometer or nanometer scale, typical mechanical measurement techniques such as the tensile and beam bending tests are simply not feasible. Scaling these macroscale tests down to the film geometry can seem like a viable solution, but the results will inevitably be a coupling of the substrate and film mechanical properties since the two remain in intimate contact. In order to accurately measure the mechanical properties of the film, the test must be somehow localized to the film or provide some means of decoupling the substrate influence from the results. As a special case for coupled measurements, careful consideration must be made in decoupling dominant substrates such as in the scenario of soft films on a hard substrate.

Another challenge, especially for nanometer thick films, is that the film property can become significantly different than the same material in bulk. Just as bulk materials can vary in strength depending on grain size, thin films can exhibit different behavior at decreasing thickness scales. Considering that semiconductor fabrication is now performed with feature sizes on the order of tens of nanometers, it is easy to see that a mechanical understanding of material behavior at this scale is necessary for accurate thin film measurement.

The challenges above highlight the difficulty of characterization based on geometrical concerns. However, another troublesome area can emerge from the morphology of the film. Attempting to measure properties at the thin film scale for complex structures can be a hard task given that the scale of the material's building units may be on the same order as the testing probe. Thus a local measurement may not necessarily be precise in predicting the bulk properties of the film. Porous thin films are a good example of this type of behavior and they will be detailed later in the chapter.

There are several popular thin film characterization techniques, but nanoindentation is by far the most utilized since it does not require significant sample preparation, is fast, and can test a large variety of films. The technique is essentially a scaled down macro-indentation test involving sample probing by a sharp diamond tip. However, unlike macroscale tests, elastic properties can be measured from the initial elastic response of the unloading segment. Measurement of film specific parameters is possible because the depth of indentations can be only several nanometers. Thus, an infinite film thickness is assumed for the most popular nanoindentation analysis technique (Oliver and Pharr, 1992). While this assumption works well for many films, it will be shown later that thin geometries and mechanically mismatched films/substrates can introduce errors from substrate influence.

Microelectromechanical systems (MEMS) are another popular field for thin film characterization. These usually describe building specific microscale systems to mechanically test at a length scale closer to that of the film thickness. Microtensile systems fall into this category by directly or indirectly measuring elongation of attached samples in response to an applied force (Yeh and Wang, 2011, Saif and MacDonald, 1998). The mechanical properties are then extracted in the same manner as a macro-tensile test. Other MEMS techniques rely on releasing portions of the film from the substrate with MEMS based fabrication methods. In this manner, deflection of the free standing film can be used to calculate the mechanical properties. Deflection for these tests is typically induced by physical probing or cavity pressure (Walker et al., 1991, Johansson et al., 1988).

The third major area of characterization involves the use of acoustics. Since the characteristics of waves inevitably depend on the mechanical constants of the system, generation and detection of waves on thin films can yield their mechanical properties. Atomic force acoustic microscopy (AFAM) is a good example of this where an AFM tip is used to accept vibration from the film in order to characterize its resonance modes. From these, the local elastic properties can be extracted (Rabe et al., 1997). The use of surface acoustic waves (SAWs) is another type of acoustic method. In this technique, a surface wave, whose propagation depends on the film and substrate properties, is generated and detected to extract the mechanical properties of both materials (Coufal et al., 1992). It is one of the major techniques utilized for this writing and it will be detailed in chapters 3-4.

1.3 Introduction to porous films

Porous films are an important part of modern dielectrics since their insulating capabilities can far outperform their dense counterparts. This is especially important to the semiconductor industry because the advancement of that sector depends on the creation and application of ultra-low dielectric constant films (ultra-low-κ). The path of porous film development has been to exploit the low dielectric constant of air, $\kappa = 1$, by introducing as much porosity to a material as possible while still retaining a sufficiently strong structure. Gel processes are a popular way to obtain such films. The technique involves replacing the liquid around the solid network of a gel by a gas through various drying methods. Aerogel and xerogel structures are examples of films that can be possible by this method and they can have extremely high porosities and low κ values (Hrubesh, 1998). Another method to obtain porous films involves film growth around a template and subsequent removal of the scaffold structure. Zeolite films can exhibit this type of formation where a composite film is formed during synthesis and the template is thermally evaporated afterwards (Johnson et al., 2007). Regardless of which technique is used for synthesis, the film must meet stringent thermal, electrical, mechanical, and chemical requirements in order to be applicable as a low-κ material. Currently, no material adequately satisfies all requirements therefore the definitive successor to the silicon oxide standard has yet to be seen.

One of the greatest challenges towards the application of porous films is the considerable drop in mechanical property associated with increasing porosity. Thus, the mechanical characterization of porous films is needed, but encounters significant difficulty. The voided microstructure is often comprised of complex linkages whose strengths can vary greatly from the bulk film properties. Additionally, porous films can have a very soft and fragile makeup requiring delicate measurements to assess the film without harm. These can be especially troublesome since the substrate may dominate the measurement by the way of a soft film on a hard substrate. Lastly, the ultra-thin geometries associated with semiconductor fabrication scales contribute even more to substrate influence.

Porous thin film technology is a field that is constantly growing and maturing in order to meet the demands from electronic applications. As the structures get more innovative and complex, characterization methods will need to adapt in order to remain accurate and effective.

1.4 Background and introduction to porous zeolite films

Zeolite materials are aluminosilicates composed primarily of SiO_4 and AlO_4 tetrahedra linked together in many distinct configurations. Today, there are over 200 different frameworks recognized with additional new structures being synthesized yearly (Meier and Olson, 1992). Each framework is given a three letter code, such as MFI, MEL, or LTA, that references the discoverer and/or structure properties. The unique porous crystalline structure of zeolites has been exploited in many industrial applications with widespread uses as separation media and as catalyzing agents. By varying the aluminum to silicon ratio, the range of application can shift dramatically with the different zeolite structures achieved. Zeolites were pioneered and popularized by the petroleum industry because of their ability to aid in the oil refinement process (Vermeiren and Gilson, 2009). However, applications today are much broader with a growing presence in areas like biotechnology where the non-toxic and benign properties (Szostak, 1992) of the material are advantageous. While the majority of zeolites in industry are still utilized in powder form, the recently discovered ability to synthesize zeolite thin films has opened up new and revolutionary areas of application.

The semiconductor industry is one area that has taken a specific interest in zeolite thin films. There is a growing demand for modern dielectric materials since the pitch of parallel electrical interconnects is now only a few tens of nanometers and there is no slowing of device miniaturization in sight (International Roadmap Committee, 2013). Superior dielectrics will be needed to prevent crosstalk in such close quarters and zeolites are a prominent candidate for this application. The porosity of zeolite allows the material to exhibit very low dielectric constants while the crystalline framework preserves mechanical strength (Li et al., 2006). Both of these parameters are essential for semiconductor dielectrics since the desired electrical properties must be matched with enough mechanical reliability to withstand processing steps during fabrication. The ability for zeolite to form a continuous low-κ film at this scale and with minimal cost is very attractive (Lew et al., 2009).

Zeolite thin films are also attracting attention in regions far beyond the common places for silicon based films. In these areas, the functional property is typically not derived from the porosity, but rather the properties of zeolites previously unexplored. These could include the high mechanical strength, corrosion resistance, hydrophobicity and hydrophillicity, biocompatibility, and anti-microbial properties. From these, there is research and commercial investment in wear and corrosion resistant coatings for industrial metals (Chow et al., 2012), antimicrobial coatings (Beving et al., 2008), biocompatibile coatings for implants (Bedi et al., 2009), and proton exchange membranes in fuel cells (Holmberg et al., 2008).

Zeolite thin films are an interesting and unique class of materials with multiple highly desirable properties. The discovery of potential applications is ongoing and is still in its infancy. The fact that zeolites are essentially natural minerals fits well with the environmentally conscious direction of modern research. Zeolite thin films are expected to find even more commercial development and popularity as the technology matures.

1.5 Overview of the research performed and organization of the dissertation

In all of the thin film zeolite applications to come to fruition, the mechanical properties have typically played some role in their functionality. Usually, the mechanical elements are secondary to the main purpose and are tailored to establish a certain degree of mechanical reliability in service. However, they can also form the main function on some films. In all cases, accurate mechanical characterization is necessary for determination of commercial viability. These measurements, though, are a difficult task given the varying porosity and the wide range of mechanical behavior of zeolite. There have been limited studies on the mechanical characterization of zeolite with most utilizing the popular nanoindentation technique for measurement. However, for soft and porous films, nanoindentation often requires correction schemes most notably because of the substrate effect. The effect describes a condition where the probe cannot properly localize measurement to the film and thus a coupled substrate and film property is determined.

Zeolites, being porous and having varying degrees of softness (i.e. modulus depending on type), present a unique opportunity for mechanical characterization. The validity of nanoindentation on films with such geometries can be determined by the use of multiple measurement techniques. The research presented in this dissertation focuses on this task by showing the mechanical characterization of zeolite thin films by two different methodologies. The research shows analysis with the established nanoindentation technique and then details the development and application of a lesser known laser-induced surface acoustic wave (LiSAW) technique.

Following the demonstration of LiSAW techniques on zeolite films, the focus will shift away from zeolites and over to applying the LiSAW and nanoindentation techniques to porous nanostructured films. These types of films are becoming increasingly popular as thin film electrodes and their mechanical characterization poses some unique challenges that are interesting to both acoustic and indentation tests. The goal here is to demonstrate the versatility of LiSAW on other challenging films and to highlight the opportunities afforded by LiSAW in the lesser researched area of thin film electrode mechanical characterization.

In chapter 2, a wear and corrosion resistant zeolite film is mechanically and tribologically characterized by a nanoindentation instrument. The technical and commercial potential of this film is determined by performing a direct comparison to chromium and cadmium films that makeup the industrial standard. For this film, only nanoindentation is employed because the film is very thick and relatively stiff. Thus, nanoindentation encounters no difficulty in characterizing its behavior. Challenges arise for thinner and softer zeolite films due to morphology and geometrical constraints for valid indentations.

Chapters 3-5 explore an alternative characterization technique using laser-induced surface acoustic waves. This technique can readily characterize thin and soft films. The chapters serve to show the theoretical and experimental aspects of the technique and the comparison of LiSAW to nanoindentation. This comparison is done to characterize the validity of nanoindentation on thin porous films.

Chapter 3 highlights the theoretical basis of the fundamental wave dispersion required for LiSAW measurements. The theoretical calculations are used to explore the expected behavior of zeolite systems for the later experimental tests. The dispersive behavior of multilayer films is also studied in an effort to produce dispersion characteristics that can be more readily realized in experiment.

Chapter 4 details the development and setup of the experimental LiSAW technique. The physical phenomena behind laser generation and detection of SAWs are shown and the experimental setup is described. The process flow of the experiment is explained through the description of each component and the mathematical methods of obtaining experimental dispersion curves are overviewed.

Chapter 5 shows the experimental results from the material systems studied. The results are discussed in the context of whether LiSAW is an accurate technique and where the method can be advantageous with respect to nanoindentation on porous films.

Chapter 6 overviews the methodologies used to optimize the LiSAW system. Experiments are performed to demonstrate the specific benefit of each optimization strategy. Some of the materials tested in previous chapters are revisited to examine the complete improvement in technique and to characterize their properties to a higher degree of accuracy.

Chapter 7 applies the LiSAW technique to a porous and delicate nanostructured film. The versatility of LiSAW is demonstrated for rough challenging films and the results are compared to nanoindentation techniques.

The dissertation concludes in Chapter 8 and possible future directions are presented in Chapter 9. Two appendices detail several significant studies that were beyond the scope of the main work. Appendix A explores the mechanical characterization of adamantane-based rod structures by nanoindentation. Appendix B investigates surface-skimming longitudinal waves and their potential use in the LiSAW technique.

1.6 Publications list and reproduction of work notification

Some arguments and figures presented in the following chapters appear in the publications listed below. The work is reproduced in this dissertation in good faith and serves only to illustrate the author's contribution to each work over the course of his graduate study. Copyrights to any of the author's previously published art appearing in this dissertation are respected and belong to their corresponding journals.

Journal:

Gabriel Chow, Evan Uchaker, Guozhong Cao, Junlan Wang. (2014). Laser-induced Surface Acoustic Wave Characterization of Porous Nanostructured V_2O_5 Thin Film Electrodes. To be submitted soon.

Gabriel Chow, Phillip Miller, Junlan Wang. (2014). Mechanical Characterization of a Nanoporous Low-κ Zeolite Film by Laser-induced Surface Acoustic Waves and Nanoindentation. *Experimental Mechanics*. Submitted – In Review.

Qianrong Fang, Shuang Gu, Qingling Liu, **Gabriel Chow**, Junlan Wang, Wolfgang Maichen, Michael W. Deem, Shilun Qiu, Yushan Yan. (2014). Designed synthesis of 3D porous covalent organic frameworks as ultra-low-k materials. *Chemical Science*. Submitted – In Review.

Gabriel Chow, Rajwant S. Bedi, Yushan Yan, Junlan Wang. (2012). Zeolite as a Wear-resistant Coating. *Microporous and Mesoporous Materials.* 151, 346-351.

Rajwant S. Bedi, **Gabriel Chow,** Laura Zanello, Junlan Wang, Yushan Yan, (2012). Bioactive Materials for Regenerative Medicine: Zeolite-Hydroxyapatite Bone Mimetic Coatings. *Advanced Materials.* 14(3). 200-206

Christopher Lew, Yan Liu, David Kisailus, Grant M. Kloster, **Gabriel Chow**, Boyan Boyanov, Minwei Sun, Junlan Wang, Yushan Yan. (2011). Insight into On-Wafer Crystallization of Pure-Silica-Zeolite Films through Nutrient Replenishment. *Langmuir.* 27(7). 3283-3285

Patent:

Yushan Yan, Junlan Wang, **Gabriel Chow**, "Wear and Corrosion Resistant Zeolite Coating," disclosed by University of California Patent Office (2009), Published (2011)

Chapter 1 References:

BEDI, R. S., BEVING, D. E., ZANELLO, L. P. & YAN, Y. 2009. Biocompatibility of corrosion-resistant zeolite coatings for titanium alloy biomedical implants. *Acta Biomaterialia,* 5**,** 3265-3271.

BEVING, D. E., O'NEILL, C. R. & YAN, Y. 2008. Hydrophilic and antimicrobial low-silica-zeolite LTA and high-silica-zeolite MFI hybrid coatings on aluminum alloys. *Microporous and Mesoporous Materials,* 108**,** 77-85.

CHOW, G., BEDI, R. S., YAN, Y. & WANG, J. 2012. Zeolite as a wear-resistant coating. *Microporous and Mesoporous Materials,* 151**,** 346-351.

COUFAL, H., GRYGIER, R., HESS, P. & NEUBRAND, A. 1992. Broadband detection of laser-excited surface acoustic waves by a novel transducer employing ferroelectric polymers. *The Journal of the Acoustical Society of America,* 92**,** 2980-2983.

FREUND, L. B. & SURESH, S. 2003. *Thin Film Materials: Stress, Defect Formation and Surface Evolution*, Cambridge University Press.

HOLMBERG, B. A., WANG, X. & YAN, Y. 2008. Nanocomposite fuel cell membranes based on Nafion and acid functionalized zeolite beta nanocrystals. *Journal of Membrane Science,* 320**,** 86-92.

HRUBESH, L. W. 1998. Aerogel applications. *Journal of Non-Crystalline Solids,* 225**,** 335-342.

INTERNATIONAL ROADMAP COMMITTEE 2013. International Technology Roadmap for Semiconductors.

JOHANSSON, S., SCHWEITZ, J.-A., TENERZ, L. & TIREN, J. 1988. Fracture testing of silicon microelements in situ in a scanning electron microscope. *Journal of Applied Physics,* 63**,** 4799-4803.

JOHNSON, M. C., WANG, J. L., LI, Z. J., LEW, C. A. & YAN, Y. S. 2007. Effect of calcination and polycrystallinity on mechanical properties of nanoporous MFI zeolites. *Materials Science and Engineering a-Structural Materials Properties Microstructure and Processing,* 456**,** 58-63.

LEW, C. M., CAI, R. & YAN, Y. 2009. Zeolite Thin Films: From Computer Chips to Space Stations. *Accounts of Chemical Research,* 43**,** 210-219.

LI, Z. J., JOHNSON, M. C., SUN, M. W., RYAN, E. T., EARL, D. J., MAICHEN, W., MARTIN, J. I., LI, S., LEW, C. M., WANG, J., DEEM, M. W., DAVIS, M. E. & YAN, Y. S. 2006. Mechanical and dielectric properties of pure-silica-zeolite low-k materials. *Angewandte Chemie-International Edition,* 45**,** 6329-6332.

MEIER, W. & OLSON, D. 1992. *Atlas of zeolite structure types,* London, Boston, Butterworth-Heinemann.

OLIVER, W. C. & PHARR, G. M. 1992. An Improved Technique for Determining Hardness and Elastic-Modulus Using Load and Displacement Sensing Indentation Experiments. *Journal of Materials Research,* 7**,** 1564-1583.

RABE, U., SCHERER, V., HIRSEKORN, S. & ARNOLD, W. Nanomechanical surface characterization by atomic force acoustic microscopy. 1997 Beijing (China). AVS, 1506-1511.

SAIF, M. T. A. & MACDONALD, N. C. 1998. Microinstruments for submicron material studies. *Journal of Materials Research,* 13**,** 3353-3356.

SZOSTAK, R. 1992. *Handbook of Molecular Sieves*, Springer.

VERMEIREN, W. & GILSON, J. P. 2009. Impact of Zeolites on the Petroleum and Petrochemical Industry. *Topics in Catalysis,* 52**,** 1131-1161.

WALKER, J., GABRIEL, K. & MEHREGANY, M. 1991. Mechanical integrity of polysilicon films exposed to hydrofluoric acid solutions. *Journal of Electronic Materials,* 20**,** 665-670.

YEH, W.-F. & WANG, J. 2011. A Force Domain Analog-to-Digital Converter Applied in Micro and Nanoscale Tensile Tests. *In:* PROULX, T. (ed.) *Experimental and Applied Mechanics, Volume 6.* Springer New York.

Chapter 2 Characterization of wear and corrosion resistant zeolite coatings by nanoindentation and nanoscratch

2.1 Background and introduction

Hard chrome (Cr) coatings are known for their excellent abrasion resistance, low friction coefficient, and their capability to produce thick layers for rebuilding worn parts back to specification (Dubpernell, 1974). Cadmium (Cd) coatings are critical to aircraft fasteners as a sacrificial wear layer and to provide mild corrosion protection (Foulke and Brown, 1963). Both types of coatings remain the industrial standards in wear and corrosion protection even though they are electroplated using precursors that are known for causing cancer and other serious diseases (U.S. EPA, 1989, U.S. EPA, 1998). Alternatives to chromium and cadmium coatings have long been desired, but new technologies have suffered in either cost, performance, or deposition simplicity (Savarimuthu et al., 2001, Legg, 2002). Furthermore, the mindset behind many prospective alternatives remains fixated on mimicking the high hardness and modulus of hard chrome whereas current research suggests that a high hardness with relatively low modulus may be more beneficial to wear resistance (Ni et al., 2005, Leyland and Matthews, 2004). The low modulus aids in deformation absorption and recovery while the high hardness reduces any permanent deformation done to the coating.

Synthetic zeolite powders have been used as catalysts and separation media by exploiting their uniform porosity (Davis, 2002). Being virtually non-toxic, zeolites have found potential in medical applications such as in magnetic resonance imaging contrast agents and biocompatible coatings for implants where they produce no hazards to human health (Balkus and Bresinska, 1994, Bedi et al., 2009b, Bedi et al., 2009a). The specific high-silica-zeolite ZSM-5 coating studied in this work has shown exceptional corrosion resistance (Cheng et al., 2001, Cai and Yan, 2008). Exhibiting a porous framework, ZSM-5 is expected to have exceptional coating flexibility which serves as a deterrent to coating cracking, an effect often seen on hard chrome as a result of substrate bending and torsion (Jorgensen et al., 1995). The coating process has been demonstrated to be able to uniformly coat surfaces of complex shape and in confined spaces (Cheng et al., 2001, Cai and Yan, 2008). The purpose of this chapter is to examine the viability of ZSM-5 coatings in wear resistant applications by characterizing and comparing their mechanical and tribological properties to commercially electroplated chromium and cadmium coatings.

2.2 Structure of ZSM-5 zeolite

ZSM-5 is a specific zeolite framework that is also known as MFI. The name is short for Zeolite-Socony-Mobil-five where “SM” honors the petroleum company who pioneered its synthesis. The number five denotes the basic five-membered ring structure which classifies ZSM-5 as a member of the pentasil family. The fundamental pentasil unit defines a unique structure formed by eight five-membered rings with the rings themselves formed by AlO_4 and SiO_4 tetrahedra (also known as T-sites). Each pentasil unit can be bonded to neighboring units to form pentasil chains. The unit cell of ZSM-5 consists of several pentasil chains with 96 T-sites in total joined together. The unit cell features rings of 10 pentasil members which makeup the pore size and distribution. The final structure is famous for its set of straight pores in one dimension and zig-zag pores in the other dimensions. Both channels are ~0.5 nm in diameter (Kokotailo et al., 1978, Flanigen et al., 1978) and they produce a total porosity of ~33%.

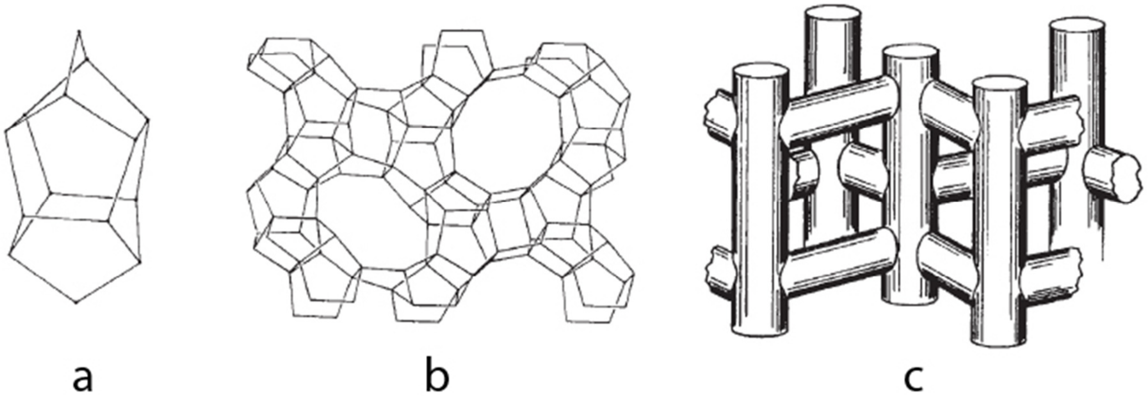

Figure 2-1. (a) single pentasil unit. (b) ZSM-5 unit cell. (c) ZSM-5 pore structure (Kokotailo et al., 1978).

2.3 Sample preparation

ZSM-5 coating synthesis was carried out following a previously established procedure (Lew et al., 2009) in a Teflon lined autoclave (Parr Instrument Co.) using tetrapropylammonium hydroxide (TPAOH, 40 wt % Sachem) as the structure directing agent (SDA), and tetraethylorthosilicate (TEOS, 97 wt % Aldrich) as the silica source. The molar composition of the solution was 0.16TPAOH : 0.64NaOH : TEOS : 92H_2O : 0.0018Al. The solution synthesis procedure is as following: 0.01040 g Al powder (200 mesh 99.95% Aldrich), 5.36 g NaOH pellets (97.5% Aldrich), and 100 g double de-ionized water were mixed and stirred for 30 minutes. 17.03 g TPAOH was then added and the solution was stirred for 15 minutes. This was followed by adding 236 g double de-ionized water and the solution was stirred for another 15 minutes. Afterwards 43.6 g TEOS was added in a dropwise fashion while stirring. The solution was left to stir for 4 hours to age. 1600 ml of solution was then added into the autoclave with two bare steel panels hanging vertically by a thin platinum wire. The panels were fully immersed in the solution with ~30 mm separation. The autoclave was subsequently sealed and heated at

175°C for 24 hours. The coated steel samples were rinsed with de-ionized water and dried in air upon removal from the autoclave.

Commonly used aircraft-grade 4130 unpolished steel from McMaster-Carr was chosen to be the substrate for all coatings (chromium, ZSM-5, and cadmium). Separate steel panels were electroplated with ~25.4 μm thick chromium following the SAE-AMS-2406 standard and ~7.6 μm thick cadmium following the SAE-AMS-QQ-P-416 standard by Multichrome Multiplate, Inglewood CA (SAE International, 2004, SAE International, 2007).

To prepare a smooth surface morphology for nanoindentation and nanoscratch, the chromium, ZSM-5, steel, and cadmium surfaces were polished to less than 10 nm root mean square (rms) surface roughness. For polishing, a Buehler Ecomet IV was used with hand force on various diamond pastes and alumina slurries. The polished chromium, ZSM-5, and cadmium coatings are smooth and with thickness of about 4, 4, and 3 μm respectively as measured by cross-sectional SEM.

2.4 Characterization Techniques

2.4.1 Nanoindentation

Nanoindentation is a more sophisticated variation of macroscale indentation, such as the Vickers and Knoop hardness tests, that has become a popular choice for thin film materials. The technique has gained attraction because it is simple to perform, easily applied to many materials, and requires little sample preparation. The test relies on a nanoscale probing tip making physical contact with the specimen, pressing inwards with a given force, and then unloading to leave an imprint on the surface. The force range is on the order of micro-newtons to milli-newtons and surface displacements are typically tens to hundreds of nanometers. This allows the deformation to be localized to the film thickness. Contrary to macroscale tests which usually only measure the plastic properties of materials, nanoindentation can provide both plastic and elastic properties by the assumption that the initial unloading of the sample contains only elastic behavior. Thus, by continuously acquiring force and displacement data during testing, the unloading region can be analyzed for the elastic properties. A schematic of a typical indentation is shown in Figure 2-2

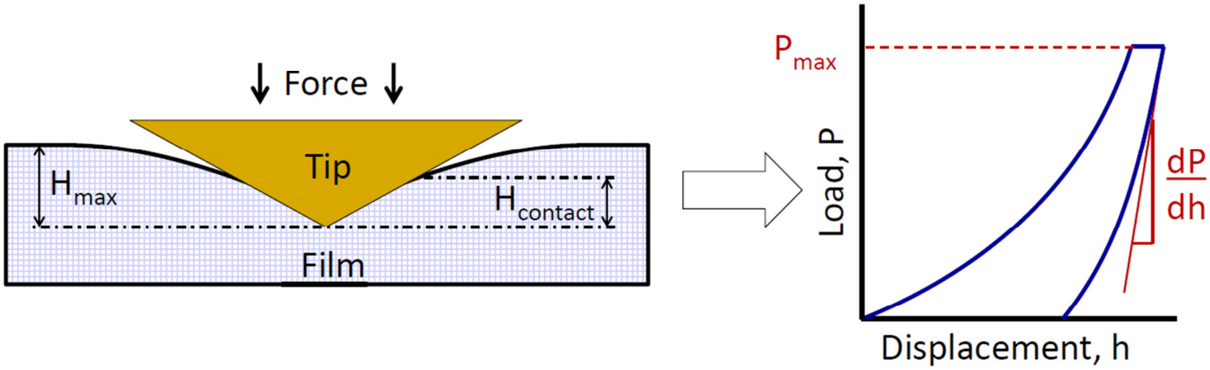

Figure 2-2. Schematic of indentation with important parameters for analysis labeled. H_{max} is the maximum penetration depth. $H_{contact}$ is the distance between the maximum depth and the depth where the sample surface loses contact with the tip. P_{max} is the maximum load. The stiffness, S, is defined as the initial slope of the unloading region dP/dh.

For a flat punch indentation into an elastic half-space, Sneddon showed that the slope of the unloading curve, defined as the indentation stiffness (S), follows the equation (Sneddon, 1965):

$$S = \frac{dP}{dh} = \beta M \sqrt{A_c} \tag{2-1}$$

where β is a constant depending on tip shape, M is the material's elastic modulus, A_c is the contact area, P is load, and h is depth. For a rigid flat punch, it was shown that $\beta = \frac{2}{\sqrt{\pi}}$.

However, several years later, King showed that various indenter shapes only change the value of β by a small amount (King, 1987). Thus, the equation above could be utilized for the more common triangular profiled indenter shapes such as the conical and Berkovich tips (3 sided pyramidal with a 142° total included angle). In the case of real materials, the indenter tip itself exhibits compliance, thus the modulus of the material and tip, M_{tip}, must be taken into account and a reduced modulus M_r must be utilized. Eq. (2-2) shows the modified form of Eq. (2-1) and the definition of the reduced modulus.

$$S = \frac{2}{\sqrt{\pi}} M_r \sqrt{A_c} \quad \text{where} \quad M_r = \left(\frac{1}{M} + \frac{1}{M_{tip}}\right)^{-1} \tag{2-2}$$

Even though nanoindentation tests exhibit considerable plastic deformation, it is assumed that initial unloading exhibits only elastic behavior. Thus Eq. (2-2), which describes an elastic indentation, can be used to extract the film properties from the elastic-plastic nanoindentation test if the stiffness and contact area at initial unloading are known.

Oliver and Pharr realized that the slope of unloading curves in nanoindentation tests were not constant and that they could be described by a power law of the following form (Oliver and Pharr, 1992):

$$P = \alpha\left(h_{max} - h_f\right)^m \tag{2-3}$$

where P is the indentation load, α and m are fitting coefficients, h_{max} is the maximum indentation depth, and h_f is the final indentation depth after unloading. After a proper fit is made, the stiffness from experimental loading curves, $S = dP/dh$, can be calculated at maximum load.

The remaining unknown in Eq. (2-2), the contact area, is a function of the tip shape and indentation depth. For tips with a varying cross-section along their indentation axes, the contact area depends on the depth at which the tip surface remains in contact with the sample, h_c, which is known as the contact depth. This parameter can be calculated in Eq. (2-4) if the elastic deflection of the surface is known.

$$h_c = h_{max} - h_s \tag{2-4}$$

where h_s is the elastic deflection of the surface. Referencing Sneddon's solution once again, the elastic deflection can be calculated by:

$$h_s = \epsilon \frac{P}{S} \tag{2-5}$$

where ϵ is a constant depending on tip shape (e.g., 0.72 for a Berkovich tip), P is the indentation load, and S is the stiffness. Once h_c is known for a specific indentation, the contact area can be found as a function of tip geometry and depth. For example, in the case of an ideal Berkovich tip, the area is $A_c = 24.5h_c^2$. However, in practice, the tip shape is not perfectly sharp and there exists some curvature at the vertex. A modified area function with additional coefficients is used to approximate the real tip with the form:

$$A_c(h_c) = C_0(h_c^2) + C_1(h_c) + C_2\left(h_c^{1/2}\right) + C_3\left(h_C^{1/4}\right) \ldots C_n(h_c^{2/2^n}) \tag{2-6}$$

where $C_{0\ldots n}$ are fitting coefficients. The area function is typically determined experimentally by indentation on a sample with established modulus (commonly fused quartz) at multiple indentation depths. Once the area function is known, the stiffness and contact area from Eq. (2-3 and 2-6) can be calculated from indentation loading curves on an unknown material and used to determine its modulus through Eq. (2-2).

Nanoindentation hardness is a function of tip geometry because the amount of plastic deformation is dependent on the tip shape. For an accurate comparison, the measurement needs to be repeated on all films with the same tip. Hardness is defined as:

$$H = \frac{P_{max}}{A_c} \tag{2-7}$$

where H is the sample hardness, P_{max} is the maximum indenter load, and A_c is the contact area.

Procedure:

Nanoindentation was performed by a Hysitron UBi1 nanomechanical test instrument (Hysitron, Minneapolis, MN). A diamond Berkovich tip (3 sided pyramidal, 142.3° total included angle, 150 nm tip radius) was employed for all measurements aside from friction where a 60° conical tip (5 µm tip radius) was used to negate scratch direction dependence. During indentation, the load followed a trapezoidal function composed of a 10 s ramp to maximum load, 5 s hold, and a 10 s unloading period. The hold time was used to mitigate any creep effects in the unloading curve. The maximum indentation force ranged from 100-5000 µN depending on the coating. The mechanical properties were calculated from the loading curves using the procedures outlined above. The tip modulus and Poisson's ratio used to extract the film modulus from the reduced modulus in Eq. (2-2) were respectively 1140 GPa and 0.07.

2.4.2 Nanoscratch

Nanoscratch measurements utilize the same indenter tip needed for nanoindentation, but introduce a lateral movement across the surface after the load is applied. This type of test can be used to determine the tribological properties of a material such as the wear resistance and friction coefficient. While the hardness of a film measured from nanoindentation can be indicative towards the wear resistance of a sample, nanoscratch tests are a better approximation of the sliding wear operation in materials.

There are several parameters measured during a nanoscratch test that are used to determine wear resistance and friction properties. For wear resistance, the final track depth after scratching for a given load is the main variable. The test needs to be performed at multiple loads, preferably much higher than the elastic limit of the material, in order to ensure that there is sufficient characterization of the plastic response. A comparison of the tip depth during scratch to the depth of the final wear track can be a good indicator of plastic response and elastic recovery. If the two depths are significantly different, then the material is exhibiting a strong elastic response and higher loads need to be investigated.

The ability to continuously monitor the normal and lateral force in nanoscratch instruments allows for the friction coefficient to be calculated from:

$$\mu = \frac{F_l}{F_n} \tag{2-8}$$

where μ is the fricition coefficient, F_l is the lateral force, and F_n is the normal force. An axisymmetric tip, such as the conical, is necessary to negate directional dependence of the scratch. In the friction test, it is desirable to use a lower force since excessive load will produce plowing effects leading to increased lateral forces.

Procedure:

Scratch testing was performed with a load function consisting of three sections. The indenter tip was pressed into the surface with no lateral movement and linearly ramped force, then moved laterally with a constant normal force, and lastly withdrawn with no lateral movement. All scratches in this study used time intervals of 3 seconds for linearly ramping force, 30 seconds for lateral movement, and 3 seconds for tip withdrawal. The scratch lengths were 4-5 μm and the maximum loads were between 100-8000 μN. The UBi1 features in-situ scanning probe microscopy (SPM) that allows for imaging of the surface before and after scratch or indentations. The final wear track depths were measured by this technique.

2.4.3 Corrosion resistance

Corrosion resistance of a part can be estimated through electrochemistry by the use of direct current (DC) polarization testing. In the test, an electrochemical cell is used to expose a specific area of the sample in question to an ionic solution. The application of an electrical potential through the solution allows for accelerated oxidation and reduction (corrosion) reactions at the metal sample. These reactions form a current that is measured continuously during the test. High corrosion currents are generally undesired and mean that the sample is more corrosive.

DC polarization testing was performed using a Solartron potentiostat SI 1287 in a three-electrode configuration and 0.856 M NaCl as the corrosive medium. The testing specimen was the working electrode, a platinum foil was the counter electrode, and an Ag/AgCl saturated KCl electrode was the reference electrode. During the test, the electric potential was ramped from -1 V to +1 V linearly with a rate of 1 mV/s while the current was continuously recorded.

2.5 Results for ZSM-5 films compared to chromium, cadmium, and steel

2.5.1 Nanoindentation results

Elastic modulus and hardness are key properties in the mechanical characterization of a wear resistant coating. The elastic modulus is an indication of resistance to elastic or recoverable deformation and hardness is an indication of resistance to plastic or permanent deformation. The modulus and hardness for chromium, ZSM-5, cadmium, and steel were measured at different loads and the average values are summarized in Table 2-1.

Table 2-1. Elastic modulus and hardness of Cr, ZSM-5, steel 4130, and Cd.

Sample	Elastic Modulus (GPa) E	Hardness (GPa) H	Resilience (MPa) U_r
Cr	265.6 ± 11.7	12.1 ± 0.3	30
ZSM-5	51.0 ± 2.5	6.3 ± 0.2	43
Steel 4130	94.0 ± 12.5	2.8 ± 0.2	4.6
Cd	80.6 ± 13.0	0.5 ± 0.1	0.2

Resilience is a property that governs how much deformation energy a material can absorb in the elastic regime and is directly related to the elastic strain limit of the material. Although hardness is usually directly related to the wear performance, one must also consider resilience because materials with higher resilience are expected to recover from a deformed state more readily. The modulus of resilience, U_r, can be expressed as:

$$U_r = \frac{\sigma_y^2}{2E} \qquad (2\text{-}9)$$

where σ_y is the yield strength, and E is the elastic modulus of the material. By using Tabor's approximation of yield strength with hardness (*H*) in compressive tests (Tabor, 1951), one can assume

$$\sigma_y \approx \frac{H}{3} \qquad (2\text{-}10)$$

then the modulus of resilience can be simplified as:

$$U_r \approx \frac{H^2}{18E} \qquad (2\text{-}11)$$

Utilizing the average hardness and modulus values, the resilience of the four materials are calculated and presented in Table 2-1.

With only ~50% the hardness of chromium as shown in Table 2-1, ZSM-5 might be expected to be less resistant to plastic deformation. However, the loading curves in Figure 2-3a shows the opposite. ZSM-5 incurs over twice the surface penetration at an indentation load of 500 μN leading to a maximum depth of 59.4 nm compared to that of chromium at 24.5 nm, but markedly recovers over 90% of the deformation upon unloading (Figure 2-3b), showing a final depth (5.0 nm) that is only half of that of chromium (9.6 nm). This demonstrates the significant role of the resilience in the ZSM-5 coating with less plastic deformation occurring in the indentation tests even with a hardness much lower than that of chromium (Figure 2-3a). Additionally, this highlights how the low modulus and high resilience of the zeolite coating can lead to exceptional flexibility as evidenced by the amount of deformation recovery compared to the other coatings.

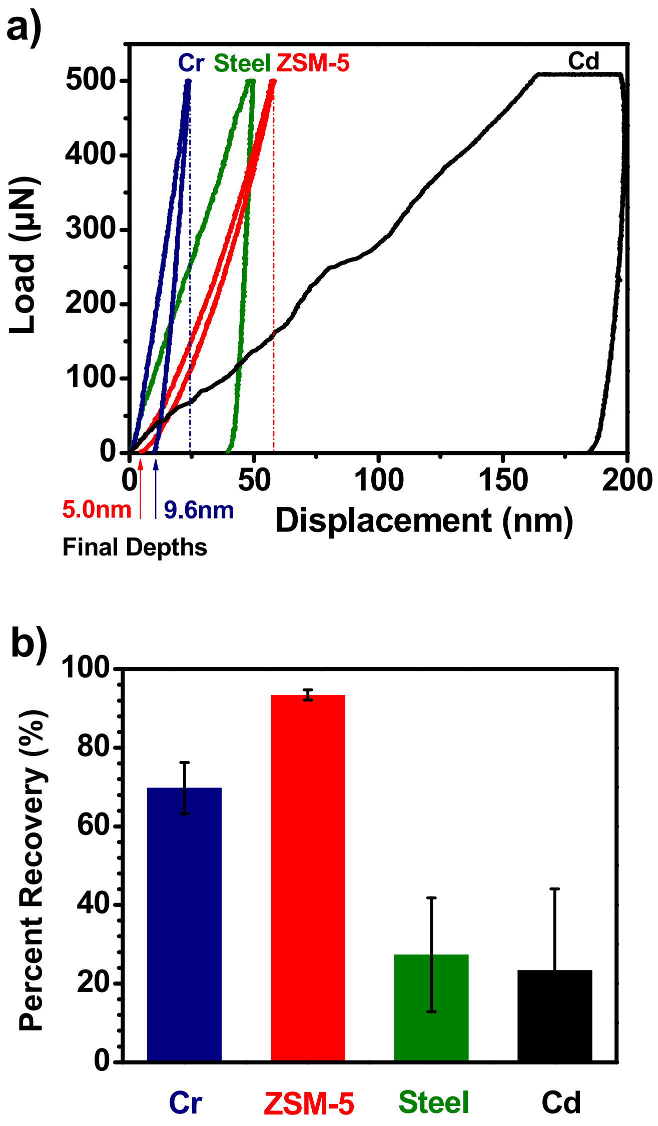

Figure 2-3. a) Hardness versus contact depth for all tested surfaces. b) Elastic modulus versus contact depth for all tested surfaces. Note: the softness of cadmium led to much larger penetration depths when compared to the other coatings even at low indentation loads such as < 100 µN. Reliable load-displacement curves required higher indentation loads thus the contact depths for cadmium used in property analysis were greater than the other coatings. The results, however, are still accurate since the elastic modulus should not

be dependent on contact depth considering the indentation depths and relatively large thicknesses of the materials investigated in this study.

From a material's point of view, the low elastic modulus of the ZSM-5 coating can be attributed to its porous framework. Theoretically, the strong ionic and covalent bonds should give zeolite a very high modulus (for example, a fully dense crystalline structure made of covalent bonds between silicon and oxygen atoms such as quartz has a Young's modulus around 72 GPa). However, it is well known that the materials with porosity can have a significantly lower elastic modulus than its dense counterpart (L. J. Gibson, 1983, Phani and Niyogi, 1987). On the other hand, the crystallinity of the zeolite coating provides the exceptional mechanical stability. When fracture is suppressed (as in the case of the current study), plasticity (or permanent deformation) happens in the same way in ceramics as in metals - dislocations move through the crystals when shear stress overcomes the lattice friction. Due to the strong ionic and covalent bonds in the crystalline structure, it takes a much larger stress to move dislocations in zeolites than in metals which gives rise to its great hardness and wear resistance.

2.5.2 Nanoscratch results

Figure 2-4 highlights the wear response of each of the four coatings to 500 μN constant normal force scratches. The plot clearly shows that the wear depth of ZSM-5 is much shallower than steel or cadmium at this load. The inset of Figure 2-4 compares ZSM-5 and chromium more directly and shows that ZSM-5 is once again shallower. From lowest to highest, the track depths were 4.2 ± 0.7 nm for ZSM-5, followed by 9.1 ± 1.0 nm for chromium, 37.0 ± 5.5 nm for steel, and 111.0 ± 27.4 nm for cadmium. Compared to chromium and ZSM-5, steel and cadmium already exhibited large amounts of deformation (9 and 26 times greater than that of ZSM-5 for steel and cadmium respectively) at the relatively small load of 500 μN, therefore testing at higher loads omitted these two surfaces.

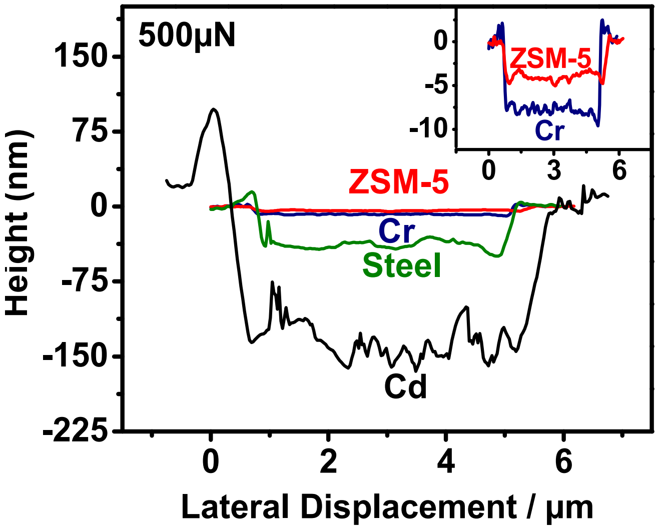

Figure 2-4. Scratch profiles (along scratch direction) for constant force 500 μN scratches on each surface.

Figure 2-5a shows scratch profiles at 1000 μN on ZSM-5 and chromium. At this loading level, ZSM-5 remains more wear resistant with shallower average scratch depth (14.2 ± 1.4 nm) compared to chromium (19.7 ± 1.0 nm). At an even higher scratch load of 1500 μN, ZSM-5 still held a slight advantage over chromium with an average scratch depth of 24.0 ± 1.8 nm compared to chromium's depth of 29.9 ± 1.6 nm. However, the difference in average depth between the two surfaces had reduced with increased load. There was only 27% difference between the average depths of ZSM-5 and chromium at 1500 μN compared to 38% at 1000 μN and 54% at 500 μN.

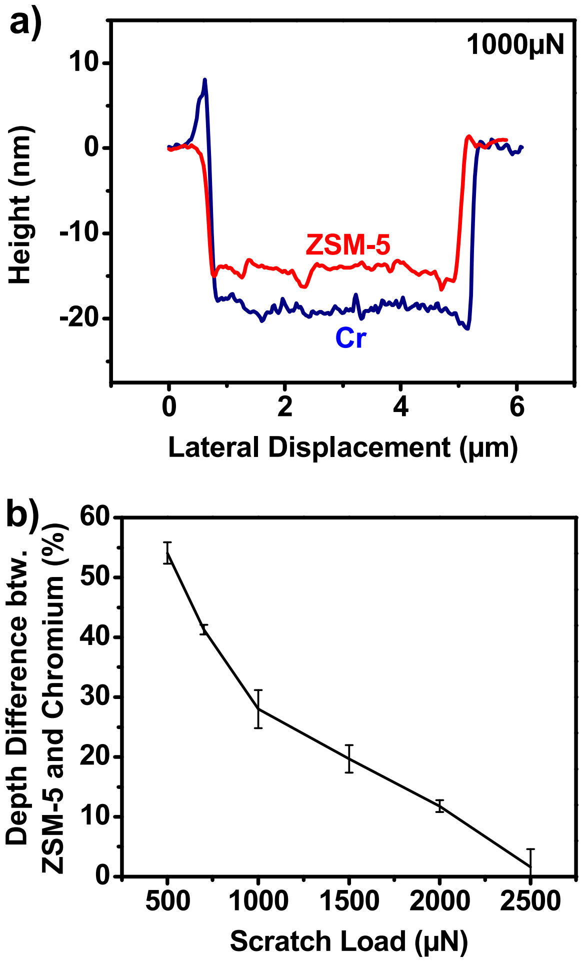

Figure 2-5. a) Scratch profiles for 1000 μN constant force scratches (5 μm in length) on ZSM-5 and Cr. b) Percent difference in average scratch depth between ZSM-5 and Cr with respect to scratch load.

Performing constant force scratches at 2000 μN and 2500 μN yielded a similar trend with average difference in the scratch depth steadily decreasing to 12% at 2000 μN and 2% at 2500 μN (Figure 2-5b). Since resilience is only applicable to the recovery of elastic deformations, the decrease in percent difference between the wear track depths of the two surfaces can be explained by plastic deformation dominating over the resilience of ZSM-5 at higher loads. Wear resistance is more dependent on hardness alone at very high loads as shown in Figure 2-5b where average depth converges at around 2500 μN. Chromium becomes more wear resistant if load were to be increased further. This is because at loads exceeding 2500 μN, non-recoverable plastic deformation dominates and zeolite does not possess the hardness, or resistance to plastic deformation, necessary to maintain a shallow wear track. Chromium, however, can rely on its high hardness, almost double that of ZSM-5, in order to be more wear-resistant at higher loads.

Although chromium does eventually become more wear resistant at ultra-high load due its higher hardness compared to ZSM-5, the stresses subjected to the ZSM-5 coating prior to the transition point are already well beyond the range of normal stresses ($\sigma = F_{Normal} / Area$) seen in many practical applications of hard chrome. In the range where ZSM-5 is more wear resistant, the highest normal stress went as high as ~3.5 GPa (Figure 2-6) whereas the maximum stresses on chromium coatings in pistons and chains rarely exceed 500 MPa (Patton, 1980, Neale, 1994, Halligan, 1983). Perhaps the instantaneously high local stresses in bearings and gears are highest at 1-4 GPa (Stolarski, 2000, Eschmann, 1985, Neale, 1993), but even then, the ZSM-5 coating is more wear resistant throughout most of that range. It should be noted that the stresses involved in a macroscale pin-on-disk test, the industrial standard in wear testing, are less than that of nanoscratch being within the megapascal range (Sundaram, 2006, Bayón et al., 2008, Fedrizzi et al., 2002). This is due to the load being applied with a blunter tip (6 mm diameter sphere); an effect that was mimicked by performing nanoindentation with a conical tip (5 μm radius). The larger tip once again showed the dominance of resilience in ZSM-5. Little plastic deformation occurs in ZSM-5 even at loads in excess of 8 mN while visible deformation was seen on the chromium coating starting at ~2 mN. This is due to the penetration of the blunt tip being absorbed over a larger area on the ZSM-5 coating therefore creating more recoverable elastic deformation.

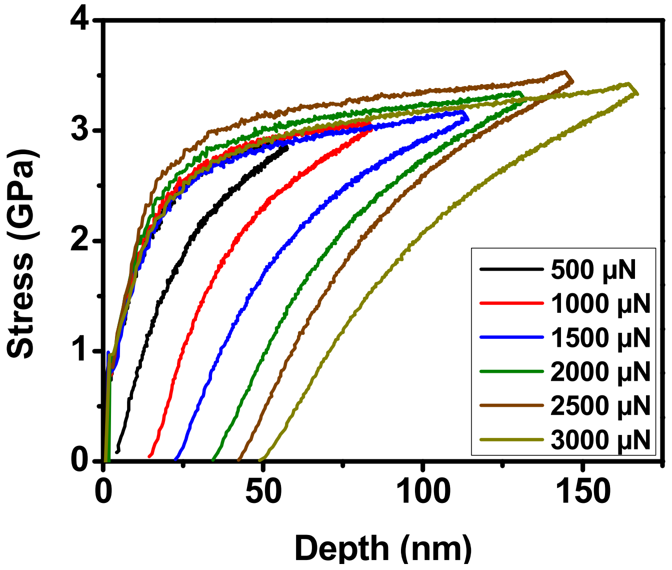

Figure 2-6. Normal stresses generated during 500-3000 µN indentations on the ZSM-5 coating with a Berkovich tip.

2.5.3 Friction results

Friction coefficients for 250 - 1500 µN constant force scratches on each material performed with the conical tip are shown in Figure 2-7. Cadmium showed high friction coefficient due to intrinsic softness leading to a plowing effect exhibited by large plastic deformations (especially at higher loads). Steel 4130 had similar friction coefficient to ZSM-5 and chromium at low loads (250 µN), but increased quickly with the onset of higher loading (0.35 at 1500 µN). Chromium and ZSM-5 both showed very similar performance throughout the entire testing range. This result indicates that ZSM-5 outperforms cadmium in lubricity on this scale and has equivalent performance to chromium. Although the friction results for cadmium are unfitting to the reported macroscale values where lubricity is similar to chromium (Oberg et al., 1992), it must be understood that the intent here was to interpret friction coupled with wear resistance. In the case for ZSM-5 and chromium, both coatings were able to maintain low friction coefficient and high wear resistance simultaneously. However, in cadmium, the poor wear resistance will negate any beneficial frictional properties since the cadmium coating is too easily removed to provide any consistent friction coefficient during intense wear conditions.

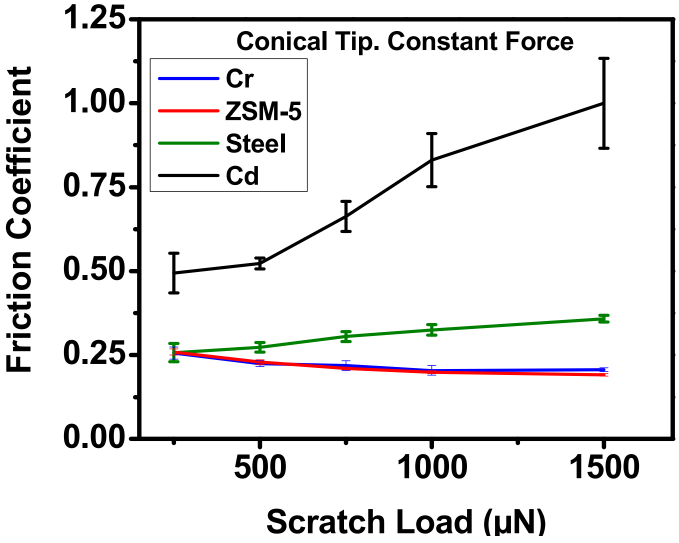

Figure 2-7. Friction coefficients for 5 μm length scratches with a 250-1500 μN loading range.

2.5.4 Corrosion results

Direct current (DC) polarization testing was performed to compare the corrosion resistance of the coatings (Figure 2-8). Materials with higher corrosion resistance are expected to exhibit lower current densities. Bare steel was used as the benchmark for comparison since it is least corrosion resistant and is used as the substrate for all coatings. Cadmium exhibited an order of magnitude less current density therefore it provided reasonable corrosion protection over steel. Chromium performed even better with about 3 orders of magnitude lower corrosion currents. But both electroplated coatings were dwarfed compared to ZSM-5 which granted 6 orders of magnitude lower corrosion currents.

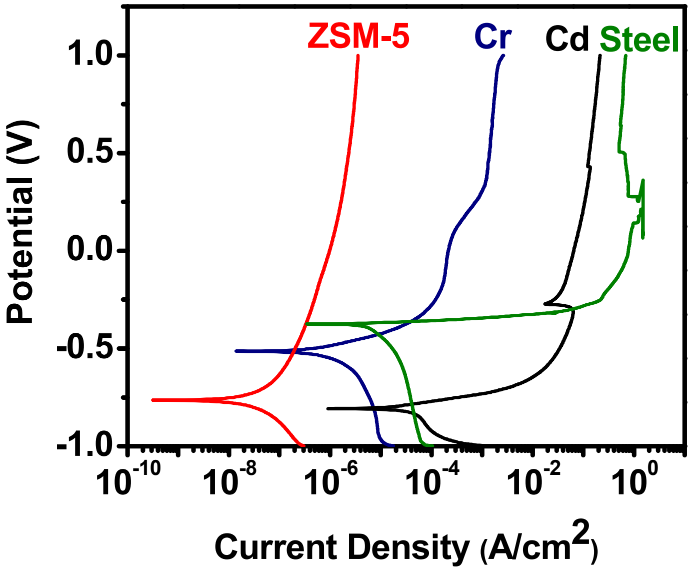

Figure 2-8. Direct Current polarization curves for ZSM-5, Cr, Cd, and steel 4130. Lower current density (x-axis in left direction) indicates more corrosion protection.

2.6 Conclusion

In summary, the ZSM-5 coating is more wear resistant than cadmium as demonstrated by an order of magnitude higher hardness and shallower depths upon scratching in each wear test. ZSM-5 coatings are also more wear resistant than chromium in most high wear applications. As for coefficient of friction, ZSM-5 is superior to cadmium and comparable to chromium. ZSM-5 coatings also dominate over both chromium and cadmium coatings in corrosion resistance by multiple orders of magnitude. In demonstrating superior wear and corrosion resistance in every test performed, ZSM-5 is unquestionably a suitable alternative to electroplated cadmium. ZSM-5 is also a viable alternative to electroplated chromium since it is more wear resistant under the conditions of most practical hard chrome applications and shows indisputably higher resilience and corrosion resistance.

Comparing with chromium, cadmium, and steel, zeolite has a relatively high hardness (~50% of Cr), but a very low elastic modulus (only ~20% of Cr). From a material perspective, the high hardness of zeolite can be attributed to its crystallinity rendered by the strong ionic and covalent bonds, while its low modulus is due to its porous structure. The unique balance between this high hardness and low elastic modulus leads to an excellent resilience (~43% higher than chromium) which in turn gives rise to an exceptional elastic recovery and also remarkable flexibility. It is this flexibility that sets ZSM-5 apart from conventional wear resistant coatings by easily springing back from a deformed state. Flexibility is also expected to offer an enhanced resistance to cracking during substrate bending and torsion.

Chapter 2 References:

BALKUS, K. J. & BRESINSKA, I. 1994. Molecular-Sieve Based Mri Contrast Agents. *Journal of Alloys and Compounds,* 207**,** 25-28.

BAYÓN, R., IGARTUA, A., RUIZ DE GOPEGUI, U. & MENDOZA, G. Corrosion-wear studies on PVD coatings for aeronautical applications. Innovation for Sustainable Production, 2008 Bruges, Belguim.

BEDI, R. S., BEVING, D. E., ZANELLO, L. P. & YAN, Y. 2009a. Biocompatibility of corrosion-resistant zeolite coatings for titanium alloy biomedical implants. *Acta Biomaterialia,* 5**,** 3265-3271.

BEDI, R. S., ZANELLO, L. P. & YAN, Y. 2009b. Osteoconductive and Osteoinductive Properties of Zeolite MFI Coatings on Titanium Alloys. *Advanced Functional Materials,* 19**,** 3856-3861.

CAI, R. & YAN, Y. 2008. Corrosion-resistant zeolite coatings. *Corrosion,* 64**,** 271-278.

CHENG, X. L., WANG, Z. B. & YAN, Y. S. 2001. Corrosion-resistant zeolite coatings by in situ crystallization. *Electrochemical and Solid State Letters,* 4**,** B23-B26.

DAVIS, M. E. 2002. Ordered porous materials for emerging applications. *Nature,* 417**,** 813-821.

DUBPERNELL, G. 1974. *Chromium,* New York, John Wiley & Sons.

ESCHMANN, P. 1985. *Ball and Roller Bearings,* New York, Wiley.

FEDRIZZI, L., ROSSI, S., BELLEI, F. & DEFLORIAN, F. 2002. Wear-corrosion mechanism of hard chromium coatings. *Wear,* 253**,** 1173-1181.

FLANIGEN, E. M., BENNETT, J. M., GROSE, R. W., COHEN, J. P., PATTON, R. L., KIRCHNER, R. M. & SMITH, J. V. 1978. Silicalite, a new hydrophobic crystalline silica molecular sieve. *Nature,* 271**,** 512-516.

FOULKE, D. G. & BROWN, H. 1963. *Cadmium,* New York, John Wiley & Sons.

HALLIGAN, B. D. 1983. *Seals for Fluid Power Equipment,* New York, Elsevier Scientific Pub. Co.

JORGENSEN, O., HORSEWELL, A., SORENSEN, B. F. & LEISNER, P. 1995. The Cracking and Spalling of Multilayered Chromium Coatings. *Acta Metallurgica Et Materialia,* 43**,** 3991-4000.

KING, R. B. 1987. Elastic analysis of some punch problems for a layered medium. *International Journal of Solids and Structures,* 23**,** 1657-1664.

KOKOTAILO, G. T., LAWTON, S. L., OLSON, D. H. & MEIER, W. M. 1978. Structure of synthetic zeolite ZSM-5. *Nature,* 272**,** 437-438.

L. J. GIBSON, M. F. A. 1983. The mechanics of three-dimensional cellular materials. *Proc. R. Soc. Lond. A,* 382**,** 43-59.

LEGG, K. Overview of Chromium and Cadmium Alternative Technologies. *In:* JEANDIN, T. S. S. A. M., ed. Surface Modification Technologies XV, 2002.

LEW, C. M., CAI, R. & YAN, Y. 2009. Zeolite Thin Films: From Computer Chips to Space Stations. *Accounts of Chemical Research,* 43**,** 210-219.

LEYLAND, A. & MATTHEWS, A. 2004. Design criteria for wear-resistant nanostructured and glassy-metal. *Surface & Coatings Technology,* 177**,** 317-324.

NEALE, M. J. 1993. *Bearings,* Boston, Butterworth-Heinemann.

NEALE, M. J. 1994. *Drives and Seals,* Boston, Butterworth-Heinemann.

NI, W. Y., CHENG, Y. T., LUKITSCH, M., WEINER, A. M., LEV, L. C. & GRUMMON, D. S. 2005. Novel layered tribological coatings using a superelastic NiTi interlayer. *Wear,* 259**,** 842-848.

OBERG, E., JONES, F. D., HORTON, H. L. & RYFFEL, H. H. 1992. *Machinery's Handbook*, Industrial Press Inc.

OLIVER, W. C. & PHARR, G. M. 1992. An Improved Technique for Determining Hardness and Elastic-Modulus Using Load and Displacement Sensing Indentation Experiments. *Journal of Materials Research,* 7**,** 1564-1583.

PATTON, W. J. 1980. *Mechanical Power Transmission,* New Jersey, Prentice-Hall.

PHANI, K. K. & NIYOGI, S. K. 1987. Young's modulus of porous brittle solids. *Journal of Materials Science,* 22**,** 257-263.

SAE INTERNATIONAL 2004. Standard. SAE-AMS-QQ-P416. Plating, Cadmium (Electrodeposited).

SAE INTERNATIONAL 2007. Standard. SAE-AMS-2406: Plating, Hard Chromium.

SAVARIMUTHU, A. C., TABER, H. F., MEGAT, I., SHADLEY, J. R., RYBICKI, E. F., CORNELL, W. C., EMERY, W. A., SOMERVILLE, D. A. & NUSE, J. D. 2001. Sliding wear behavior of tungsten carbide thermal spray coatings for replacement of chromium electroplate in aircraft applications. *Journal of Thermal Spray Technology,* 10**,** 502-510.

SNEDDON, I. N. 1965. The relation between load and penetration in the axisymmetric boussinesq problem for a punch of arbitrary profile. *International Journal of Engineering Science,* 3**,** 47-57.

STOLARSKI, T. A. 2000. *Tribology in Machine Design,* Boston, Butterworth Heinemann.

SUNDARAM, V. S. 2006. Diamond like carbon film as a protective coating for high strength steel and titanium alloy. *Surface & Coatings Technology,* 201**,** 2707-2711.

TABOR, D. 1951. *The Hardness of Metals,* New York, Oxford University Press.

U.S. EPA 1989. Toxicological Review of Cadmium.

U.S. EPA 1998. Toxicological Review of Hexavalent Chromium.

Chapter 3 Theoretical basis of surface acoustic waves on thin films

3.1 Preface to the following chapters

The mechanical processes of waves in matter naturally allow for the study of mechanical behavior through wave motion. The investigation of wave propagation characteristics has yielded many mathematical formulations that couple the behavior to mechanical parameters. There are many types of wave motion. However, one type in particular, the Rayleigh wave, is of specific interest to thin films. Rayleigh waves exhibit unique dispersive behavior on layered materials that allows for the isolation of film and substrate properties. They are also easily measured due to their localized propagation on the surface of materials.

The use of Rayleigh waves to determine the mechanical properties of layered systems is a problem that must be completed on two fronts. On the experimental side, a method to generate repeatable Rayleigh waves at a specific location in the unknown system must be employed in order to achieve reliable waveforms. A separate system is needed to detect the propagating wave in order to capture the motion for later analysis. The experimental Rayleigh waves by themselves are meaningless and require fitting to a theoretical model that predicts the wave motion for given mechanical parameters. This forms the second major front, the theoretical side. From theory, mechanical properties and system geometry are used to calculate the behavior of waves in a material system. The primary goal is to develop a theoretical wave that matches the experimentally observed results and then export the mechanical properties used to generate such a wave.

The experimental and theoretical studies are usually performed together to complement one another. However, they can also be done completely separately. For example, the theoretical studies do not have to solely fit mechanical properties to the experimental results. The model can also be used to predict expected behavior for systems that have yet to be tested. This is a powerful tool that can be used to determine the experimental viability of a system in question prior to testing. Chapter 3 is devoted to detailing the theoretical side by providing an introduction to wave characteristics and describing the mathematical formulations behind Rayleigh waves on different material systems.

Chapter 4 details the experimental side by describing the generation and detection of SAWs in practice. Signal processing techniques are overviewed and the process of readying each signal for theoretical comparison is described.

Chapter 5 puts the two sides together by showing the application of the complete technique. Several layered systems are investigated and discussed in detail. The results for zeolite films are presented and a critique of mechanical characterization by LiSAW and nanoindentation for such films is given.

From the experiments conducted in Chapter 5, several areas for potential LiSAW optimization came to light. Chapter 6 investigates these optimizations with specific interest in extending the frequency and dispersion response of SAWs. These two parameters combined could significantly enhance the quality of dispersion curves obtained in the LiSAW experiment.

In Chapter 7, LiSAW is utilized to explore a porous nanostructured electrode thin film. The surface engineering of these films produces substantial challenges towards consistent nanoindentation tests and the methodology may be impossible to apply in certain scenarios. Thus, LiSAW is investigated as an alternative technique for the mechanical characterization of such media.

3.2 Background and introduction to surface waves

Of the many types of waves found in nature, surface waves have fallen into particular interest for engineering applications. Unlike traditional longitudinal and transverse body waves, surface waves propagate along and are localized to the boundary between two materials and/or phases. The ability to generate and detect surface waves externally is an obvious advantage for non-destructive testing and it was found that significant information about the material could be gathered by such waves.

Surface waves were first detailed by Lord Rayleigh in the late 19th century when he correctly predicted the existence of an elastic wave localized to within a few wavelengths of the surface (Rayleigh, 1885). The motion features both compression and shear modes giving particles an elliptical path as the wave passes. Rayleigh waves exhibit motion similar to rolling oceanic waves, however their movements are derived and sustained from elasticity rather than gravity (for liquid waves). The wave decays exponentially into the surface such that the majority of the energy is dissipated in a single wavelength. Rayleigh waves quickly became critical in the understanding of seismology with considerable research devoted to the area. Other surface waves were soon discovered. In 1911, Love found purely transversal surface waves that exist in the presence of a layered structure with differing acoustic properties (Love, 1911). These became known as Love waves and they are a significant contributor to the horizontal movement in earthquakes derived from the earth's layered crust. In 1917, Lamb described body waves in thin plates that had surface characteristics similar to that of Rayleigh waves (Lamb, 1917). One key aspect for Lamb waves is that they are dispersive in nature, that is, their velocity is a function of frequency. It is shown later that this condition can be very useful for mechanical characterization. However, the requirement of a thin geometry for Lamb waves limits their applicability. The last notable surface wave is the Stoneley wave which is confined along the interface of two materials (Stoneley, 1924). Typically, they are seen at the liquid solid interface, but can also exist between two solids.

The wave types mentioned above have revolutionized the field of seismology. The understanding of their wave characteristics has led to many practical applications in engineering. Rayleigh waves in particular makeup a large fraction of these applications since there are no constraints to their existence, as long as a free surface is available. The majority of surface wave energy is devoted to propagation of the Rayleigh mode and their relatively long attenuation distances make them practical to measure (Woods, 1968). The ability for Rayleigh waves to become dispersive in layered systems is fundamental to their utility in thin films and it forms the topic of the next section.

3.3 Application of Rayleigh waves to thin films

Rayleigh waves have become very popular in the field of ultrasonic non-destructive testing as a means of inspecting structural members. The presence of defects, residual stresses, and other material flaws can be acquired by analyzing the attenuation and scattering of Rayleigh waves as they travel across a sample surface (Cook and Berthelot, 2001, Warren et al., 1996, Vu and Kinra, 1985). This is possible in part due to the fact that Rayleigh waves in bulk materials are non-dispersive therefore their waveforms should remain intact during propagation. Upon arrival at a surface defect, the wave can be diffracted with dependence on the size and shape of the flaw. It is common to detect Rayleigh waves at multiple distances away from the source in order to see their behavior change with propagation distance. These evaluation methods are generally limited to bulk materials. For thin films, the method of characterization is based on dispersion of Rayleigh waves, rather than their scattering.

For a homogeneous isotropic material, the Rayleigh wave speed, c_r can be approximated by:

$$c_r = \frac{0.87+1.12\nu}{1+\nu}\sqrt{\frac{E}{2\rho(1+\nu)}} \qquad (3\text{-}1)$$

where ν is the Poisson's ratio, E is the elastic modulus, and ρ is the material density. Equation (3-1) shows that there can be no variation of wave speed with respect to frequency for bulk materials. However, for layered structures, such as the case of thin films on substrates, the behavior of Rayleigh waves becomes dispersive because the acoustic properties of the substrate and layer are dissimilar. The dispersion can be explained as follows: imagine that the layer has some preferred Rayleigh wave speed and the substrate has another. Knowing that the motion of Rayleigh waves is, for the most part, constrained to within one wavelength of the surface, then longer wavelengths should penetrate deeper into the material while shorter wavelengths stay near the surface. Thus, the velocity of low frequencies is more influenced by the substrate while the velocity of high frequencies sees more influence from the film. The effect is shown in Figure 3-1.

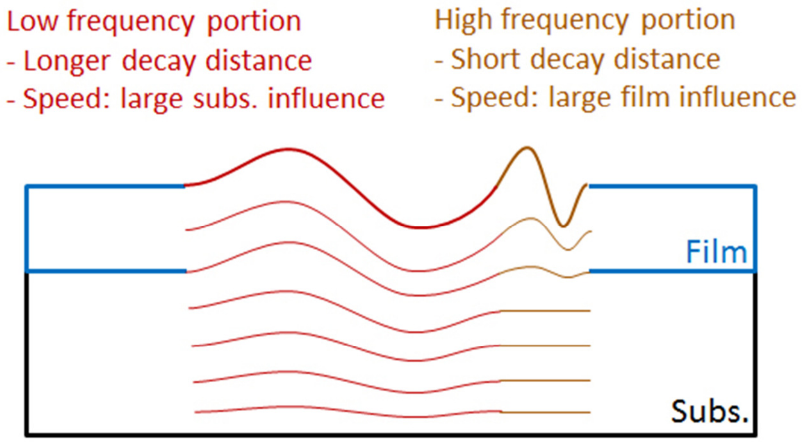

Figure 3-1. Illustration of the decay of Rayleigh waves with varying frequency.

It is now apparent that for a layered system, the Rayleigh wave speed does not have a single solution. Instead it takes the form:

$$c_r(f) = F(E_f, \nu_f, \rho_f, E_s, \nu_s, \rho_s, t_f) \tag{3-2}$$

where f is frequency, F denotes a function, $E_f, \nu_f,$ and ρ_f are the modulus, Poisson's ratio, and density of the film, $E_s, \nu_s,$ and ρ_s are the properties of the substrate, and t_f is the film thickness. From Eq. (3-2), it is seen that the dispersion of Rayleigh waves on layered systems is dependent on the mechanical properties of the materials involved. Since the combination of all three mechanical parameters between two materials can vary greatly, the dispersion relation for any one specific layered structure of a given thickness can be considered unique. This forms the basis of mechanical characterization by surface acoustic waves. There exists a theoretical solution for the dispersion relation of a layered system if all of the parameters in Eq. (3-2) are either known or assumed. If a dispersion relation is determined from experiment with unknown materials, theoretical dispersion relations can be calculated and fit to the result by successively adjusting the variables until a good correlation is achieved between theory and experiment. This process is aided by the fact that multiple film and substrate properties are usually known. The procedure for calculating dispersion relations (i.e. solving Eq. (3-2)) from theory is given in the next section.

3.4 Mathematical derivation of dispersion curves

3.4.1 Isotropic films and substrates

The derivation of dispersion relations for a layered system with assumed mechanical parameters and geometry was first detailed by Farnell (Farnell and Adler, 1972). His procedure described an isotropic layer on an isotropic substrate which is the simplest of all cases. In this scenario, the derivation can be performed analytically up until the final stages. The end goal is to produce dispersion curves which plot the relation for Rayleigh wave speed with respect to frequency (or wavelength). These curves can be used to fit mechanical properties to experimental results or predict the behavior of any layered system.

In the derivation, we consider a layered structure with the coordinate system shown in Figure 3-2. In the system, x_1 is the direction of SAW propagation and x_3 defines the direction normal to the layer with its origin set at the interface. It is assumed that all parallel SAWs propagate with the same dispersion therefore negating x_2 dependence.

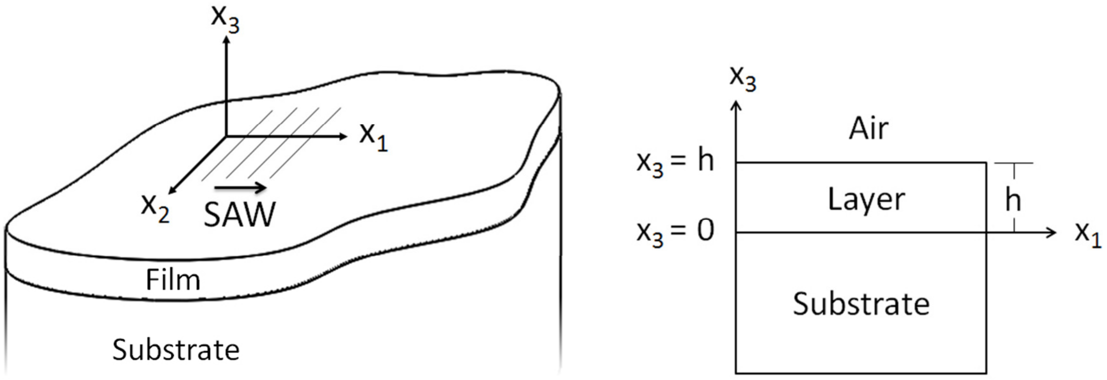

Figure 3-2. Schematic of layer and substrate with coordinate axes drawn (Farnell and Adler, 1972).

The governing equation for particle displacements is derived from the equilibrium equation. In the layer, the equation is defined as:

$$\rho \frac{\partial^2 u_j}{\partial t^2} = c_{ijkl} \frac{\partial^2 u_k}{\partial x_i \partial x_l} \qquad (i, j, k, l = 1,2,3) \tag{3-3}$$

where ρ is the density, u_j is the particle displacements along the j-direction, and c_{ijkl} is the stiffness tensor. Although the stiffness tensor should have 81 components, symmetry relations provide significant reduction and the tensor can be written in matrix form (c_{mn}) with 36 components. For isotropic materials, this matrix simplifies further with only two independent elastic constants. For a SAW propagating along the x_1 direction on the layer, we assume a generalized wave equation where the SAW is composed of linear combinations of partial waves:

$$u_j = \alpha_j \exp(ikbx_3) \exp[ik(x_1 - vt)] \tag{3-4}$$

where α is the relative amplitude of each partial wave, k is the wave number, b is a complex term that has information on the phase and variation of amplitude with depth of partial waves, and v is the phase velocity. Eq. (3-4) must satisfy the governing equation therefore substituting into Eq. (3-3) gives 3 equations:

$$\alpha_1 c_{11} + \alpha_1 c_{55} b^2 + \alpha_3 c_{13} b = \alpha_1 \rho v^2 \tag{3-5a}$$

$$\alpha_2 c_{66} + \alpha_2 c_{44} b^2 = \alpha_2 \rho v^2 \tag{3-5b}$$

$$\alpha_1 c_{31} b + \alpha_3 c_{55} + \alpha_3 c_{33} b^2 = \alpha_3 \rho v^2 \tag{3-5c}$$

Notice that the exponential components present in all terms of Eq. (3-5) have been cancelled out. We know that $c_{44} = c_{55} = c_{66}$ and $c_{13} = c_{31} = c_{11} - c_{44}$ for isotropic materials therefore the equations can be simplified further. Combining Eq. (3-5) into matrix form gives:

$$\begin{bmatrix} c_{11} + b^2 c_{44} - \rho v^2 & 0 & b(c_{11} - c_{44}) \\ 0 & c_{44} + b^2 c_{44} - \rho v^2 & 0 \\ b(c_{11} - c_{44}) & 0 & c_{11} + b^2 c_{44} - \rho v^2 \end{bmatrix} \begin{bmatrix} \alpha_1 \\ \alpha_2 \\ \alpha_3 \end{bmatrix} = 0 \tag{3-6}$$

This is an eigenvalue problem of the form $[\Gamma_{ij} - \rho v^2 \delta_{ij}]\alpha_k = 0$. By taking the determinant of the 3×3 matrix and equating to zero (for non-trivial solutions), the characteristic equation for the eigenvalues is given by:

$$(c_{44} + c_{44} b^2 - \rho v^2)^2 (c_{11} b^2 - \rho v^2 + c_{11}) = 0 \tag{3-7}$$

For an assumed phase velocity, solving for b yields roots of the following form:

$$b = \pm \frac{\sqrt{c_{44}(-c_{44} + \rho v^2)}}{c_{44}}, \pm \frac{\sqrt{c_{11}(-c_{11} + \rho v^2)}}{c_{11}} \tag{3-8}$$

The roots in Eq. (3-8) are for the layer. We can follow the same procedure as presented in Eq. (3-2 to 3-8) for the substrate and will arrive at similar roots (material properties embedded in the stiffness terms will be the difference) since like the layer, the substrate is isotropic. The corresponding eigenvectors for each root can be found by substituting each root into Eq. (3-6) and solving for the alpha column vector successively.

In total we will have 8 independent roots for the substrate and layer. Since we assume an infinite substrate, the wave must decay with depth therefore only the negative roots for the substrate are retained. The layer has a finite thickness therefore all layer roots are admissible (the SAW can grow, decay, or stay constant with respect to depth). By considering the transverse and longitudinal wave speeds, v_t and v_l respectively:

$$v_t = \sqrt{\frac{c_{44}}{\rho}} \quad , \quad v_l = \sqrt{\frac{c_{11}}{\rho}} \tag{3-9}$$

we can further simplify Eq. (3-8) to:

$$\frac{\sqrt{c_{44}(-c_{44}+\rho v^2)}}{c_{44}} \Rightarrow i\sqrt{\frac{c_{44}-\rho v^2}{c_{44}}} \Rightarrow i\sqrt{1-v^2(\frac{\rho}{c_{44}})} \Rightarrow i\sqrt{1-(\frac{v}{v_t})^2} \tag{3-10}$$

This simplification can be applied similarly to all roots whereby the final roots for the substrate and layer (denoted with carats) and their corresponding eigenvectors are:

Layer:

$$b^{(1)} = +i\sqrt{1-(v/\hat{v}_t)^2} \qquad \alpha^{(1)} = (-b^{(1)},0,1) \tag{3-11}$$

$$b^{(2)} = +i\sqrt{1-(v/\hat{v}_l)^2} \qquad \alpha^{(2)} = (1,0,b^{(2)})$$

$$b^{(3)} = -i\sqrt{1-(v/\hat{v}_t)^2} \qquad \alpha^{(3)} = (-b^{(3)},0,1)$$

$$b^{(4)} = -i\sqrt{1-(v/\hat{v}_l)^2} \qquad \alpha^{(4)} = (1,0,b^{(4)})$$

Substrate:

$$b^{(c)} = -i\sqrt{1-(v/v_t)^2} \qquad \alpha^{(c)} = (-b^{(c)},0,1) \tag{3-12}$$

$$b^{(d)} = -i\sqrt{1-(v/v_l)^2} \qquad \alpha^{(d)} = (1,0,b^{(d)})$$

The physical meaning of this is that there are four partial wave solutions in the layer and two in the substrate.

Boundary Conditions:

For this problem, the following six boundary conditions are set forth. Remember, the origin of x_3 is set at the interface.

@ $x_3 = 0$: $u_1 = \hat{u}_1$, $u_3 = \hat{u}_3$, $\sigma_{31} = \hat{\sigma}_{31}$, $\sigma_{33} = \hat{\sigma}_{33}$

@ $x_3 = h$: $\hat{\sigma}_{31} = 0$, $\hat{\sigma}_{33} = 0$

The boundary conditions represent displacement and stress continuity at the interface and zero free surface stress. The shear and normal stresses in our problem can be expressed by:

$$\sigma_{3j} = c_{3jkl} \frac{\partial u_k}{\partial x_l} \tag{3-13}$$

To satisfy these boundary conditions, we apply weighting factors, C_n, to each partial wave and then sum the waves together for our displacement solutions:

Layer: $$\hat{u}_j = \left\{ \sum_n C_n \alpha_j^{(n)} \exp(ikb^{(n)} x_3) \right\} \exp[ik(x_1 - vt)] \tag{3-14}$$

Substrate: $$u_j = \left\{ \sum_m C_m \alpha_j^{(m)} \exp(ikb^{(m)} x_3) \right\} \exp[ik(x_1 - vt)] \tag{3-15}$$

For the layer, $n = 1,2,3,4$ corresponding to the four layer roots and their eigenvectors. Similarly for the substrate, $m = c, d$. With six boundary conditions, six partial waves, and six weighting factors, we can express the equations generated by Eq. (3-13 to 3-15) in a 6×6 matrix as shown in Figure 3-3 and Eq. (3-16).

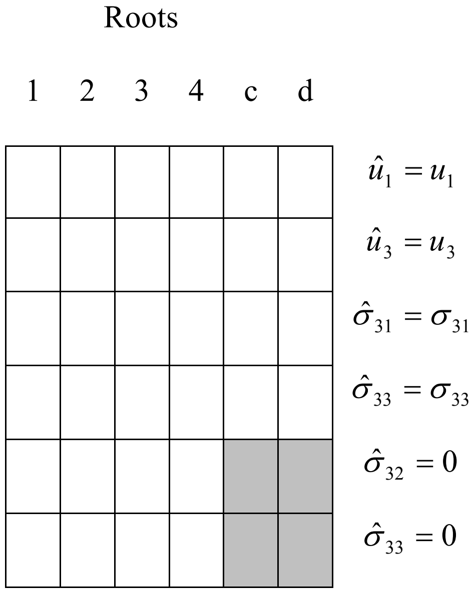

Figure 3-3. Format of 6×6 boundary condition matrix.

$$\begin{bmatrix} -\alpha_1^{(1)} & -\alpha_1^{(2)} & -\alpha_1^{(3)} & -\alpha_1^{(4)} & \alpha_1^{(c)} & \alpha_1^{(d)} \\ -\alpha_3^{(1)} & -\alpha_3^{(2)} & -\alpha_3^{(3)} & -\alpha_3^{(4)} & \alpha_3^{(c)} & \alpha_3^{(d)} \\ \begin{array}{l}[-(\hat{c}_{15}+\hat{c}_{55}b^{(1)})\alpha_1^{(1)}\ldots \\ \ldots-(\hat{c}_{55}+\hat{c}_{35}b^{(1)})\alpha_3^{(1)}]\end{array} & (\ldots) & (\ldots) & (\ldots) & \begin{array}{l}[-(c_{15}+c_{55}b^{(c)})\alpha_1^{(c)}\ldots \\ \ldots-(c_{55}+c_{35}b^{(c)})\alpha_3^{(c)}]\end{array} & (\ldots) \\ \begin{array}{l}[-(\hat{c}_{13}+\hat{c}_{35}b^{(1)})\alpha_1^{(1)}\ldots \\ \ldots-(\hat{c}_{35}+\hat{c}_{33}b^{(1)})\alpha_3^{(1)}]\end{array} & (\ldots) & (\ldots) & (\ldots) & \begin{array}{l}[-(c_{13}+c_{35}b^{(c)})\alpha_1^{(c)}\ldots \\ \ldots-(c_{35}+c_{33}b^{(c)})\alpha_3^{(c)}]\end{array} & (\ldots) \\ \begin{array}{l}[-(\hat{c}_{15}+\hat{c}_{55}b^{(1)})\alpha_1^{(1)}\ldots \\ \ldots-(\hat{c}_{55}+\hat{c}_{35}b^{(1)})\alpha_3^{(1)}]\ldots \\ \ldots\times[\exp(ikb^{(1)}h)]\end{array} & (\ldots) & (\ldots) & (\ldots) & 0 & 0 \\ \begin{array}{l}[-(\hat{c}_{13}+\hat{c}_{35}b^{(1)})\alpha_1^{(1)}\ldots \\ \ldots-(\hat{c}_{35}+\hat{c}_{33}b^{(1)})\alpha_3^{(1)}]\ldots \\ \times[\exp(ikb^{(1)}h)]\end{array} & (\ldots) & (\ldots) & (\ldots) & 0 & 0 \end{bmatrix} \begin{bmatrix} C_1 \\ C_2 \\ C_3 \\ C_4 \\ C_c \\ C_d \end{bmatrix} = 0$$

(Eq. 3-16)

In order to satisfy the matrix for the first four boundary conditions, the four corresponding rows in Eq. (3-16) are equated to zero therefore a negative sign is distributed into the layer terms. Inserting the eigenvector terms from Eq. (3-11 and 3-12) into Eq. (3-16) and noting that c_{15} and c_{35} are zero in the stiffness matrix, we have:

$$\begin{bmatrix} b^{(1)} & -1 & b^{(3)} & -1 & -b^{(c)} & 1 \\ -1 & -b^{(6)} & -1 & -b^{(8)} & 1 & b^{(d)} \\ -\hat{c}_{55}(1-b^{(1)2}) & -\hat{c}_{55}(2b^{(2)2}) & -\hat{c}_{55}(1-b^{(3)2}) & -\hat{c}_{55}(2b^{(4)2}) & c_{55}(1-b^{(c)2}) & 2c_{55}b^{(d)} \\ (\hat{c}_{13}-\hat{c}_{33})b^{(1)} & -\hat{c}_{13}-\hat{c}_{33}b^{(2)2} & (\hat{c}_{13}-\hat{c}_{33})b^{(3)} & -\hat{c}_{13}-\hat{c}_{33}b^{(4)2} & -(c_{13}-c_{33})b^{(c)} & c_{13}+c_{33}b^{(d)} \\ [(1-b^{(1)2})\ldots & [2b^{(2)2}\ldots & [(1-b^{(3)2})\ldots & [2b^{(4)2}\ldots & 0 & 0 \\ \ldots\exp(ikb^{(1)}h)] & \ldots\exp(ikb^{(2)}h)] & \ldots\exp(ikb^{(3)}h)] & \ldots\exp(ikb^{(2)}h)] & & \\ [(\hat{c}_{13}-\hat{c}_{33})b^{(1)}\ldots & [(-\hat{c}_{13}-\hat{c}_{33}b^{(2)2})\ldots & (\hat{c}_{13}-\hat{c}_{33})b^{(3)}\ldots & [(-\hat{c}_{13}-\hat{c}_{33}b^{(4)2})\ldots & 0 & 0 \\ \ldots\exp(ikb^{(1)}h)] & \ldots\exp(ikb^{(2)}h)] & \ldots\exp(ikb^{(3)}h)] & \ldots\exp(ikb^{(4)}h)] & & \end{bmatrix}$$

Eq. (3-17)

The following relations can be used to simplify Eq. (3-17) further:

$$r = c_{55} / \hat{c}_{55} \quad , \quad \hat{c}_{33} - \hat{c}_{13} = 2c_{55} \quad , \quad -\hat{c}_{13} - \hat{c}_{33}b^{(2)2} = -\hat{c}_{55}(1-b^{(1)2}) \qquad (3\text{-}18)$$

therefore the final simplification of Eq. (3-16) is:

$$\begin{bmatrix} b^{(1)} & -1 & b^{(3)} & -1 & -b^{(c)} & 1 \\ -1 & -b^{(2)} & -1 & -b^{(4)} & 1 & b^{(d)} \\ 1-b^{(1)2} & 2b^{(2)} & 1-b^{(3)2} & 2b^{(4)} & -r(1-b^{(c)2}) & -2rb^{(d)} \\ 2b^{(1)} & -(1-b^{(1)2}) & 2b^{(3)} & -(1-b^{(3)2}) & -2rb^{(c)} & r(1-b^{(c)2} \\ [(1-b^{(1)2})\ldots & [2b^{(2)}\ldots & [(1-b^{(3)2})\ldots & [2b^{(4)}\ldots & 0 & 0 \\ \ldots\exp(ikb^{(1)}h)] & \ldots\exp(ikb^{(2)}h)] & \ldots\exp(ikb^{(3)}h)] & \ldots\exp(ikb^{(4)}h)] & & \\ [2b^{(1)}\ldots & [-(1-b^{(1)2})\ldots & [2b^{(3)}\ldots & [-(1-b^{(3)2})\ldots & 0 & 0 \\ \ldots\exp(ikb^{(1)}h)] & \ldots\exp(ikb^{(2)}h)] & \ldots\exp(ikb^{(3)}h)] & \ldots\exp(ikb^{(4)}h)] & & \end{bmatrix} \begin{bmatrix} C_1 \\ C_2 \\ C_3 \\ C_4 \\ C_c \\ C_d \end{bmatrix} = 0$$

Eq. (3-19)

For non-trivial solutions to Eq. (3-19), we set the determinant of the 6×6 matrix, known as the boundary determinant, to zero.

$$\left| \ \textit{Boundary matrix} \ \right| = 0 \qquad (3\text{-}20)$$

The only non-defined variable in the determinant should be k, the wave vector. At this point, computational methods need to be incorporated to minimize the boundary determinant to zero yielding solutions to k. The real root of k is related to the frequency f and the propagation velocity v by:

$$f = kv / 2\pi \tag{3-21}$$

Equation (3-21) describes frequency as a function of velocity. We now have all information necessary to construct the dispersion curve since the frequency at all velocities can be obtained.

3.4.2 Anisotropic substrates

Since the dispersion of layered systems is, in part, a function of the wave speeds of the materials involved, it is beneficial to have very dissimilar wave speeds between the substrate and layer in order to generate greater dispersion. The majority of engineering metals exhibit Rayleigh wave speeds between $2000 - 3000\, m/s$ (Rinehart, 1975) therefore in research, it is practical to use a substrate with significantly faster wave speed. Silicon ($c_r \sim 5000\, m/s$) is a common choice. However, its anisotropic behavior will require modification of the dispersion calculations from section 3.4.1.

The analysis is very close to the case for isotropic materials, with a few differences. The wave equation now has directional dependence since the wave speed can vary depending on crystal direction. The equation can be written as:

$$u_j = \alpha_j \exp(ikbx_3) \exp[ik(l_1 x_1 + l_2 x_2 + l_3 x_3 - vt)] \tag{3-22}$$

It can be seen that if propagation is in the [100] direction, that is $l_1 = 1, l_2 = 0, l_3 = 0,$ then the equation reduces down to the same form as the isotropic case in section 3.4.1. The analysis can then proceed in a similar fashion as before where the wave equation is substituted into the governing equation to obtain three equations for the substrate and film. However, for the anisotropic substrate, the 3×3 matrix formed cannot be simplified to the same extent as before since the stiffness matrix now has more unique terms. Equation (3-6) from 3.4.1 now becomes:

$$\begin{bmatrix} c_{11}+b^2c_{44}-\rho v^2 & 0 & bc_{13} \\ 0 & c_{44}+b^2c_{44}-\rho v^2 & 0 \\ bc_{31} & 0 & c_{11}+b^2c_{44}-\rho v^2 \end{bmatrix} \begin{bmatrix} \alpha_1 \\ \alpha_2 \\ \alpha_3 \end{bmatrix} = 0 \qquad \text{(3-23)}$$

The determinant of Eq. (3-23) is set to zero once again, but many terms are retained from the inability so simplify. Computational methods are now employed to find the characteristic roots, b, and the α vector. The boundary conditions remain the same and the creation of the boundary matrix can be completed with the modified variables. The determinant of the boundary matrix is minimized to zero to obtain the dispersion relation in the same manner as before.

3.4.3 Double layer systems

In the experiments performed on zeolite thin films, an optical detection mechanism was utilized. Since the zeolite films studied are partially transparent, an additional top layer was needed to provide reflectivity for optical detection. The use of an additional top layer can also be beneficial for films with poor optical absorption in the infrared range since the majority of laser based generation systems operate around those wavelengths. Modification of the dispersion relation calculation is needed in order to accommodate the addition of a second layer. The process flow is very similar, but now includes four additional variables representing the mechanical parameters of the additional top layer and its thickness.

In the derivation, we consider a double layered structure with the coordinate system shown in Figure 3-4. In the system, x_1 is the direction of SAW propagation and x_3 defines the direction normal to the layer with its origin set at the interface of the second layer and the substrate. It is assumed that all parallel SAWs propagate with the same dispersion therefore negating x_2 dependence.

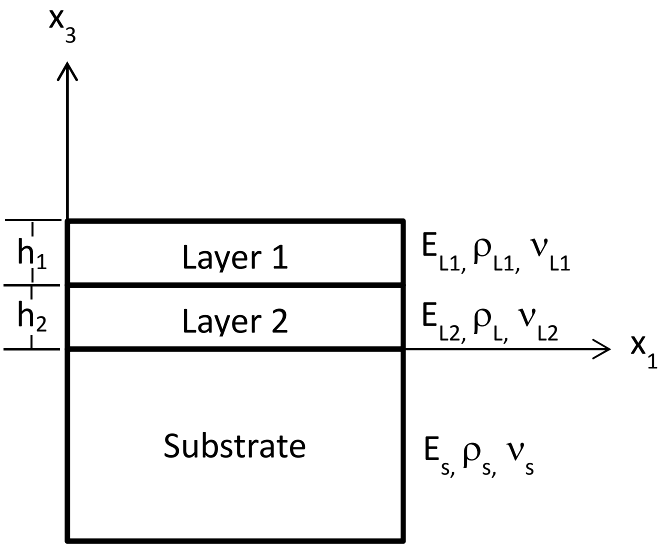

Figure 3-4. Schematic with coordinate system and layers drawn.

For the sake of simplicity, the substrate and layers are assumed to be isotropic. For anisotropic materials, the same procedure outlined in section 3.4.2 can be applied to the layers or substrate in this section. For isotropic materials, the derivation can proceed in the same manner as in section 3.4.1 where the characteristic roots are found for the substrate and each layer. Instead of having six total roots, two for the layer and four for the film, there will now be four additional roots representing the additional top layer.

Layer 1:

$$b^{(1)} = +i\sqrt{1-(v/\hat{v}_t)^2} \qquad \alpha^{(1)} = (-b^{(1)},0,1) \tag{3-24}$$

$$b^{(2)} = +i\sqrt{1-(v/\hat{v}_l)^2} \qquad \alpha^{(2)} = (1,0,b^{(2)})$$

$$b^{(3)} = -i\sqrt{1-(v/\hat{v}_t)^2} \qquad \alpha^{(3)} = (-b^{(3)},0,1)$$

$$b^{(4)} = -i\sqrt{1-(v/\hat{v}_l)^2} \qquad \alpha^{(4)} = (1,0,b^{(4)})$$

Layer 2: $b^{(5)} = +i\sqrt{1-(v/\hat{\hat{v}}_t)^2}$ $\alpha^{(5)} = (-b^{(5)},0,1)$ (3-25)

$b^{(6)} = +i\sqrt{1-(v/\hat{\hat{v}}_l)^2}$ $\alpha^{(6)} = (1,0,b^{(6)})$

$b^{(7)} = -i\sqrt{1-(v/\hat{\hat{v}}_t)^2}$ $\alpha^{(7)} = (-b^{(7)},0,1)$

$b^{(8)} = -i\sqrt{1-(v/\hat{\hat{v}}_l)^2}$ $\alpha^{(8)} = (1,0,b^{(8)})$

Substrate: $b^{(c)} = -i\sqrt{1-(v/v_t)^2}$ $\alpha^{(c)} = (-b^{(c)},0,1)$ (3-26)

$b^{(d)} = -i\sqrt{1-(v/v_l)^2}$ $\alpha^{(d)} = (1,0,b^{(d)})$

Boundary Conditions:

For this problem, the following 10 boundary conditions are set forth:

@ $x_3 = 0$: $u_1 = \hat{\hat{u}}_1$, $u_3 = \hat{\hat{u}}_3$, $\sigma_{31} = \hat{\hat{\sigma}}_{31}$, $\sigma_{33} = \hat{\hat{\sigma}}_{33}$

@ $x_3 = h_2$: $\hat{u}_1 = \hat{\hat{u}}_1$, $\hat{u}_3 = \hat{\hat{u}}_3$, $\hat{\sigma}_{31} = \hat{\hat{\sigma}}_{31}$, $\hat{\sigma}_{33} = \hat{\sigma}_{33}$

@ $x_3 = h_1 + h_2 = h$: $\hat{\sigma}_{31} = 0$, $\hat{\sigma}_{33} = 0$

The boundary conditions represent displacement and stress continuity at the interfaces and zero free surface stress. The shear and normal stresses in our problem can be expressed by:

$$\sigma_{3j} = c_{3jkl}\frac{\partial u_k}{\partial x_l} \tag{3-27}$$

The complete SAW solution is realized as the combination of partial waves, with each partial wave satisfying one of the boundary conditions. Weighting coefficients, C_n, are applied to each partial wave changing the displacement solution to the following form:

Layer 1: $$\hat{u}_j = \left\{\sum_n C_n \alpha_j^{(n)} \exp(ikb^{(n)}x_3)\right\}\exp[ik(x_1 - vt)] \tag{3-28}$$

Layer 2: $$\hat{\hat{u}}_j = \left\{ \sum_m C_m \alpha_j^{(m)} \exp(ikb^{(m)} x_3) \right\} \exp[ik(x_1 - vt)] \tag{3-29}$$

Substrate: $$u_j = \left\{ \sum_p C_p \alpha_j^{(p)} \exp(ikb^{(p)} x_3) \right\} \exp[ik(x_1 - vt)] \tag{3-30}$$

For layer 1, $n = 1,2,3,4$ corresponding to the four layer 1 roots and their eigenvectors. Similarly for layer 2 and the substrate, $m = 5,6,7,8$ and $p = c,d$ respectively. The coupling between the boundary conditions, partial waves, and roots can be illustrated in a 10×10 matrix with the form shown in Figure 3-5.

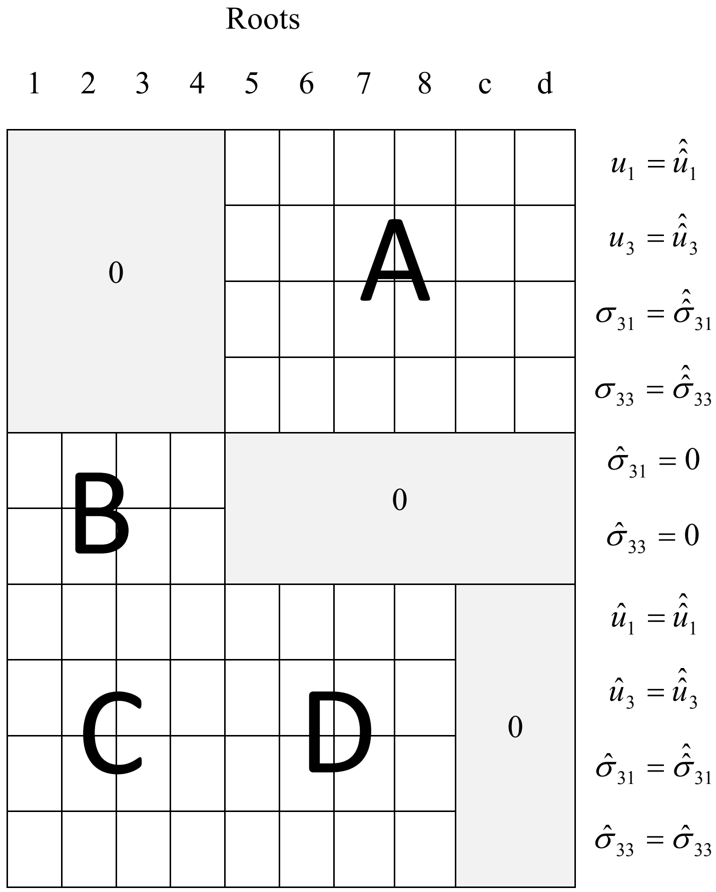

Figure 3-5. Format of 10×10 boundary condition matrix.

Since the matrix is large, letters A-D describe various smaller matrices that are pieces of the full version. The mathematical formulation of the boundary matrix problem should be of the following form

$$\left[\,10\times 10\, Boundary\ Matrix\,\right]\begin{bmatrix} C_1 \\ \dots \\ C_{10} \end{bmatrix} = 0 \tag{3-31}$$

Since the boundary matrix equates all conditions to zero, a negative sign will be distributed to the substrate contributions for rows 1-6 and to the layer one terms in rows 6-10. With some factoring and simplification of the exponential terms, the sub-matrices are:

$$A = \begin{bmatrix} \alpha_1^{(5)} & \alpha_1^{(6)} & \alpha_1^{(7)} & \alpha_1^{(8)} & -\alpha_1^{(c)} & -\alpha_1^{(d)} \\ \alpha_3^{(5)} & \alpha_3^{(6)} & \alpha_3^{(7)} & \alpha_3^{(8)} & -\alpha_3^{(c)} & -\alpha_3^{(d)} \\ \hat{\hat{c}}_{44}(b_5\alpha_1^{(5)}+\alpha_3^{(5)}) & \hat{\hat{c}}_{44}(b_6\alpha_1^{(6)}+\alpha_3^{(6)}) & \hat{\hat{c}}_{44}(b_7\alpha_1^{(7)}+\alpha_3^{(7)}) & \hat{\hat{c}}_{44}(b_8\alpha_1^{(8)}+\alpha_3^{(8)}) & -c_{44}(b_c\alpha_1^{(c)}+\alpha_3^{(c)}) & -c_{44}(b_d\alpha_1^{(d)}+\alpha_3^{(d)}) \\ \hat{\hat{c}}_{33}b_5\alpha_3^{(5)}+\hat{\hat{c}}_{31}\alpha_1^{(5)} & \hat{\hat{c}}_{33}b_6\alpha_3^{(6)}+\hat{\hat{c}}_{31}\alpha_1^{(6)} & \hat{\hat{c}}_{33}b_7\alpha_3^{(7)}+\hat{\hat{c}}_{31}\alpha_1^{(7)} & \hat{\hat{c}}_{33}b_8\alpha_3^{(8)}+\hat{\hat{c}}_{31}\alpha_1^{(8)} & -\hat{\hat{c}}_{33}b_c\alpha_3^{(c)}-\hat{\hat{c}}_{31}\alpha_1^{(c)} & -\hat{\hat{c}}_{33}b_d\alpha_3^{(d)}-\hat{\hat{c}}_{31}\alpha_1^{(d)} \end{bmatrix}$$

$$B = \begin{bmatrix} \hat{c}_{44}(b_1\alpha_1^{(1)}+\alpha_3^{(1)})\exp(ikb_1h) & \hat{c}_{44}(b_2\alpha_1^{(2)}+\alpha_3^{(2)})\exp(ikb_2h) & \hat{c}_{44}(b_3\alpha_1^{(3)}+\alpha_3^{(3)})\exp(ikb_3h) & \hat{c}_{44}(b_4\alpha_1^{(4)}+\alpha_3^{(4)})\exp(ikb_4h) \\ (\hat{c}_{33}b_1\alpha_3^{(1)}+\hat{c}_{31}\alpha_1^{(1)})\exp(ikb_1h) & (\hat{c}_{33}b_2\alpha_3^{(2)}+\hat{c}_{31}\alpha_1^{(2)})\exp(ikb_2h) & (\hat{c}_{33}b_3\alpha_3^{(3)}+\hat{c}_{31}\alpha_1^{(3)})\exp(ikb_3h) & (\hat{c}_{33}b_4\alpha_3^{(4)}+\hat{c}_{31}\alpha_1^{(4)})\exp(ikb_4h) \end{bmatrix}$$

$$C = \begin{bmatrix} -\alpha_1^{(1)}\exp(ikb_1h_2) & -\alpha_1^{(2)}\exp(ikb_2h_2) & -\alpha_1^{(3)}\exp(ikb_3h_2) & -\alpha_1^{(4)}\exp(ikb_4h_2) \\ -\alpha_3^{(1)}\exp(ikb_1h_2) & -\alpha_3^{(2)}\exp(ikb_2h_2) & -\alpha_3^{(3)}\exp(ikb_3h_2) & -\alpha_3^{(4)}\exp(ikb_4h_2) \\ -\hat{c}_{44}(b_1\alpha_1^{(1)}+\alpha_3^{(1)})\exp(ikb_1h_2) & -\hat{c}_{44}(b_2\alpha_1^{(2)}+\alpha_3^{(2)})\exp(ikb_2h_2) & -\hat{c}_{44}(b_3\alpha_1^{(3)}+\alpha_3^{(3)})\exp(ikb_3h_2) & -\hat{c}_{44}(b_4\alpha_1^{(4)}+\alpha_3^{(4)})\exp(ikb_4h_2) \\ -(\hat{c}_{33}b_1\alpha_3^{(1)}+\hat{c}_{31}\alpha_1^{(1)})\exp(ikb_1h_2) & -(\hat{c}_{33}b_2\alpha_3^{(2)}+\hat{c}_{31}\alpha_1^{(2)})\exp(ikb_2h_2) & -(\hat{c}_{33}b_3\alpha_3^{(3)}+\hat{c}_{31}\alpha_1^{(3)})\exp(ikb_3h_2) & -(\hat{c}_{33}b_4\alpha_3^{(4)}+\hat{c}_{31}\alpha_1^{(4)})\exp(ikb_4h_2) \end{bmatrix}$$

$$D = \begin{bmatrix} \alpha_1^{(5)}\exp(ikb_5h_2) & \alpha_1^{(6)}\exp(ikb_6h_2) & \alpha_1^{(7)}\exp(ikb_7h_2) & \alpha_1^{(8)}\exp(ikb_8h_2) \\ \alpha_3^{(5)}\exp(ikb_5h_2) & \alpha_3^{(6)}\exp(ikb_6h_2) & \alpha_3^{(7)}\exp(ikb_7h_2) & \alpha_3^{(8)}\exp(ikb_8h_2) \\ \hat{\hat{c}}_{44}(b_5\alpha_1^{(5)}+\alpha_3^{(5)})\exp(ikb_5h_2) & \hat{\hat{c}}_{44}(b_6\alpha_1^{(6)}+\alpha_3^{(6)})\exp(ikb_6h_2) & \hat{\hat{c}}_{44}(b_7\alpha_1^{(7)}+\alpha_3^{(7)})\exp(ikb_7h_2) & \hat{\hat{c}}_{44}(b_8\alpha_1^{(8)}+\alpha_3^{(8)})\exp(ikb_8h_2) \\ (\hat{\hat{c}}_{33}b_5\alpha_3^{(5)}+\hat{\hat{c}}_{31}\alpha_1^{(5)})\exp(ikb_5h_2) & (\hat{\hat{c}}_{33}b_6\alpha_3^{(6)}+\hat{\hat{c}}_{31}\alpha_1^{(6)})\exp(ikb_6h_2) & (\hat{\hat{c}}_{33}b_7\alpha_3^{(7)}+\hat{\hat{c}}_{31}\alpha_1^{(7)})\exp(ikb_7h_2) & (\hat{\hat{c}}_{33}b_8\alpha_3^{(8)}+\hat{\hat{c}}_{31}\alpha_1^{(8)})\exp(ikb_8h_2) \end{bmatrix}$$

Inserting the eigenvector values, performing general simplifications, and using the following relations:

$$c_{33} - c_{31} = 2c_{44} \qquad , \qquad c_{31} + c_{33} b_2^2 = -c_{44}(1 - b_1^2) \tag{3-32}$$

the sub-matrices can then reduce to:

$$A = \begin{bmatrix} -b_5 & 1 & -b_6 & 1 & b_c & -1 \\ 1 & b_6 & 1 & b_7 & -1 & -b_d \\ \hat{\hat{c}}_{44}(1-b_5^2) & \hat{\hat{c}}_{44}(2b_6) & \hat{\hat{c}}_{44}(1-b_7^2) & \hat{\hat{c}}_{44}(2b_8) & -c_{44}(1-b_c^2) & -c_{44}(2b_d) \\ \hat{\hat{c}}_{44}(2b_5) & -\hat{\hat{c}}_{44}(1-b_5^2) & \hat{\hat{c}}_{44}(2b_7) & -\hat{\hat{c}}_{44}(1-b_7^2) & -c_{44}(2b_c) & c_{44}(1-b_c^2) \end{bmatrix}$$

$$B = \begin{bmatrix} (1-b_1^2)\exp(ikb_1 h) & 2b_2 \exp(ikb_2 h) & (1-b_3^2)\exp(ikb_3 h) & 2b_4 \exp(ikb_4 h) \\ 2b_1 \exp(ikb_1 h) & -(1-b_1^2)\exp(ikb_2 h) & 2b_3 \exp(ikb_3 h) & -(1-b_3^2)\exp(ikb_4 h) \end{bmatrix}$$

$$C = \begin{bmatrix} b_1 \exp(ikb_1 h_2) & -\exp(ikb_2 h_2) & b_3 \exp(ikb_3 h_2) & -\exp(ikb_4 h_2) \\ -\exp(ikb_1 h_2) & -b_2 \exp(ikb_2 h_2) & -\exp(ikb_3 h_2) & -b_4 \exp(ikb_4 h_2) \\ -\hat{c}_{44}(1-b_1^2)\exp(ikb_1 h_2) & -\hat{c}_{44}(2b_2)\exp(ikb_2 h_2) & -\hat{c}_{44}(1-b_3^2)\exp(ikb_3 h_2) & -\hat{c}_{44}(2b_4)\exp(ikb_4 h_2) \\ -\hat{c}_{44}(2b_1)\exp(ikb_1 h_2) & \hat{c}_{44}(1-b_1^2)\exp(ikb_2 h_2) & -\hat{c}_{44}(2b_3)\exp(ikb_3 h_2) & \hat{c}_{44}(1-b_3^2)\exp(ikb_4 h_2) \end{bmatrix}$$

$$D = \begin{bmatrix} -b_5 \exp(ikb_5 h_2) & \exp(ikb_6 h_2) & -b_7 \exp(ikb_7 h_2) & \exp(ikb_8 h_2) \\ \exp(ikb_5 h_2) & b_6 \exp(ikb_6 h_2) & \exp(ikb_7 h_2) & b_8 \exp(ikb_8 h_2) \\ \hat{\hat{c}}_{44}(1-b_5^2)\exp(ikb_5 h_2) & \hat{\hat{c}}_{44}(2b_6)\exp(ikb_6 h_2) & \hat{\hat{c}}_{44}(1-b_7^2)\exp(ikb_7 h_2) & \hat{\hat{c}}_{44}(2b_8)\exp(ikb_8 h_2) \\ \hat{\hat{c}}_{44}(2b_5)\exp(ikb_5 h_2) & -\hat{\hat{c}}_{44}(1-b_5^2)\exp(ikb_6 h_2) & \hat{\hat{c}}_{44}(2b_7)\exp(ikb_7 h_2) & -\hat{\hat{c}}_{44}(1-b_7^2)\exp(ikb_8 h_2) \end{bmatrix}$$

For non-trivial solutions to Eq. (3-31), we set the determinant of the 10×10 matrix, known as the boundary determinant, to zero.

$$\left| \; Boundary\ matrix \; \right| = 0 \tag{3-33}$$

The only non-defined variable in the determinant should be k, the wave vector. At this point, computational methods need to be incorporated to minimize the boundary determinant to zero yielding solutions to k. The real root of k is related to the frequency f and the propagation velocity v by:

$$f = kv/2\pi \tag{3-34}$$

Equation (3-34) describes frequency as a function of velocity. We now have all information necessary to construct the dispersion curve since the frequency at all velocities can be obtained.

3.5 Some insights from theoretical dispersion curves

3.5.1 Sensitivity of dispersion parameters

This section studies the effect of each fitting parameter on the dispersion curve by altering the variables successively in a specific range and plotting the results. This is not in an attempt to fully characterize the effect of each variable since that answer will change depending on the materials involved. It is rather a broad visualization to see generally how sensitive each variable is to change (i.e. which variable induces the largest change in dispersion behavior). For this study, a double layer structure consisting of zeolite and aluminum films on a silicon substrate is simulated because it closely matches the films studied in chapter 5. The starting properties for the zeolite film were: $E = 46\ GPa$, $\rho = 1.99 g/cc$, $\nu = 0.166$, and $t = 500\ nm$ where $E, \rho, \nu,$ and t are respectively the elastic modulus, density, Poisson's ratio, and film thickness. The same properties for aluminum were: $E = 70\ GPa$, $\rho = 2.7\ g/cc$, $\nu = 0.33$, and $t = 280\ nm$. Lastly, for the silicon substrate: $c_{11} = 165.7\ GPa$, $c_{44} = 79.6\ GPa$, $c_{12} = 63.9\ GPa$, and $\rho = 2.33\ g/cc$. In the study, the dispersion relation for the system with all of the properties referenced above is calculated and plotted as a single black line. Then, each parameter for the zeolite film is modified by ±10% successively forming two curves for each parameter, one that describes the +10% result and another for the -10% result. The area between these curves is shaded with a specific color depending on the property varied and the amount of shaded area is a measure of how sensitive the parameter is to change. The result is shown in Figure 3-6.

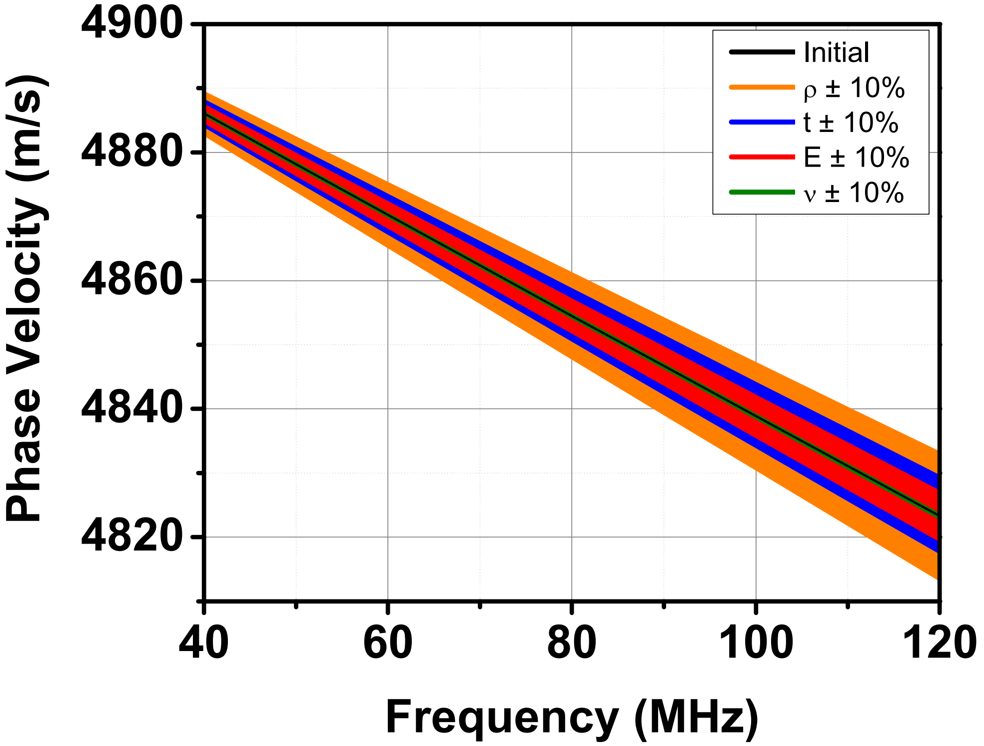

Figure 3-6. Sensitivity of dispersion variables. Shaded regions represent ±10% bounds of each variable.

The results indicated that the density of the material was the most sensitive dispersion parameter with the largest bounds in the dispersion in the plot. Thickness and elastic modulus were both about half as sensitive as density, and the Poisson's ratio was largely insensitive to change. These findings are important for the fitting of experimental curves later on since they show the degree of potential error in each variable. For example, if the density is being fit, then a ±5% error range will be quite large and the theoretical results can be finely tuned whereas for Poisson's ratio fitting, the range will be very small and it may be hard to determine the best fit.

Fortunately, the elastic modulus is the main fitting parameter for the later experiments and these results show that there is a good response to variation in that parameter.

3.5.2 Effect of the second layer

Since zeolite films require the addition of an additional top layer, typically aluminum, for reflectivity, an investigation into the effect of this top layer was warranted. The initial assumption was that a very thin layer may have negligible effect on the dispersion relation of the entire system. However, it was found that even a 100 nm thick layer of aluminum had considerable effect as shown in Figure 3-7.

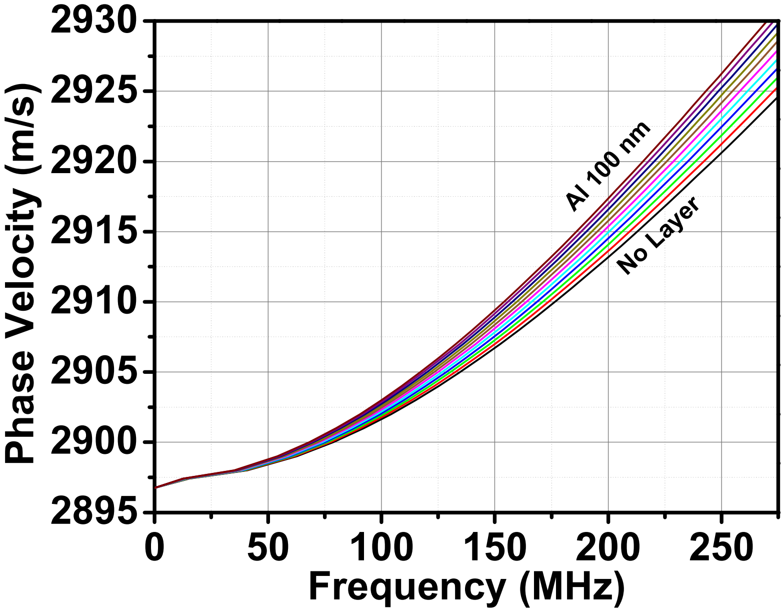

Figure 3-7. Secondary aluminum layer of varying thickness on a 3 μm ZSM-5 layer with an aluminum substrate.

The effect of the additional top layer was more apparent at higher frequency which is expected since the Rayleigh wave sees more influence from the layer with shorter wavelength. An interesting observation from this plot was that the addition of the layer steepened the dispersion curve at all frequencies. The effect is explained by the fact that larger layer thicknesses can generate increased dispersion because the Rayleigh wave has a larger interaction volume with the film. This is shown in Figure 3-8 where dispersion curves are plotted for increasing aluminum layer thickness on a silicon substrate.

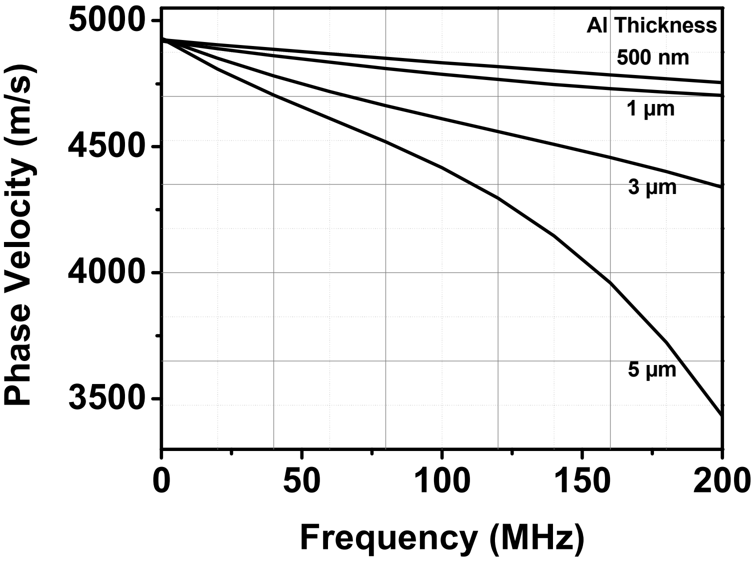

Figure 3-8. Dispersion curves for an aluminum films of varying thickness on a silicon substrate.

In Figure 3-8, it is seen that there is an initial linear region on the dispersion curves that dominate at low thicknesses. As thickness increases, so does the amount of dispersion and a non-linear region enters the plot since the larger frequencies are more substantially affected by the aluminum film. This non-linear dispersion region is highly desirable for experimental fitting since it allows for multiple variables to be fit. It is often out of the frequency range of experiments whose bandwidths are typically < 200 MHz therefore the shift to lower frequency is welcomed. From section 3.3, it is shown that the film modulus, density, and Poisson's ratio can be fit to experiment. For linear dispersion curves, only one variable can be extracted and the others must be known or assumed. If the plot is non-linear, then the simultaneous extraction of multiple variables may be possible.

This is potentially very beneficial for double layer systems where one of the layers has one or more unknown parameters. The observation in Figure 3-7 means that the increase in thickness of any layer in the system can generate more dispersion. Additionally, as the thickness is increased, a nonlinear region of dispersion may be reached. This is remarkable because nonlinear dispersion is potentially possible with no modifications to the unknown film. The only requirement would be to deposit a thicker film, preferably with known properties.

Another interesting finding is that this effect of thickness dominates over the wave speed of the layers involved. For example, consider a double layer system where the substrate is aluminum ($v \sim 2900\, m/s$), the first layer is zeolite ($v \sim 3100\, m/s$), and the second (top) layer is aluminum. Since the top layer, Al, has a lower wave speed than zeolite and is closer to that of the substrate (also aluminum), then it is expected that dispersion of the system will decrease as the layer is added. However, Figure 3-9 shows that the dispersion will actually increase and for frequencies below ~ 100 MHz, this increase is comparable to that of a single layer system with an equivalent increase in first layer thickness. Thus, the effect of increasing thickness dominates meaning that the choice of material to achieve non-linear dispersion is less important than the amount deposited.

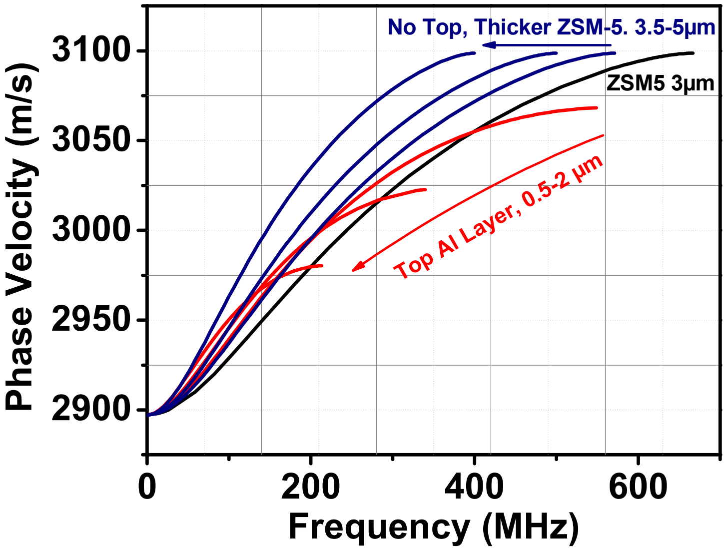

Figure 3-9. The effect on dispersion of a second layer with specific thickness (red) is compared to the equivalent thickness increase in a single layer (blue). The results overlap at low frequency.

3.6 Conclusion

In this chapter, the mathematical derivation of dispersion on layered structures was detailed. The theory presented allows for the calculation of dispersion curves on any unknown material system. Solutions were first presented for the simplest case, an isotropic substrate supporting an isotropic film. It was later shown that the isotropic solution could be modified to include anisotropic materials, allowing for the use of silicon substrates which have an advantageous fast wave speed. However, it was recognized that the materials to be tested may not be reflective and would thus require a secondary reflective layer for optical detection methods. To characterize the effect of another layer, derivation of dispersion for a two layer model was shown and the solution represents the main types of films that will be tested later on.

The theoretical solutions were used to predict the response of each mechanical parameter on the dispersion of a model system. It was shown that density is the most sensitive to dispersion, followed by the film thickness and elastic modulus with about half of the sensitivity of the density, and then a generally insensitive Poisson’s ratio.

From theory, it was shown that the addition of thickness can be valuable to increasing the dispersion response of the system. The increase in dispersion can turn a normally linear dispersion curve to a non-linear curve where simultaneous fitting of multiple properties could be done. Specifically for double layered materials, this increase in dispersion was shown to be possible by only modifying one film instead of both. This means that nonlinear dispersion in a double layer system could potentially be achieved by simply adding a thicker secondary layer while leaving the unknown film for testing intact.

Chapter 3 References:

COOK, D. A. & BERTHELOT, Y. H. 2001. Detection of small surface-breaking fatigue cracks in steel using scattering of Rayleigh waves. *NDT & E International,* 34**,** 483-492.

FARNELL, G. W. & ADLER, E. L. 1972. Types and properties of surface waves. *In:* MASON, W. P. & THURSTON, R. N. (eds.) *Physical Acoustics.* New York: Academic Press.

LAMB, H. 1917. On Waves in an Elastic Plate. *Proceedings of the Royal Society of London. Series A,* 93**,** 114-128.

LOVE, A. E. H. 1911. *Some problems of geodynamics: being an essay to which the Adams prize in the University of Cambridge was adjudged in 1911*, University Press.

RAYLEIGH, L. 1885. On Waves Propagated along the Plane Surface of an Elastic Solid. *Proceedings of the London Mathematical Society,* s1-17**,** 4-11.

RINEHART, J. S. 1975. *Stress transients in solids*, HyperDynamics.

STONELEY, R. 1924. Elastic Waves at the Surface of Separation of Two Solids. *Proceedings of the Royal Society of London. Series A,* 106**,** 416-428.

VU, B. Q. & KINRA, V. K. 1985. Diffraction of Rayleigh waves in a half-space. I. Normal edge crack. *The Journal of the Acoustical Society of America,* 77**,** 1425-1430.

WARREN, P. D., PECORARI, C., KOLOSOV, O. V., ROBERTS, S. G. & BRIGGS, G. A. D. 1996. Characterization of surface damage via surface acoustic waves. *Nanotechnology,* 7**,** 295-301.

WOODS, R. D. 1968. Screening of surface waves in soils. *Am Soc Civil Engr J Soil Mech.*

Chapter 4 Experimental implementation of LiSAW characterization

4.1 Introduction

4.1.1 Laser generation of surface acoustic waves

Laser generation of elastic waves commenced almost simultaneously with laser development in the 1960's (White, 1963). The high energy fluence, short pulse widths, and excellent repeatability were found to be an optimal source for broadband ultrasound. Initial studies focused on the generation of body waves for the study of high strain rate behavior (Anderhol.Nc, 1970, Bell and Landt, 1967). However, it was soon realized that lasers could also reliably generate surface Rayleigh waves (Ledbetter and Moulder, 1979, Ash et al., 1980). A number of studies (Hutchins et al., 1981, Karabutov, 1985, Dewhurst et al., 1982) were performed to establish the mechanisms behind laser generation phenomena and they explain the behavior as follows: When laser light irradiates a solid body, transverse, longitudinal, and Rayleigh waves are created. For Rayleigh waves, the fluence of light is important to the regime of their formation. For power densities below $10^7\ W/cm^2$, the thermoelastic regime exists where waves are only formed by thermal mechanisms. The laser pulse heats the irradiated zone causing strains by thermoelastic expansion with subsequent contraction. The wave proceeds radially for a circular source. The strain, or wave amplitude, is proportional to the amount of laser energy absorbed and inversely proportional to wavelength of light (Aindow et al., 1981). Width of the source beam directly affects the width of the Rayleigh wave profile such that tighter focusing can produce higher frequency. The same is true for the temporal profile of the pulse. Higher frequencies can be realized with shorter pulse times (Scruby and Drain, 1990).

For power densities above $10^7\ W/cm^2$, ablation of the sample begins resulting in a plasma formation. The recoil from the ejected material and pressure from expanding plasma supplements thermoelastic generation, thus larger elastic wave amplitudes can be achieved. This can be useful for producing surface waves that are readily detectable, but excessive sample damage can be detrimental to subsequent generation. The relations governing wave bandwidth remain the same with tight focusing and short temporal pulse width preferred (Dewhurst et al., 1982).

A constrained surface source regime can occur when a transparent confining layer such as oil or resin is used to effectively create a buried source. This regime can occur at both thermoelastic and ablation energy densities. Confinement of the source negates the stress-free surface traction allowing for normal forces to form in the layer. This is found to increase the amplitude of the surface waves generated (Davies et al., 1993). The constrained surface regime is not as relevant to thin films since it introduces another degree of complexity by requiring additional layers to an already layered system.

4.1.2 Detection of surface acoustic waves

Once Rayleigh waves are generated, there are several popular ways to detect the waves for analysis. These can be broken down into two categories, physical probing and optical methods. Piezoelectric probes are common forms of SAW detection, but rely on constant contact with the film surface. Typically, they are composed of a piezoelectric foil at the tip of a wedge geometry. When in contact with the sample surface, out of plane displacement will compress the piezoelectric resulting in a voltage signal. This voltage signal can be digitized by an oscilloscope and used to extract the surface displacement. Since this technique relies on measuring only vertical displacement, the sharpness of the wedge must be sufficient in order to resolve the peaks of the passing SAW. Thus the measurable bandwidth is limited by the piezoelectric response and wedge geometry. Frequencies up to ~200 MHz are attained with this technique (Schneider et al., 1997, Coufal et al., 1992). However, the reliance on physical contact can be burdensome for some applications.

Optical methods are another popular choice for detection and have the main benefit of creating a fully non-contact testing apparatus. However, they often require good reflectivity from the sample surface. These techniques typically involve the use of a separate laser in beam deflection (Kolomenskii et al., 2004, H. Coufal, 1994) or interferometry configurations. Michelson interferometry is the most prevalent due to its low complexity. Michelson interferometers are based on the interference of a single laser beam that is broken into two paths and later recombined. One path guides the beam to the sample surface and the other path to a stationary mirror. Any displacement at the sample surface will introduce a relative phase shift for light in that path, thus after reflection from each surface and recombination, the two beams will constructively and destructively interfere. The result is an interference, or fringe, signal whose name arises from the oscillating light and dark patterns that describe the sample movement. The bandwidth for SAW detection is based on the laser spot size, since the displacement recorded is an average of this region. Likewise to piezoelectric probes, the spot size, or degree of laser focus, must be small enough to resolve the distance between SAW peaks for the desired frequency. The light intensity as a function of the phase difference between two beams can be seen in Figure 4-1.

For a Michelson interferometer, the phase difference is also divided by a factor of two since the beam is reflected in the same path as incoming light, thus traversing the displacement twice.

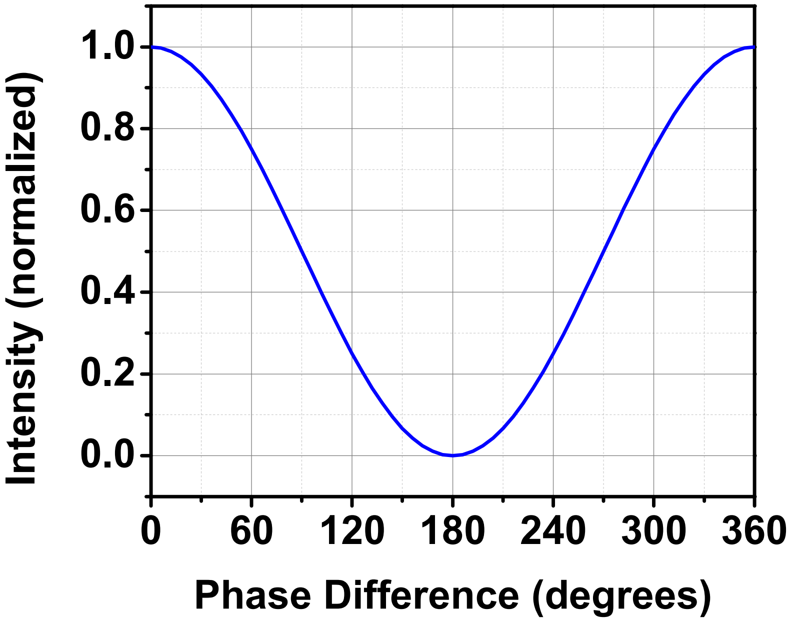

Figure 4-1. Light intensity as a function of the phase difference between interferometer paths.

In Figure 4-1, the light intensity can be summarized as a nonlinear region from 0-60° followed by a relatively linear region from 60-120°. In the non-linear region, the change in light intensity for each unit change in phase difference can be small, especially near 0°. Thus, the change in intensity per unit displacement is small and displacement measurement is harder to realize. In the linear region, the slope is highest meaning that there is the highest change in intensity per unit of displacement. Thus, for small displacements, it is generally preferred to confine the experiment to this region. Path-stabilized Michelson interferometers are used to accomplish this task by attaching a piezoelectric stage to the reference mirror. The stage is moved such that the phase difference between the two legs remains constant and in the linear region. Since the two paths are also affected by background noise, these types of interferometers can stabilize the paths and cancel out background vibrations in the kilohertz range and below.

4.2 Experimental setup

The experimental setup was completely built in-house specifically for LiSAW testing. It is highlighted by two pulsed Nd:YAG lasers for generation, one with a 50 ps pulse width (Continuum Leopard SS, Santa Clara, CA) and the other with a 5 ns pulse width (New Wave Tempest, Fremont, CA). Both are capable of delivering ~250 mJ of energy, but are significantly attenuated for the scope of this experiment. SAW detection is performed by a continuous wave argon-ion laser (Coherent Innova 90, Santa Clara, CA) in a Michelson interferometer configuration. The experimental setup is diagramed in Figure 4-2.

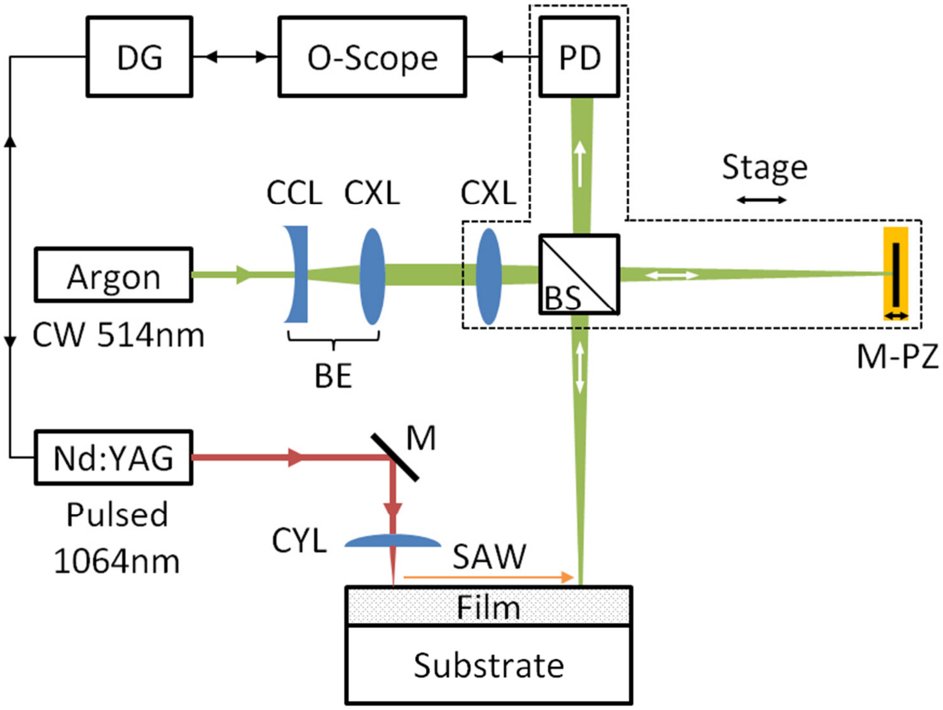

Figure 4-2. Experimental setup. Abbreviations are: DG: delay generator, O-scope: oscilloscope, PD: photo detector, CXL: convex lens, CCL: concave lens, BE: beam expander, BS: beam splitter, M-PZ: mirror mounted on piezoelectric stage, M: mirror, CYL: cylindrical lens.

4.2.1 Generation

Two lasers were able to provide SAW generation for this setup although the majority of work in this and the next chapter was performed with the 5 ns pulse width Tempest. While the faster Leopard laser can theoretically generate higher frequencies, sample damage and timing complexities limited its use, especially prior to the detection frequency optimizations in Chapter 6. A comparison of Rayleigh waves generated by both lasers prior to any optimizations is shown in section 5.5. Generation from both lasers is compared once again post optimization in section 6.3.

The process of SAW generation begins with the firing of the 1064 nm Nd:YAG laser at full power (300 mJ for the tempest and 260 mJ for the leopard). The light then passes through a variable optical attenuator comprised of a half wave plate and thin film polarizer. The energy of light exiting is typically controlled to be 15 mJ or less depending on the sample. Light is then steered by mirrors towards the sample surface passing through a cylindrical lens on the way in order to create a line source. This allows the SAW wavefront to be planar as opposed to radial if the beam is left circular. The source width on the sample surface is typically ~5-10 µm as measured by a microscope on laser-sensitive paper.

4.2.2 Detection

The generated SAWs are detected by the continuous wave (CW) argon-ion laser after propagating a distance in the range of 5-25 mm. Laser light is emitted by the argon laser at a wavelength of 514.5 nm and with ~ 3 mm beam diameter. Since the detection bandwidth is a function of spot size, the beam must be focused to a sufficiently small diameter depending on the materials being tested. The spatial wavelength of Rayleigh waves is governed by:

$$v = \lambda f \tag{4-1}$$

where v is the wave velocity, λ is the wavelength, and f is the frequency. For a 100 MHz wave propagating on a silicon substrate ($v \sim 5000\, m/s$), the spatial wavelength is ~50 μm. Thus for the detection technique to operate at the Nyquist sampling rate (minimum requirement), the beam diameter must be 25 μm. Even smaller diameters are preferred as they will serve to increase the peak resolution. The focusability of light is governed by the diffraction limit and follows the equation:

$$w = \frac{1.22 f \lambda}{D} \tag{4-2}$$

where w is the focused beam width, f is the focal length, λ is the wavelength, and D is the initial diameter. For a 3 mm beam being focused by a 150 mm lens, the final diameter is ~ 31 μm. This is insufficient for SAW detection, therefore the focal length or initial diameter must be altered. In this setup, a beam expander, comprised of a concave and convex lens in succession, is used to expand the diameter by 10 fold. The 30 mm beam can now be theoretically focused using the same 150 mm lens to a diameter of 3.1 μm. However, lens aberrations and sample drift will increase the achievable spot size. Typically, ~10 μm spots are recorded on laser paper in the experiment.

After passing through the beam expander, the light travels through the main focusing lens and begins to converge. On the way to the sample, the light is directed to two paths in a 50/50 ratio by a beam splitter. One path goes to the sample surface and the other to a reference mirror. The focusing lens, beam splitter, and reference leg optics are all mounted on a translation stage that allows for movement of the detection probe across the sample to an accuracy of ± 1 μm. Thus, measurement at multiple positions can be performed with a high degree of precision over the separation distance. Note that the actual source to receiver distance at each position is not accurately known and does not need to be known for dispersion calculations.

After arriving at the reference mirror and sample surface, the light is reflected back to the beam splitter and recombined to interfere based on sample displacement. The interference pattern is detected using a 1.2 GHz bandwidth photodetector (EOT Technologies ET-2030, Traverse City, MI) and digitized by a 5 GHz oscilloscope at a sampling rate of 20 gigasamples/sec (LeCroy Wavemaster 8500A, Chestnut Ridge, NY).

4.2.3 Interferometer synchronization

It was mentioned previously in section 4.1.2 that path-stabilization is a popular technique to ensure detection in the linear, most sensitive, range of an interferometer signal. This stabilization can be cumbersome because it requires the use of active electronics in order to parse the photodiode signal and send the correct feedback to the piezoelectric stage. In this work, it was discovered that localization to the linear range can be achieved by vibrating the reference mirror to achieve a specific interference signal and then timing the laser firing to this motion. The only equipment needed is a piezoelectric stage and an oscilloscope that can trigger out from an input signal (common).

To explain this effect more clearly, consider a Michelson interferometer with a piezoelectric stage attached to the reference mirror. If the stage is inactive, then normal background vibrations, on the order of < 1 KHz, will exist and generate interference. If the stage is turned on and set to vibrate at several hundred Hz with a displacement of several microns (many fringes), then the background noise is effectively lost since the piezoelectric movement dominates. Figure 4-3 shows an interference pattern for a piezoelectric stage vibrating at ~200 Hz which demonstrates this behavior. Notice that all fringes, aside from the ends of vibration, traverse the full voltage range. The effect of background noise is now simply an extra partial or full fringe with each oscillation.

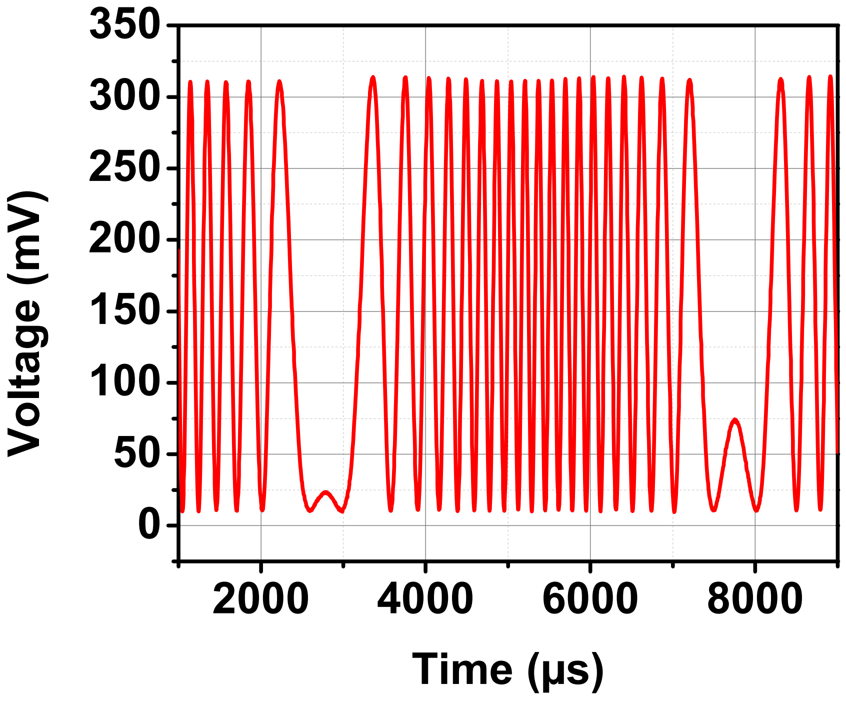

Figure 4-3. Interference signal for a vibrating reference mirror at ~200 Hz.

The wavelengths in the fringe signal are highly repeatable, but vary since the velocity changes from minimum to maximum during each oscillation. An oscilloscope can be used to keep track of the rise and fall times of this signal, in effect calculating the half wavelength of each fringe. The oscilloscope can then be set to trigger an output signal for a specific wavelength, preferably in the middle of each oscillation where velocity is nearly constant (meaning consistent fringe wavelengths). If the laser fire time is on the same order as the selected wavelength, then SAW generation can be set to occur in the linear region with good precision. Figure 4-4 illustrates this for the Tempest laser whose trigger to fire time is 190 μs.

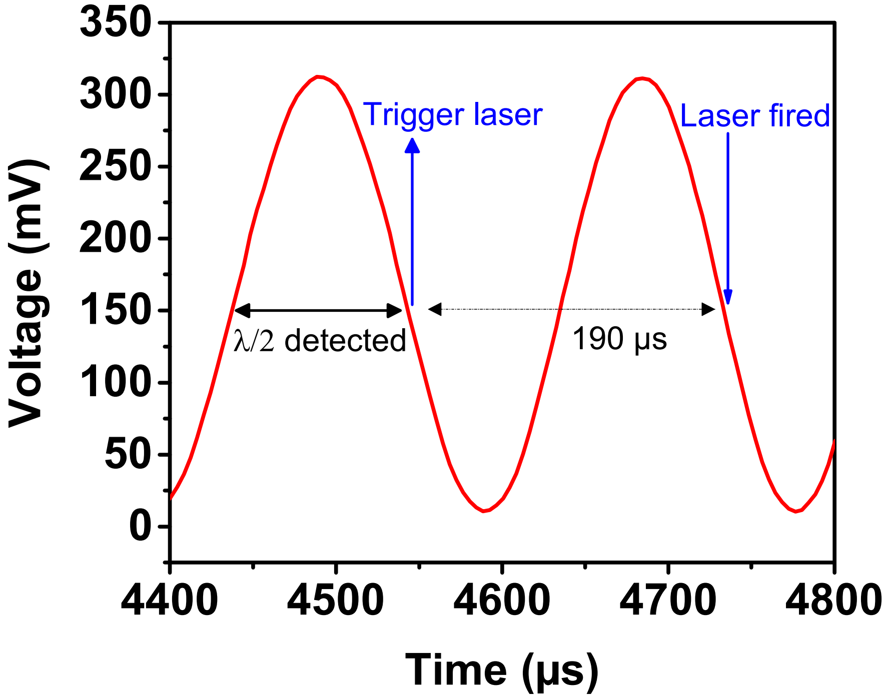

Figure 4-4. Schematic of laser synchronization mechanism for SAW generation in the linear region.

The key to this technique is that the reference mirror is vibrated quickly enough to overcome background noise, but not so fast as to enter the SAW timescale. Rayleigh waves generated in this setup typically last on the order of 100 ns with a 15 mm propagation time of ~3 μs on silicon. This is an order of magnitude lower than the triggering wavelength timescale, therefore the voltage at the photodiode during SAW detection remains in the middle of the linear range and essentially constant. The consistency of fringe wavelengths allows for generation to occur within a ± 10 mV range for a 300 mV fringe signal amplitude. For comparison, the size of the linear region is roughly 200 mV for such signals.

4.3 Signal processing techniques

The use of high bandwidth photodetectors and oscilloscopes to capture the MHz phenomena inherently creates significant noise in the SAW measurement. Increasing laser power can create larger amplitude waves, however, excessive surface damage commences rapidly due to the sharp laser focus. Even in the ablation regime, SAW amplitudes are typically less than tens of nanometers. The dark current noise of the detector was measured to be around ± 6 mV which accounts for several nanometers in the linear range. Thus the signal to noise ratio (SNR) of a raw signal can be quite poor. However, since SAW generation is a highly repeatable process, many signals can be averaged together to enhance the SNR. Figure 4-5 shows the effect on detector noise from averaging 10 shots. The noise is attenuated by a factor of ~4 by this simple process. Averaging additional signals can produce even better results and the amount of averaging necessary depends on the wave amplitude (laser power).

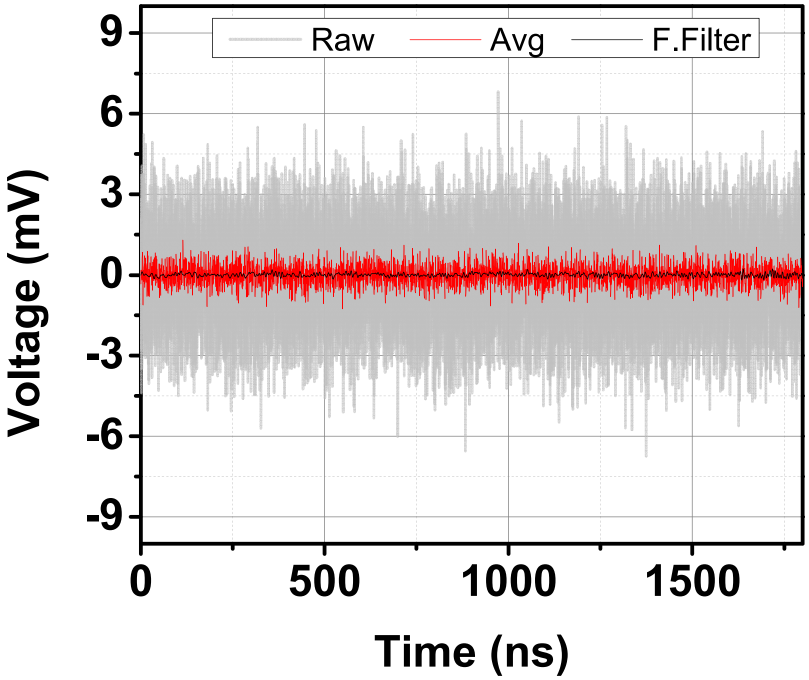

Figure 4-5. A plot of raw waveforms versus their average and Fourier filtered average.

In Figure 4-5, it can be seen that that averaged signal retains some degree of noise. Much of this is very high frequency fluctuation well outside the bandwidth of the experiment. Further reduction can be performed through the use of Fourier filtering with cutoff or band-pass filters. In this process, a discrete Fourier transform is used to plot the detected signal in the frequency domain. Now without spatial convolution, selected frequencies can be suppressed. An inverse Fourier transform is then used to resolve the filtered signal back into the time domain. Figure 4-5 shows an example of the raw signal (grey) versus the Fourier filtered average signal (black). The filter featured is a 300 MHz cutoff filter such that all higher frequencies are suppressed. A similar operation can be used to filter out low frequency noise if necessary.

After filtering and averaging of the raw signal, the SAW waveform can be obtained with a SNR > 30 quite readily. This is sufficient to suppress noise in the dispersion curve calculations performed later. However, it is desirable to isolate the SAW waveform so that any noise outside of the SAW does not interfere with dispersion curve generation. This can be done by signal windowing where the range of the SAW signal is multiplied by an amplitude modulated function. The effect is that the signal amplitudes outside of the SAW limits are reduced to zero. A rectangular window, which allows signal in range to have full amplitude and zeroes otherwise, is the simplest case. However, the sharp discontinuities produced can be troublesome for Fourier transform operations later. There are many types of other window functions available and they are generally described by Gaussian shapes with varying edges. The edges of each function are used to illicit a specific signal cutoff shape. Figure 4-6 shows popular window types. Blackman-Harris and Tukey type windows were found to work well in this experiment. The effect of windowing on a SAW signal is shown in Figure 4-7.

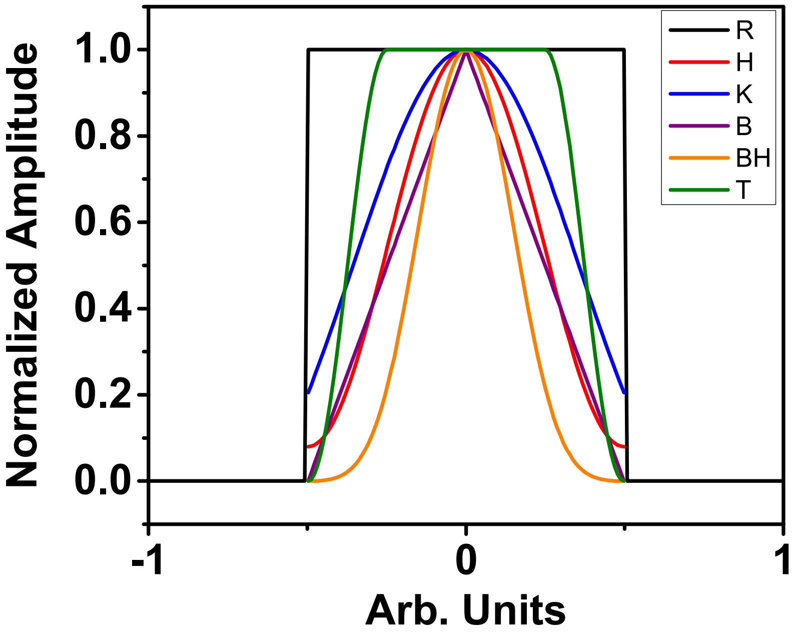

Figure 4-6. Popular window functions. R: Rectangular, H: Hamming, K: Kaiser, B: Bartlett, BH: Blackman-Harris, T: Tukey.

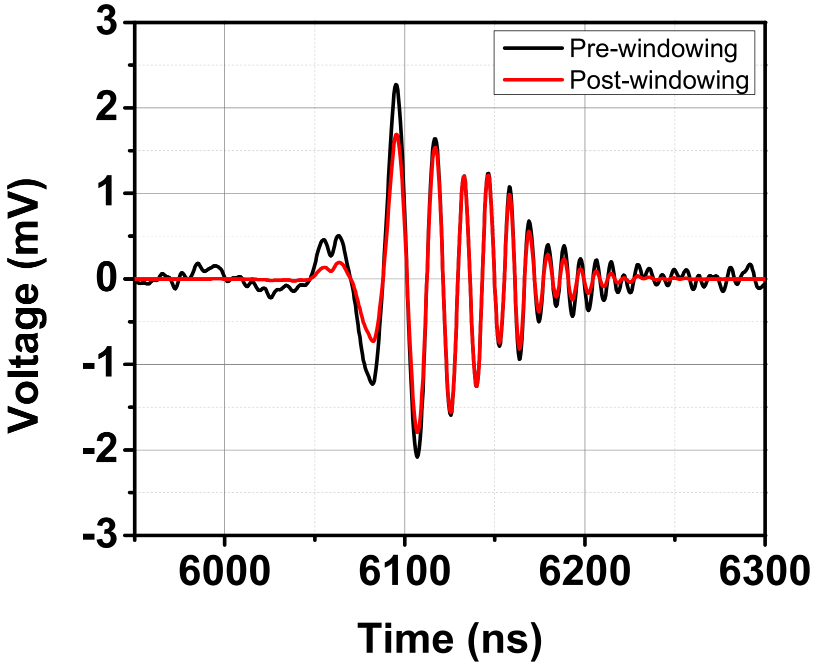

Figure 4-7. Sample SAW with a Blackman-Harris type window function applied.

Note in Figure 4-7 that the sides of the signal become suppressed and the transition is smooth and continuous. Windowing can be useful especially for the trailing high frequency portions of SAWs since detection limits may under-sample displacement in this region. Thus extraneous frequencies that persist through filtering can be properly minimized.

At this point, the signal remains as a function of voltage versus time. It is necessary to extract displacement from the interference pattern. For the Michelson interferometer, the intensity of light is related to the fringe count by:

$$I(t) = \frac{I_{max}+I_{min}}{2} + \frac{I_{max}-I_{min}}{2}\sin(2\pi n(t) + \phi) \tag{4-3}$$

where I_{max} and I_{min} are the maximum and minimum intensity of each fringe, $n(t)$ is the fringe count, and ϕ is the phase angle. The fringe count is related to displacement through:

$$u(t) = \frac{\lambda n(t)}{2} \tag{4-4}$$

where λ is the laser wavelength. It can be seen that the displacement necessary to traverse a full fringe is $\lambda/2$ therefore the bright field to dark field displacement is $\lambda/4$. This corresponds to sample movement of ~130 nm for an argon-ion laser with a 514.5 nm wavelength. Since SAWs stay well within this range, the signal is considered to be sub-fringe, meaning that an entire fringe is not travelled. For these displacements, the raw voltage signal and calculated displacement are nearly identical. An important note is that the filtering routine inevitably affects the amplitude of the measured signal therefore the calculated displacements are not exact. However, the absolute displacements are not necessary for dispersion calculation as long as their frequency components remain intact.

4.4 Calculation of dispersion from experimental signals

Since dispersion curves are a plot of velocity information, two signals from experiment with a known separation distance apart are required for calculation. With this data, time of propagation over the specified distance for each frequency can be obtained through spectral analysis. To begin, the discrete Fourier transform, $X(k)$, of each signal must to be calculated:

$$X(f) = \sum_{n=0}^{N-1} x(n) e^{-\frac{2\pi i n f}{N}} \qquad f = 0 \ldots (N-1) \tag{4-5}$$

where n is an index of time steps, N is the size of the data set, $x(n)$ is the array of data, and f is an index of spectral lines. The transform yields real and complex components corresponding to the sine, cosine, and phase contribution from each frequency. The magnitude of each frequency, $M(f)$, can be calculated by:

$$|M(f)| = \sqrt{Re[X(f)]^2 + Im[X(f)]^2} \tag{4-6}$$

where Re and Im denote the real and imaginary components. The phase spectra, $\Phi(f)$, can then be determined by:

$$\Phi(f) = \tan^{-1}(\frac{Im[X(f)]}{Re[X(f)]}) \tag{4-7}$$

Once the phase spectra for each signal are known, they can be used to determine the dispersion relation by comparing the phase difference of each frequency acquired from propagation. The final dispersion data, $c(f)$, is calculated by:

$$c(f) = \frac{2\pi f(x_2-x_1)}{\Phi_2(f)-\Phi_1(f)} \tag{4-8}$$

where $c(f)$ is the phase velocity as a function of frequency, f is frequency, $(x_2 - x_1)$ is the separation distance between the two sites of detection, and Φ_n is the phase spectra of each signal. Note that the actual source to receiver distance at each position is not required, only the distance between the two sites. The experimental dispersion curves are now complete and ready for theoretical fitting.

4.5 Estimation of error

The experimental measurement of SAW velocity involves several major instruments working together with all of them contributing some degree of error to the final waveforms. The sources of error from instrumentation include the frequency stability of the detection laser, pulse jitter from the generation laser, time variance of the oscilloscope, and accuracy of the positioning stage. A standard uncertainty model can be used to estimate the propagation of error for the velocity measurement by:

$$\left|\frac{\Delta c}{c}\right| = \left|\frac{\Delta\lambda}{\lambda}\right| + \left|\frac{\Delta t_j}{t_j}\right| + \left|\frac{\Delta t_o}{t_{o2}-t_{o1}}\right| + \left|\frac{\Delta x}{x_2-x_1}\right| \tag{4-9}$$

where c is the measured velocity, λ is the detection wavelength, t_j is the time of jitter, $t_{o2} - t_{o1}$ is the time of propagation from the oscilloscope, and $x_2 - x_1$ is the separation distance. Jitter on a Q-switched Nd:YAG laser is inherently low and for this system it is less than 1 ns. This can be further reduced to a negligible amount by using a photodetector to record the exact time of laser firing for each pulse. An oscilloscope or software can then be used to align pulses by these maxima. Frequency stability of the detection laser can be enhanced through the use of an etalon as a band-pass transmission filter. In this configuration, laser linewidths of 100 MHz are achievable corresponding to a wavelength deviation of only 0.08 pm which contributes negligible error to this experiment. The remaining sources of error from the oscilloscope and translation stage can be calculated given an average propagation distance of 15 mm. With a resolution of 3 ps and 1μm respectively for the oscilloscope and stage, the error in velocity is $< 7 \times 10^{-5}$ corresponding to a velocity deviation of < 1 m/s. In the calculation, it is seen that the translation stage error dominates and the result is a shift of the entire dispersion curve by the specified error. For linear SAW behavior, this error can be estimated by performing a linear fit to the experimental curve and extrapolating to zero frequency. At zero frequency, the velocity of propagation should be the bulk substrate Rayleigh wave speed.

The signal to noise ratio can be a large contributor to error if the frequencies cannot be properly resolved. The best way to improve SNR ratio is through the averaging of additional signals. A SNR ratio of > 30 is generally acceptable for analysis. Errors from noise, whether it is from electronics or optics, will propagate to the dispersion curve and result in increased data scatter.

The scatter of dispersion curves can be estimated by calculating the residuals from the experimental and theoretical data. The standard deviation of the difference can be used as an estimate of uncertainty. Theoretical dispersion curves encompassing the deviation range can then be derived to estimate the percentage error of the fitting parameters.

4.6 Conclusion

This chapter summarized the fundamentals of laser generated ultrasound and overviewed the experimental setup used for the studies in the following chapter. Three SAW generation regimes were detailed, the thermoelastic, ablative, and confined. The ablative regime creates the highest amplitude SAWs, but at the cost of sample damage. The lasers used to generate SAWs for this writing were highlighted and a non-contact Michelson interferometer detection system was described. Several techniques were established for optimal displacement and frequency sensitivity. These included one for the fine focusing of the detection beam for enhanced signal bandwidth and a method to synchronize SAW detection to the linear portion of a fringe signal. The synchronization technique is required for optimal displacement sensitivity and mimics the effect of path stabilization without active electronics.

For signal processing, the averaging and Fourier filtering process was detailed to show its effect in heavily suppressing signal noise. Processed signals with sufficient SNR ratios can undergo spectral analysis to generate dispersion curves from the experimental data. The procedure essentially compares the phase information at each frequency after a Fourier transform is taken of two signals from different distances. The curves obtained can be compared to the ones derived in chapter 3 for mechanical property extraction. A process of estimating error in this comparison is shown involving a standard deviation of the residuals from the two data sets.

Chapter 4 References:

AINDOW, A., DEWHURST, R. J., HUTCHINS, D. A. & PALMER, S. B. 1981. Characteristics Of A Laser-Generated Acoustic Source In Metals. 478-485.

ANDERHOL.NC 1970. Laser-Generated Stress waves. *Applied Physics Letters,* 16**,** 113-&.

ASH, E. A., DIEULESAINT, E. & RAKOUTH, H. 1980. Generation of Surface Acoustic Waves by Means of a C.W. Laser. *Electronics Letters,* 16**,** 470-472.

BELL, C. E. & LANDT, J. A. 1967. Laser-Induced High-Pressure Shock Waves in Water. *Applied Physics Letters,* 10**,** 46-&.

COUFAL, H., GRYGIER, R., HESS, P. & NEUBRAND, A. 1992. Broadband detection of laser-excited surface acoustic waves by a novel transducer employing ferroelectric polymers. *The Journal of the Acoustical Society of America,* 92**,** 2980-2983.

DAVIES, S. J., EDWARDS, C., TAYLOR, G. S. & PALMER, S. B. 1993. Laser-generated ultrasound: its properties, mechanisms and multifarious applications. *Journal of Physics D: Applied Physics,* 26**,** 329.

DEWHURST, R. J., HUTCHINS, D. A., PALMER, S. B. & SCRUBY, C. B. 1982. Quantitative Measurements of Laser-Generated Acoustic Waveforms. *Journal of Applied Physics,* 53**,** 4064-4071.

H. COUFAL, K. M., R. K. GRYGIER, M. DE VRIES, D. JENRICH, P. HESS 1994. Measurement of Elastic Properties of Evaporated C_{60} Films by Surface Acoustic Waves. *Applied Physics A,* 59**,** 83-86.

HUTCHINS, D. A., DEWHURST, R. J., PALMER, S. B. & SCRUBY, C. B. 1981. Laser Generation as a Standard Acoustic Source in Metals. *Applied Physics Letters,* 38**,** 677-679.

KARABUTOV, A. A. 1985. Laser Excitation of Surface Acoustical Waves - a New Branch in the Optico-Acoustical Spectroscopy of Solids. *Uspekhi Fizicheskikh Nauk,* 147**,** 605-620.

KOLOMENSKII, A. A., JEREBTSOV, S. N. & SCHUESSLER, H. A. 2004. Propagation of surface acoustic pulses generated by a femtosecond laser in thin films on solid substrates. *International Journal of Thermophysics,* 25**,** 473-483.

LEDBETTER, H. M. & MOULDER, J. C. 1979. Laser-induced Rayleigh waves in aluminum. *The Journal of the Acoustical Society of America,* 65**,** 840-842.

SCHNEIDER, D., SCHWARZ, T., SCHEIBE, H.-J. & PANZNER, M. 1997. Non-destructive evaluation of diamond and diamond-like carbon films by laser induced surface acoustic waves. *Thin Solid Films,* 295**,** 107-116.

SCRUBY, C. B. & DRAIN, L. E. 1990. *Laser ultrasonics: techniques and applications*, Adam Hilger.

WHITE, R. M. 1963. Elastic Wave Generation by Electron Bombardment or Electromagnetic Wave Absorption. *Journal of Applied Physics,* 34**,** 2123-2124.

Chapter 5 Correlation of LiSAW and nanoindentation on a bMFI zeolite thin film

5.1 Introduction

The progression of thin film technology towards ultra-thin and complex frameworks produces significant challenges towards the mechanical characterization of such media. In the last two decades, nanoindentation has become an essential tool in analyzing thin films due to the simplicity of technique, quickness of results, relatively nondestructive nature, and the ability to test a wide variety of films. However, the original indentation methodology outlined by Oliver and Pharr (Oliver and Pharr, 1992) encounters difficulty for soft and very thin films. Substrate effects are often seen in both cases since the interaction volume underneath the tip can become considerably influenced by the mechanical properties of the substrate (Saha and Nix, 2002, Chen et al., 2004). Specific to soft films, viscoelastic effects can become a problem as tip displacement becomes sensitive to loading rates (Zhang et al., 2005). Porous films introduce an even larger challenge because they couple their often intrinsic softness with a complex morphology. Along with substrate effects, the characterization of porous films can be skewed by densification as the tip compacts the sample during probing (Chen et al., 2006, Lu et al., 2012). Numerous correction schemes have been introduced to account for substrate and densification effects both separately (Chen and Vlassak, 2001, Bamber et al., 2001, Li and Vlassak, 2009, Menčík et al., 1997) and together (Chen et al., 2006) with good accuracy, however limitations remain concerning the fraction of indentation depth to film thickness and for films with a high degree of porosity.

The LiSAW technique eliminates substrate issues altogether since analysis of SAWs inherently requires the substrate conditions. As such, LiSAWs have been shown to be able to measure very soft and thin films (Chudoba et al., 2004, Schneider et al., 2005, Cote et al., 2009) that would normally prove difficult for traditional nanoindentation.

There have been several LiSAW studies on porous films (Cho et al., 1996, Xiao et al., 2004, Schneider et al., 2005, Takimura et al., 2008, Xiao et al., 2011) with each confirming the capability of LiSAW to handle porous samples effectively. Especially of interest to this writing though are the reports containing simultaneous study with nanoindentation. For fully dense films, LiSAW and nanoindentation are expected to be in close agreement, however the measurements seem to deviate when applied to soft porous frameworks. Flannery *et al.* (Flannery and Hurley, 2003) reported a threefold increase in the nanoindentation elastic modulus for a porous aerogel low-κ (low dielectric constant) film. Maosen *et al.* (Maosen et al., 2011) also observed a tripling of modulus on porous silicon films. Chapelon *et al.* (Chapelon et al., 2006) similarly reported, though to a lesser degree, an increase of the modulus by nanoindentation on a low-κ a-SiOC:H film. Interestingly, the work of Herrmann *et al.* (Herrmann et al., 2006) shows a 5-15% underestimation of the film modulus by nanoindentation, but was done utilizing a modified indentation methodology and extrapolating the plot of moduli versus indentation depth/film ratio to zero. All of these works focused on porous ultra-low-κ films with moduli less than 3 GPa. It has been proposed that an ideal low-κ material for semiconductor applications must match its dielectric properties with a minimum modulus of 6 GPa (International Roadmap Committee, 2013) in order to withstand polishing and packaging steps during chip fabrication. Thus, the intention of this paper is to add to the discussion by studying another porous low-κ film, but with a more intermediate stiffness. Since traditional nanoindentation remains the main method of characterization for such films, this study critiques the validity of indentation for porous low-κ films in this higher stiffness range by comparing its results to LiSAW.

The film studied is a nanoporous low-κ bMFI zeolite material. The name denotes the MFI framework with specific film orientation in the b-axis (Figure 5-1). The bMFI film has the same crystal structure as the ZSM5-MFI structure studied in chapter 2. However, bMFI is a pure-silica zeolite (PSZ) with no aluminum T-sites therefore it exhibits slightly different mechanical properties. The pore size and distribution remain similar with ~5 Å pores running along two axes and a total porosity of ~33% (Flanigen et al., 1978). Discovery of thin film MFI synthesis has led to considerable interest as a low-κ medium since the porosity allows for a κ of 2.7 (Wang et al., 2001) while the ordered crystalline framework retains a high mechanical stiffness of > 30 GPa (Li et al., 2006). This film is of particular interest to since it provides the unique ability to study the mechanical properties of as-synthesized films with occluded pores and the same films post-calcination with voided pores. Both structures will be analyzed and compared between LiSAW and nanoindentation.

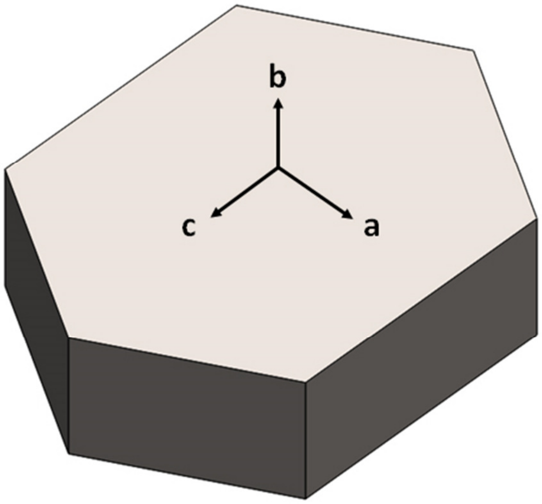

Figure 5-1. MFI crystal with orientation axes shown.

5.2 Sample preparation

B-MFI films were prepared on silicon substrates (100) by an established procedure reported earlier (Wang and Yan, 2001). The procedure requires preparation of a synthesis solution with a molar composition of 0.32TPAOH:TEOS:165H_2O. This is done by adding tetraethylotrthosilicate (TEOS 98% wt, Sigma Aldrich) dropwise into a stirring solution of water and tetrapropylammonium hydroxide (TPAOH 40% wt, Sachem). The solution is then aged for 4 hours while stirring. Silicon panels are cleaned and placed vertically in a Teflon lined autoclave (Parr Instruments). Around 50 g of the solution is added before sealing the autoclave and placing it into a 165° C oven for two hours. Upon extraction, the bMFI coated substrates are washed by hand with water and dried in air. Some of the films underwent calcination to remove the organic template occluding pores. This is performed by baking the sample in a 450 °C oven for 12 hours. Some films were mechanically polished to eliminate secondary crystals on the sample surface left over from synthesis. For these samples, a Buehler auto-head polisher (Buehler EcoMet, Lake Bluff, IL) was used with 0.1 μm diamond paste. Lastly, aluminum films of various thicknesses were deposited by magnetron sputtering on top of the bMFI to serve as a reflecting layer for optical SAW detection.

5.3 Characterization Methods

Nanoindentation was performed using a Hysitron Ubi nanomechanical test instrument (Hysitron, Minneapolis, MN) following the same procedures as outlined in chapter 2. However, some samples were indented with a cube corner tip (90° total included angle, 40 nm tip radius), as opposed to the Berkovich in previous tests, because the sharper geometry produces a smaller plastic zone and is therefore less prone to substrate effects for thinner films. The LiSAW measurement was conducted with the system outlined in Chapter 4. All methods used to generate, detect, analyze, and compare SAW signals are found in their respective sections in Chapters 3-4.

Thickness is an important parameter because it is one of the fitting parameters used for theoretical LiSAW curves. For sputtered metallic films, a tape mask was used to create a step height from the bare substrate to the film. This was then profiled with SPM imaging by the Hysitron UBi1 (Hysitron, Minneapolis MN) which allows for thickness measurements up to 1.5 μm. For bMFI films, the thicknesses were measured by spectroscopic ellipsometry (Woollam M-2000, Lincoln, NE) since a reliable step height could not be produced with the hydrothermal synthesis procedure.

5.4 Validation studies

5.4.1 Aluminum film on a silicon substrate

Before bMFI samples could be tested, the LiSAW system required validation through measurement of a film with well-known mechanical properties. Aluminum films on silicon (100) substrates were chosen since both materials have been studied extensively by others. Magnetron sputtering was used to deposit a 230 nm layer of aluminum on silicon and the film was tested with LiSAW using both the Tempest and Leopard lasers as SAW sources. SAW waveforms were collected at roughly 18 and 22 mm from the source in the [100] direction of the silicon wafer. The waveforms generated by each laser can be seen in Figure 5-2 and Figure 5-3.

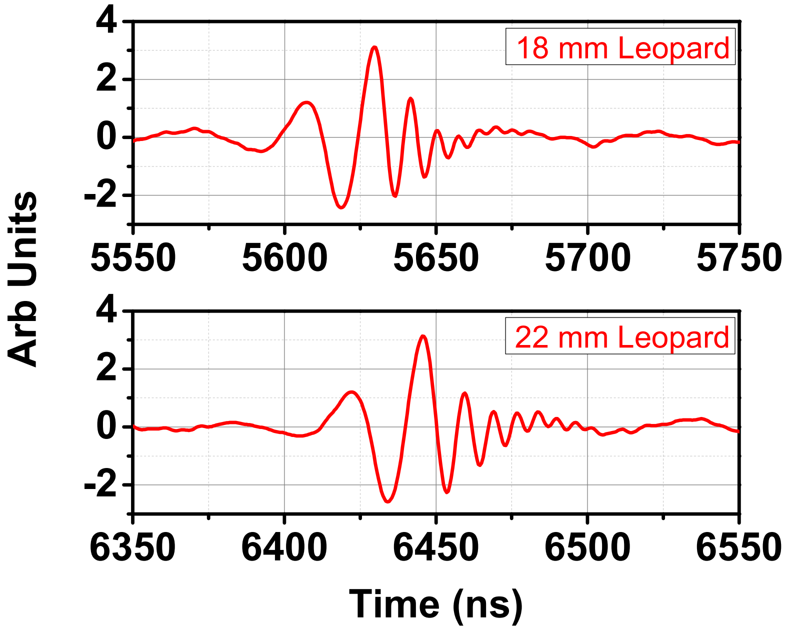

Figure 5-2. SAW signals recorded for a 230 nm Al film on silicon in the [100] direction at various distances from the Leopard laser point of generation.

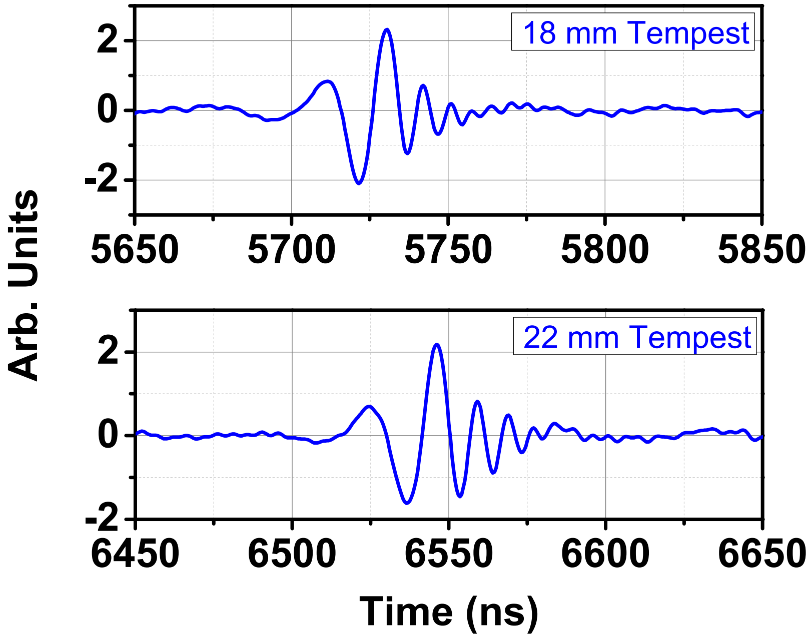

Figure 5-3. SAW signals recorded for a 230 nm Al film on silicon in the [100] direction at various distances from the Tempest laser point of generation.

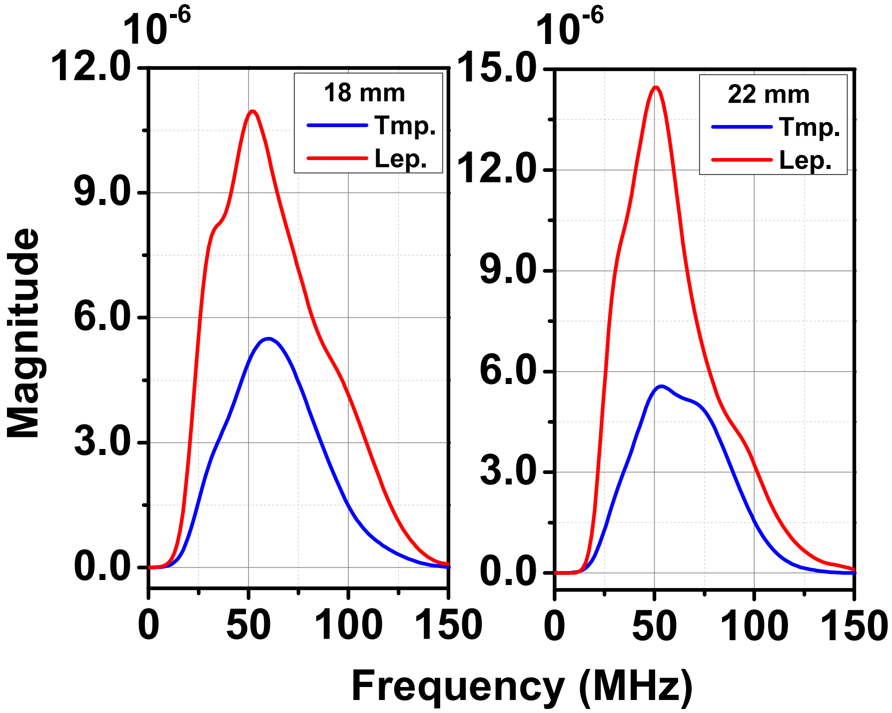

Figure 5-4. Frequency spectrum of signals in Figs. 5-1 and 5-2.

Figures Figure 5-2 and Figure 5-3 show that the waveforms generated by both lasers are nearly identical. The Leopard laser, having a shorter pulse width, is expected to increase the bandwidth of generation. However, the detection of high frequencies requires optimal focusing of the detection beam. At least a 25 µm spot size is necessary to detect a 100 MHz wave traveling on a silicon substrate and the measured spot size for this setup was ~10 µm. Since the leopard signal shows no signs of increased frequency, the experiment was determined to be detection limited. To analyze the frequency bandwidth, a fast Fourier transform (FFT) of both signals was calculated and plotted in Figure 5-4. It can be seen that the Leopard dominates in magnitude at both distances. This can be attributed to the differences in power used to generate the SAW for each laser. The Tempest only required ~10 mJ for generation while the Leopard required ~30 mJ resulting in higher amplitude of displacement. It is believed that the increased damage from the

Leopard, based on its pulse-width, affects the efficiency of generation. If the frequency spectrum for the Leopard signals were scaled down to the Tempest, then the upper limit of detection is comparable between both lasers at ~120 MHz. This is in line with the hypothesis that the system is detection limited from the spot size of 10 µm.

The bandwidth available was more than adequate to form dispersion curves. For the Al/Si system in this experiment, dispersion was expected to be very linear for the first several hundred megahertz. However, the wave amplitude diminishes down to the noise level as the waveforms trail off towards the end of a SAW. This introduces nonlinearities at high and low frequencies in the dispersion plot, thus since linear dispersion is expected, only the linear portions of the dispersion plot are selected for fitting. This can be done by taking only the frequencies within the full width half maximum (FWHM) of the frequency spectrum, or by inspection after dispersion is calculated for the entire range. The dispersion curves are shown in Figure 5-5.

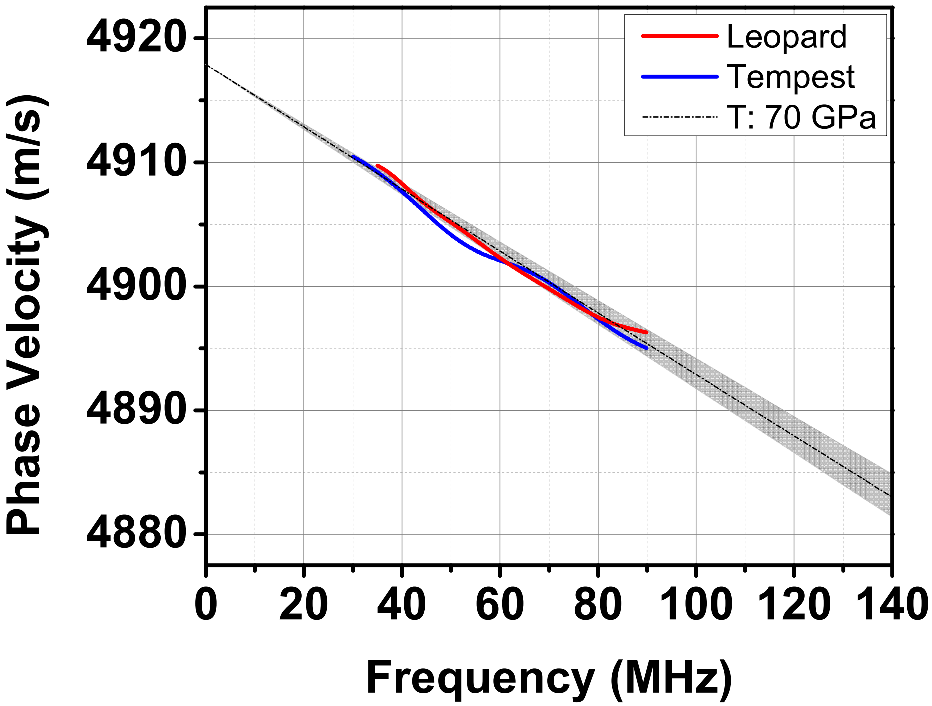

Figure 5-5. Dispersion curves for 230 nm Al film on silicon in the [100] direction. Grey region shows a ± 5% error to the elastic modulus.

The dispersion curves in Figure 5-5 were fitted to a theoretical curve (dotted black line) for an aluminum film with the following properties: $E = 70\ GPa$, $\nu = 0.33$, $\rho = 2700\ kg/m^3$, and $t = 230\ nm$ where E is the elastic modulus, ν is the Poisson's ratio, ρ is the density, and t is the film thickness. The properties of the silicon substrate were: $c_{11} = 165.7\ GPa$, $c_{44} = 79.6\ GPa$, $c_{12} = 63.9\ GPa$, and $\rho = 2.33\ g/cc$. The fit is good with the majority of points falling within the ±5% error region. An elastic modulus of 70 GPa is within the generally accepted range of 69-72 GPa (Serway et al., 2008) for bulk aluminum. The results successfully validated the LiSAW system by demonstrating the capability to extract the elastic modulus from experimental dispersion curves by fitting with theoretically derived curves. Additionally, it was discovered that the system is detection limited therefore the waveforms generated by the higher damaging

Leopard laser provided no significant bandwidth gain. Later films were predominantly tested with the Tempest laser for this reason.

5.4.2 Aluminum film on a fused silica substrate

This second validation study actually predated the aluminum on silicon system and was in fact one of the first successful SAWs measurements obtained with the system. The study involved a 390 nm aluminum film on a fused silica substrate tested with the Tempest laser. The slower wave speed of the fused silica (3410 m/s) meant that there would be a lower degree of dispersion with the aluminum film (2900 m/s). From theory, it was determined that the velocity would only change by ~10 m/s over the 100 MHz testing range. Therefore, this study was performed to answer several key questions about the developing LiSAW system: whether it could work with isotropic substrates (this predated anisotropic work), what the quality of SAWs were on slower substrates, and most importantly, the fidelity of the system (whether it could pick up the small degree of dispersion).

The study is presented here, even though it was completed earlier than the aluminum on silicon film, because at the time, there was no precise translation stage installed for sample movement. Therefore the separation distance used for the dispersion calculation had a large error. However, a method was devised to mitigate this error by exploiting the expected linear dispersion of the material system. This involved linearly extrapolating the experimentally determined curve to zero frequency and then modifying the separation distance, in effect shifting the entire curve up and down, until the zero-intercept equaled the Rayleigh wave speed of the substrate. Since the substrate properties are known and the dispersion is linear, this shift is acceptable because the wave speed at low frequencies must approach the base substrate speed. The elastic modulus of the film, which only alters the slope of the curve and not the intercept, was then fit to the experimental results. Waveforms were detected at roughly 15 mm and 25 mm for this system. Extra propagation distance was given since the degree of dispersion, and thus the change in the waveform with distance, was lower. The signals detected are shown in Figure 5-6.

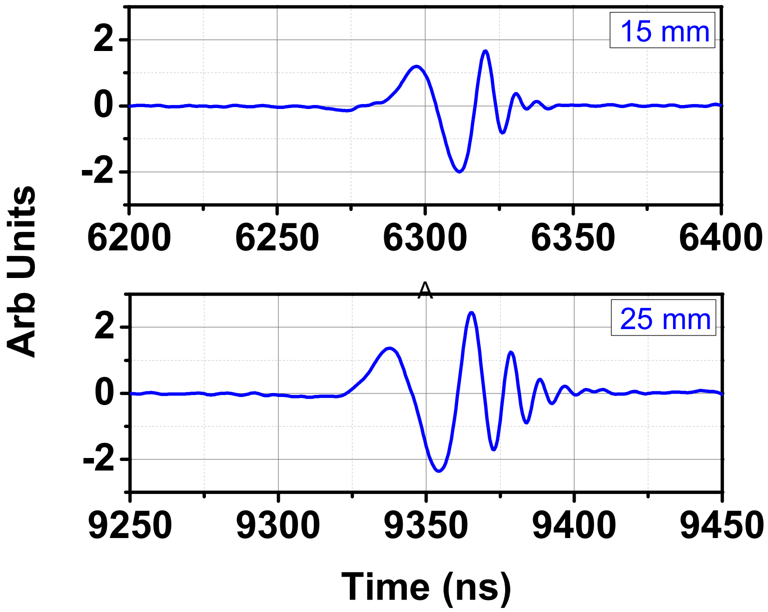

Figure 5-6. Detected SAW signals for a 390 nm Al film on a fused silica substrate.

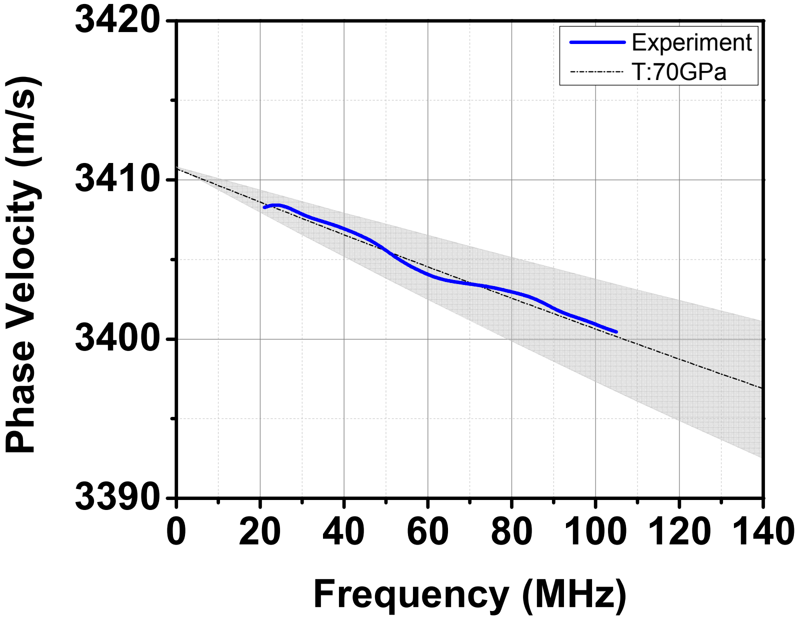

Figure 5-7. Dispersion curve calculated for the signals in Fig. 5-5. Dotted black line represents a 70 GPa aluminum film. Grey area shows a ±5% error on the modulus.

The dispersion curve for the aluminum film on fused silica is shown in Figure 5-7. As mentioned previously, this curve was linearly fit and extrapolated to zero frequency. The separation distance was then modified in the dispersion calculation until the zero-intercept fit the substrate Rayleigh wave speed. The fused silica substrate properties used for fitting were: $E = 73\ GPa$, $\rho = 2200\ kg/m^3$, and $\nu = 0.17$ where E is the elastic modulus, ν is the Poisson's ratio, ρ is the density. The elastic modulus of the film was best fit to a theoretical aluminum film with the following properties: $E = 70\ GPa$, $\nu = 0.33$, $\rho = 2700\ kg/m^3$, and $t = 390\ nm$ where t is the film thickness. These are the same properties used to fit the previous aluminum/silicon system. The results from this study satisfactorily answered the questions posed at the beginning of this work. It showed the ability to generate SAWs on isotropic substrates, the ability to detect SAWs reliably for these types of systems, and the ability to resolve low degrees of dispersion.

Additionally, the elastic modulus fit for the aluminum film was consistent with accepted values and the other validation study.

5.5 Results and discussion for bMFI films

With confidence in the LiSAW system provided by the previous validation studies, bMFI films were synthesized and prepared for testing. However, during the synthesis process, it was discovered that there were secondary crystals being formed on top of the main film (Figure 5-8). These were documented previously (Wang and Yan, 2001) and their adhesion seemed to be a function of film orientation during synthesis. The authors from the earlier report noted that they were able to remove the crystals easily by hand force if the panels were placed horizontally in the reactor during synthesis. However, for this study, the silicon panels were restricted to a vertical orientation due to geometrical constraints and the crystals were not easily removed. These crystals were undesired because they introduced significant roughness to the film thus affecting optical quality. They also presented a source of error in the film thickness. Furthermore, it was thought that they could contribute to the scattering of higher frequencies in the Rayleigh wave.

The continuous film underneath the extra crystals is composed of a ~430 nm layer of unit thickness b-oriented MFI crystals and the secondary crystals appeared to be around the same thickness (Figure 5-9). This suggested that the crystals were formed after the continuous layer is deposited quite possibly from unreacted components in the solution. They were, in effect, an incomplete second layer to the film. A study was conducted to find the optimal synthesis conditions to minimize these secondary crystals and it was found that reducing the bake and age times by 5-10% was most helpful. The crystals were reduced, but not completely eliminated because any further reduction in time resulted in a discontinuous main film.

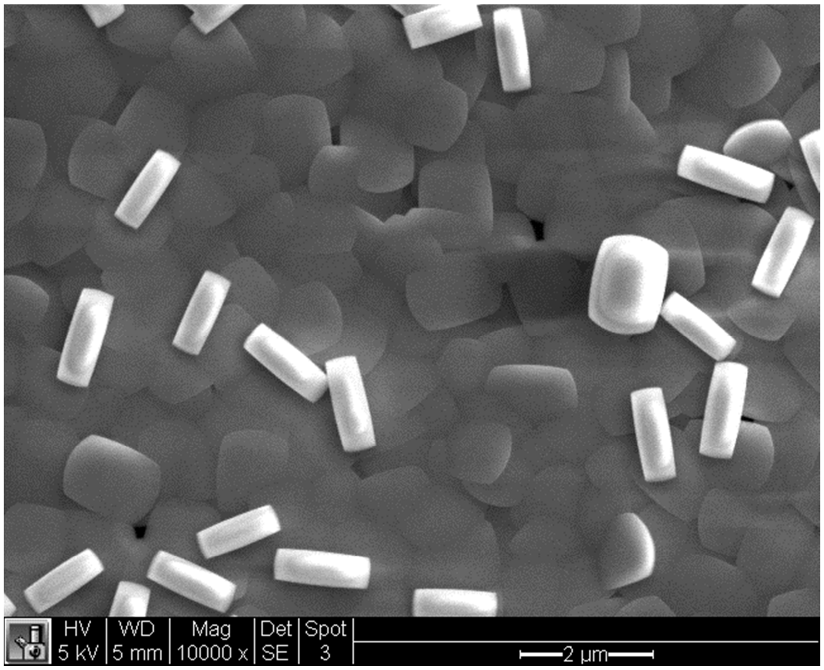

Figure 5-8. SEM image of bMFI film surface with secondary crystals.

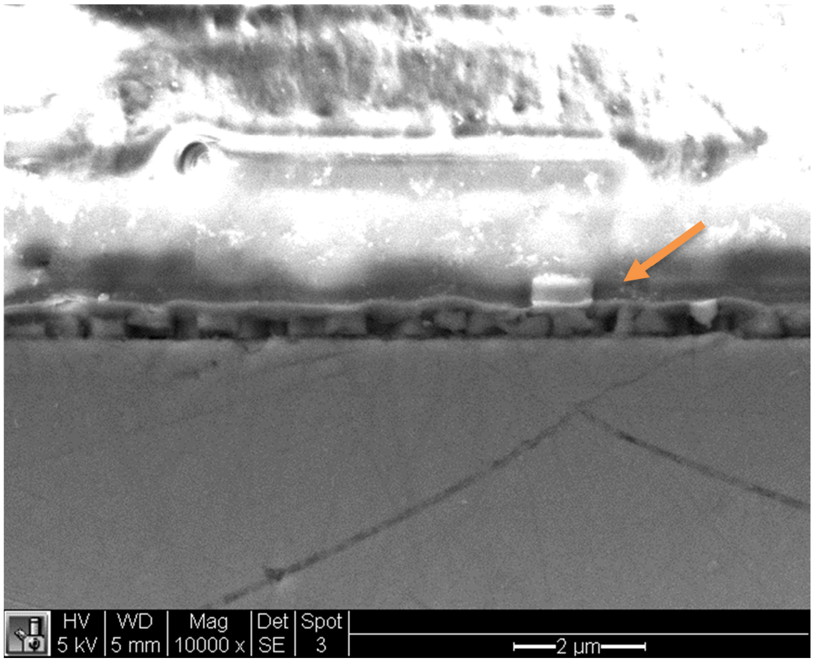

Figure 5-9. Cross-section of bMFI film with secondary crystal seen towards right. Top half is epoxy molding.

In an effort to avoid polishing since the process could introduce non-uniformity in film thickness, the first few bMFI LiSAW studies were conducted with the secondary crystals intact. Polished films were later characterized to see what effect, if any, the secondary crystals had on dispersion.

5.5.1 Unpolished bMFI films – Set #1: Tempest

The first set of calcined and noncalcined bMFI films were evaluated using the Tempest laser as the SAW source. The films were ~430 nm in thickness and had a 275 nm layer of aluminum deposited on top. The waveforms were collected at distances of 15 mm and 10 mm in the [100] direction of silicon and are shown in Figure 5-10 and Figure 5-11. The propagation distance is reduced from the previous validation studies because there was uncertainty about the top crystals scattering high frequencies and because the samples were only ~20×20 mm.

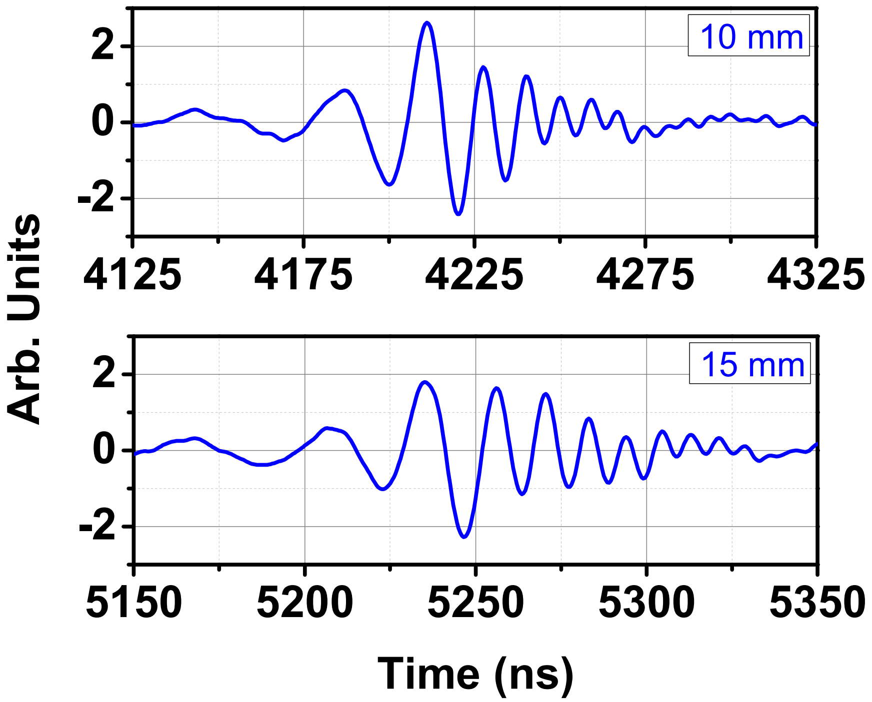

Figure 5-10. SAW waveforms obtained for the non-calcined sample of set #1.

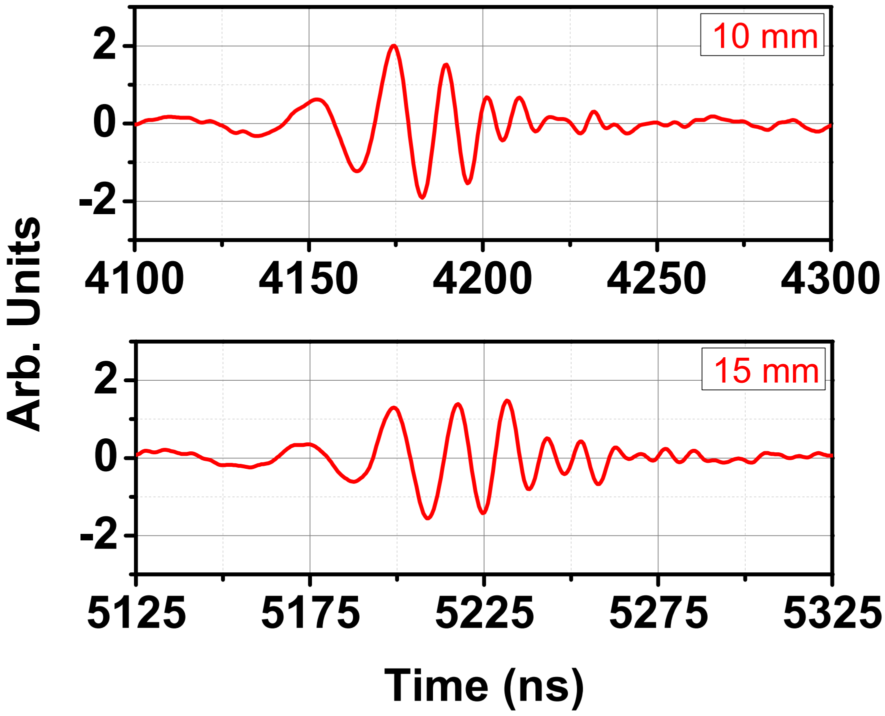

Figure 5-11. SAW waveforms obtained for the calcined sample of set #1.

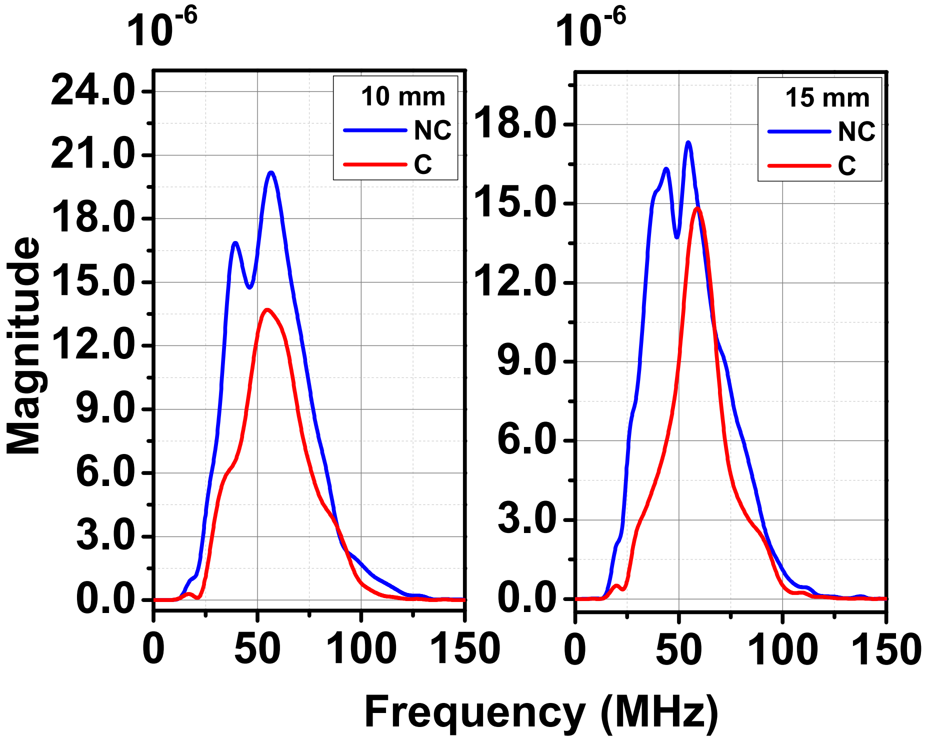

Figure 5-12. FFT of calcined and non-calcined signals in set #1.

Looking at the signals in Figure 5-10 and Figure 5-11, the difference between calcined and non-calcined waveforms is not apparent. The oscillation structure and length of the wave group are similar. This is somewhat expected since the elastic properties between calcined and non-calcined films are not likely to change dramatically. The non-calcined films seem to have slightly higher amplitudes in the high frequency range, but this could be due to variation in the testing position and signal averaging. The FFT of each signal, shown in Figure 5-12, confirms that the frequency spectrums between the calcined and non-calcined samples are similar. The non-calcined sample does indeed have a higher amplitude, but once again, this could come from signal processing. Signal bandwidth is a more important parameter rather than raw amplitude and both samples exhibit a response range of ~30-110 MHz.

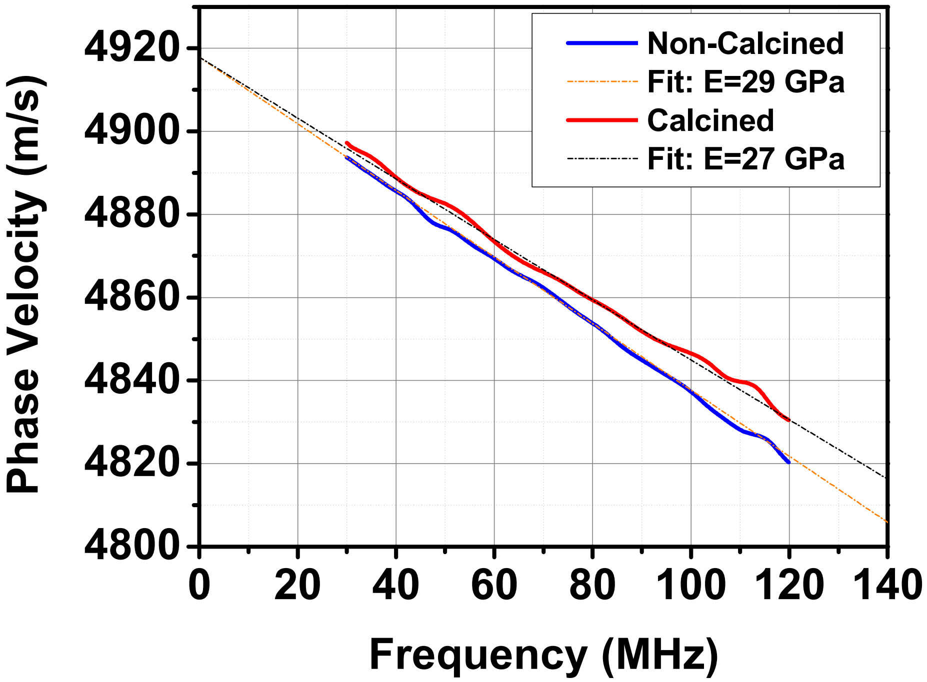

Figure 5-13. Dispersion curves for non-calcined and calcined samples in set #1.

Figure 5-13 shows the calculated dispersion curves. For linear dispersion, only one parameter could be fit therefore to obtain the elastic modulus, the density, thickness, and Poisson's ratio of the film needed to be known. The thickness was measured previously and the Poisson's ratio appears in literature (Sanchez-Valle et al., 2008). The density, however, was not known for thin film bMFI and could not be obtained easily. The only references to density in literature are for the powder form where the authors report values of 1.99 and 1.75 g/cc for non-calcined and calcined powders respectively (Flanigen et al., 1978). From the SEM pictures above, it is clear that the bMFI film is a single layer of fully formed MFI crystals attached together, therefore the density should be similar to the powder with the differences coming from the grain boundaries. Since there are agglomerations of MFI crystals attached together at the bottom of the reactor after synthesis, these were used to estimate the density of the film. The non-calcined clumps were evaluated by mercury porosimetry and pycnometry with respective results of 1.94 g/cc and 1.90 g/cc. These results are in line with the powder values and may be slightly lower due to presence of voids in the agglomerations that could not be intruded on. Since the results were comparable, the original powder values were used for calculations.

The dispersion curves were fit to theoretical curves having the following properties: Non-calcined - $E = 29\ GPa, \nu = 0.166, \rho = 1.99\ g/cc, t = 430\ nm$ and calcined - $E = 27\ GPa, \nu = 0.166, \rho = 1.75\ g/cc, t = 430\ nm$. The properties for the aluminum film and silicon substrate were the same as those in the validation studies. The 2 GPa drop in modulus between the non-calcined and calcined films was in the range of acceptable values, but another film was warranted in order to repeat the results.

5.5.2 Unpolished bMFI films - Set #2: Leopard

A second round of testing was completed, but this time with the Leopard laser as the SAW source. While the shorter pulse-width Leopard seemed to give no significant benefit during validation testing with the aluminum film, there was still interest in how the bMFI film would react to the higher power fluence. The film conditions were similar to that of the first round. A ~430 nm bMFI film was split in half with one side undergoing calcination. Both received a 280 nm layer of aluminum for reflectivity. Similar to the validation study, the Leopard laser required more power for SAW generation (30-40 mJ) and was well into the ablation regime. The signals were generated in the [100] direction of silicon and their waveforms after various propagation distances appear in Figure 5-14 and Figure 5-15.

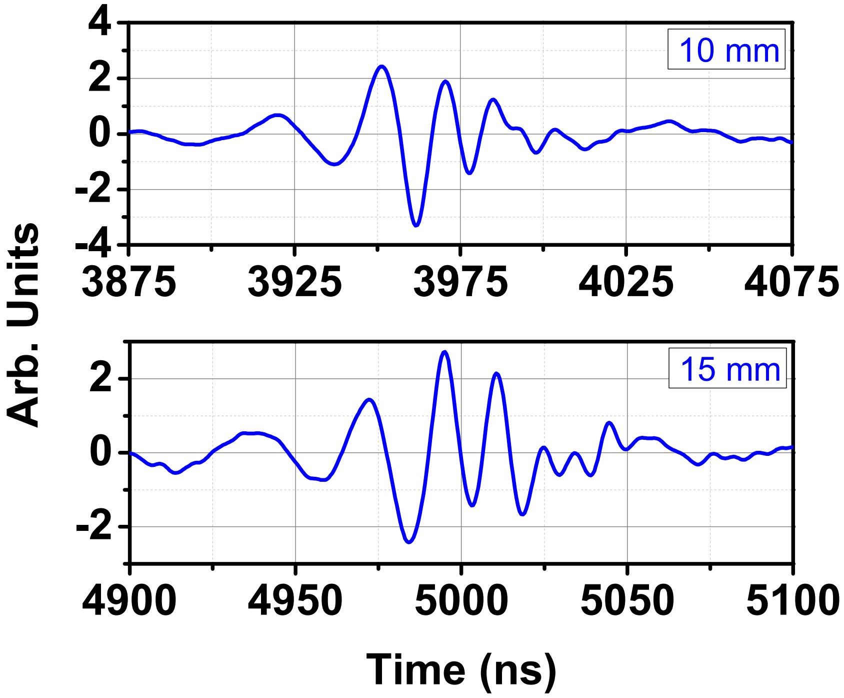

Figure 5-14. Signals detected for the non-calcined sample of set #2.

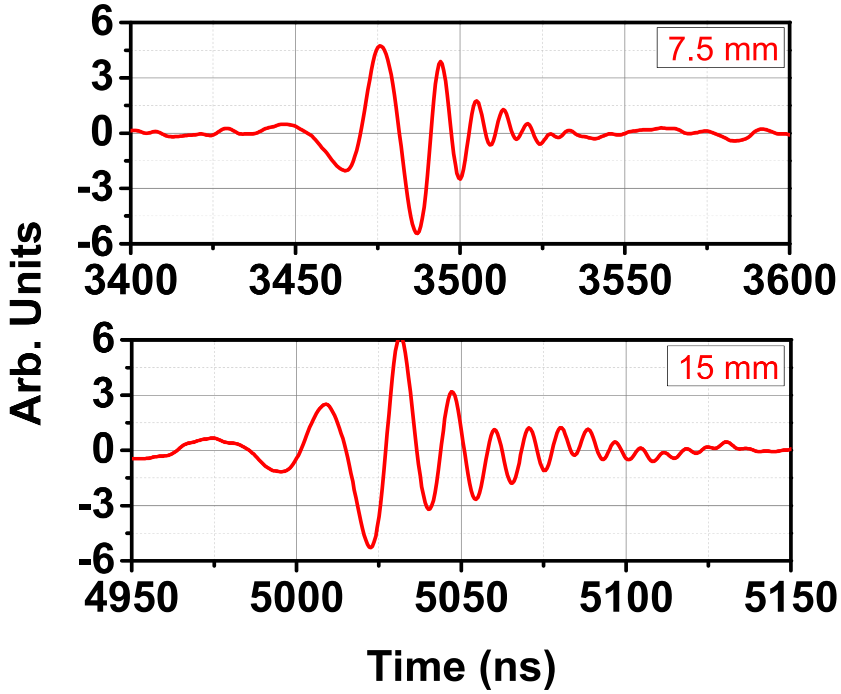

Figure 5-15. Signals detected for the calcined sample of set #2.

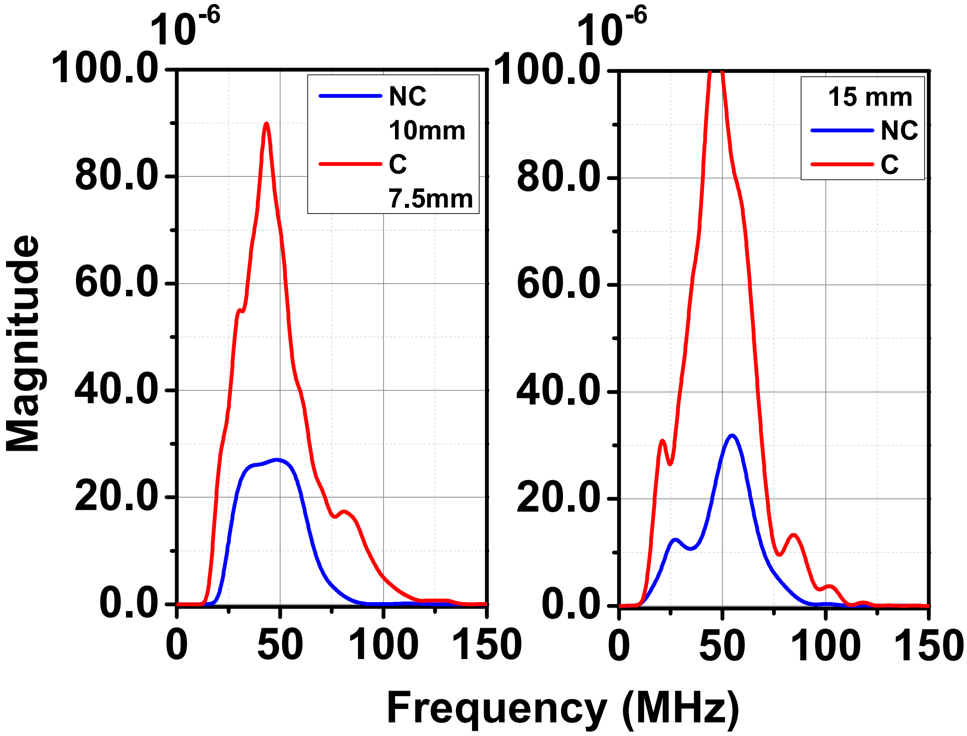

Figure 5-16. FFT of calcined and non-calcined signals in set #2.

From looking at Figure 5-14 and Figure 5-15, it is clear that the non-calcined sample had poorer waveforms especially for the 10 mm case. The exact cause for this is not known since the calcined sample fared much better and came from the same batch. One potential cause could be improper focusing, however the 15 mm case performed immediately afterwards did not appear to have trouble extending to the higher frequency region. For the calcined sample, signals were detected at 15mm, 10mm, and 7.5 mm therefore the 7.5 mm measurement was used for analysis for a greater degree of dispersion. The dispersion curve should remain the same no matter what separation distance is used. The FFT plots of each signal, plotted in Figure 5-16, show that the entire frequency spectrum was attenuated for the non-calcined film at both distances. While the result is peculiar, it did not affect the final dispersion curves since their formation depends on phase comparison at each frequency instead of their amplitudes. Additionally, there was sufficient bandwidth from the non-calcined sample to form an acceptable range of dispersion. The dispersion result is plotted in Figure 5-17.

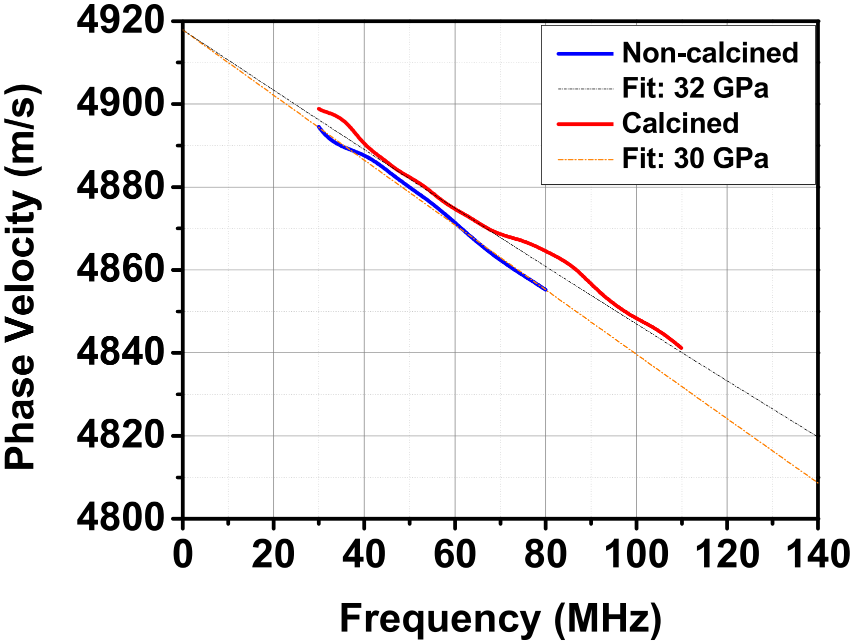

Figure 5-17. Dispersion curves for non-calcined and calcined samples in set #1.

The dispersion curves in Figure 5-17 were fit to theoretical curves with the same known parameters (Poisson's ratio, density, elastic constants) for the aluminum film and substrate as referenced in the prior section. The test specific parameters were: non-calcined: $E = 32\ GPa,$ $t = 430\ nm$, and calcined, $E = 30\ GPa, t = 430\ nm$. The results repeated the slight modulus drop from calcination, but also increased all fitted moduli by ~ 10%. It was unlikely that the error came from the poorer waveforms since their lower frequency components were still intact. However, the 10% error for linear dispersion was a bit higher than expected. Looking back at the bMFI fitting parameters, it was realized that the assumption of a constant thickness may not be accurate. The effect of the secondary crystals may add to the thickness and throw off the fitting of the modulus, therefore a polished film needed to be tested.

5.5.3 Polished bMFI films – Tempest

In order to characterize the effect of the secondary crystals, several bMFI films were mechanically polished to produce a smooth surface free of artifacts. Polishing was avoided at first since it was feared that the process would introduce non-uniformity of the sample thickness, but thickness measurement after polishing alleviated these concerns by showing < 10% variance in thickness from edge to edge. The majority of the variance existed very close to the sample edges therefore the testing region was quite uniform. The samples followed the same calcination routines as before and both received a 250 nm aluminum layer. Testing was performed in the [100] direction of silicon once again.

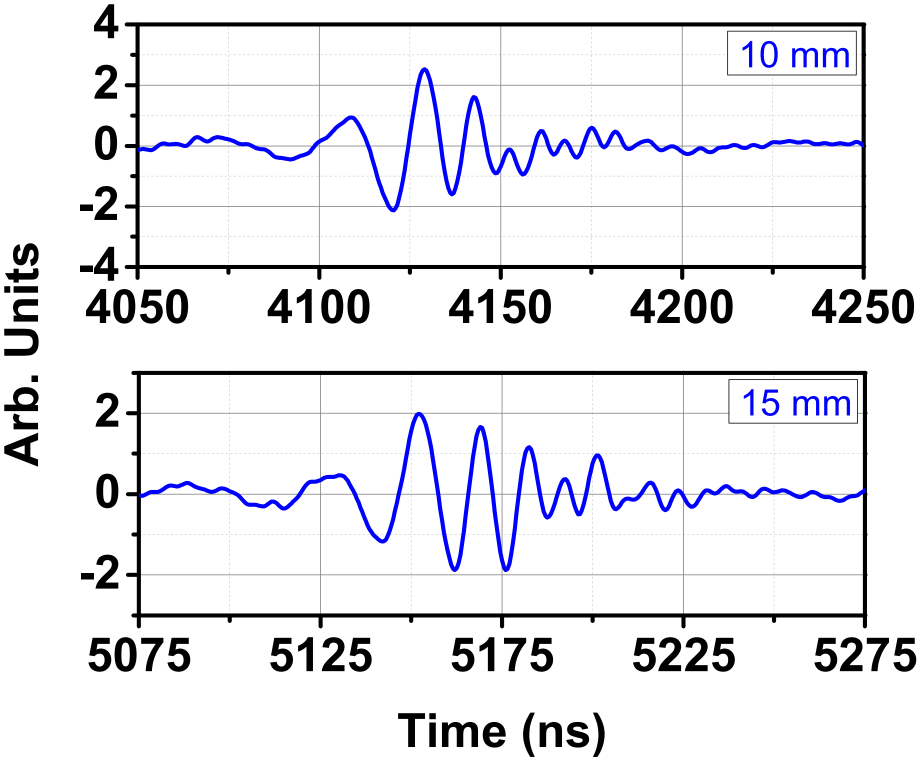

Figure 5-18. SAWs detected for the polished non-calcined sample.

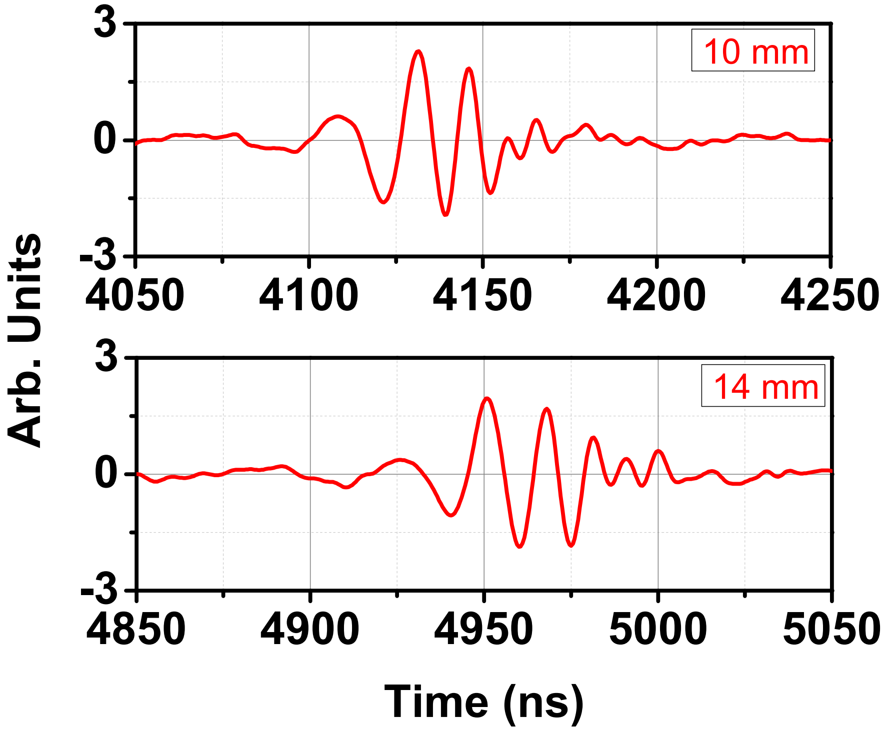

Figure 5-19. SAWs detected for the polished calcined sample.

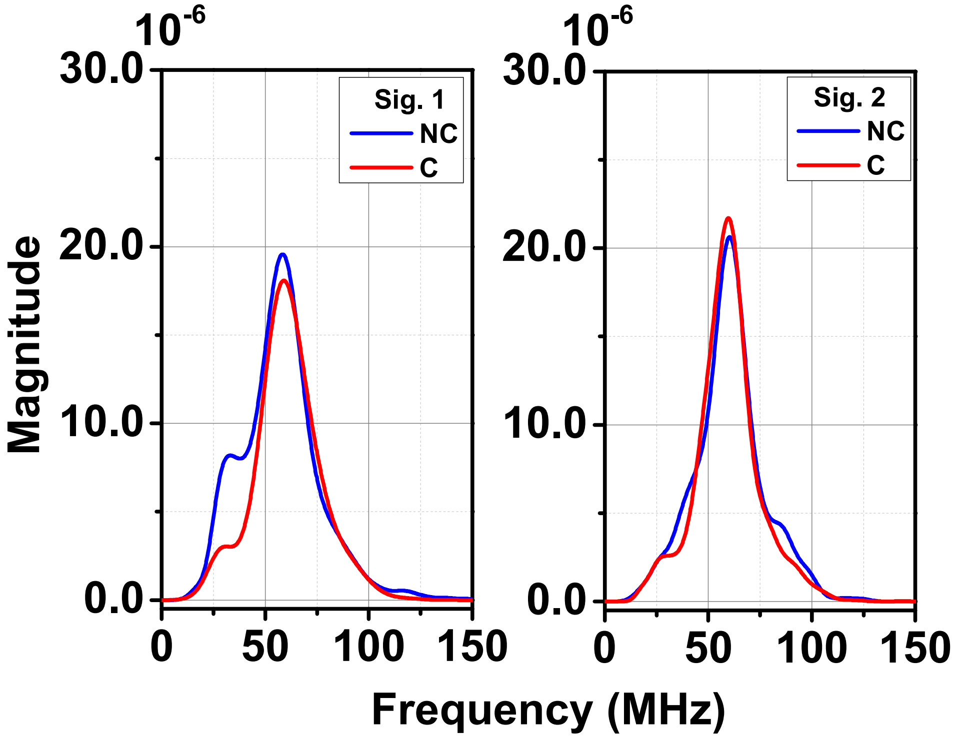

Figure 5-20. FFT of polished calcined and non-calcined signals.

The signals shown in Figure 5-18 and Figure 5-19 are quite similar to the previous unpolished Tempest results. The high frequency regions did not look any better or worse therefore the effect of secondary crystal scattering was determined not to be a factor. The Fourier transform of the signals exhibited a typical bandwidth seen in this setup, although it was somewhat smoother than the unpolished Tempest results (Figure 5-20). The dispersion curves calculated from these signals can be seen in Figure 5-21.

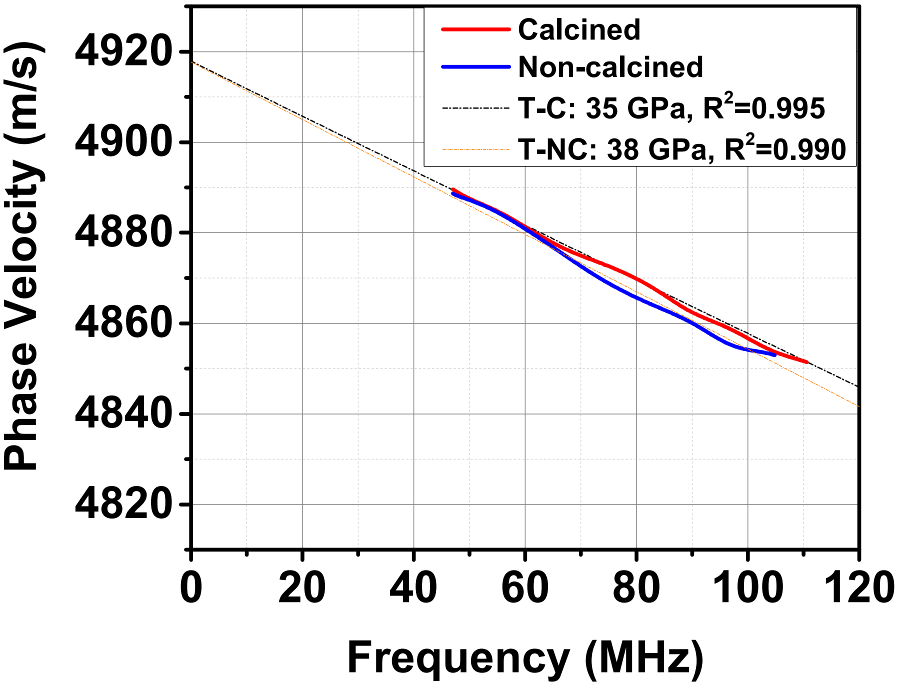

Figure 5-21. Dispersion curves for polished calcined and non-calcined films.

The films were fit using the same Poisson's ratio and density as with earlier films. The other parameters were: Non-calcined - $E = 38\,GPa$, $t = 350\,nm$, and Calcined - $E = 35\,GPa$, $t = 360\,nm$. The results for the elastic modulus are about 30% higher than the previous studies and indicated that there may be some effect going on with the secondary crystals. Indentation studies were performed to see if there were significant differences between the first two sets and the last polished set. The indentations would also serve as a critical point of comparison amongst the two techniques.

5.5.4 Comparison of LiSAW results to nanoindentation

Nanoindentation was performed on all samples in order to compare the modulus measured from both techniques. Since the films were less than 430 nm in thickness and considerably softer than the substrate, a cube corner tip was used to avoid influence from the harder silicon. An empirical rule of indentation depths staying below 10% of the sample thickness was attempted, but the 43 nm range left little to draw results from. The sharper cube corner tip was expected to help decrease the plastic zone size allowing for deeper indentations therefore the maximum depths were confined to < 85 nm (t/5) and extra caution was employed to look for substrate effects. The results from indentation for the first two unpolished films are shown in Figure 5-22.

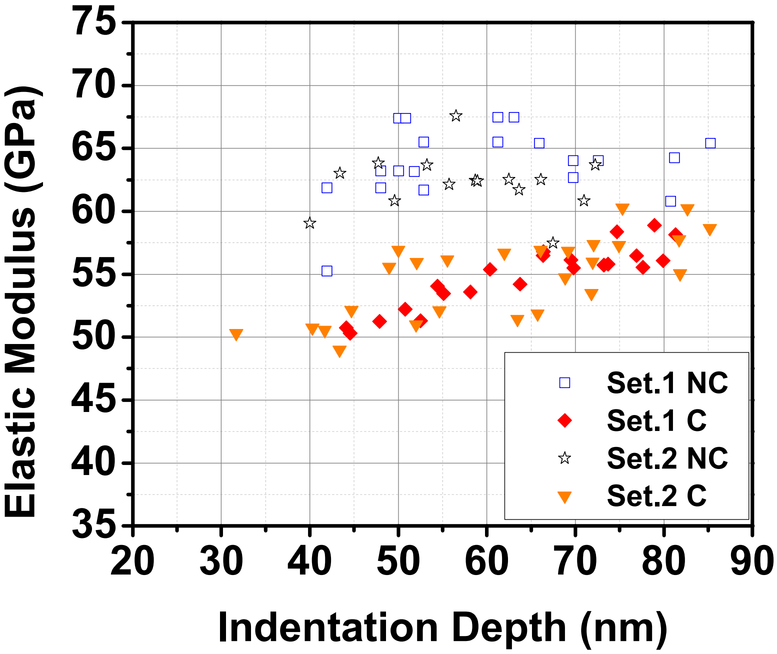

Figure 5-22. Indentation results for unpolished bMFI films.

For unpolished bMFI films, the indentation results correlated well between non-calcined and calcined samples of each set. The samples had a combined modulus of 62.8 ± 3.5 GPa for the non-calcined films and 54.8 ± 2.9 GPa for the calcined films. These results are almost two times higher than the ~30 GPa values obtained from LiSAW. Upon closer inspection of the indentation data, it is clear that there are substrate effects happening since the trend for all curves slopes upwards. For some films, such as the non-calcined film from set #1, the effect is not as apparent, however since all films are the same thickness and indented to around the same depth, the substrate effect should be similar. For subsequent indentation on the polished films, indentation loads were decreased to see if the substrate effect could be prevented.

Mechanical polishing of the films reduced their thicknesses to ~350 nm. This was expected to increase the substrate effect even if the indentation loads were lowered. For these films, the same

$t/5$ indentation depth ratio was used for the upper boundary whereas the lower boundary was allowed to approach the 10 nm limit of the area function. The results of indentation are shown in Figure 5-23.

The results for polished films show a strong substrate effect for both the non-calcined and calcined structures. The averaged modulus for each film type is very similar to the unpolished films and their values are 59.5 ± 5.3 GPa and 54.0 ± 4.7 GPa for the non-calcined and calcined films respectively. It is clear that the moduli from indentation are being inflated by the substrate effect and that the cube corner tip is not sufficient for making measurements on these films. Additionally, the results from below 10% of the film thickness also exhibit a positive slope therefore the empirical rule of staying below this depth range does not apply to these films. These findings show that the LiSAW measurement is capable of avoiding the substrate effect and making measurements on thin porous films. However, the discrepancies for LiSAW between the unpolished and polished films remained unclear.

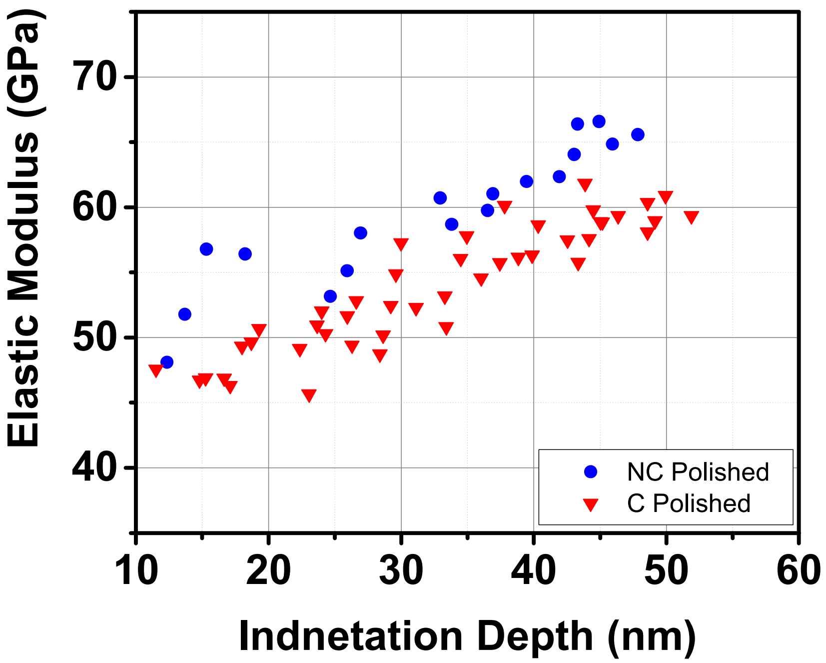

Figure 5-23. Indentation results for polished bMFI films.

5.5.5 Indentation correction scheme

While the majority of indentation analysis is still performed with the Oliver-Pharr method such as in this study earlier, there have been a variety of correction schemes that attempt to correct for the substrate influence. Several of these were highlighted in the introduction to this chapter and one of them, Li's solution (Li and Vlassak, 2009), was applied to these results. The goal was to use the correction scheme to estimate a more accurate indentation modulus for the polished films since they were the ones free of secondary crystals. The corrected moduli could then be compared to the LiSAW results to see if they were within acceptable ranges of each other.

The Oliver-Pharr method uses Sneddon's contact solution for an elastic half-space therefore it is easy to see why the method has trouble with the finite thickness of a thin film. The technique was never made to handle thin films to begin with. For thick films where the indentation depth is only a small fraction of the thickness, the assumption of an infinite layer can hold true. However for thinner films, the contact solution must be modified. The correction scheme utilized here does just that and employs Yu's elastic contact solution for a layered half-space (Yu et al., 1990). By involving the substrate in the analysis, indentation substrate effects can be potentially eliminated in the same manner that LiSAW considers the substrate for SAW analysis. Unfortunately, the solution is much more complex than Sneddon's therefore it will not be described in full detail here.

Li's solution proceeds similarly to Oliver-Pharr in that the experimental indentation behavior (i.e. measured stiffness and load) is used in an elastic solution to extract the mechanical constants from an elastic-plastic indentation. However, for a plastic indentation on a layered system, the film thickness underneath the tip will vary as the tip is pressed into the surface meaning that the film thickness used in Yu's solution is non-constant. Li introduced a parameter, η, to describe the thinning effect that is unique to each material. For an assumed η and film modulus, M_f, a relationship between the stiffness and contact radius (or contact area) of an indentation could be developed from the experimental data. Using the same M_f and η, a similar relationship could be simultaneously determined solely by Yu's contact solution. Li called these the experimental and theoretical S-a (stiffness-contact radius) curves and showed that when the two solutions are equal, then the assumed M_f and η are the properties of the film. Thus, the correction scheme involves computationally varying M_f and η for a given set of indentation data until the theoretical contact solution matches the elastic behavior from the experiment. While Li demonstrated that the substrate effect could be eliminated by this scheme, the computational intensity involved has limited widespread adoption.

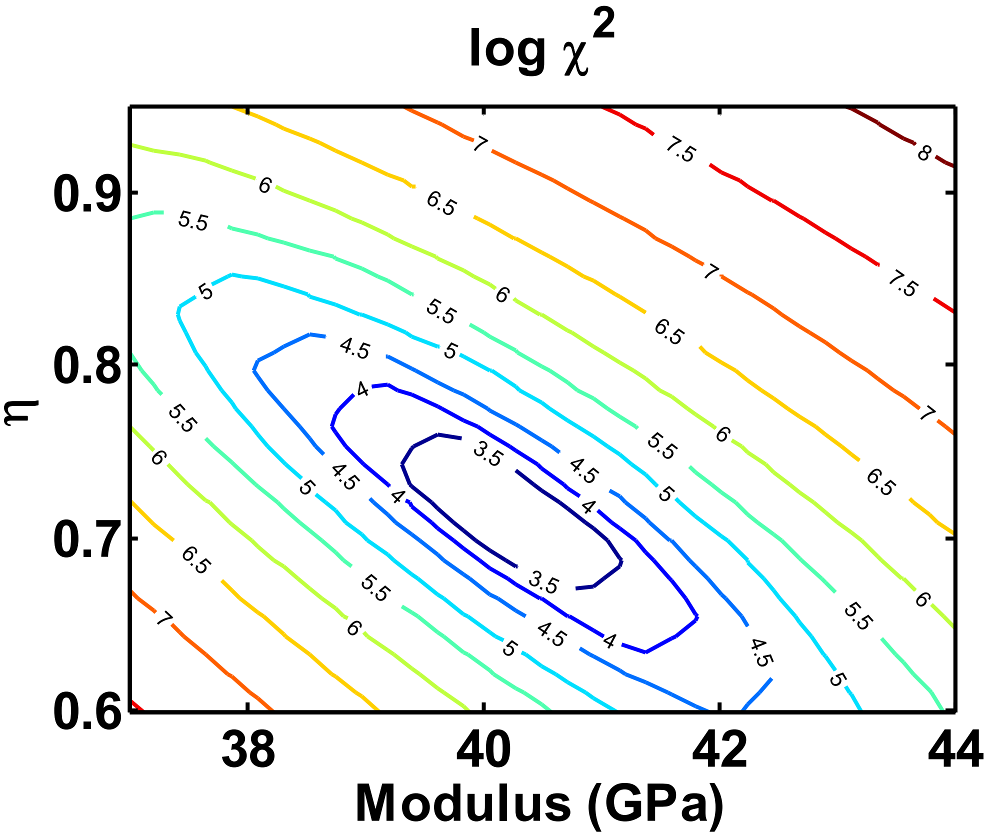

Figure 5-24. Result of nanoindentation correct scheme for the polished non-calcined film.

The results are presented as a contour plot of the residuals (χ^2) between the experimental and theoretical S-a curves. The minimum in these plots are the film modulus and η values that represent the film properties. The result obtained for the polished non-calcined film is shown in Figure 5-24. M_f and η for this film were respectively 40 GPa and 0.70. For the calcined film, the values obtained were 35 GPa and 0.65 respectively for M_f and η.

The results from nanoindentation with the substrate correction scheme applied are a good match to the results obtained from LiSAW. This shows that nanoindentation can be applied to thin and porous materials if the substrate is accounted for in the analysis. It also shows that LiSAW is capable of delivering the same result, but without the need for lengthy computation. While a sharper cube corner tip can help reduce the substrate effect, it cannot fully eliminate substrate influence even at very low loads and shallow indentations. As for the very low modulus results for the first set of unpolished films, these were most likely caused by the secondary crystals adding thickness to the film. By taking the modulus from the polished results, now confirmed by indentation, and fitting film thickness to the unpolished films, the thickness rises to ~475 nm for all of the initial results (Figure 5-25). The increase in thickness likely describes the average effect of the secondary crystals over the relatively long propagation of the SAW (millimeters) compared to the scattering range of the crystals (microns). The 10% difference between set#1 and set#2 can then be attributed to a slight difference in the density of secondary crystals.

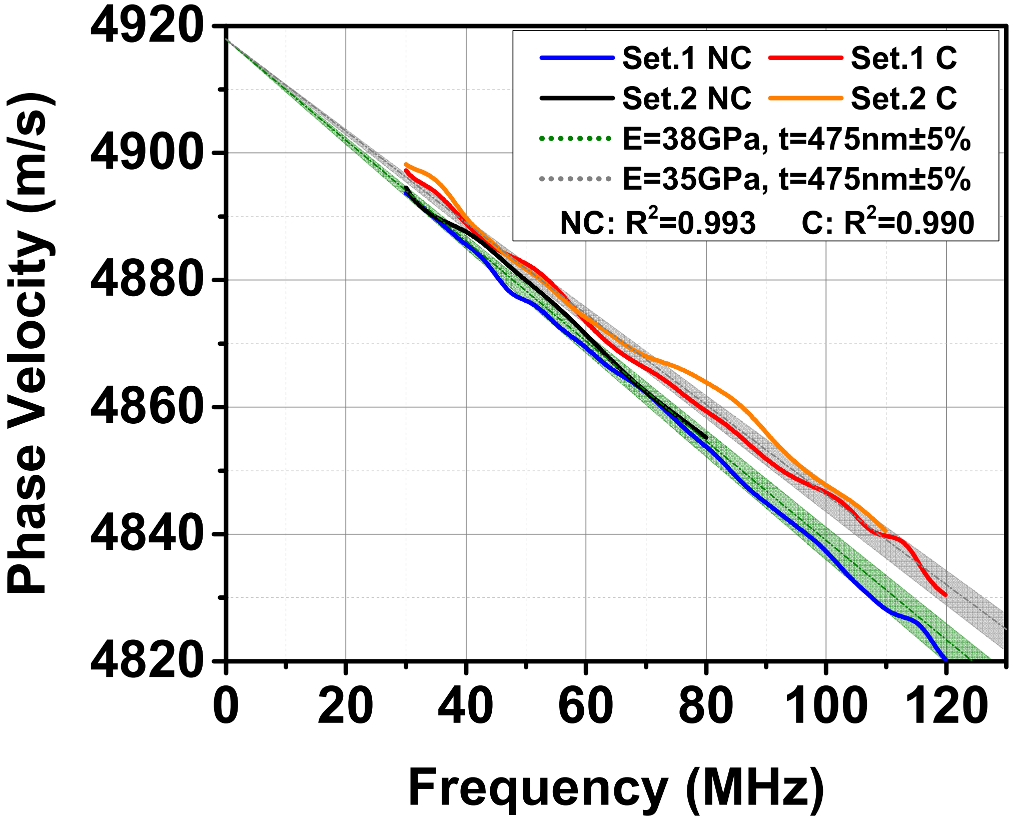

Figure 5-25. Set 1 & 2 results plotted with moduli from polished films and fitted thickness.

5.6 Conclusion

In this chapter, the LiSAW technique was successfully applied to bMFI films and extraction of their elastic moduli was demonstrated on porous (calcined) and non-porous (non-calcined) layers. Confidence in the bMFI results and the system as a whole was achieved by performing two validation studies on systems with known properties. These included aluminum films on silicon substrates and aluminum films on fused silica substrates. Successful SAW generation and detection was shown for both validation systems and the fitted elastic modulus of the aluminum film was consistent and in agreement with literature values for both tests. Aside from showing the general working ability of the whole system, the validation studies demonstrated the bandwidth of the system (~120 MHz), the fine resolution of dispersion detection, and the SAW generation ability with both the Tempest and Leopard lasers. The increase of bandwidth expected form the shorter pulse-width Leopard laser was not observed in experiment. The cause is attributed to limitations in the detection scheme for high frequencies. In Chapter 6, this problem is addressed through optimization of the detection spot size and high frequency generation from both lasers are explored again.

For bMFI films, testing began on unpolished films which featured left over crystals from synthesis scattered amongst the sample surface. Each sample was cut in half with one side receiving calcination to remove the organic template thereby introducing porosity. Two sets of unpolished films, with calcined and non-calcined samples for each set, were studied with the final fitted elastic moduli of ~28.5 GPa for the calcined films and ~30.5 GPa for the non-calcined film. The results from both sets were within 10% each other. Polished bMFI films were studied to observe any changes in dispersion from the removal of the scattered secondary crystals. The results from these films exhibited ~20-25% increase in the fitted moduli with measured values of 35 GPa for the calcined film and 38 GPa for the non-calcined film.

The nanoindentation results showed little difference between the unpolished and polished films therefore their structures were identical. However, both film types had nanoindentation moduli almost double that of the values from LiSAW. Inspection of the indentation results showed a strong substrate effect even for indentation depths below 10% of the film thickness. A nanoindentation correction scheme was followed to account for the substrate influence and the corrected moduli were in agreement to LiSAW having values of 35 GPa for calcined films and

40 GPa for non-calcined films. With confidence in the elastic moduli obtained from LiSAW on polished films, the higher moduli were used in the original lower results to fit the film thickness. It was observed that a film thickness of 475 nm fit the original unpolished films well. This result shows the global effect of the secondary crystals as a small thickness increase to the bMFI layer.

Overall, the extraction of mechanical properties by the LiSAW technique was successfully demonstrated on porous and non-porous zeolites. Compared to nanoindentation, the same results could not be obtained, even with a sharp cube corner tip, unless a computationally intensive correction scheme was utilized to account for the substrate effect on the thin geometry. While both techniques can deliver accurate results, the SAW technique has demonstrated the possibility of being faster and easier for challenging films of thin and porous nature.

Chapter 5 References:

BAMBER, M. J., COOKE, K. E., MANN, A. B. & DERBY, B. 2001. Accurate determination of Young's modulus and Poisson's ratio of thin films by a combination of acoustic microscopy and nanoindentation. *Thin Solid Films,* 398–399**,** 299-305.

CHAPELON, L. L., VITIELLO, J., NEIRA, D., TORRES, J., ROYER, J. C., BARBIER, D., NAUDIN, F., TAS, G., MUKUNDHAN, P. & CLERICO, J. 2006. Measuring the Young's modulus of ultralow-k materials with the non destructive picosecond ultrasonic method. *Microelectron. Eng.,* 83**,** 2346-2350.

CHEN, S. H., LIU, L. & WANG, T. C. 2004. Size dependent nanoindentation of a soft film on a hard substrate. *Acta Materialia,* 52**,** 1089-1095.

CHEN, X. & VLASSAK, J. J. 2001. Numerical study on the measurement of thin film mechanical properties by means of nanoindentation. *Journal of Materials Research,* 16**,** 2974-2982.

CHEN, X., XIANG, Y. & VLASSAK, J. J. 2006. Novel technique for measuring the mechanical properties of porous materials by nanoindentation. *Journal of Materials Research,* 21**,** 715-724.

CHO, H., SATO, H., TAKEMOTO, M., SATO, A. & YAMANAKA, K. 1996. Surface Acoustic Wave Velocity and Attenuation Dispersion Measurement by Phase Velocity Scanning of Laser Interference Fringes. *Japanese Journal of Applied Physics,* 35**,** 3062.

CHUDOBA, T., GRIEPENTROG, M., DUCK, A., SCHNEIDER, D. & RICHTER, F. 2004. Young's modulus measurements on ultra-thin coatings. *Journal of Materials Research,* 19**,** 301-314.

COTE, R., VAN DER DONCK, T., CELIS, J. P. & GLORIEUX, C. 2009. Surface acoustic wave characterization of a thin, rough polymer film. *Thin Solid Films,* 517**,** 2697-2701.

FLANIGEN, E. M., BENNETT, J. M., GROSE, R. W., COHEN, J. P., PATTON, R. L. & KIRCHNER, R. M. 1978. Silicalite, a new hydrophobic crystalline silica moelcular sieve. *Nature,* 271.

FLANNERY, C. M. & HURLEY, D. C. 2003. Laser Ultrasound: An Inspection Tool of Soft Porous Low-Dielectric Constant Films for Microelectronic Interconnect. *AIP Conference Proceedings,* 657**,** 1463-1470.

HERRMANN, A., SCHWARZER, N., RICHTER, F., FRUHAUF, S. & SCHULZ, S. E. 2006. Determination of Young's modulus and yield stress of porous low-k materials by nanoindentation. *Surface & Coatings Technology,* 201**,** 4305-4310.

INTERNATIONAL ROADMAP COMMITTEE 2013. International Technology Roadmap for Semiconductors.

LI, H. & VLASSAK, J. J. 2009. Determining the elastic modulus and hardness of an ultra-thin film on a substrate using nanoindentation. *Journal of Materials Research,* 24**,** 1114-1126.

LI, Z. J., JOHNSON, M. C., SUN, M. W., RYAN, E. T., EARL, D. J., MAICHEN, W., MARTIN, J. I., LI, S., LEW, C. M., WANG, J., DEEM, M. W., DAVIS, M. E. & YAN, Y. S. 2006. Mechanical and dielectric properties of pure-silica-zeolite low-k materials. *Angewandte Chemie-International Edition,* 45**,** 6329-6332.

LU, X., XIAO, P. & LI, H. 2012. Effect of densification distribution on the Young's modulus of porous coatings after nano-indentation. *Acta Metall. Sin. (Engl. Lett.),* 25**,** 383-390.

MAOSEN, B., XING, F., DORANTES, D. & BAOYIN, J. 2011. Young's modulus determination of low-k porous films by wide-band DCC/LD LSAW. *J. Semicond.,* 32.

MENČÍK, J., MUNZ, D., QUANDT, E., WEPPELMANN, E. R. & SWAIN, M. V. 1997. Determination of elastic modulus of thin layers using nanoindentation. *Journal of Materials Research,* 12**,** 2475-2484.

OLIVER, W. C. & PHARR, G. M. 1992. An Improved Technique for Determining Hardness and Elastic-Modulus Using Load and Displacement Sensing Indentation Experiments. *Journal of Materials Research,* 7**,** 1564-1583.

SAHA, R. & NIX, W. D. 2002. Effects of the substrate on the determination of thin film mechanical properties by nanoindentation. *Acta Materialia,* 50**,** 23-38.

SANCHEZ-VALLE, C., LETHBRIDGE, Z. A. D., SINOGEIKIN, S. V., WILLIAMS, J. J., WALTON, R. I., EVANS, K. E. & BASS, J. D. 2008. Negative Poisson's ratios in siliceous zeolite MFI-silicalite. *The Journal of Chemical Physics,* 128**,** 184503-5.

SCHNEIDER, D., FRÜHAUF, S., SCHULZ, S. E. & GESSNER, T. 2005. The current limits of the laser-acoustic test method to characterize low-k films. *Microelectronic Engineering,* 82**,** 393-398.

SERWAY, R. A., VUILLE, C. & FAUGHN, J. S. 2008. *College physics*, BROOKS COLE Publishing Company.

TAKIMURA, T., HATA, N., TAKADA, S. & YSHINO, T. 2008. Determination of mechanical properties of porous silica low-k films on si substrates using orientation dependence of surface acoustic wave. *Japanese Journal of Applied Physics,* 47**,** 5400-5403.

WANG, Z., WANG, H., MITRA, A., HUANG, L. & YAN, Y. 2001. Pure-Silica Zeolite Low-k Dielectric Thin Films. *Advanced Materials,* 13**,** 746-749.

WANG, Z. & YAN, Y. 2001. Oriented zeolite MFI monolayer films on metal substrates by in situ crystallization. *Microporous and Mesoporous Materials,* 48**,** 229-238.

XIAO, X., HATA, N., YAMADA, K. & KIKKAWA, T. 2004. Mechanical Property Determination of Thin Porous Low-k Films by Twin-Transducer Laser Generated Surface Acoustic Waves. *Japanese Journal of Applied Physics,* 43**,** 508-513.

XIAO, X., SHAN, X. M., KAYABA, Y., KOHMURA, K., TANAKA, H. & KIKKAWA, T. 2011. Young's modulus evaluation by SAWs for porous silica low-k film with cesium doping. *Microelectronic Engineering,* 88**,** 666-670.

YU, H. Y., SANDAY, S. C. & RATH, B. B. 1990. The effect of substrate on the elastic properties of films determined by the indentation test — axisymmetric boussinesq problem. *Journal of the Mechanics and Physics of Solids,* 38**,** 745-764.

ZHANG, C. Y., ZHANG, Y. W., ZENG, K. Y. & SHEN, L. 2005. Nanoindentation of Polymers with a Sharp Indenter. *Journal of Materials Research,* 20**,** 1597-1605.

Chapter 6 Optimizations to frequency detection and acoustic mismatch

6.1 Background and introduction

One of the limitations to LiSAW characterization of thin films is that the resolution of the technique is directly related to the bandwidth of the experiment (Rogers et al., 2000). This is because for dispersive SAWs, the degree of film influence depends largely on the frequency of the signal. Therefore, the impact from the film properties becomes more apparent only at higher frequencies (Chudoba et al., 2004). This means that the ability to accurately characterize ultra-thin films goes in hand with the ability to generate and detect higher frequencies. For example, in the two validation studies presented in chapter 5, the ±5% error region on the dispersion curve of the aluminum on silicon study was much smaller than same error region on the aluminum film on fused silica dispersion plot. This is due in part to the fact that the aluminum film on fused silica was almost twice as thick. The thicker film was able to capture more film influence at each frequency thus giving rise to a higher resolution of property measurement for the film. Since generating thicker films is not always viable, detection at higher frequencies is necessary to maintain film resolution capability as film thickness decreases.

Aside from frequency bandwidth enhancements, another way to improve detection sensitivity, and thus the accuracy of the LiSAW technique, is to tailor systems towards maximum Rayleigh wave dispersion (Xiao and You, 2006). For double layer systems, this can be accomplished by careful selection of the top layer parameters. In Chapter 3, it was shown how the thickness of the top layer can have a profound effect on dispersion, but what was not discussed, and of potentially greater influence to dispersion, was the choice of the material itself. By selecting materials with substantially lower base Rayleigh wave speeds, the elastic mismatch of the system can significantly increase resulting in additional dispersion. For high levels of elastic mismatch, drastic elongation of the SAW may be witnessed since the transition from low to high frequency spans a larger range of phase velocities (Murray et al., 1999). This effect, to a lesser degree, can be seen by comparing the SAW waveforms from aluminum films on fused silica and silicon substrates in Chapter 5. It is readily apparent that the silicon substrate gives rise to longer waveforms caused by the larger mismatch between aluminum ($c_r \sim 2900\ m/s$) and silicon [100] ($c_r \sim 4920\ m/s$) compared to fused silica ($c_r \sim 3400\ m/s$). The longer waveforms are superior for dispersion analysis because the frequencies are more spread out in time, thus allowing for clearer frequency and phase identification. Additionally, they are less susceptible to noise and more easily aligned and averaged. All of these characteristics are conducive to smoother dispersion curves for higher accuracy.

One of the major findings from the theoretical dispersion derivations in Chapter 3 was that nonlinear dispersion could be achieved in double layer systems through the deposition of a thicker second layer. However, a balance between first and second layer thickness needs to be achieved in order to maintain dispersion sensitivity in the buried layer (Salenbien et al., 2011). The addition of frequency detection enhancement and top layer material tailoring create more favorable conditions for nonlinear dispersion development without the need of thick layers. Depending on the degree of nonlinearity in the detected dispersion, multiple property fitting may be feasible, thus allowing for the measurement of films where one or more of the typical non-fitting parameters, such as film density, are not easily obtained. This can be especially useful for films that are too delicate for physical measurements.

In this chapter, a brief review of laser displacement detection schemes is presented and the improved experimental setup is overviewed. The new frequency detection range is then investigated by revisiting aluminum films on silicon substrates. Since higher frequencies were expected, both the Leopard and Tempest lasers were employed in order to explore whether the extended range reveals differences in SAW generation from shorter (Leopard, 50 ps) and longer (Tempest, 5 ns) pulse-width lasers. For alternative top layers, an overview of prospective materials is presented and the choice of tin is discussed. To demonstrate the effect of top layer choice, LiSAW results are shown for tin films with silicon substrates. The combination of frequency enhancement and tin top layers was then used to measure bMFI films once again to investigate the total improvement in technique compared to previous experiments.

6.2 Methodologies to improve detection

For optical SAW detection methods, the main challenge of high frequency resolution comes from the ability to generate a sufficiently small spot size and the ability to improve the signal to noise ratio. For the latter, quadrature configurations and heterodyning are popular methods. In a quadrature setup, the s and p polarizations of linearly polarized incoming light undergo separate interference by retarding one polarization with respect to the other (Zumberge et al., 2004). This is shown in Figure 6-1 and involves inserting an eighth wave plate into the reference leg for a total of $\lambda/4$ retardation in that path (since the light passes through once traveling towards the sample and once traveling away from the sample). The s and p interference is then isolated from one another by using a polarized beam splitter that outputs to two photodetectors.

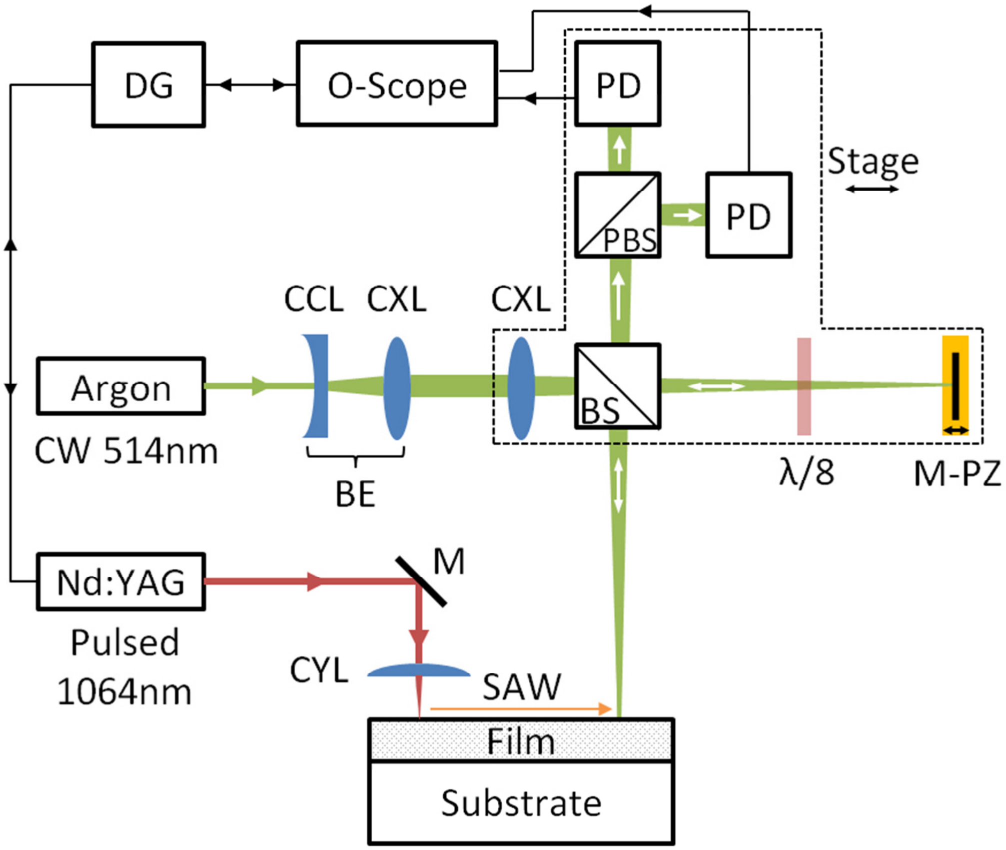

Figure 6-1. Michelson interferometer in a quadrature configuration. Abbreviations are: DG: delay generator, O-scope: oscilloscope, PD: photo detector, CXL: convex lens, CCL: concave lens, BE: beam expander, BS: beam splitter, M-PZ: mirror mounted on piezoelectric stage, M: mirror, CYL: cylindrical lens, PBS: polarized beam splitter, $\lambda/8$: eighth wave plate.

The two phase shifted signals can then be analyzed separately or together for extra sensitivity. However, this setup requires additional probing beam power since a separation of polarization states and extra beam splitter are involved. In experimenting with this setup, it was found that the broadband dielectric steering mirrors were poor at preserving linearly polarized light, thus the resulting elliptical polarization created unbalanced intensity during detection. While uncoated silver mirrors could preserve the original laser polarization more accurately, the amount of steering necessary prior to the Michelson interferometer, in the author's case, was detrimental. Quadrature is also typically combined with other stabilization schemes for optimal performance (Hurley et al., 2001b).

Heterodyning is another popular technique to increase the signal to noise ratio. The basic concept revolves around mixing two signals together to obtain heterodynes. These are new signals at different frequencies that represent the summation or difference of the original signals. For example, in an optical heterodyne setup, two laser wavelengths are used simultaneously thus making it possible to obtain two separate interference patterns (Tiziani, 1992). The real benefit, though, comes from the use of two very similar wavelengths, thus creating a long heterodyne wavelength analogous to long acoustic beat frequencies. The interference obtained remains a function of the phase difference between the two signals, but it is now modulated to the lower, and more easily measured, beat frequency. This allows for measurement of high frequency events, but in a more noise-free and manageable detection range (Bramhavar et al., 2009). These systems typically require more sophisticated electronics (Hernandez et al., 2002, Hayashi et al., 1997), thus in the current work, improvement by minimizing laser spot size was preferred.

For the current system, it was shown that the frequency bandwidth is detection limited since the maximum frequencies recorded correlated well to the measured detection spot sizes on the sample surface. While the observed 120 MHz bandwidth was sufficient for the previous studies, higher bandwidth, as discussed previously, would allow for greater extension of the dispersion curve thereby producing larger data sets to fit to theoretical dispersion curves. This decreases the fitting error and, more importantly, increases the ability to resolve film properties. For example, in the bMFI films studied previously, a 10% change in modulus produced only several meters-per-second change at 50 MHz, however the difference can be triple that at 150 MHz.

Since the spot size averages displacement in the entire field for any point in time, it can be thought of as the sampling rate of a time-domain signal whereby decreasing the spot size is akin to decreasing the time step. In Chapter 4, it was shown that the focusability of laser light follows the equation:

$$w = \frac{1.22 f \lambda}{D} \tag{6-1}$$

where w is the final beam diameter, f is the focal length, λ is the wavelength of laser light, and D is the original beam diameter. The current system utilizes a beam expander to increase D to ten times its original value (3 mm to 30 mm) therefore further expansion is not feasible since the beam would be too big for the optics. Therefore, the only other variable that can be changed is the focal distance. The current focal distance of 150 mm is set so that the focusing optic comes before the beam splitter. In this manner, the spot size on the sample and reference mirror are focused exactly the same. However, for smaller focal distances, the focusing optic will be required to be in the sample leg of the interferometer, thus another lens will have to be inserted into the reference leg. This introduces additional complexity since the lenses themselves will introduce path-length differences and the focus of each will have to be matched manually. However, a smaller focal length, for example of 50 mm, can potentially decrease the final beam diameter by three-fold.

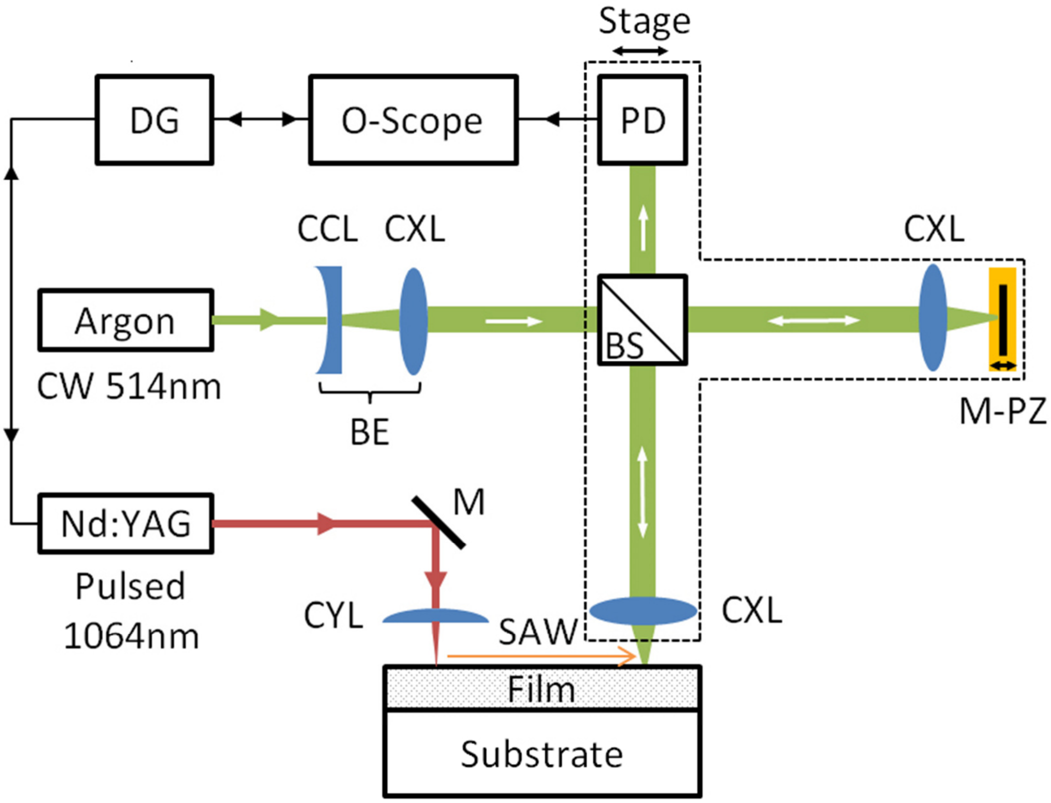

Figure 6-2. Schematic of improved setup with focusing lenses in each interferometer leg. Abbreviations are: DG: delay generator, O-scope: oscilloscope, PD: photo detector, CXL: convex lens, CCL: concave lens, BE: beam expander, BS: beam splitter, M-PZ: mirror mounted on piezoelectric stage, M: mirror, CYL: cylindrical lens.

Two lenses, with 50 mm focal lengths, were installed into the setup. The new arrangement is shown in Figure 6-2. It is immediately clear that the lenses, now in each interferometer arm, affect the ability to operate at the zero-order fringe level which occurs at perfectly symmetric path lengths and wave fronts. With the previous setup, it was possible to achieve a near zero light intensity in fringe troughs at the zero-order fringe. However, in the current setup, minute differences in lens shape, tilt, and level of focus create a persistent "dark" intensity that exists outside of the zero-order fringe. Minimizing the dark intensity is difficult because of the amount of variables involved including lens positions with respect to the beam splitter, mirror (or sample) positions with respect to the lenses, and tilt of each lens with respect to each other. Optimization of each parameter was performed, but a dark intensity approximately equal to the fringe intensity could not be mitigated. This does not affect the resolution of the interferometer, but decreases the peak-to-peak intensity of the interference signal such that additional laser power is needed.

6.3 Effect of laser-pulse duration on high frequency detection

To test the frequency bandwidth of the improved experimental setup, SAWs on aluminum films with silicon substrates were measured and compared to results from the original setup. The previous results, in Chapter 5, indicated a frequency limit of ~120 MHz which was in correlation to the spot size of ~10 µm. This was achieved with a 150 mm lens that has a theoretical spot size of 3.1 µm governed by the diffraction limit. In practice, defects in lens shape and inexactness in the detection focal plane limited the spot size to the larger measurement of 10 µm. While the newly installed 50 mm lenses have the capacity to decrease the spot size to 1 µm, the sharper convergence angle increases the difficulty to detect at the tightest focal plane. Coupled with the dual lens setup where separate, but balanced, focusing is necessary at each leg, a threefold increase in detection frequency may not be feasible. However, an improvement of only 67% would increase the detection range past 200 MHz.

For laser SAW generation, the spectral bandwidth depends primarily on matching focused line width dimension to SAW wavelengths (Levy et al., 2001). For silicon, a 5-500 MHz range corresponds to wavelengths between 10 µm and 1 mm. Such line-widths are easily achieved by the current cylindrical lens, but it is also hypothesized that the frequency limit of laser SAW generation is directly proportional to the pulse-width, in time, of laser deposition (Scruby and Drain, 1990). This is because the temporal movement of the surface mimics the temporal profile of the laser. Therefore, the 5 ns pulse-width Tempest laser should theoretically have a generation limit of ~100 MHz. This is quite close to the limit of the original detection scheme. Therefore, with higher expected frequencies, the Leopard laser, with a 50 ps pulse-width, was also used for generation. The goal of the following section's experiment was to discover the detectable frequency range of the improved setup while also comparing SAW generation between the two different pulse-width lasers. The slower 5 ns laser was expected to reach a frequency generation limit and it was of interest to find the frequency at which this occurs.

To minimize inconsistencies introduced by multiple samples, one large sample was used for all testing and it remained fixed throughout the experiment. The beam paths of the Tempest and Leopard lasers were made to overlap away from the main experiment such that switching between the two sources of generation did not disturb sample alignment and focus. All SAWs were generated and detected on a 600 nm aluminum film that was sputter coated onto a (100) silicon substrate. For both the Tempest and Leopard lasers, SAWs were detected 10 mm and 20 mm away from the irradiation site along the [100] direction of the silicon wafer. The SAW waveforms detected from generation by the Tempest laser are shown in Figure 6-3 and the corresponding Leopard results are shown in Figure 6-4.

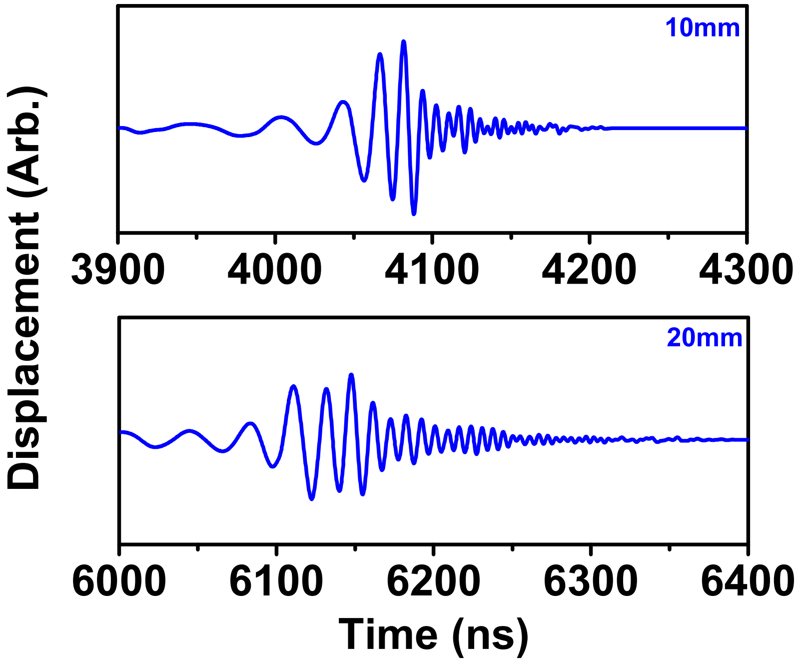

Figure 6-3. SAW signals generated by the Tempest laser and detected at 10 mm and 20 mm away from the irradiation site by the improved detection setup.

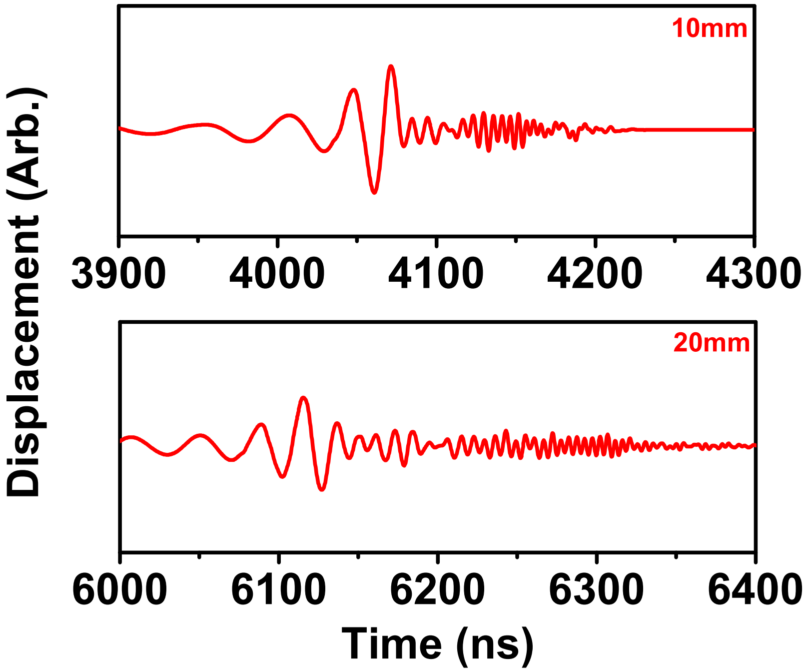

Figure 6-4. SAW signals generated by the Leopard laser and detected at 10 mm and 20 mm away from the irradiation site by the improved detection setup.

From visual inspection, it is clear that there are higher frequencies being detected since the waveforms are significantly elongated from those seen in Chapter 5. A preliminary measurement of the high frequency temporal wavelengths gives values ~5 ns corresponding to a ~200 MHz frequency. The amplitude distribution of the Tempest signals follow a more familiar Gaussian shape whereas the Leopard generates a more jagged distribution, but with higher and more constant amplitudes in the critical high frequencies. This could possibly be attributed to the energy levels necessary to generate similar amplitude SAWs from both lasers. The Tempest required ~7 mJ of energy while the Leopard required over 35 mJ for generation, which was well into the ablative regime. The larger energies may be beneficial to high frequency generation, but appears to negatively affect the lower frequencies. Especially of note is where the Leopard signal seems to lose uniform oscillation around the middle of each waveform. This is more apparent in Figure 6-5 which shows a direct comparison by overlaying the signals detected at 20 mm.

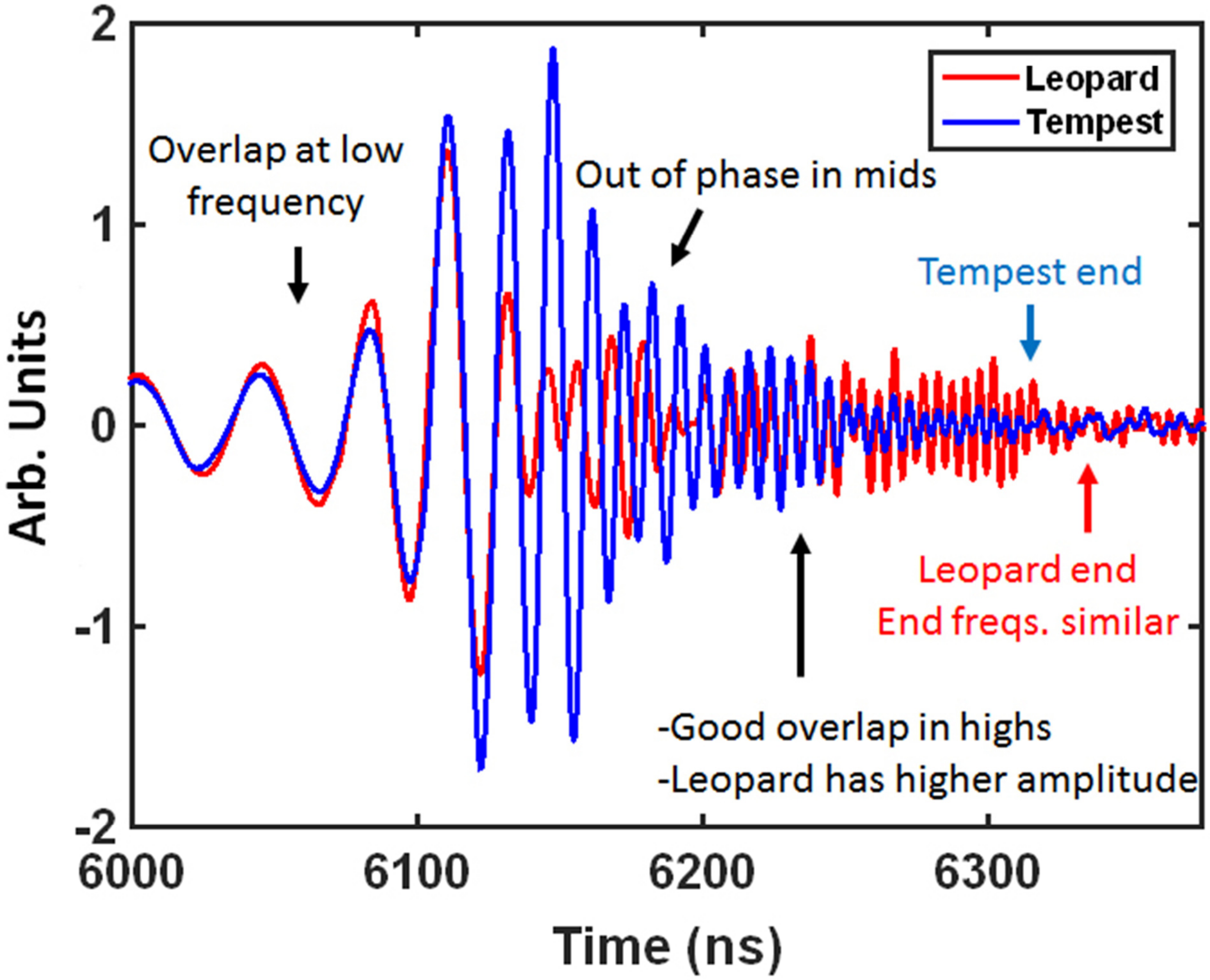

Figure 6-5. Comparison of the SAWs generated by the Tempest and Leopard lasers detected at a distance of 20 mm.

In Figure 6-5, it is depicted how the two signals overlap well at low frequencies, but then become out of phase shortly thereafter (~6125 ns). In this region, the oscillation amplitude of the Leopard signal drops drastically compared to the Tempest and the Leopard signal appears to omit several wavelengths. However, the two signals become in phase once again at higher frequencies (~6200 ns) where the Leopard sustains higher amplitude oscillation. Both signals taper off to background noise levels at around the same point indicating that the frequency range may once again be detection limited.

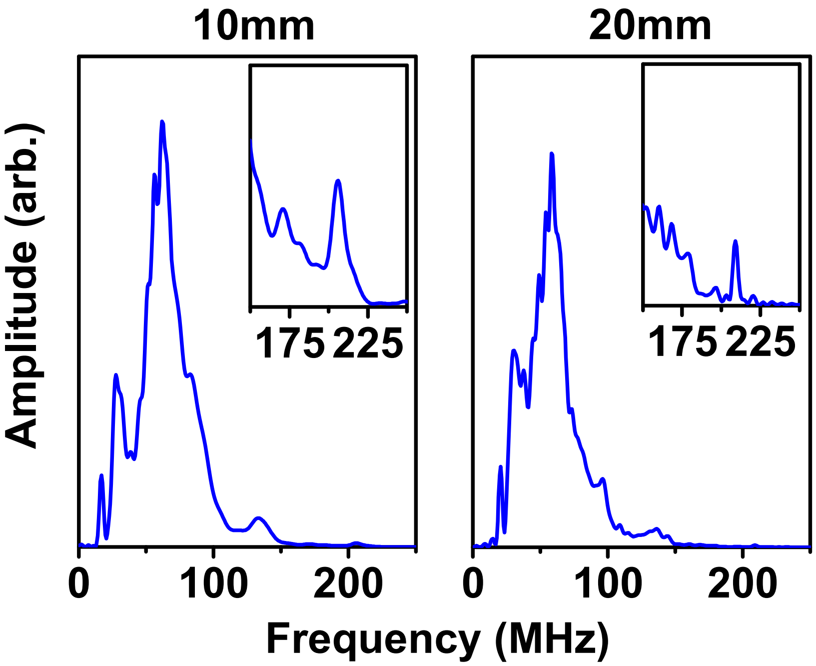

Figure 6-6. Fourier transform of the Tempest SAW signals.

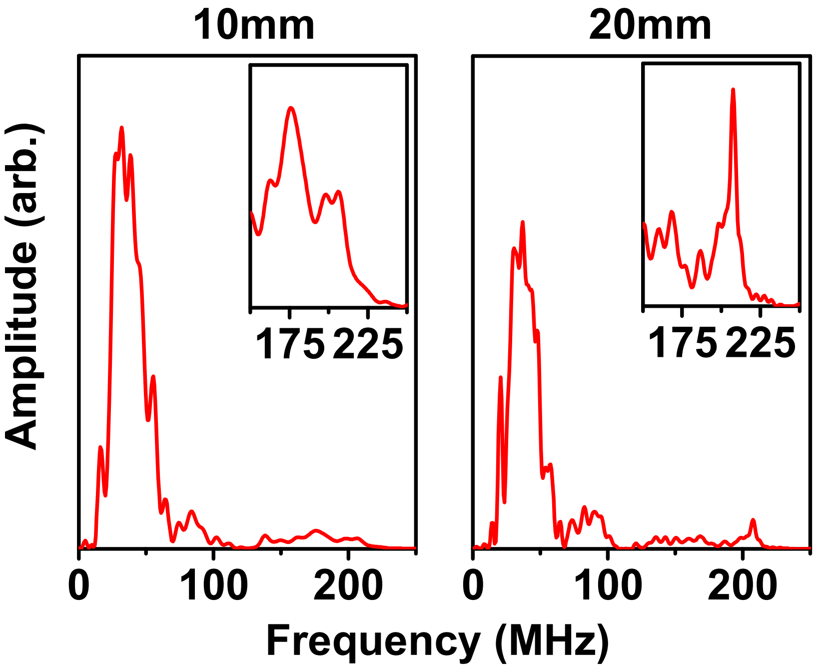

Figure 6-7. Fourier transform of the Leopard SAW signals.

The Fourier transform of the detected signals appear in Figure 6-6 and Figure 6-7 for the Tempest and Leopard SAWs respectively. For the Tempest frequency spectrum, the majority of the intensity diminishes by ~150 MHz, but from the figure insets, it is shown that there exists a frequency response up to ~225 MHz. For the Leopard frequency spectrum, the intensity suddenly reduces to near zero at ~75 MHz in both the 10 mm and 20 mm signals. The intensity grows and decays between 75-120 MHz, before a steady response region from 120 - 230 MHz. By taking a second look at Figure 6-5, it is now possible to correlate the Leopard's 75 MHz drop off to the region where the Leopard signal first goes out of phase with respect to the Tempest and the 120 MHz drop off to where the Leopard signal omits several wavelengths, just prior to becoming in phase once again. The exact reasoning for the peculiar SAW behavior is unknown, but the behavior is a repeatable observation since these signals represent the average of many waveforms. This may be attributed to the much larger energies necessary for generation with the Leopard perhaps leading to uncharacterized ablation effects, but these are beyond the scope of this particular experiment. What can be concluded is that the detection limit of the improved experimental setup is ~225 MHz which represents an 83% improvement from the original configuration. This frequency limit is comparable to other optical detection setups in literature (Hurley et al., 2001a, Hernandez et al., 2002), but without the need of sophisticated stabilization schemes. Surprisingly, the Tempest exhibits no problems in generating such frequencies even if the timescale of oscillatory movement required is beyond the laser temporal pulse-width. This suggests that the frequency limit of SAW generation may not be as limited by the laser pulse-width.

The dispersion curves generated by the Leopard and Tempest SAWs are shown in Figure 6-8. The well behaved Tempest signals generate a smoother dispersion curve that is highly linear and easily fit. The Leopard dispersion curve exhibits collinear regions to the Tempest for low frequencies (< 75 MHz) and high frequencies (> 125 MHz), but an unsteady signal response in the region between 75-120 MHz. This matches the strange behavior witnessed in the Fourier transform and is ultimately detrimental to the final dispersion curve in this range. Therefore, the Tempest laser is clearly a better candidate for consistent SAW generation in frequencies below 225 MHz. While the amplitude of the high frequency region from the Leopard signal is attractive, the problems in the mid-range frequencies outweigh the potential benefits.

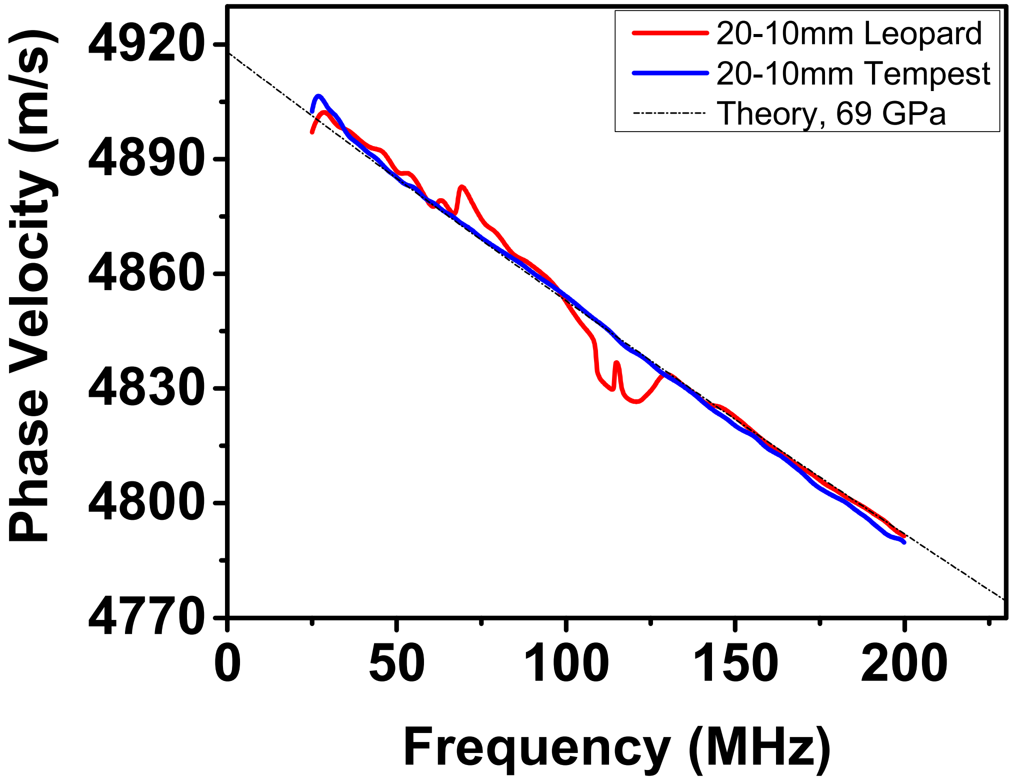

Figure 6-8. Dispersion curves generated by Leopard and Tempest SAWs on an aluminum film and silicon substrate.

In this section, the improved experimental setup was tested by revisiting aluminum films on silicon substrates. The upper limit of detectable frequency response was determined to be 225 MHz which is a significant increase allowing for a much larger fitting region to theory. In comparing the SAWs generated by the Leopard and Tempest lasers, it was found that the Tempest creates more consistent and well-behaved SAWs. The Leopard SAWs, while exhibiting favorable waveform amplitudes in the high frequency region, experiences trouble in accurately sustaining mid-range frequencies. Therefore, the resulting dispersion is jagged and troublesome in that range. Since both lasers extinguished at around the same frequency, the detection ability is most likely limited by the spot size once again, although the improved detection range is far greater than before and sufficient for potential nonlinear dispersion resolution.

6.4 Alternative top layer materials for dispersion enhancement

Up until this point, aluminum films served as the reflective media in double layer systems. This was because aluminum is readily sputtered to a wide range of thicknesses with excellent surface quality. While the Rayleigh wave speed of aluminum, $c_r \sim 2900\, m/s$, is significantly lower than that of silicon ($c_r \sim 4920\, m/s$), it closely neighbors the wave speed of many other popular metallic materials. In fact, many industrial materials reside in the range of $2500 - 3500\, m/s$ as demonstrated in Table 6-1. This range appears to be intrinsically favored in nature therefore the probability of testing layers falling into this range is high. For example, the bMFI zeolite tested in Chapter 5 has a $c_r \sim 2650\, m/s$. When aluminum top layers are used on such materials, they serve well in creating reflectivity, but do little in increasing the elastic mismatch of the system. Therefore, it is favorable to explore other top layer materials capable of providing a reflective surface, yet having a much lower wave speed to exacerbate SAW dispersion. Candidate materials for these conditions appear towards the bottom of Table 6-1.

Table 6-1. Estimated Rayleigh wave speeds for various materials. The bottom half of the table focuses on low Rayleigh wave speed reflective materials. Speeds were tabulated with material properties from literature (Callister and Rethwisch, 2009)

Material	c_r
Silicon [100]	4917
Chromium	3670
Molybdenum	3262
Steel (4130)	2947
Magnesium	2934
Aluminum	2910
Titanium	2889
Stainless Steel (304)	2854
Nickel	2720
Copper	2078
Tantalum	1906
Palladium	1789
Antimony	1667
Silver	1593
Tin	1479
Gold	1128
Lead	662

From Table 6-1, it can be seen that there are several metals capable of being sputtered to a reflective surface and with exceptionally low Rayleigh wave speeds. Of these, lead has the lowest wave speed, but the toxicity in handling and typically dull surface quality of sputtered lead coatings make it unfavorable. Gold and silver are good candidates by meeting reflectivity requirements and producing sputtered films with excellent surface qualities, but are cost prohibitive. This leaves tin as the ideal choice. Tin has a low cost, is easily sputtered, and is very reflective. However, sputtering layers in excess of several hundred nanometers produces a dull surface lacking luster. This can be overcome by a short fine polishing step post deposition, but adds an additional process. Antimony, palladium, and copper are friendlier in terms of surface quality for thicker sputtering, but the exceptionally low wave speed of tin is difficult to discount. Thus, tin was chosen as the alternative top layer material to significantly enhance dispersion by having a Rayleigh wave speed only ~50% that of aluminum layers.

To test the level of dispersion enhancement offered by tin materials, tin films were sputtered onto silicon (100) substrates and tested with the LiSAW system. The tin films were sputtered to a thickness of ~1.4 μm, but in the as-deposited state, they did not provide good reflectivity due to considerable surface roughness. To improve the surface quality for SAW testing, the film was polished with 0.05 μm alumina slurry on a low-nap polishing cloth to a final thickness of 1.07 μm. SAWs were generated by the Tempest laser (5 ns pulse-width) in the [100] direction of the silicon crystal lattice and detected at ~10 mm and ~15 mm from the irradiation site.

The SAWs detected at 10 mm and 15 mm for the tin film are shown in Figure 6-9. The effect of the large Rayleigh wave speed mismatch between tin ($c_r \sim 1479\, m/s$) and silicon ($c_r \sim 4917\, m/s$) is clearly demonstrated by the significant elongation of the waveforms. This suggests that the slower frequencies are outpacing the higher frequencies at a much larger rate than before which is consistent with additional dispersion. A direct comparison between SAWs measured after a 10 mm propagation distance on a 0.60 μm Al film (from section 6.3) and the 1.07 μm tin film is shown in Figure 6-10. It is evident that the primary effect of the lower Rayleigh wave speed is the elongation of the SAW from a total length of ~200 ns to over 800 ns.

This spreads out the frequency response in time as opposed to the more compact waveform seen on the aluminum film. It is important to note that this does not make the frequencies any easier to detect since the spatial profile of each frequency remains unchanged. Thus the benefit can be thought of as an increase in oscillatory motion for each frequency allowing for more accurate phase identification (and thus dispersion) of each frequency.

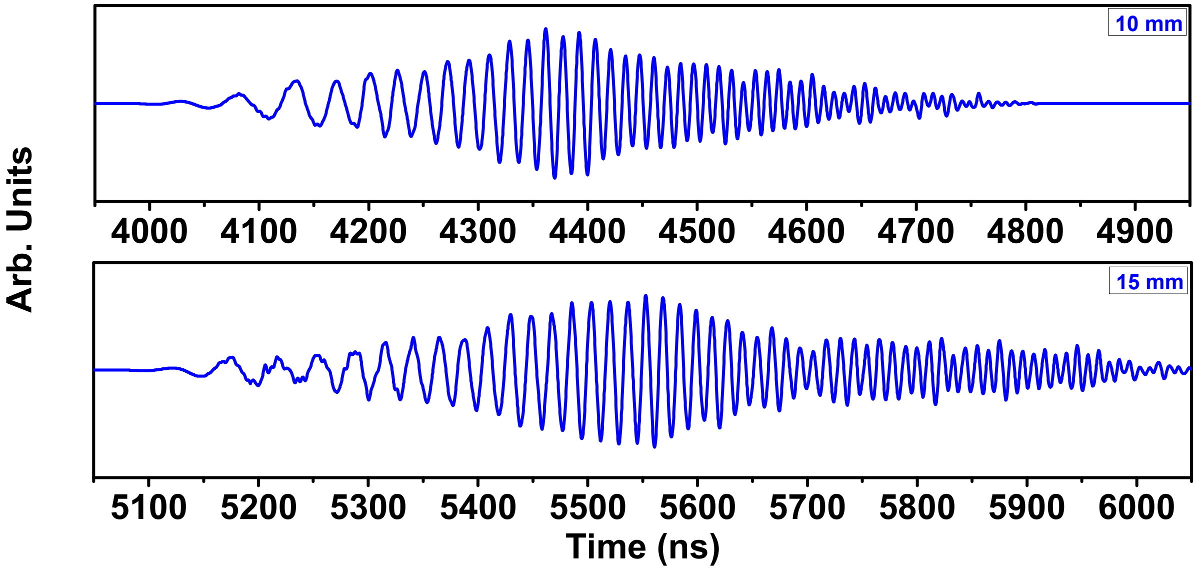

Figure 6-9. SAWs detected on a 1.07 µm tin film with a silicon substrate after propagation distances of 10 and 15 mm.

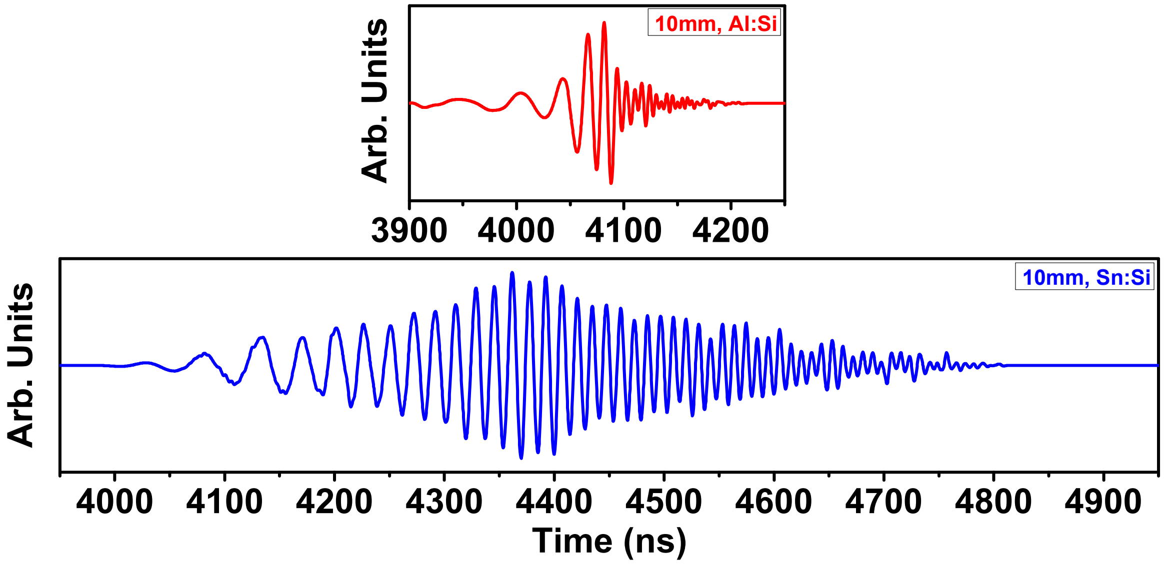

Figure 6-10. Direct comparison of SAWs detected at 10 mm on a 0.60 µm aluminum film (red) and on a 1.07µm tin film (blue). *x*-scale for both signal plots are identical. Only the range has been modified.

Fourier transforms of the tin film SAWs were calculated to analyze the frequency response of each signal and the results appear in Figure 6-11. While the signals recorded have substantially more oscillatory motion than any signals captured previously, the response range only spanned from 20 - 115 MHz. From previous testing in Section 6.3, it was shown that the improved experimental setup was capable of detecting frequencies up to 225 MHz therefore the lack of frequency response was unexpected. Errors in achieving the correct focal plane could account for some frequency loss. However, even 150 MHz should be easily feasible with the new lenses, especially considering the amount of oscillation observed. Thus, the high frequency attenuation must be derived from the film itself. A targeted method for investigating this phenomenon appears in Chapter 8.

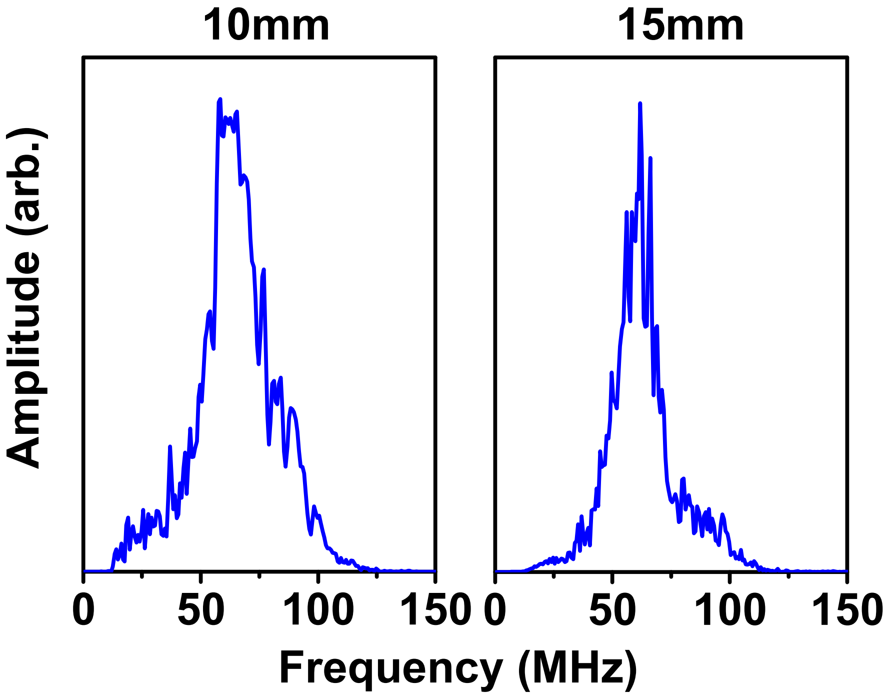

Figure 6-11. Fourier transforms of SAW signals detected on a 1.07 μm tin film at distances of 10 mm and 15 mm from the irradiation site.

The experimental dispersion curve calculated from the measured SAWs on tin appears in Figure 6-12. The dispersion is observed to be very linear and fits well to a theoretical curve with the following literature properties (Callister and Rethwisch, 2009) for tin: $E = 50\ GPa$, $t = 1.07\ \mu m$, $\rho = 7365\ kg/m^3$, and $\nu = 0.36$. For reference, the theoretical dispersion curve of a 1 μm aluminum layer is also plotted in order to visualize the substantial increase in dispersion that tin allows for at the same thickness. In the first 100 MHz, the phase velocity drops only ~100 m/s for the aluminum film whereas for tin, the same drop is over 500 m/s. While the aluminum on fused silica results in Chapter 5 demonstrated how the LiSAW system could detect dispersion spanning just 10 m/s, the much larger range afforded by tin layers creates dispersion that is easier to detect since the waveforms change more drastically during propagation.

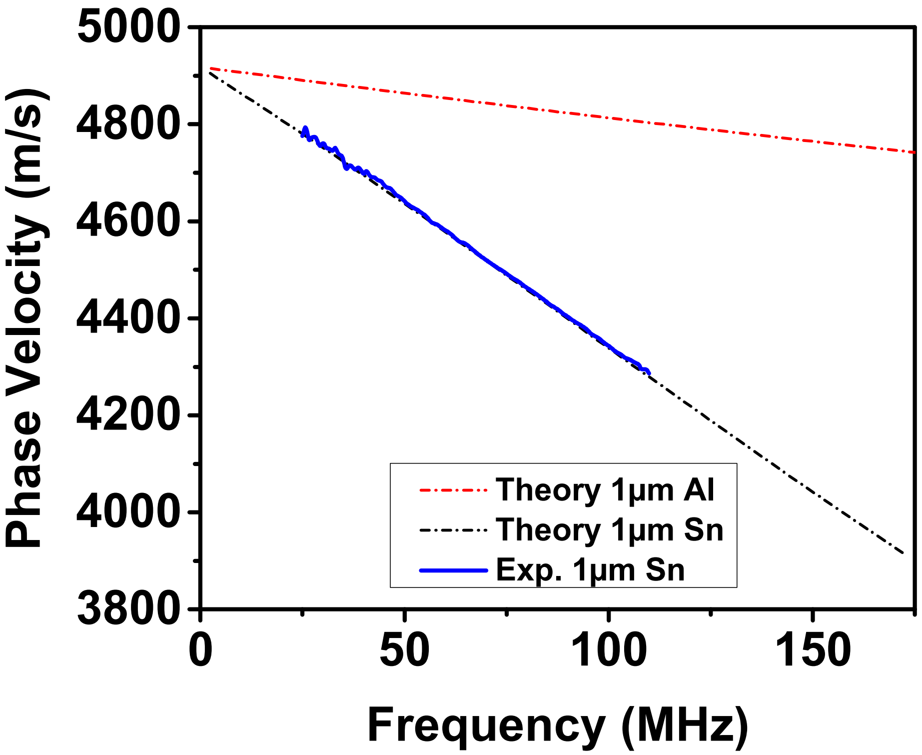

Figure 6-12. Dispersion curve generated by a 1.07 μm tin film on a silicon substrate. Theoretical dispersion curves are plotted for tin and aluminum layers of the same thickness.

The SAW results from tin films on silicon substrates demonstrate the substantial alteration to dispersion that occurs when a material with much lower Rayleigh wave speed is utilized. The SAW waveform is observed to elongate significantly as the frequencies stretch to accommodate the enhanced dispersion. This produces many more oscillations in the SAW which aids in dispersion analysis since frequency and phase are more spread out in time thus being clearer for identification. However, the very slow Rayleigh wave speed of the tin layer appeared to attenuate high frequencies such that a response from the full 225 MHz bandwidth of the improved system could not be realized. Therefore, nonlinear dispersion was not observed since only the first ~100 MHz was probed. Even with the smaller frequency range, the degree of dispersion generated was still significantly larger than what would have been supplied with aluminum films of the same thickness, thus tin layers are favorable for future testing.

6.5 Experimental results for bMFI films with improved frequency and dispersion

The methodologies to increase frequency detection and dispersion generation highlighted by this chapter were combined and utilized to revisit the bMFI films from Chapter 5. In the previous study, the maximum frequencies observed were 25-120 MHz spanning a phase velocity range of $\sim 4820 - 4900\, m/s$. It was concluded that the upper limit of frequency was caused by detection limitations therefore the major goal of this second study was probe the response at higher frequencies. Additionally, tin was chosen over aluminum for secondary reflective layers since the additional acoustic contrast that tin offers was experimentally shown to drastically increase dispersion. Prior to any experiments, theoretical curves for a double layer system containing various thicknesses of tin (250 nm to 1 μm) and a 350 nm layer of bMFI on a silicon substrate were generated and appear in Figure 6-13. As expected, increasing the tin top layer thickness results in a similar growth in the dispersion response of the system. Additionally, slight nonlinearity is seen starting at around 500 nm in tin thickness. In the previous study on single layers of tin, it was discovered that a ~1μm tin layer produces significant high frequency attenuation therefore larger thicknesses were undesirable for this experiment. With this in mind, the goal of achieving a 500 nm of tin top layer was set as a means to balance the dispersion enhancement and frequency attenuation effects while producing some nonlinearity.

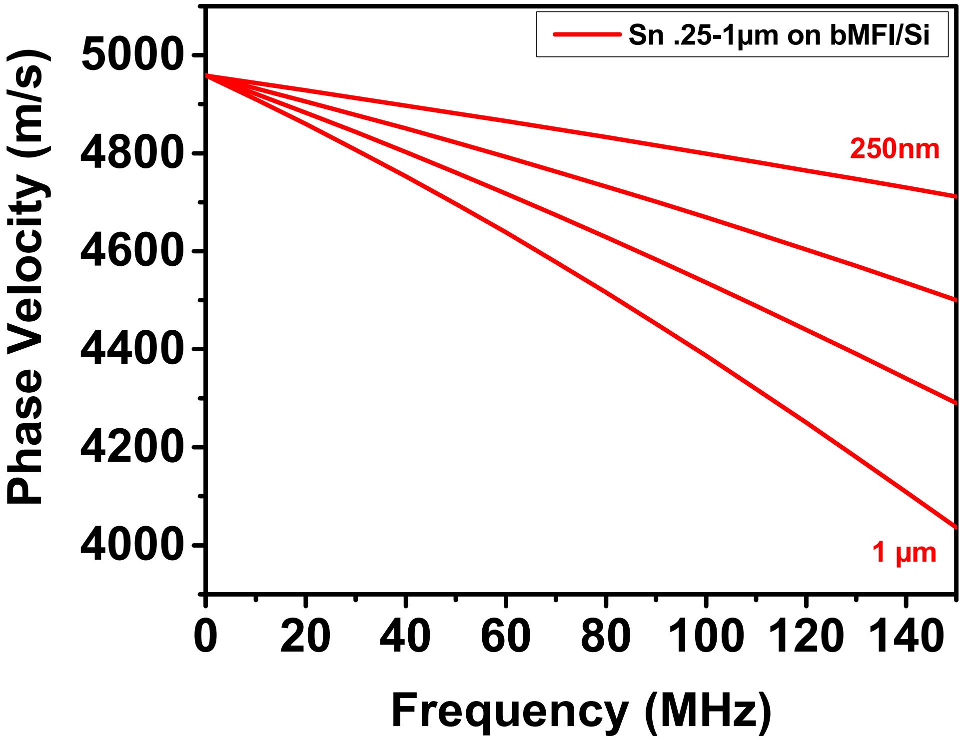

Figure 6-13. Tin layers of varying thickness on top of bMFI zeolite and a silicon substrate.

Similar to the previous study, two bMFI samples on silicon substrates were tested, one calcined (porous) and the other non-calcined (non-porous, as-synthesized). To maximize sample consistency, each specimen tested was a product of the same synthesis batch. The samples were polished simultaneously by a Buehler automated polishing system with a on a low-nap polishing cloth and 0.05 μm alumina slurry. The measured thickness of the bMFI layers post polishing was 350 nm for both samples. Afterwards, one specimen was calcined by heat treatment for 12 hours at 450°C to introduce porosity. Both samples were then sputter coated with tin and then polished simultaneously to a final thickness of 400 nm for the tin layer. SAWs were generated by the Tempest laser (5 ns pulse-width) following the [100] direction of the silicon substrate and detected between $10 - 15\ mm$ from the irradiation site.

The SAWs obtained for the non-calcined and calcined samples are shown respectively in Figure 6-14 and Figure 6-15. The effect of tin top layers, as opposed to aluminum in Chapter 5, is clearly evident and the dispersion enhancement has created significantly longer SAWs. Measurements of the high frequency temporal wavelengths are on the order of 6 - 8 ns therefore frequencies are well above the 115 MHz limit seen on the 1 µm tin single layer films. This suggests that the high frequency attenuation observed on tin layers may be a thickness dependent phenomenon. In comparing the non-calcined and calcined waveforms, there appears to be no major differences. Overall, the SAWs detected on both samples were qualitatively sound with a normal distribution in amplitude and no evidence of foul oscillations.

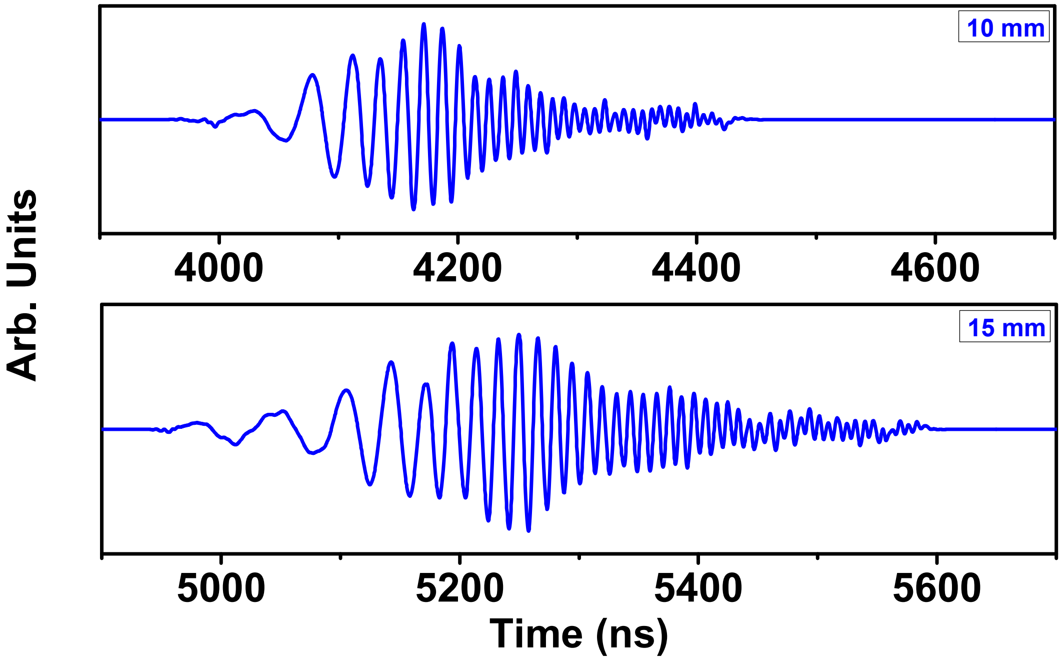

Figure 6-14. SAWs detected at 10 mm and 15 mm on the non-calcined sample.

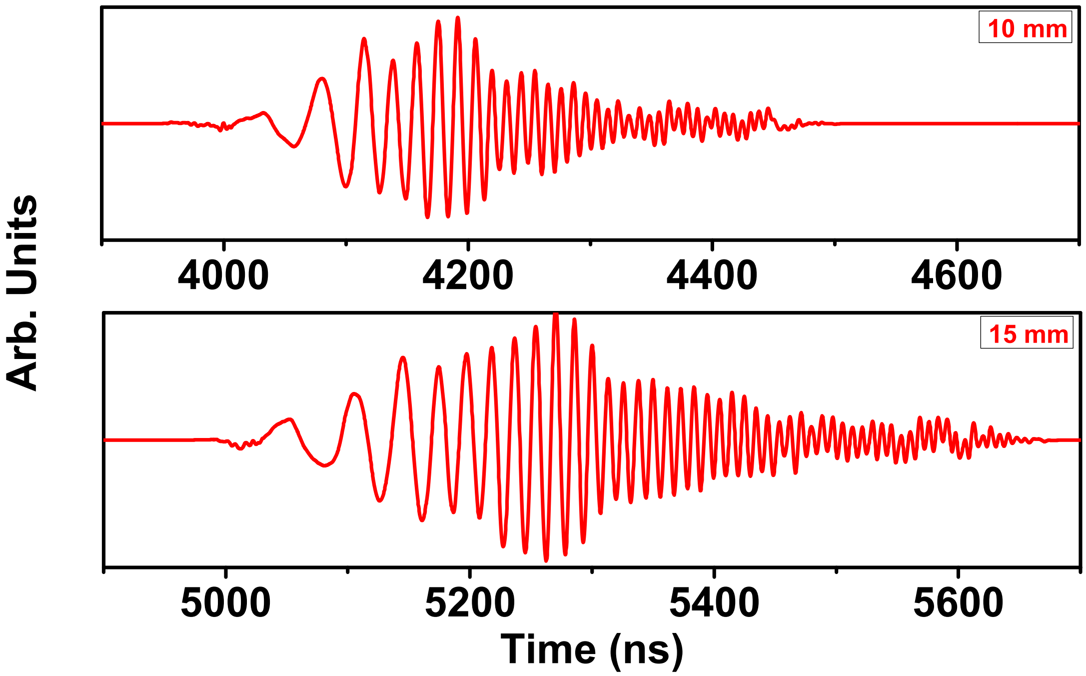

Figure 6-15. SAWs detected at 10 mm and 15 mm on the calcined sample.

Fourier transforms of the signals were calculated to investigate the frequency bandwidth and the results are plotted in Figure 6-16. Both the non-calcined and calcined samples sustained SAWs with a frequency spectrum ranging from 20 – 150 MHz. This confirms that the frequencies achieved were higher than the results on single layer tin films. However, the range was still substantially lower than the 225 MHz limit that was measured on aluminum films. This is likely caused by the tin top layer since their high frequency attenuation affects were measured previously. The bMFI layer, with a Rayleigh wave speed of $\sim 2600\ m/s$, is quite close to the wave speed of aluminum therefore it is unlikely to cause frequency loss in the system if the attenuation is indeed linked to slower wave speeds and thickness.

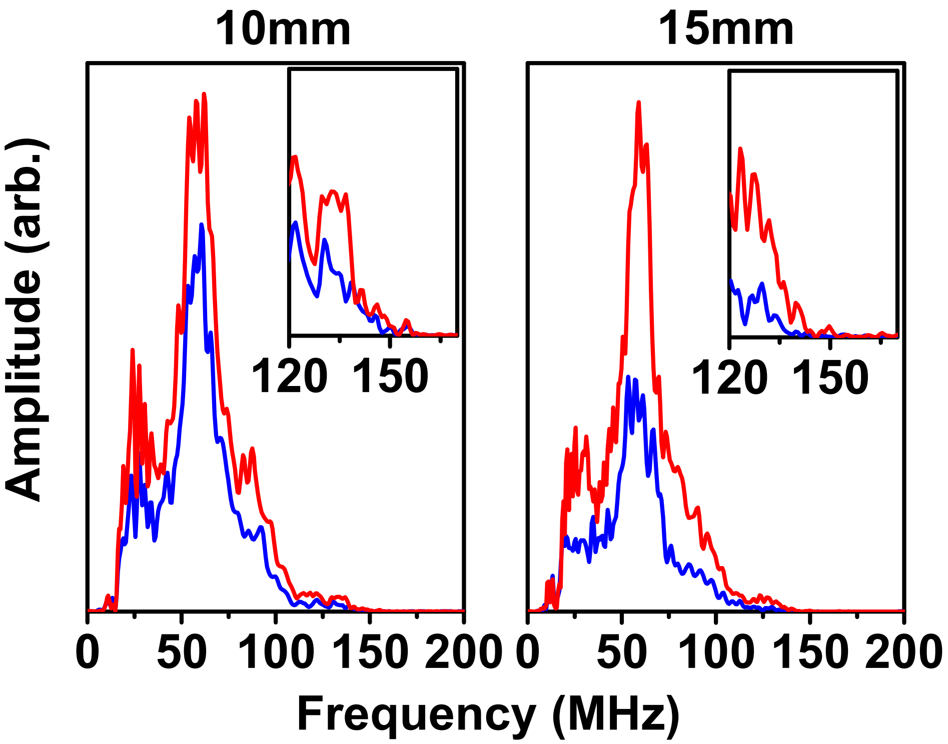

Figure 6-16. Frequency spectrum of the non-calcined (blue) and calcined (red) SAWs detected at 10 mm and 15 mm.

Dispersion curves from the bMFI SAWs are presented in Figure 6-17. While only the 15 mm and 10 mm results were discussed in detail above, other signals at 14 mm and 11 mm were captured and the dispersion curves generated from those signals are also plotted. As predicted by Figure 6-13, the 400 nm tin layer significantly increased the dispersion of the system and created slight nonlinearity in the dispersion curves. Unfortunately, the degree of nonlinearity was quite low therefore the small second order parameters did not allow for multiple property fitting. Using the same properties of silicon and bMFI ($\rho_{calcined} = 1750\ kg/m^3$, $\rho_{non-calcined} = 1900\ kg/m^3$) as previous studies, the elastic modulus was fit for both the non-calcined and calcined films. It is observed that the theoretical 37 GPa and 35 GPa curves respectively for the non-calcined and calcined films fit very well with the results. This reconfirms the properties of the bMFI film by closely matching the values determined from the previous study.

The dispersion curves in Figure 6-17 directly demonstrate the effects of the improved detection scheme and the use of tin top layers. The frequency range of detection has been extended from 120 MHz to 150 MHz for a significant 25% increase. From a detection standpoint, the upper limit of frequency could have been much greater if tin did not produce attenuation. However, the tin layer is responsible for producing much more dispersion in the system allowing for a phase velocity range of ~350 m/s that is over three times greater than before. The combined effect of these techniques is the extension and overall smoothness of the experimental dispersion curves. Looking back at the corresponding dispersion plot from the previous bMFI study, Figure 5-25, one can easily observe the far greater noise in those curves compared to the ones in this chapter. Thus, the smoother experimental curves in the present study produce much better correlation to theoretical curves and therefore provide results with greater confidence.

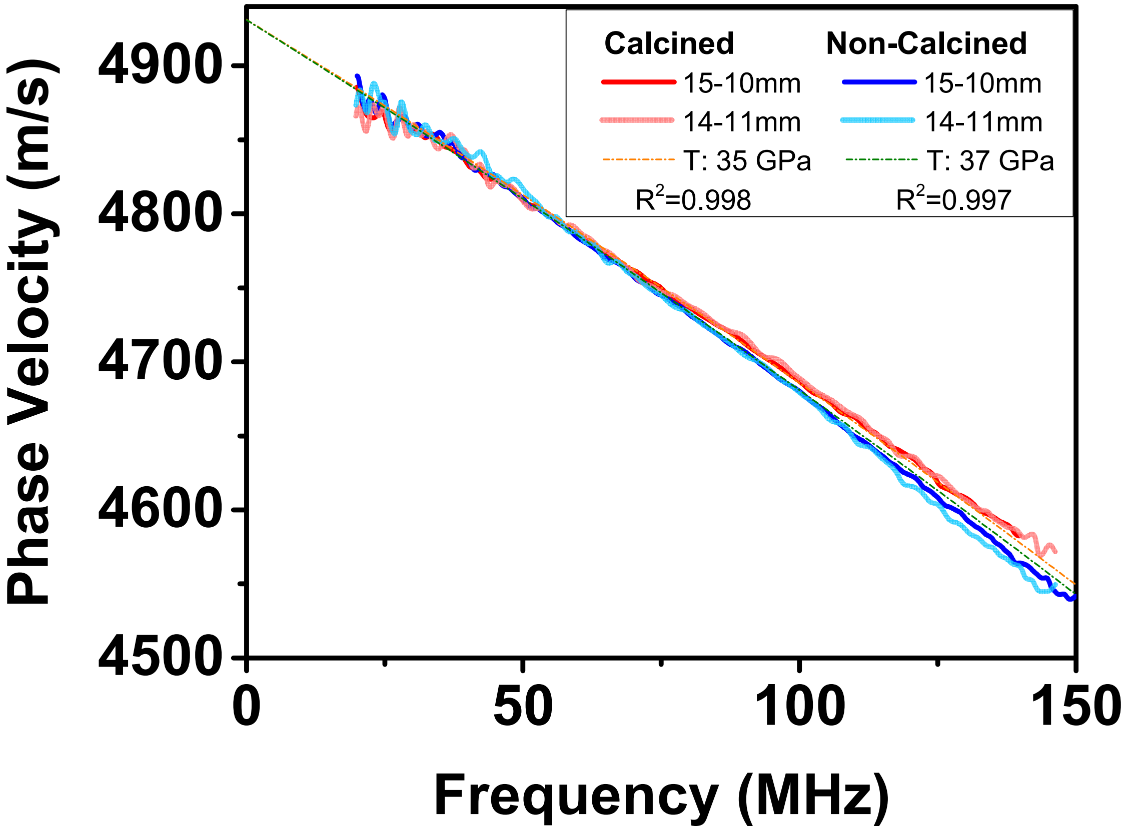

Figure 6-17. Dispersion curves for non-calcined and calcined bMFI films. "T" denotes theoretical curves.

6.6 Conclusion

This chapter overviewed methodologies to create dispersion with extended frequency range and increased acoustic contrast. Both techniques contribute to producing experimental dispersion curves that have less noise and that have a larger frequency response. The increased frequency range reduces fitting error by providing longer fitting windows and the suppression of noise creates conditions for better curve correlation between experiment and theory. Combined, the result is a LiSAW measurement that has a higher accuracy and greater repeatability.

To increase the frequency range, the spot size of the detection beam was reduced to one-third of its size from the previous configuration. This was done by using two short focal length lenses, one in each interferometer leg, as opposed to one long focal length lens prior to the beam splitter. Shorter focal lengths allow for smaller spot sizes because the angle of convergence is greater, but as a result, the spot size grows much faster for each unit of distance away from the ideal focal plane. Additionally, the two lens setup adds many challenges to path length balancing such as the distance from the beam splitter to each lens, the tilt of each lens, and the distance from the lens to each surface, therefore careful refinement to the setup was required to ensure that the two paths remain optimally balanced.

The result of the frequency enhancement was tested by generating and detecting SAWs on aluminum films with silicon substrates. Previous tests on such films yielded a detection limit of around 120 MHz. With the improved setup, the frequency range was extended to 225 MHz which is a substantial increase that almost doubles the range for dispersion fitting. As a secondary experiment, SAWs were generated with two lasers, one with a shorter pulse width (Leopard, 50 ps) and one with a longer pulse-width (Tempest, 5 ns). It was observed that the Leopard required significantly more power to generate SAWs of the same amplitude, but had a better behaved high frequency region at above 130 MHz. However, the Leopard SAWs also exhibited periods of consistent frequency extinction between 75 – 120 MHz perhaps from ill effects associated with the higher power and sample ablation. The Tempest SAWs exhibited no such problems, but the high frequency regions were noticeably smaller in amplitude compared to the Leopard. However, the frequency limit detected from the SAWs of both lasers was identical at ~225 MHz. This proved that the Tempest and Leopard lasers were both capable of producing high frequency SAWs up to the current limit of detection which is an surprising result since the longer pulse-width Tempest was expected to attenuate around 100 MHz.

To increase acoustic contrast in the system, tin layers were chosen as an alternative top layer material to replace aluminum. Tin, with a Rayleigh wave speed of just 1479 m/s (compared to 2910 m/s for aluminum), was theoretically shown to drastically increase the dispersion thus producing experimental dispersion curves over a much broader phase velocity range. To investigate this dispersion enhancement effect, single layer tin films on silicon substrates were tested by LiSAW and compared to the results for aluminum films in the previous experiment. The results confirmed the increase in dispersion by showing waves that were substantially elongated as the low and high frequencies propagated at great disparities in speed. This produced waveforms containing many more oscillations therefore allowing for clearer frequency and phase identification. The result was dispersion curves that were much smoother across the detection range thus allowing for lower error in theoretical fitting. However, the maximum frequency achieved was only 110 MHz which is much lower than the range of the improved detection system. Therefore the slower tin film was producing high frequency attenuation that was hypothesized to be thickness dependent. Future work addresses an experiment to investigate this effect.

The combined effect of the frequency detection improvement and the dispersion enhancement by tin films was examined by revisiting bMFI films. 400 nm layers of tin were sputtered on top of two 350 nm bMFI films, one non-calcined (non-porous, as-synthesized) and one calcined (porous). The SAWs detected exhibited both the dispersion enhancement, as evidenced by significant waveform elongation, and frequency enhancement with a detection limit of 150 MHz. The frequency response was a 25% improvement from before and most likely stifled by high frequency attenuation of the tin film. However, the tin film was extremely beneficial in increasing dispersion by producing a phase velocity range over three times greater than before (80 m/s vs 350 m/s). The resulting dispersion curves had very low noise fluctuations and were extended in frequency response. By fitting the experimental curves to theory for the elastic moduli of the bMFI films, it was found that their values matched closely to those from the previous study. Moduli of 37 GPa for the non-calcined film and 35 GPa for the calcined film were extracted. Although some nonlinearity existed in the dispersion curves, the strength of second order parameters was not sufficient for multiple property fitting.

Experiments with lower Rayleigh wave speed top layers and the improved detection scheme demonstrated the large benefits that these enhancements provided to the LiSAW technique. Both satisfy the aim of increasing LiSAW accuracy by providing a larger data range for fitting and decreasing the noise of experimental dispersion curves. The utilization of tin layers is especially interesting since it produces such drastic elongations to the SAW waveforms. While the additional oscillations create a frequency spread that is beneficial to spectral analysis, some high frequencies are being lost for reasons yet to be characterized and this is a topic ripe for future study.

Chapter 6 References:

BRAMHAVAR, S., POUET, B. & MURRAY, T. W. 2009. Superheterodyne detection of laser generated acoustic waves. *Applied Physics Letters,* 94**,** -.

CALLISTER, W. D. & RETHWISCH, D. G. 2009. *Materials Science and Engineering: An Introduction*, John Wiley & Sons Canada, Limited.

CHUDOBA, T., GRIEPENTROG, M., DUCK, A., SCHNEIDER, D. & RICHTER, F. 2004. Young's modulus measurements on ultra-thin coatings. *Journal of Materials Research,* 19**,** 301-314.

HAYASHI, Y., OGAWA, S., CHO, H. & TAKEMOTO, M. 1997. Non-contact estimation of the thickness and elastic properties of metallic foils by wavelet transform of laser generated lamb waves. *NDT and E International,* 30**,** 405-405.

HERNANDEZ, C. M., MURRAY, T. W. & KRISHNASWAMY, S. 2002. Photoacoustic characterization of the mechanical properties of thin films. *Applied Physics Letters,* 80**,** 691-693.

HURLEY, D. C., TEWARY, V. K. & RICHARDS, A. J. 2001a. Surface acoustic wave methods to determine the anisotropic elastic properties of thin films. *Measurement Science & Technology,* 12**,** 1486-1494.

HURLEY, D. C., TEWARY, V. K. & RICHARDS, A. J. 2001b. Thin-film elastic-property measurements with laser-ultrasonic SAW spectrometry. *Thin Solid Films,* 398**,** 326-330.

LEVY, M., BASS, H. & STERN, R. 2001. *Modern Acoustical Techniques for the Measurement of Mechanical Properties*, Elsevier Science.

MURRAY, T. W., KRISHNASWAMY, S. & ACHENBACH, J. D. 1999. Laser generation of ultrasound in films and coatings. *Applied Physics Letters,* 74**,** 3561-3563.

ROGERS, J. A., MAZNEV, A. A., BANET, M. J. & NELSON, K. A. 2000. Optical generation and characterization of accoustic waves in thin films: fundamental s and applications. *Annual Review of Materials Science,* 30**,** 117-157.

SALENBIEN, R., CÔTE, R., GOOSSENS, J., LIMAYE, P., LABIE, R. & GLORIEUX, C. 2011. Laser-based surface acoustic wave dispersion spectroscopy for extraction of thicknesses, depth, and elastic parameters of a subsurface layer: Feasibility study on intermetallic layer structure in integrated circuit solder joint. *Journal of Applied Physics,* 109**,** -.

SCRUBY, C. B. & DRAIN, L. E. 1990. *Laser ultrasonics: techniques and applications*, Adam Hilger.

TIZIANI, H. J. Heterodyne interferometry using two wavelengths for dimensional measurements. 1992. 490-501.

XIAO, X. & YOU, X. 2006. Numerical study on surface acoustic wave method for determining Young's modulus of low-k films involved in multi-layered structures. *Applied Surface Science,* 253**,** 2958-2963.

ZUMBERGE, M. A., BERGER, J., DZIECIUCH, M. A. & PARKER, R. L. 2004. Resolving Quadrature Fringes in Real Time. *Applied Optics,* 43**,** 771-775.

Chapter 7 Mechanical characterization of porous nanostructured V_2O_5 films by LiSAW and nanoindentation

7.1 Introduction

Lithium ion batteries are an integral part of today's energy storage landscape, but the constant miniaturization of electronic devices is currently challenging the technology to fit into reduced form factors. While smaller electronics have allowed for great advancement in many areas such as portable consumer electronics and biologically implantable devices (Holmes, 2001), their energy requirements can often remain similar, if not greater than, before (Whittingham, 2012). Thin film Li-ion batteries are capable of meeting the limited size requirements, but alternatives to the traditional graphite and lithium metal oxide electrode materials are necessary to maintain capacity and performance with diminished battery mass (Ji et al., 2011, Ellis et al., 2010). Nanostructured materials are of interest in this field because they can exhibit very high surface energies which enhance charge transfer kinetics and ion storage capacity (Liu and Cao, 2010, Song et al., 2011, Zhang et al., 2013). Additionally, nanostructures, especially when coupled with porosity, can be more tolerant to the large physical deformations associated with Li-ion insertion and removal thus reducing the mechanical breakdown of the electrode and improving the battery life cycle (Vu et al., 2012, Hayner et al., 2012).

It is well known that the effects of the electrode volume change during each charge cycle, producing modest strains of 2% in $LiCoO_2$ cathodes (Reimers and Dahn, 1992) and 7% in $LiFePO_4$ cathodes (Meethong et al., 2007), contributes greatly to the loss of charge capacity over time (Cabana et al., 2010). Yet for such a mechanically rich process, there has been relatively little investigation correlating the breakdown to the mechanical properties of the electrode. While many studies have targeted and identified the main degradation mechanism, the proliferation of micro-cracks (Ebner et al., 2013), comprehensive mechanical design criteria to mitigate such issues in new electrode materials have yet to be determined. With many other electrochemical considerations to contend with, it is easy to see why mechanical aspects are often overlooked, but with links between mechanics and rate capability (Meethong et al., 2007) and the emergence of higher capacity materials with larger expected volume changes, nanomechanical characterization may become critical in understanding optimal electrode design.

The prevalence of nanoindentation in thin film mechanical analysis is especially valuable to the characterization of thin film electrodes. Indentation tests can quickly determine the elastic and plastic properties of a material with the elastic modulus being especially useful here. While electrode degradation is a complex problem with both electrochemical and mechanical considerations, the modulus can breathe insight into the flexibility and reliability of a material and thus aid in understanding how it may cope with lithiation induced strain. Several recent studies have successfully applied nanoindentation to electrode materials. Qu *et al.* reported on the elastic modulus, density, and fracture toughness of individual $LiCoO_2$ grains and noted that the experimentally determined modulus of 174 GPa was much lower than the previously predicted value of 315-516 GPa (Qu et al., 2012). This suggests a more compliant structure than once thought. Ramdon and Bhushan reported on the elastic modulus, hardness, and wear properties of $LiFePO_4$ cathodes before and after multiple charge cycles. They found that the modulus did not change significantly through cycling, but that the hardness increased by almost 100% giving rise to a durable, yet brittle structure (Ramdon and Bhushan, 2014). Zhu *et al.*

performed indentations on RuO_2 anodes and found that the elastic modulus decreases by an order of magnitude after 50 cycles (Zhu et al., 2013). With such a limited quantity of studies, it is difficult to correlate the elastic modulus, or any other mechanical property, to battery performance over time therefore this area begs for further investigation.

The lack of nanomechanical studies could possibly be attributed to the difficulty of nanoindentation on thin film electrode materials. For consistent results that are free of indentation substrate effects, it is necessary to have films with low surface roughness and a thickness many times that of the penetration depth. This can be especially problematic to nanostructured or porous films since their engineered roughness may be too delicate for mechanical polishing and their thicknesses could be very small. While substrate effects from low thicknesses can be overcome by utilizing an alternative indentation analysis scheme (Li and Vlassak, 2009), albeit with significant computational intensity, defeating roughness through deep indents may not always be viable. In this scenario, it may be more efficient to use a laser-induced surface acoustic wave (LiSAW) technique to determine the elastic modulus.

The LiSAW technique is valuable to thin and porous films because it requires only elastic deformations, it features non-contact measurements, and the mechanical property extraction naturally considers and isolates substrate coupling (Hess, 1996, Schneider and Tucker, 1996, Xiao et al., 2011). In the experiment, an Nd:YAG laser is used to excite Rayleigh waves that subsequently propagate across the layered system. Due to elastic mismatch between the film and substrate, frequency dispersion of the wave occurs. Since the relationship between mechanical properties and dispersion is well documented in wave mechanics (Farnell and Adler, 1972), LiSAW can seek unknown parameters of the film or substrate by experimentally quantifying the dispersion. In this manner, if enough nonlinearity exists in the dispersion curve, the film thicknesses, Poisson's ratios, densities, and elastic moduli of the materials involved can be found. Typically, many of these parameters are known at the onset, thus only one or two parameters may require fitting. LiSAW can deliver these results on the same time-scale as typical indentation tests and with no substrate influence. Due to the micron scale of SAW wavelengths, the technique can work well on moderately rough films (Cote et al., 2009) and, depending on SAW detection scheme, with little or no surface preparation.

The limiting factor of many current Li-ion batteries lies in the low energy density of the cathode. Common cathode materials based on layered lithium metal oxides, such as $LiCoO_2$ and $LiFePO_4$, have capacities of just 140 $mAhg^{-1}$ and 170 $mAhg^{-1}$ respectively (Nazri and Pistoia, 2009). Significant research has been completed on the oxides of other first row transition metals in order to achieve higher capacities. From these studies, vanadium oxides have emerged with great potential due to their wide range of available oxidation states, high reversibility, and favorable layered structures, all of which are conducive to the electrochemical lithiation process (Ding et al., 2009). Specifically, V_2O_5, with a theoretical capacity of 450 $mAhg^{-1}$ (Liu et al., 2011a), has been extensively studied and remains a leading candidate amongst alternative cathode materials. While V_2O_5 has been known for inadequate structural stability and slow electrochemical kinetics, nanostructured V_2O_5 forms have recently been shown to overcome these challenges by demonstrating excellent capacity, rate capability, and cyclability (Liu et al., 2011b, Pomerantseva et al., 2012, Augustyn and Dunn, 2010).

In this paper, the mechanical properties of a porous nanostructured V_2O_5 cathode film are investigated by nanoindentation and LiSAW. This particular film is especially attractive because it is synthesized by a simple and cost effective procedure via electrodeposition and exhibits excellent electrochemical properties. A previous report showed that the film has an initial charge capacity of 402 mAhg^{-1} and a retention of 240 mAhg^{-1} after 200 cycles at a discharging rate of 1.3C (Liu et al., 2011a). From a mechanical standpoint, the film's roughness and delicate nature, both properties common to nanostructured electrode materials and for which mechanical polishing is not viable, makes it an interesting specimen for testing the limits of traditional nanoindentation. The goal of this study is to perform LiSAW and discover whether the technique is reliable for such films. The results will then be compared to findings from nanoindentation with the intent of identifying the most efficient means for mechanical characterization of such media. It is hoped that the methodologies identified from this research will guide and fuel additional investigations in order to develop a further understanding of the relationship between electrode performance and its mechanical properties.

7.2 Sample preparation

Electrodeposited V_2O_5 films were prepared on single crystal silicon wafers with (100) orientation by the procedure reported in literature (Liu et al., 2011a). In brief, a vanadium pentoxide solution was formed by combining commercial V_2O_5 powder (99.8% Alfa-AESAR) with H_2O_2 (30 wt.% in water, Sigma-Aldrich) and de-ionized water. The solution was stirred for 15 minutes and then sonicated for 15 minutes in water at constant temperature. Afterwards, the V_2O_5 concentration was diluted from $C_V = 0.3\ M$ to $C_V = 0.06\ M$ and the resulting solution was sonicated for 1 h. A final dilution, this time to $C_V = 0.0075\ M$, completed the V_2O_5 solution and prepared it for use in electrodeposition.

Prior to electrodeposition, the Si substrates were sputter coated with < 5 nm of gold palladium to enhance conductivity. They were then lowered into the V_2O_5 solution parallel to a platinum plate counter electrode. Deposition was carried out at -2.4 V for 1 h with a separation distance between the electrodes of ~15 mm. Upon completion, the films were dried in air at 70 °C for 1 h and then annealed in air at 450 °C for 3 h. To obtain free standing films for density measurements, the procedure was carried out on nickel foil substrates (99.9% Sigma-Aldrich) instead of silicon. After electrodeposition, the undried gel films were carefully detached from the foil and bridged across a ~20 mm gap on wax paper. The films were dried and cut free from the wax paper to isolate their spanning areas prior to annealing. Drying and annealing conditions remained unchanged from before. All film thicknesses were measured by profilometry (Dektak, Tucson, AZ).

7.3 Experimental results for V_2O_5 films

7.3.1 Microstructure and crystallinity of electrodeposited V_2O_5 films

Two samples were synthesized for LiSAW testing with each having dimensions of ~25×25 mm. The electrodeposited films were characterized by X-ray diffraction to confirm the presence of V_2O_5. The resulting spectrum, shown in Figure 7-1, clearly displays the prominent (001) and (101) peaks of orthorhombic V_2O_5 thus confirming the oxide structure. Figure 7-2 shows the rough nanostructured surface as imaged by a scanning electron microscope. The film thicknesses were measured to be 1.7 μm which is much larger than the films in the previous report containing electrochemical results (Liu et al., 2011a). In the previous study, the films were grown for 3 – 20 min whereas the films here were grown for 1 h. The two sets of films are structurally identical. It was the intent of the authors to create thicker films in order to isolate the challenge of nanostructured roughness from the substrate effect during latter indentation tests.

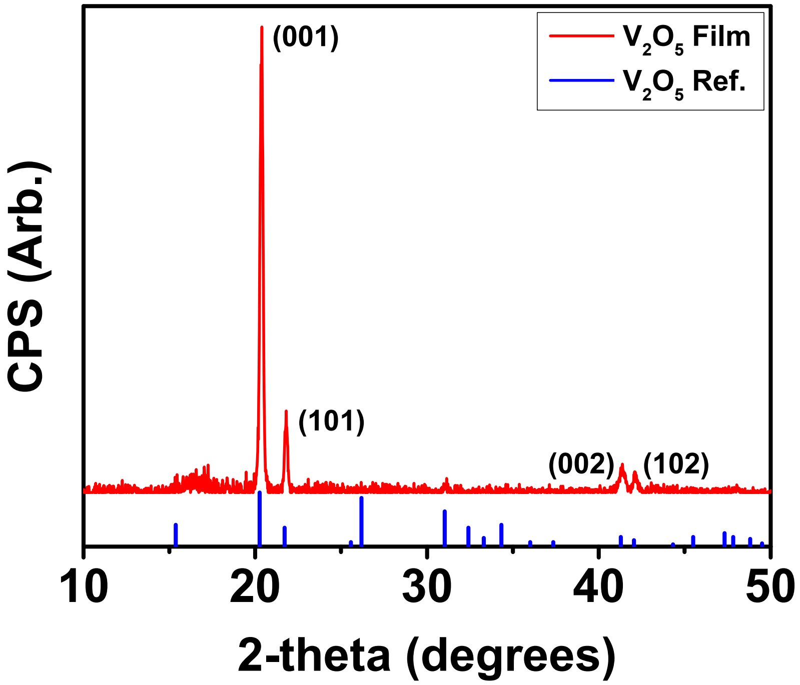

Figure 7-1. X-ray diffraction spectrum of the nanostructured V_2O_5 film compared to a reference spectrum (National Bureau of Standards, 1959).

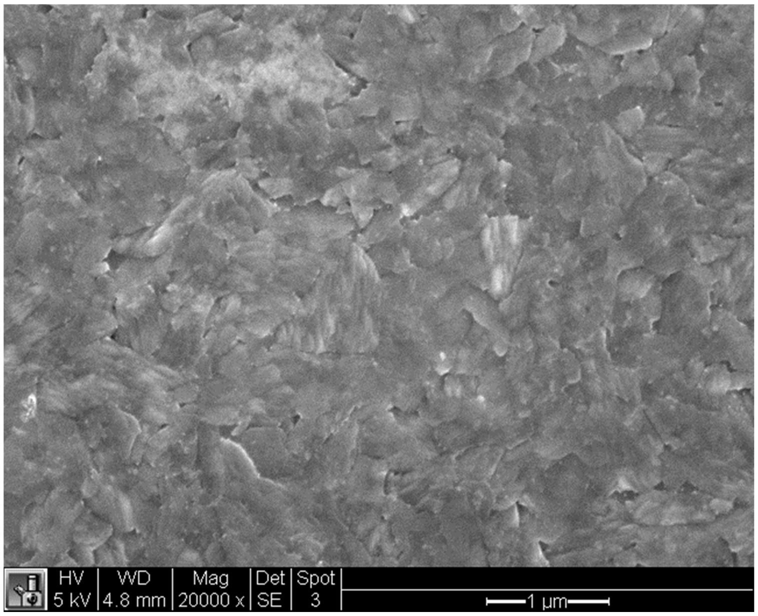

Figure 7-2. Image of the V_2O_5 surface taken by a scanning electron microscope.

7.3.2 Effect of large dopant concentrations on silicon Rayleigh wave speed

To facilitate electrodeposition, low resistivity silicon wafers were used for substrates. Heavy doping, with impurity concentrations on the order of 10^{19} cm^{-3}, was necessary to achieve resistivities < 0.002 Ω-cm and this has been shown to modify the elastic constants of silicon (Keyes, 1982). While the variations in elastic parameters are expected to be ~1% for the doping levels here, they can still have a significant effect on Rayleigh wave speed (c_r). To account for the change, LiSAW was performed on bare silicon wafers prior to film deposition. The results were used to fit the c_{11} stiffness tensor for subsequent analysis in theoretical curve determination. The doped wafers were found to have $c_r = 4896\, m/s$ in the [100] direction (Figure 7-3) which is a bit lower than the results for undoped wafers ($c_r = 4917\, m/s$). This corresponded to -1% decrease in c_{11} lowering it from 165.7 GPa to 163.8 GPa. This value was used for all theoretical calculations to follow. The other silicon constants remained unchanged and their values were $c_{12} = 63.9$ GPa, $c_{44} = 79.6$ GPa, and $\rho = 2330\ kg/m^3$.

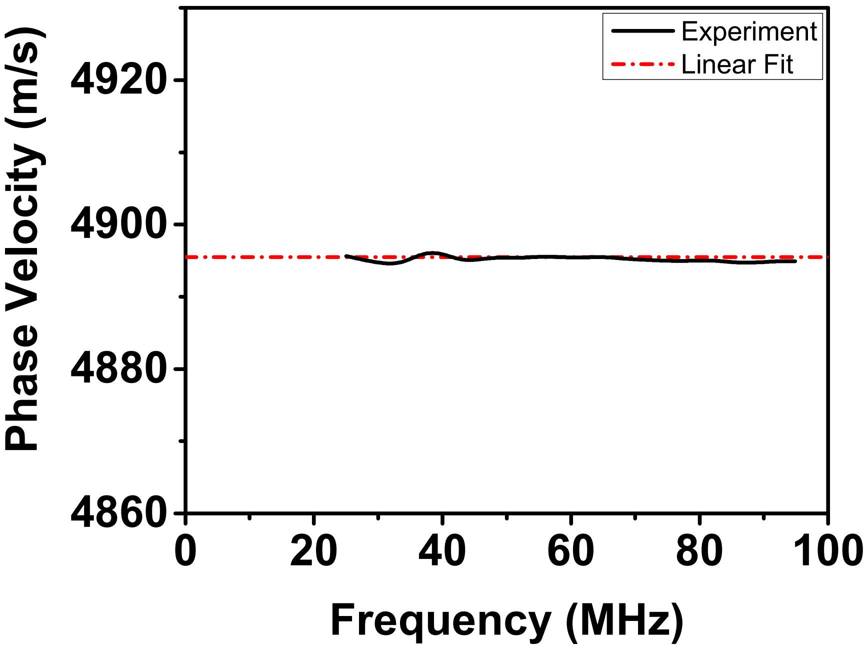

Figure 7-3. Dispersion curve of heavily doped n-type wafer with no film (non-dispersive). Linear fit shows that the Rayleigh wave speed is 4896 m/s.

7.3.3 LiSAW results

To make the V_2O_5 surface more reflective for optical detection methods, a thin layer of aluminum was deposited on top of the V_2O_5 by magnetron sputtering (AJA International, Scituate, MA) as a secondary top film. The elastic modulus of the sputtered aluminum films, a key parameter for theoretical fitting, was confirmed by performing LiSAW and nanoindentation on separate samples without V_2O_5. Both techniques measured a modulus of 70 GPa which is in agreement with literature (Serway et al., 2008). The other properties of aluminum used for theoretical dispersion curves were $\rho = 2700\ kg/m^3$ and $\nu = 0.33$. While tin top layers were previously discovered to induce larger dispersion effects than aluminum, the inability to polish the V_2O_5 film limited their usage. Tin films require a secondary polishing step since they often exhibit dull surface quality in the as-sputtered state.

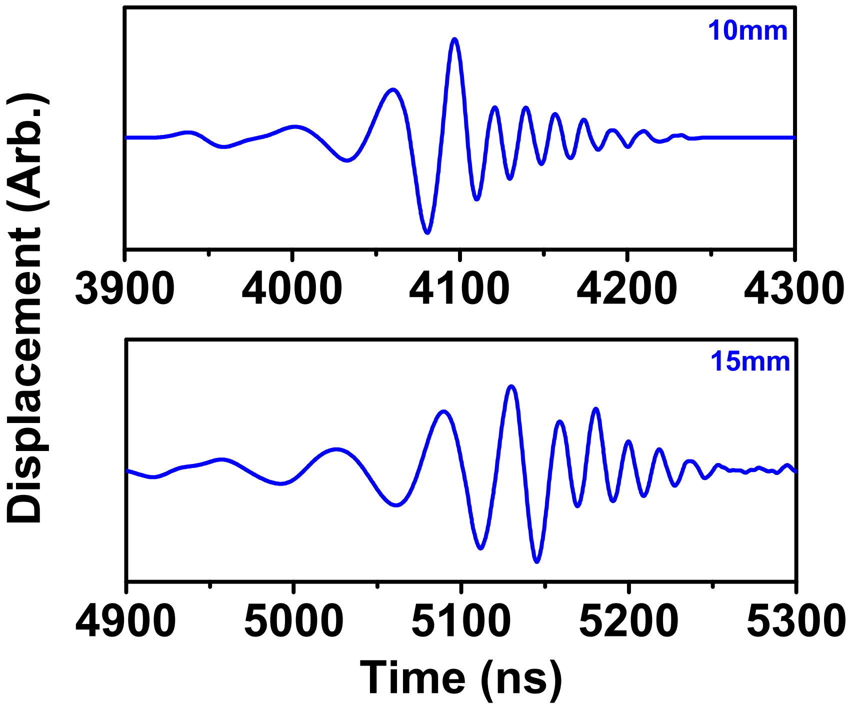

Figure 7-4. SAW signals recorded on the first V_2O_5 sample at a distance of 10 mm and 15 mm from the source. To aid in shot to shot alignment, the x timescale is offset by 2 µs such that sample irradiation occurs at ~2000 ns.

The first V_2O_5 film tested received a 100 nm aluminum top layer. SAWs were generated in the [100] direction of the silicon substrate and detected after traveling various distances ranging between 10 mm and 15 mm from the irradiation site. SAW waveforms obtained at 10 mm and 15 mm are shown in Figure 7-4. Dispersion of the signals is evident from the waveform elongation on the 15 mm signal, especially apparent at low frequencies. Spectral analysis showed a frequency response between 15 – 60 MHz in both signals (Figure 7-5). The upper bound of the detected frequencies is a quite low considering that the detection spot size of < 10 µm is sufficient to identify frequencies well in excess of 100 MHz. However, the nanostructured roughness was a likely cause of high frequency attenuation. It should be noted that the penetration depth of SAWs is on the order of one wavelength therefore a 50 MHz wave propagating on silicon has an influence of almost 100 µm. The film region represents only a small fraction of this influence, yet significant detectable dispersion occurs even at low frequencies. Thus, while a large bandwidth is desirable, it is not always necessary, as is the case in this sample where there was more than adequate bandwidth for dispersion analysis. This reasoning is why LiSAW is an attractive and effective technique for very thin films of delicate nature.

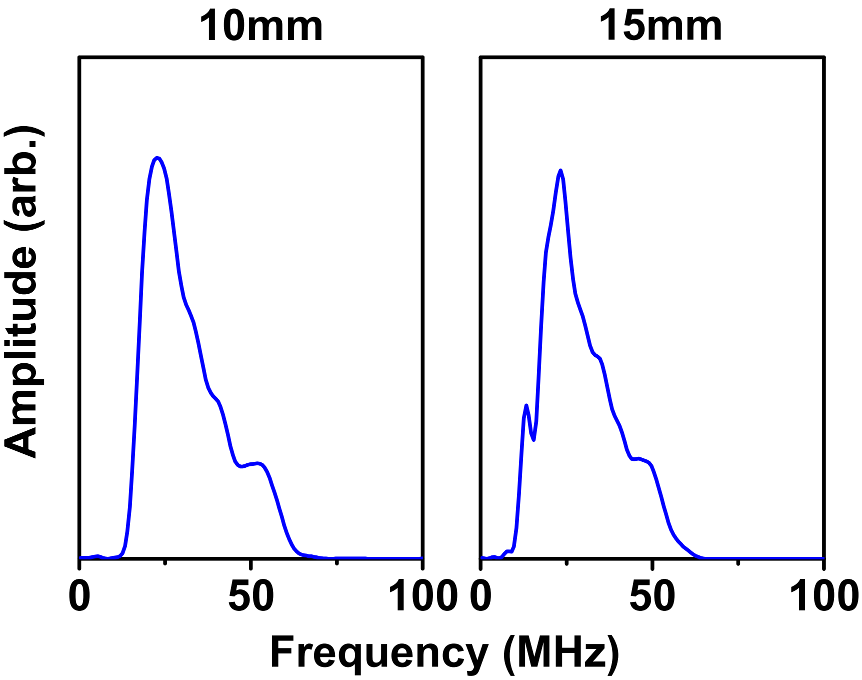

Figure 7-5. Frequency spectrum of the SAWs from the first V_2O_5 sample.

Experimental dispersion curves were calculated for the signals in Figure 7-4 and other signals captured at 11 mm and 14 mm. The elastic modulus was extracted through fitting of theoretical curve and the results appear in Figure 7-6. Four film parameters are necessary for fitting:

Poisson's ratio, film thickness, density, and elastic modulus. Since we have linear dispersion, three of the four parameters must be known in advance. Fortunately, the Poisson's ratio (0.3 was used) has a negligible influence on dispersion (Xiao and You, 2006) and the thickness (1.7 µm) can be measured to a high degree of certainty. Density can typically be determined by methodologies involving Archimedes principle such as the case in this study where a pycnometer was utilized. The measured density was $2.28 \pm 0.11\ g/cm^3$. While the porosity for this film has not been characterized, it is considerably less dense than an ideally packed V_2O_5 structure which has a density of $3.36\ g/cm^3$. With all of the substrate and film parameters accounted for, the experimental dispersion curve was fit to a modulus of 53 ± 4 GPa. The error bars are a result of the uncertainty in density measurement. Fitting error was low and did not contribute significantly to error since the experimental curves were linear and thus correlated well with the fit (14-11mm: $R^2 = 0.968$, 15-10mm: $R^2 = 0.887$).

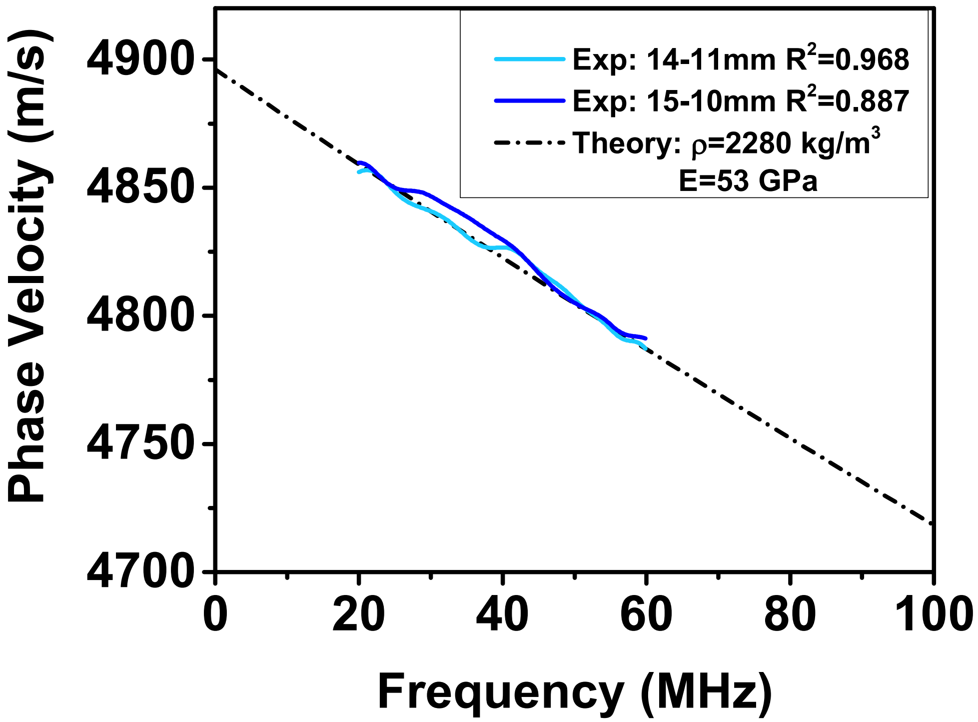

Figure 7-6. Dispersion curves and theoretical fit for the first V_2O_5 sample.

A second V_2O_5 film, with identical specifications as the first film, was tested to demonstrate measurement repeatability. On this sample, a 200 nm aluminum reflective layer was sputtered prior to testing. The SAWs were detected at smaller propagation distances, 5 – 11 mm, in an effort to capture higher frequencies before they attenuated. The signals detected are shown in Figure 7-7. Inspection of the frequency response, shown in Figure 7-8, reveals a slight increase to the frequency limit with a new range of 15 – 75 MHz. The difference in frequency bandwidth from the 5 mm to the 11 mm signal is 5 MHz. This suggests that some propagation dependent attenuation does occur. However, capturing SAWs even closer to the irradiation site is potentially hazardous in the current setup since the scattered Nd:YAG light may damage the detection photodetector. Proper 1064 nm filtering could alleviate this issue.

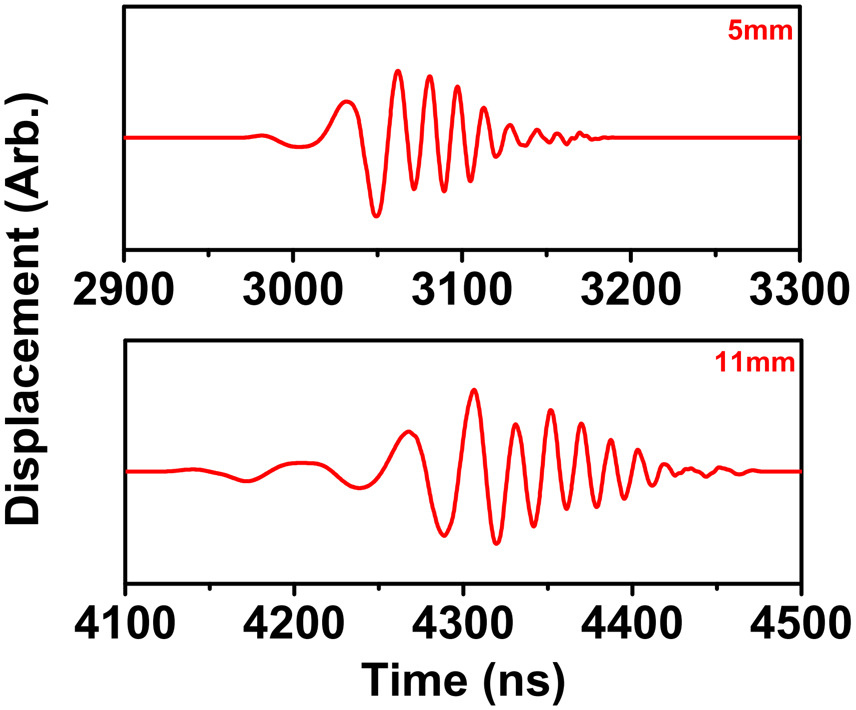

Figure 7-7. SAW signals recorded on the second V_2O_5 sample at a distance of 5 mm and 11 mm from the source.

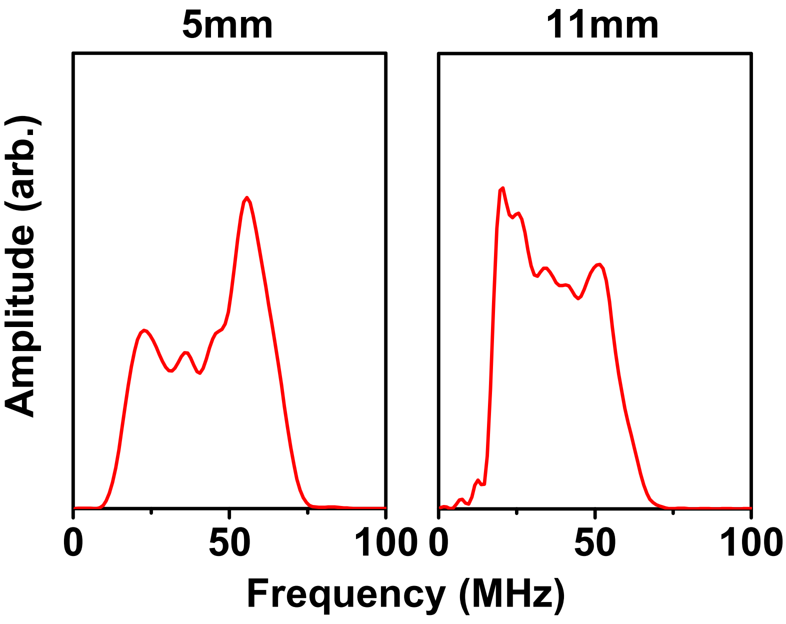

Figure 7-8. Frequency spectrum of the SAWs from the second V_2O_5 sample.

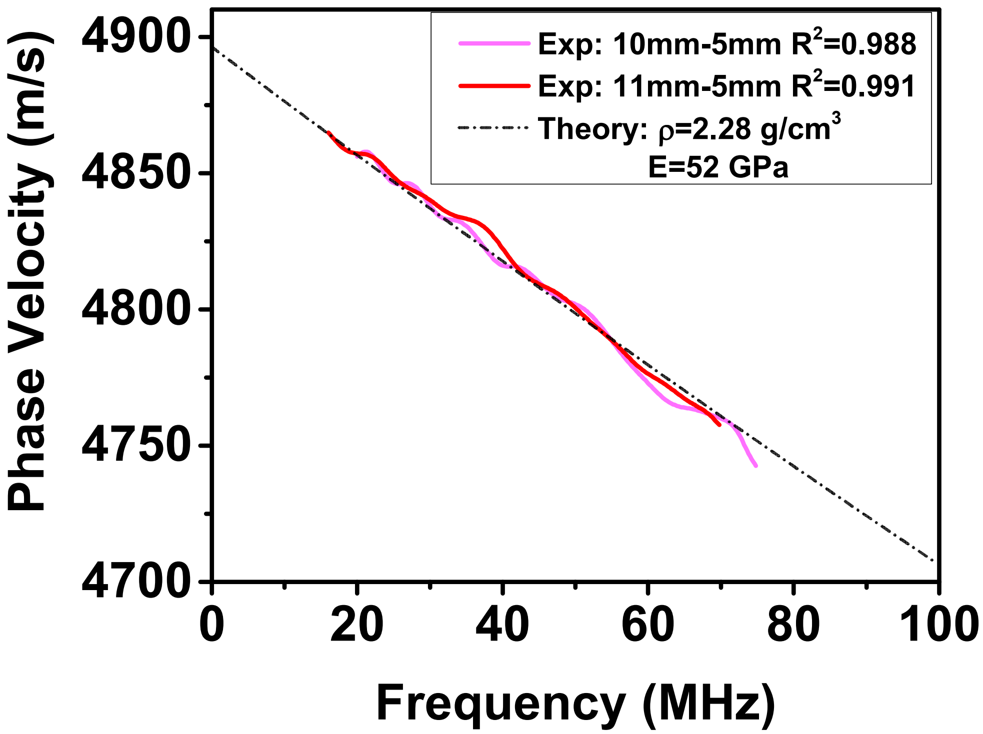

Figure 7-9. Dispersion curves and theoretical fit for the second V_2O_5 sample.

The experimental dispersion curves generated from combinations of signals detected at 5 mm, 10 mm, and 11 mm are shown in Figure 7-9. Similar to the first V_2O_5 sample, the experimental curves were very linear, but they were not directly comparable since the aluminum layer was thicker on this sample thus creating slightly more dispersion. Theoretical curves were generated and to fit the experimental curves and the best fit revealed a modulus of 52 GPa which was in excellent agreement to the first sample.

7.3.4 Nanoindentation results

Nanoindentation was performed on the first of the two LiSAW samples described above. The test preceded the LiSAW study and was conducted before the reflective aluminum layer was deposited. The in-situ scanning probe microscopy (SPM) capability of the indentation system allowed for surface analysis prior to indentation. An SPM topography image is shown in Figure 7-10. The roughness of the film is visibly evident and the measured RMS roughness resulting from a 10×10 µm area was 40 nm. Manual polishing was attempted with 0.05 µm alumina slurry on a low nap fine polishing cloth (Ted Pella, Redding, CA), but the film delaminated and detached too easily. The film could not be reliably polished even with just the sample holder weight of approximately 100 g applied. Thus, tests were performed on the as-synthesized state without polishing.

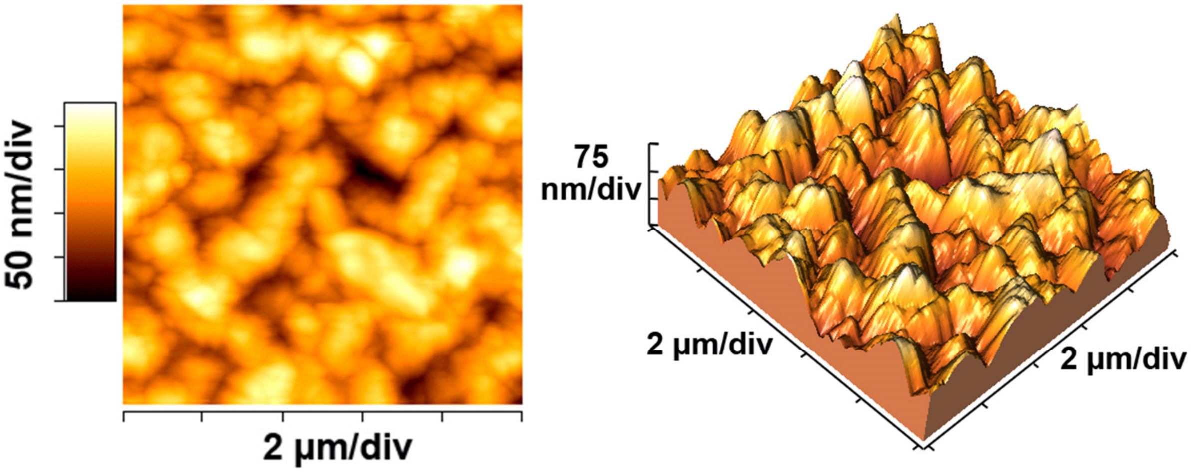

Figure 7-10. Left: 10×10 µm SPM topography image of the V_2O_5 surface. Right: 3-dimensional plot of the left image.

Initially, nanoindentation proceeded to depths of only 75 nm in order to simulate characterization of the thickest film for which electrochemical data was reported on previously. This corresponds to 10% (in order to minimize substrate effects) of the 750 nm thick film created by a deposition time of 20 min. For thin film electrodes, this 750 nm thickness is still quite large since most are considerably thinner (i.e. 3 min, 125 nm film) in order to minimize Li-ion diffusion time and thus maximize power capability (Wang and Cao, 2008). Indentations were performed ranging from 13 – 74 nm in maximum depth and the calculated film modulus was 50 ± 10 GPa. It is apparent that the roughness is a likely culprit for the high standard deviation since many of the indentations were comparable in size to surface asperities.

It should be noted that the modulus extracted from indentation loading curves is known as the reduced modulus (or indentation modulus), E_r, and its value represents a combination of film and indenter tip properties. Eq. 7-1 can be used to isolate the film modulus, E_f, requiring the tip properties (modulus $E_i = 1140\ GPa$ and Poisson's ratio $\nu_i = 0.07$ for the diamond Berkovich tip) and the film Poisson's ratio (ν_f), but unlike LiSAW, the extraction is quite sensitive to the Poisson's ratio.

$$\frac{1}{E_r} = \frac{(1-\nu_i^2)}{E_i} + \frac{(1-\nu_f^2)}{E_f} \tag{7-1}$$

A Poisson's ratio of 0.3 (identical to LiSAW fitting) was used to obtain the 50 GPa value reported above, but considering a range of $\nu = 0.2 - 0.35$, the modulus can differ by as much as 47.9 – 52.4 GPa. Thus, uncertainty in the Poisson's ratio can affect the nanoindentation measurement error in addition to the normal site to site error; in this case, the additional error was 4 – 5%. A similar argument can be made about the LiSAW technique which requires and is sensitive to the film density. However, density is typically less challenging to procure by direct means and the site to site error is lower for LiSAW since the measurement naturally averages over the SAW propagation distance.

A second round of indentation was performed to larger depths in order to explore whether the roughness could be overcome. The maximum depth was extended to 170 nm representing 10% of the film thickness. The indentations revealed a modulus of 51 ± 9 GPa, a slight increase compared to the previous tests with an improvement on the error. The increase is well within the error bars of the previous test, but could be explained by possible collapse of the porous network at shallow indentation depths prior to densification at larger depths (Lu et al., 2012). No substrate effects were witnessed since the film was sufficiently thick. Overall, the nanoindentation data produced results similar to the LiSAW tests, but with substantially higher measurement error. Considering the film roughness of 40 nm, even the deeper indentations could easily be affected by the surface features. This highlights one of the advantages of the LiSAW technique by demonstrating accurate analysis on a rough nanostructured film.

7.4 Conclusion

From the tests performed, it is clear that both LiSAW and nanoindentation are valuable techniques in the field of thin film mechanical electrode materials characterization. They were both able to measure the elastic modulus of the porous nanostructured V_2O_5 electrode in a timely manner, but LiSAW was more accurate on the rough film. Two LiSAW samples were tested resulting in an elastic modulus of 53 ± 4 GPa for the first sample and 52 ± 4 GPa for the second. Both samples exhibited very linear dispersion curves which correlated well to the theoretical fit thus the major contribution to error came from uncertainty in the film density. Nanoindentation produced a modulus of 50 ± 10 GPa at shallow indentation depths and 51 ± 9 GPa at depths up to 170 nm, or 10% of the film thickness. Roughness had a pronounced effect as evident by the large standard deviations. Uncertainty in the film Poisson's ratio, which is necessary to extract elastic modulus from indentation loading curves, can contribute an additional 4-5% error for this film if $\nu = 0.2 - 0.35$ ($\nu = 0.3$ was used) are considered. The slightly lower results from nanoindentation could be the result of indentation induced pore collapse at low loading. However it is noted that the results are all within the error bars of one another, although the uncertainty of nanoindentation measurements was considerably larger.

Overall, the results extracted from both techniques were similar, but the nanostructured roughness of the sample contributed to increased error in the nanoindentation measurement. LiSAW, on the other hand, did not encounter such challenges since the measurement considers a much larger film area. For thinner films, the advantages of LiSAW are even greater since the technique naturally accounts for substrate influence. While both techniques have been demonstrated to be viable for these nanostructured electrode films, LiSAW extracts the mechanical constants with less error and with comparable ease to indentation tests. This study shows how LiSAW can be a suitable alternative to nanoindentation and how it behaves well with delicate porous films. It is hoped that the technique can be applied to many more electrode materials such that a deeper understanding of the relationship between mechanical properties and electrode performance can be discovered.

Chapter 7 References:

AUGUSTYN, V. & DUNN, B. 2010. Vanadium oxide aerogels: Nanostructured materials for enhanced energy storage. *Comptes Rendus Chimie,* 13**,** 130-141.

CABANA, J., MONCONDUIT, L., LARCHER, D. & PALACIN, M. R. 2010. Beyond Intercalation-Based Li-Ion Batteries: The State of the Art and Challenges of Electrode Materials Reacting Through Conversion Reactions. *Advanced Materials,* 22**,** E170-E192.

COTE, R., VAN DER DONCK, T., CELIS, J. P. & GLORIEUX, C. 2009. Surface acoustic wave characterization of a thin, rough polymer film. *Thin Solid Films,* 517**,** 2697-2701.

DING, N., FENG, X., LIU, S., XU, J., FANG, X., LIEBERWIRTH, I. & CHEN, C. 2009. High capacity and excellent cyclability of vanadium (IV) oxide in lithium battery applications. *Electrochemistry Communications,* 11**,** 538-541.

EBNER, M., MARONE, F., STAMPANONI, M. & WOOD, V. 2013. Visualization and Quantification of Electrochemical and Mechanical Degradation in Li Ion Batteries. *Science,* 342**,** 716-720.

ELLIS, B. L., LEE, K. T. & NAZAR, L. F. 2010. Positive Electrode Materials for Li-Ion and Li-Batteries. *Chemistry of Materials,* 22**,** 691-714.

FARNELL, G. W. & ADLER, E. L. 1972. Types and properties of surface waves. *In:* MASON, W. P. & THURSTON, R. N. (eds.) *Physical Acoustics.* New York: Academic Press.

HAYNER, C. M., ZHAO, X. & KUNG, H. H. 2012. Materials for Rechargeable Lithium-Ion Batteries. *Annual Review of Chemical and Biomolecular Engineering, Vol 3,* 3**,** 445-471.

HESS, P. 1996. Laser diagnostics of mechanical and elastic properties of silicon and carbon films. *Applied Surface Science,* 106**,** 429-437.

HOLMES, C. F. 2001. The role of lithium batteries in modem health care. *Journal of Power Sources,* 97-8**,** 739-741.

JI, L. W., LIN, Z., ALCOUTLABI, M. & ZHANG, X. W. 2011. Recent developments in nanostructured anode materials for rechargeable lithium-ion batteries. *Energy & Environmental Science,* 4**,** 2682-2699.

KEYES, R. W. 1982. Device Implications of the Electronic Effect in the Elastic Constants of Silicon. *Sonics and Ultrasonics, IEEE Transactions on,* 29**,** 99-103.

LI, H. & VLASSAK, J. J. 2009. Determining the elastic modulus and hardness of an ultra-thin film on a substrate using nanoindentation. *Journal of Materials Research,* 24**,** 1114-1126.

LIU, D. W. & CAO, G. Z. 2010. Engineering nanostructured electrodes and fabrication of film electrodes for efficient lithium ion intercalation. *Energy & Environmental Science,* 3**,** 1218-1237.

LIU, Y. Y., CLARK, M., ZHANG, Q. F., YU, D. M., LIU, D. W., LIU, J. & CAO, G. Z. 2011a. V2O5 Nano-Electrodes with High Power and Energy Densities for Thin Film Li-Ion Batteries. *Advanced Energy Materials,* 1**,** 194-202.

LIU, Y. Y., LI, J. G., ZHANG, Q. F., ZHOU, N., UCHAKER, E. & CAO, G. Z. 2011b. Porous nanostructured V2O5 film electrode with excellent Li-ion intercalation properties. *Electrochemistry Communications,* 13**,** 1276-1279.

LU, X., XIAO, P. & LI, H. 2012. Effect of densification distribution on the Young's modulus of porous coatings after nano-indentation. *Acta. Metall. Sin.,* 25**,** 383-390.

MEETHONG, N., HUANG, H. Y. S., SPEAKMAN, S. A., CARTER, W. C. & CHIANG, Y. M. 2007. Strain accommodation during phase transformations in olivine-based cathodes as a materials selection criterion for high-power rechargeable batteries. *Advanced Functional Materials,* 17**,** 1115-1123.

NATIONAL BUREAU OF STANDARDS, U. S. 1959. Circ. 539.

NAZRI, G. A. & PISTOIA, G. 2009. *Lithium Batteries: Science and Technology*, Springer.

POMERANTSEVA, E., GERASOPOULOS, K., CHEN, X. Y., RUBLOFF, G. & GHODSSI, R. 2012. Electrochemical performance of the nanostructured biotemplated V2O5 cathode for lithium-ion batteries. *Journal of Power Sources,* 206**,** 282-287.

QU, M., WOODFORD, W. H., MALONEY, J. M., CARTER, W. C., CHIANG, Y.-M. & VAN VLIET, K. J. 2012. Nanomechanical Quantification of Elastic, Plastic, and Fracture Properties of LiCoO2. *Advanced Energy Materials,* 2**,** 940-944.

RAMDON, S. & BHUSHAN, B. 2014. Nanomechanical characterization and mechanical integrity of unaged and aged Li-ion battery cathodes. *Journal of Power Sources,* 246**,** 219-224.

REIMERS, J. N. & DAHN, J. R. 1992. Electrochemical and In Situ X-Ray Diffraction Studies of Lithium Intercalation in Li x CoO2. *Journal of The Electrochemical Society,* 139**,** 2091-2097.

SCHNEIDER, D. & TUCKER, M. D. 1996. Non-destructive characterization and evaluation of thin films by laser-induced ultrasonic surface waves. *Thin Solid Films,* 290-291**,** 305-311.

SERWAY, R. A., VUILLE, C. & FAUGHN, J. S. 2008. *College physics*, BROOKS COLE Publishing Company.

SONG, M. K., PARK, S., ALAMGIR, F. M., CHO, J. & LIU, M. L. 2011. Nanostructured electrodes for lithium-ion and lithium-air batteries: the latest developments, challenges, and perspectives. *Materials Science & Engineering R-Reports,* 72**,** 203-252.

VU, A., QIAN, Y. Q. & STEIN, A. 2012. Porous Electrode Materials for Lithium-Ion Batteries - How to Prepare Them and What Makes Them Special. *Advanced Energy Materials,* 2**,** 1056-1085.

WANG, Y. & CAO, G. 2008. Developments in Nanostructured Cathode Materials for High-Performance Lithium-Ion Batteries. *Advanced Materials,* 20**,** 2251-2269.

WHITTINGHAM, M. S. 2012. History, Evolution, and Future Status of Energy Storage. *Proceedings of the Ieee,* 100**,** 1518-1534.

XIAO, X., SHAN, X. M., KAYABA, Y., KOHMURA, K., TANAKA, H. & KIKKAWA, T. 2011. Young's modulus evaluation by SAWs for porous silica low-k film with cesium doping. *Microelectronic Engineering,* 88**,** 666-670.

XIAO, X. & YOU, X. 2006. Numerical study on surface acoustic wave method for determining Young's modulus of low-k films involved in multi-layered structures. *Applied Surface Science,* 253**,** 2958-2963.

ZHANG, Q. F., UCHAKER, E., CANDELARIA, S. L. & CAO, G. Z. 2013. Nanomaterials for energy conversion and storage. *Chemical Society Reviews,* 42**,** 3127-3171.

ZHU, J., ZENG, K. Y. & LU, L. 2013. Cycling Effect on Morphological and Interfacial Properties of RuO2 Anode Film in Thin-Film Lithium Ion Microbatteries. *Metallurgical and Materials Transactions a-Physical Metallurgy and Materials Science,* 44A**,** 26-34.

Chapter 8 Final Remarks

Thin films are a fundamental part of engineering with applications reaching into seemingly every field. Semiconductors are especially invested since their whole existence can be attributed to thin film development. There are many qualities, such as thermal, mechanical, optical, chemical, and electrical, that are demanded from thin films and the characterization of each has its own challenges. However, the mechanical properties often require more involvement in measurement. This is because mechanical measurement inherently requires some physical interaction with the sample in order to create particle movement for a measureable response. At the thin film length scales, this becomes increasingly difficult due to size constraints, changes in materials behavior, and morphology considerations.

This dissertation presented how nanoindentation can be a very useful technique in thin film characterization. Nanoindentation was used extensively to show that a wear and corrosion resistant ZSM-5 zeolite film could perform at the same level as chromium and cadmium coatings from industry. In the study, nanoindentation demonstrated the exceptional resilience of ZSM-5 and showed that its wear resistance could be excellent because of the large elastic recovery. However, the nanoindentation study took place on films that were microns in thickness where the assumption of an infinite layer was valid. Indentation tests for such films are the obvious choice. However, for thinner and softer films, such as the case of porous films, indentation tests become challenging because of an enhanced substrate influence on the results.

As an alternative to indentation, LiSAW can deliver mechanical properties with little sample preparation and in the same timely manner as indentation tests. Chapters 3 and 4 highlighted the two major facets of the technique: experimental measurement of SAWs and theoretical derivation of dispersion. Depending on the degree of the nonlinearity in the dispersion curve, one or more than one of the mechanical and physical properties of the film (elastic modulus, Poisson's ratio, density, and thickness) can be extracted by fitting experimentally measured dispersion data to theoretical predictions for a given system. The in-house developed system demonstrated this ability by accurately extracting the elastic modulus of aluminum films from aluminum on silicon and aluminum on fused silica structures.

Applying the same technique to nonporous (non-calcined) and porous (calcined) bMFI type zeolite films, it was shown that the elastic properties drop slightly from the calcination process and that the SAW technique could extract properties from multilayer systems without difficulty. Subsequent nanoindentation tests demonstrated that the traditional analysis schemes were inadequate in characterizing either of the nonporous and porous films with both films having inflated values from the substrate effect. This was attributed to the sub-micron film thickness and heavy elastic mismatch between the film and substrate. Although a correction scheme could be used to obtain results in agreement to LiSAW, the procedure requires significant time in computation. Therefore, LiSAW is a great alternative to indentation for thin, soft, and porous films by demonstrating the ability to accurately characterize films with all of those qualities.

Optimizations to the LiSAW system were made to increase the detectable range of frequency and to increase the range of dispersion. Both of these characteristics improve the quality and length of experimental dispersion curves thus providing a better foundation for theoretical fitting. The optimizations consisted of altering the experimental setup to achieve a much smaller detection spot size for increased spatial wavelength resolution and experimenting with slower Rayleigh wave speed top layers for additional acoustic contrast. Aluminum and tin films on silicon substrates were used as pilot studies to quantify the improvements and it was discovered that substantial increases in frequency range and dispersion were occurring. The optimized system was then used to revisit bMFI films where longer and smoother dispersion curves were observed. These proved the benefit of the improvements by producing dispersion curves that were visibly and statistically higher in quality.

The ability of LiSAW to characterize other challenging porous films was demonstrated by investigating a porous nanostructured V_2O_5 thin film electrode. The engineered surface of the film was particularly interesting since the scale of roughness was enough to affect typical indentation tests. It was found that the roughness contributed to a larger error in the indentation results while the LiSAW technique could readily extract the elastic parameters with greater accuracy. Some high frequency attenuation was observed, but not nearly enough to diminish the capability of the measurement. This experiment directly demonstrated how the mechanical properties of thin film electrodes of delicate and rough nature could be investigated and thus provides a solid foundation for future electrode study.

Possible future directions include fundamental work exploring the spectral bandwidth of generation on slow Rayleigh wave speed materials and continuing the work on thin film electrodes. The first topic arose from the tests on tin films where the frequencies generated seemed to be limited with increasing thickness of the slow top layer. The lack of targeted studies involving high frequency generation on such media presents a good opportunity for a fundamental study with such aims. Mechanical characterization of thin film electrodes is an area with many possible research directions since relatively few mechanical studies exist. It is hoped that LiSAW and nanoindentation can be used together in quantifying the modulus, hardness, and fracture toughness of electrode materials. The results can then be used to correlate electrode performance to mechanical properties in an effort to define optimal mechanical standards in battery design.

From the studies presented in this writing, it is apparent that the characterization of thin films is an ever changing problem with a constant stream of new structures requiring new or modified tools. Old methodologies may lose applicability and new methods may spawn, but the lessons learned along the way are critical towards continued adaption and advancement of the art.

Chapter 9 Future directions

In this dissertation, nanoindentation and LiSAW techniques have been used extensively to demonstrate their capabilities in thin films analysis. The LiSAW technique in particular has been shown to be a powerful and versatile method for the mechanical characterization of challenging films. However, the diversity in methodology for laser generation and detection of elastic waves naturally creates an abundance of possibilities, many of which have not been experimentally investigated. In performing the research contained in this dissertation, multiple areas for future study came to light. One point of interest delves into a more fundamental nature of the technique whereas another area focuses on materials applications.

9.1 High frequency attenuation from low Rayleigh wave speed materials

The experiments in Chapter 6 with tin films on silicon substrates demonstrated a significant reduction in high frequency response that merited further investigation. It was shown that for aluminum films, the frequency limit of detection was 225 MHz. However, for the tin films, only 110 MHz could be achieved. While misalignment of detection optics or differing sample surface qualities could affect frequency throughput, these parameters were not significantly different between the aluminum and tin tests. Thus, the difference in response appears to be material driven. This reduction in spectral bandwidth for dispersion with slower wave speed materials presents an interesting area for fundamental study.

In typical dispersion scenarios for slow on fast systems, such as the case for tin films on silicon substrates, the dispersion generally decays asymptotically from the Rayleigh wave speed of the substrate to the Rayleigh wave speed of the film (Levy et al., 2001). This is demonstrated in Figure 9-1 as a function of kh where k is the wave vector and h is the film thickness. k is related to the frequency of dispersion through:

$$k = \frac{2\pi f}{v} \tag{8-1}$$

where f is the frequency and v is the phase velocity. In Figure 9-1, it is shown that the dispersion decays linearly at first, but then trends to nonlinearity for $kh > 1$. Since the experiments preformed previously dealt with relatively thin films (small h, kh < 1), the majority of dispersion was linear. This also explains why increasing thickness allows for nonlinear dispersion.

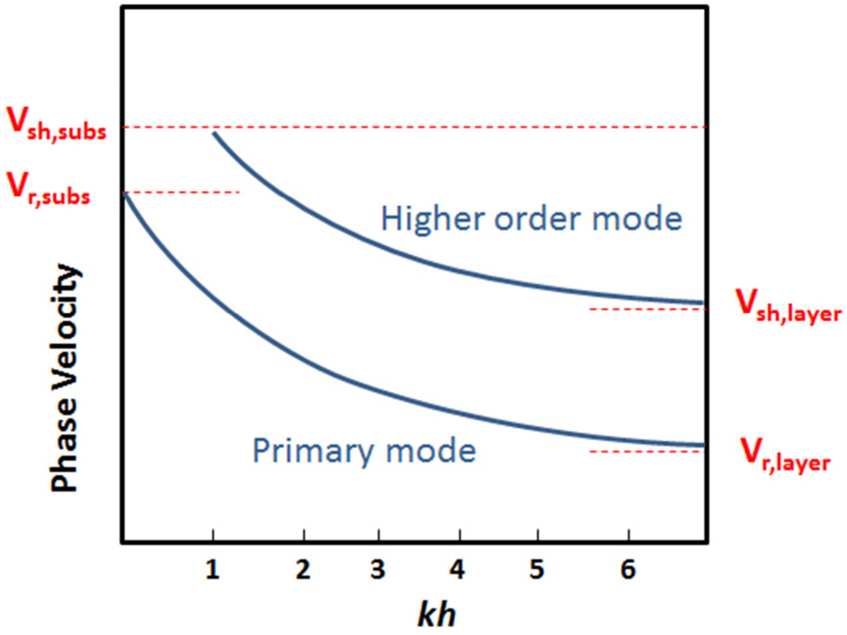

Figure 9-1. General Rayleigh wave dispersion response for a slow film on a fast substrate. kh is the product of wave vector and film thickness, V_{sh} demontes the shear wave speed, and V_r denotes the Rayleigh wave speed.

Cutoff frequencies have been observed in fast on slow systems (increasing dispersion rather than the decreasing dispersion plotted above) because the increasing phase velocities interact with the shear and longitudinal velocities of the substrate (Shen et al., 2010). Anomalous dispersion has also been observed for fast on slow systems where the Rayleigh wave velocity exceeds that of the layer for certain frequencies (Hadjoub et al., 2007). However for slow on fast systems, these issues are not encountered. Referencing Figure 9-1 once again, the primary Rayleigh wave does not encounter the substrate shear and longitudinal velocities since those exist above the substrate Rayleigh wave velocity. Higher order modes have a possibility to interfere, but those occur at $kh > 1$. For the 1 μm tin layer on silicon, the kh value at a frequency of 100 MHz is merely ~ 0.16 therefore higher mode interaction is unlikely.

From the experiments with Sn/Si and Sn/bMFI/Si systems, it appeared that the frequency of extinction was dependent on the thickness of the layer. Intuitively, the longer waveforms generated by the more strongly dispersive thicker layers may have difficulties sustaining higher frequencies at sufficient amplitude for detection. Also, as the SAW wavelength approaches that of the film thickness, it may be a possibility that interface interactions could attenuate the Rayleigh wave. To the author's knowledge, there does not appear to be literature targeting slow wave speed materials at high frequency, therefore, an experiment involving tin layers of varying thickness could be useful. If the high frequencies exist, but are escaping detection due to low amplitude, improving the experimental setup for higher resolution may be necessary. However, it may also be possible to probe the frequencies with higher generation power (well into the ablation range). Generation through grating methods may also be valuable in order to selectively produce higher frequencies (Rogers et al., 2000). Through these experiments, a trend in frequency response with respect to film thickness can be developed and may prove to be fruitful for tailoring double layer experiments to optimal spectral bandwidth.

9.2 Mechanical properties of porous nanostructured electrode thin films

As discussed in Chapter 7, the mechanical properties of thin film electrodes are often overlooked since there is understandable focus on electrical or chemical development. However, the failure of electrodes is, in part, a mechanically governed process. Therefore, thorough mechanical analysis may reveal useful relationships between material properties and electrode reliability. The demonstration of LiSAW on porous nanostructured films opens up many materials to analysis since these are the types of films that may have been unfavorable for poplar indentation tests. By measuring the elastic modulus with LiSAW on many thin film electrodes, it is hoped that the values can be correlated to critical electrical parameters such as cyclability.

While LiSAW is useful for elastic property measurement on delicate films, an ideal mechanical investigation would combine LiSAW with nanoindentation. It has already been shown that the film's hardness changes with cycling (Ramdon and Bhushan, 2014) therefore it may be a key parameter governing electrode life cycle. Indentation tests could provide the hardness since those measurements can evade substrate effects even at large indentation depth to film thickness ratios (Li and Vlassak, 2009). Another key parameter attainable through nanoindentation is the fracture toughness. It is well known that the ultimate failure of electrodes is heavily related to active material disintegration therefore quantification of fracture toughness throughout the battery life cycle may provide substantial information on suppressing electrode decay with cycling.

The mechanical testing of new electrode materials is a relatively uncharted field with many possible research aims. It is hoped that the field grows and develops towards the ideal goal of providing optimal electrode material parameters. Efficient energy storage is an area with obvious human and environmental implications therefore it is critical that the technology is refined with approaches from every possible angle.

Chapter 9 References:

HADJOUB, Z., BELDI, I. & DOGHMANE, A. 2007. Origin and quantification of anomalous behaviour in velocity dispersion curves of stiffening layer/substrate configurations. *Comptes Rendus Physique,* 8**,** 948-954.

LEVY, M., BASS, H. & STERN, R. 2001. *Modern Acoustical Techniques for the Measurement of Mechanical Properties*, Elsevier Science.

LI, H. & VLASSAK, J. J. 2009. Determining the elastic modulus and hardness of an ultra-thin film on a substrate using nanoindentation. *Journal of Materials Research,* 24**,** 1114-1126.

RAMDON, S. & BHUSHAN, B. 2014. Nanomechanical characterization and mechanical integrity of unaged and aged Li-ion battery cathodes. *Journal of Power Sources,* 246**,** 219-224.

ROGERS, J. A., MAZNEV, A. A., BANET, M. J. & NELSON, K. A. 2000. Optical generation and characterization of accoustic waves in thin films: fundamental s and applications. *Annual Review of Materials Science,* 30**,** 117-157.

SHEN, Z. H., LOMONOSOV, A. M., HESS, P., FISCHER, M., GSELL, S. & SCHRECK, M. 2010. Multimode photoacoustic method for the evaluation of mechanical properties of heteroepitaxial diamond layers. *Journal of Applied Physics,* 108**,** -.

Appendix A Nanoindentation on adamantane-based rod structures

A.1 Introduction

In this section, the mechanical properties of adamantane-based covalent organic framework (COF) rod structures are explored by nanoindentation. Similar to the zeolite materials explored previously, COFs exhibit a porous crystalline structure that is provided by periodic building units. However, unlike the silica or metal based tetrahedral structures found in zeolite, COFs are typically composed of lighter elements, such as B, C, O, and N, therefore their densities can be substantially lower (Feng et al., 2012). The mechanical properties of highly porous low density structures are typically very low, but the crystalline structure of COFs allows for a greater mechanical stiffness. This makes COFs especially interesting as low-k materials since they can provide potentially groundbreaking dielectric properties while retaining the necessary mechanical reliability for semiconductor fabrication processes.

Adamantane COF rods (ACOF) were obtained through a self-condensation reaction of 1,3,5,7-tetrakis(4-(dihydroxy)borylphenyl)adamantane (TBPA). The rods are depicted in Figure A-1. It can be seen that the rods have a generally rectangular cross-section that produces flat sides around 1-2 μm in width and running the length of the rod. This is favorable for indentation tests since the parallel sides can offer stability during force application. However, some fixation to the substrate is required since sample probing involves scanning the tip laterally across each rod. This sort of probing cannot be circumvented since each rod needs to be located through the tip surface scanning process when identifying indentation sites.

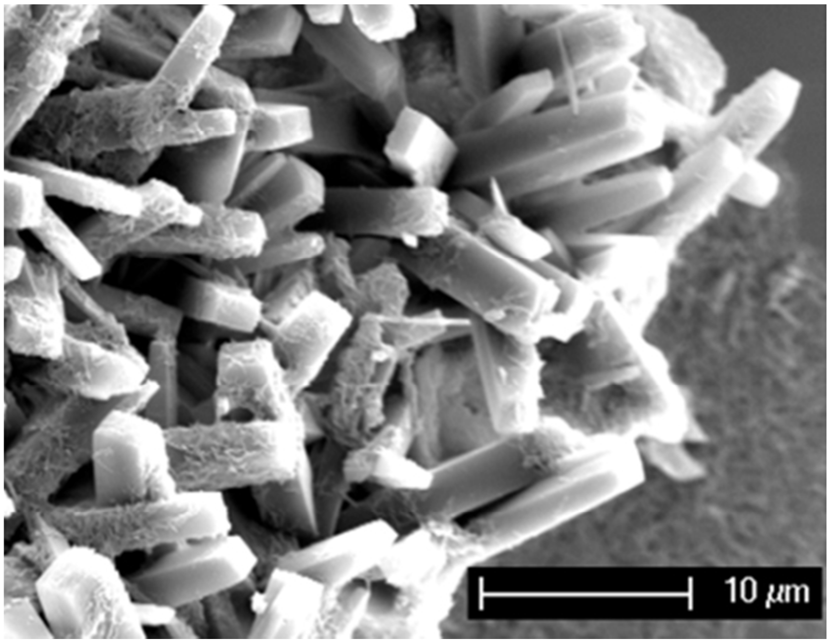

Figure A-1. SEM image of ACOF rods (Fang et al., 2014).

A.2 Rod fixation schemes

The ACOF structures to be tested were synthesized in a powder form that was composed of mostly agglomerated rods exactly as shown in Figure A-1. These agglomerates presented no clear areas for indentation tests since the individual rods contained within had no preferred orientation or fixation. However, the powder also contained isolated rods that had broken off of the main agglomerates which were suitable for indentation. To indent on the isolated rods, several fixation schemes were attempted.

Initially, it was believed that the scale of the rods were sufficiently small to allow scanning probe microscopy (SPM) by the tip with Van der Waals forces being dominant for rod fixation. Thus, the rods were dispersed over the surface of glass and SPM was performed. It was discovered that the rods could not be consistently scanned with a tip normal force of 2 μN, which is typical of

SPM imaging. The rods had inadequate fixation and were being dislodged by the tip as initial lateral contact was being made. In lowering the normal force to 1 and 0.5 μN, some images could be made of smaller rods, but consistent scanning after several passes in the same location was not possible.

To produce a more intimate contact with the substrate, the rods were mixed with isopropyl alcohol (IPA) and then dispersed onto the glass slide. As the IPA evaporated around and underneath the rods, it was hoped that the rods would settle onto the substrate. SPM confirmed that the fixation was stronger by allowing the scan of rods at 2 μN. However, consistent scanning through multiple passes was still producing rod movement or complete eviction from the scanning area. Thus it was clear that simple dispersal and Van der Waals attraction was not enough to fixate the rods for scanning purposes. While indentation can be performed after only a single pass to identify the rod location, there is no guarantee that the target remained fixed for the entirety of the scan (hence the necessity for multiple passes), thus making localized indentation on rod centers very difficult.

A new strategy was employed to ensure rod fixation by embedding them into a mold material. While a mold ensures rigidity during scanning, an exposed rod surface is necessary for indentation testing. To achieve this, the rods were dispersed with IPA onto a glass slide and then left to evaporate as before. Next, epoxy resin for sample cross-sectioning (Ted Pella, Redding, CA) was carefully poured over the rods and left to harden. After hardening, the resin was peeled away from the glass producing an epoxy surface with exposed rod surfaces.

Another mold fixation scheme was employed whereby Crystalbond adhesive (Ted Pella, Redding, CA) was heated and liquefied. The adhesive was then spread onto a glass substrate and allowed to cool. At varying time periods between 10 s and 5 m during cooling, ACOF rods were dispersed onto the Crystalbond surface. The goal was to find a period in time for which the viscosity of the Crystalbond allowed for rod fixation without sinking below the surface (too soft) or lack of adhesion (too hard). It was determined that ~25 – 30 s of cooling in room temperature prior to rod dispersal was optimal to create protruding rod surfaces with sufficient fixation.

A.3 Experimental results for epoxy fixation

Figure A-2 depicts an optical microscope image of an epoxy surface with ACOF rods embedded. The large black areas are rod agglomerates. Smaller black areas are either small clusters of rods, individual rods (labelled and darker), or holes where rods once were (lighter). The abundance of holes is caused by rods falling out or remaining fixed to the substrate during the epoxy peeling process. For indentation, larger rods, with lengths exceeding 10 μm, were chosen since they were easier to locate and they had dimensions that maximized the surface area for indentations. Since the thickness of the rods were 1 μm or above and the substrate was not very soft or hard, significant substrate effects were not expected. Indentations were performed with a cube corner tip in order to minimize the penetration depth and area necessary for indentation analysis.

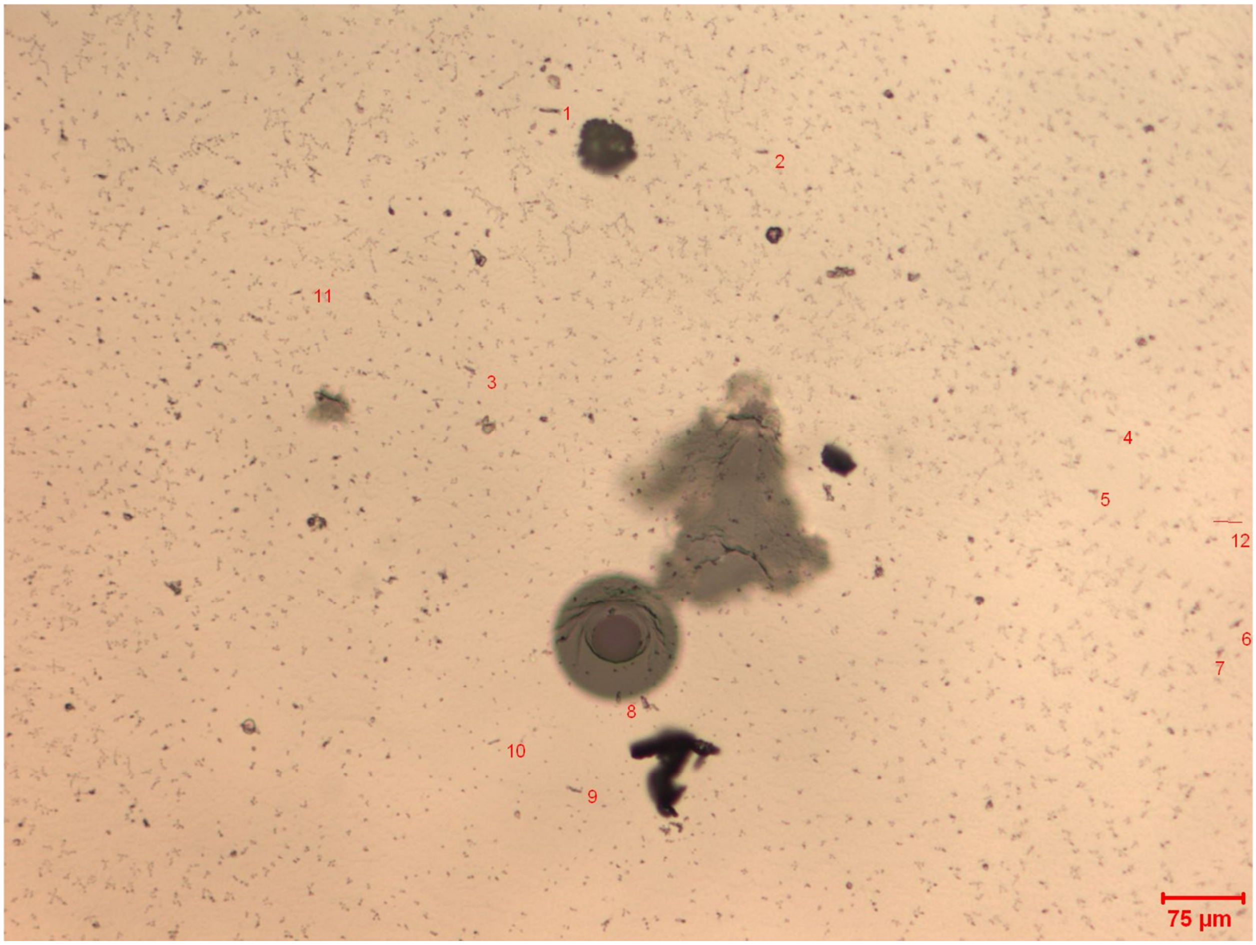

Figure A-2. Hardened epoxy resin peeled from a glass substrate with rods embedded and labelled.

Table A-1 shows the results of indentations on each of the labelled rods in Figure A-2. Figure A-3 to Figure A-11 show an optical image and gradient image from SPM for each rod. Gradient images are created by the force correction response of the tip as it passes over a surface asperity and they depict a much clearer surface than typical topography images. However, no tip displacement information is given on such images and the surface profile is inferred from lighter and darker regions corresponding to lower and more force correction respectively. All SPM gradient images shown represent a 10 × 10 µm area.

Table A-1. Results for indentation tests on ACOF rods with an epoxy substrate. Red highlights rods with clearly exposed areas for indentation therefore their measurements should have less epoxy influence.

Sample	E (GPa)	H (GPa)
Epoxy	4.11 ± 0.16	0.25 ± 0.01
Rod 1	2.06 ± 0.69	0.08 ± 0.02
Rod 2	4.15 ± 1.07	0.12 ± 0.05
Rod 3	6.01 ± 1.52	0.32 ± 0.15
Rod 4	9.47 0.26	0.80 ± 0.11
Rod 5	1.92 ± 0.25	0.05 ± 0.01
Rod 6	2.62 ± 0.64	0.09 ± 0.03
Rod 7	4.10 ± 1.66	0.21 ± 0.11
Rod 8	2.83 ± 1.18	0.08 ± 0.01
Rod 9	10.66 ± 0.37	0.8 ± 0.08
Rod 10	7.75± 0.88	0.54 ± 0.22
Rod 11	3.06 ± 0.06	0.09 ± 0.03

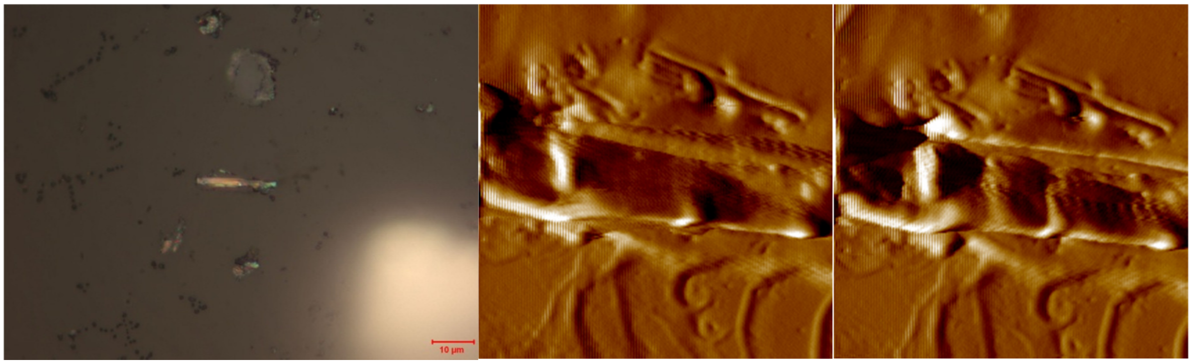

Figure A-3. Rod 1, optical microscope image and gradient SPM images before and after indentations.

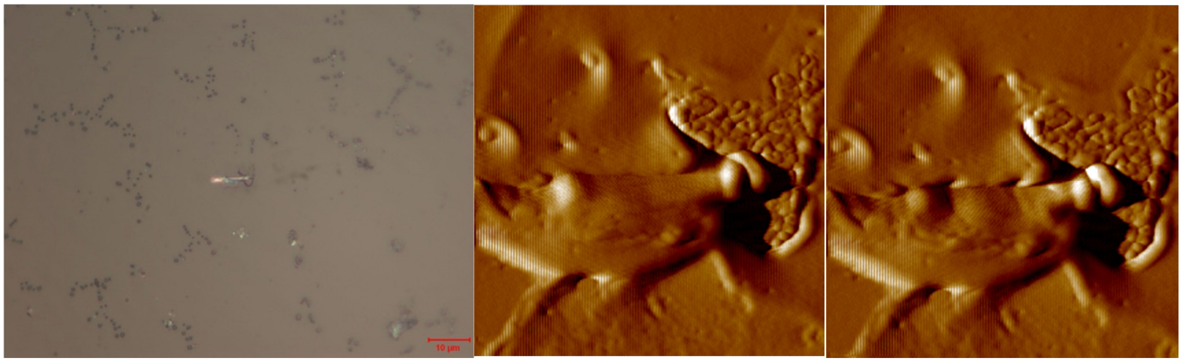

Figure A-4. Rod 2, optical microscope image and gradient SPM images before and after indentations.

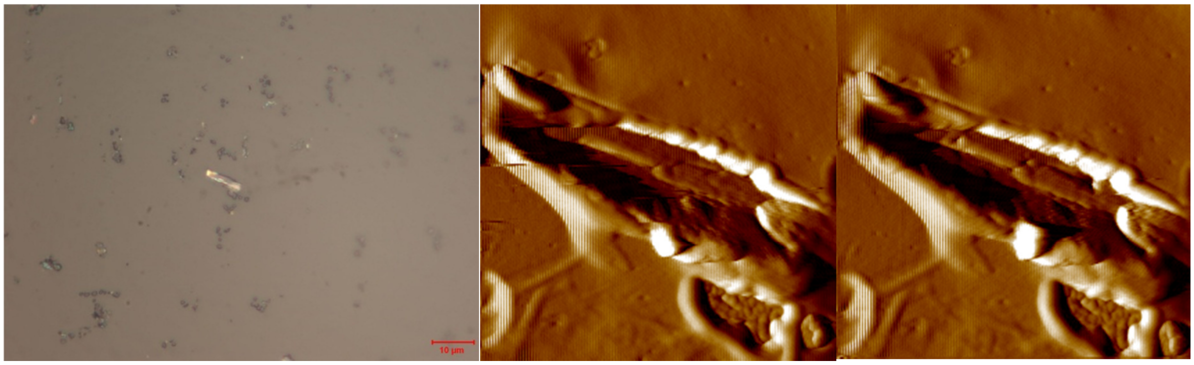

Figure A-5. Rod 3, optical microscope image and gradient SPM images before and after indentations.

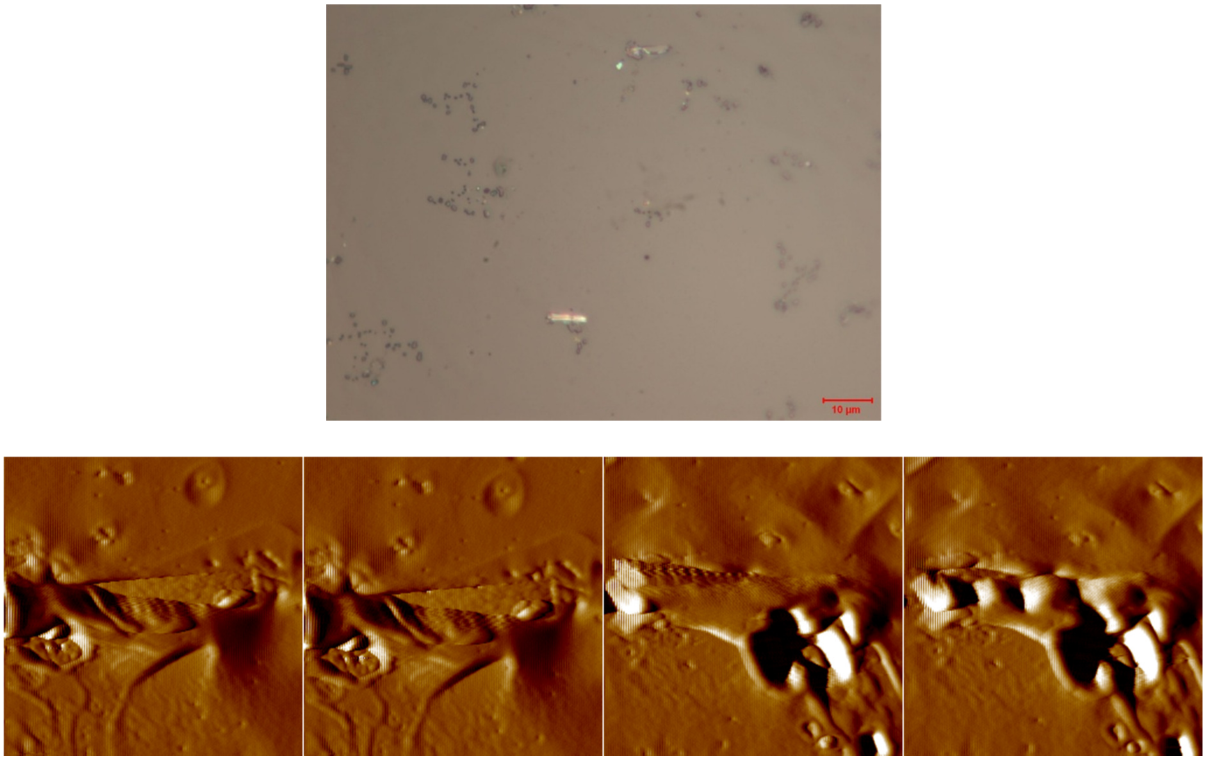

Figure A-6. Rods 4-5, optical microscope image and gradient SPM images before and after indentations.

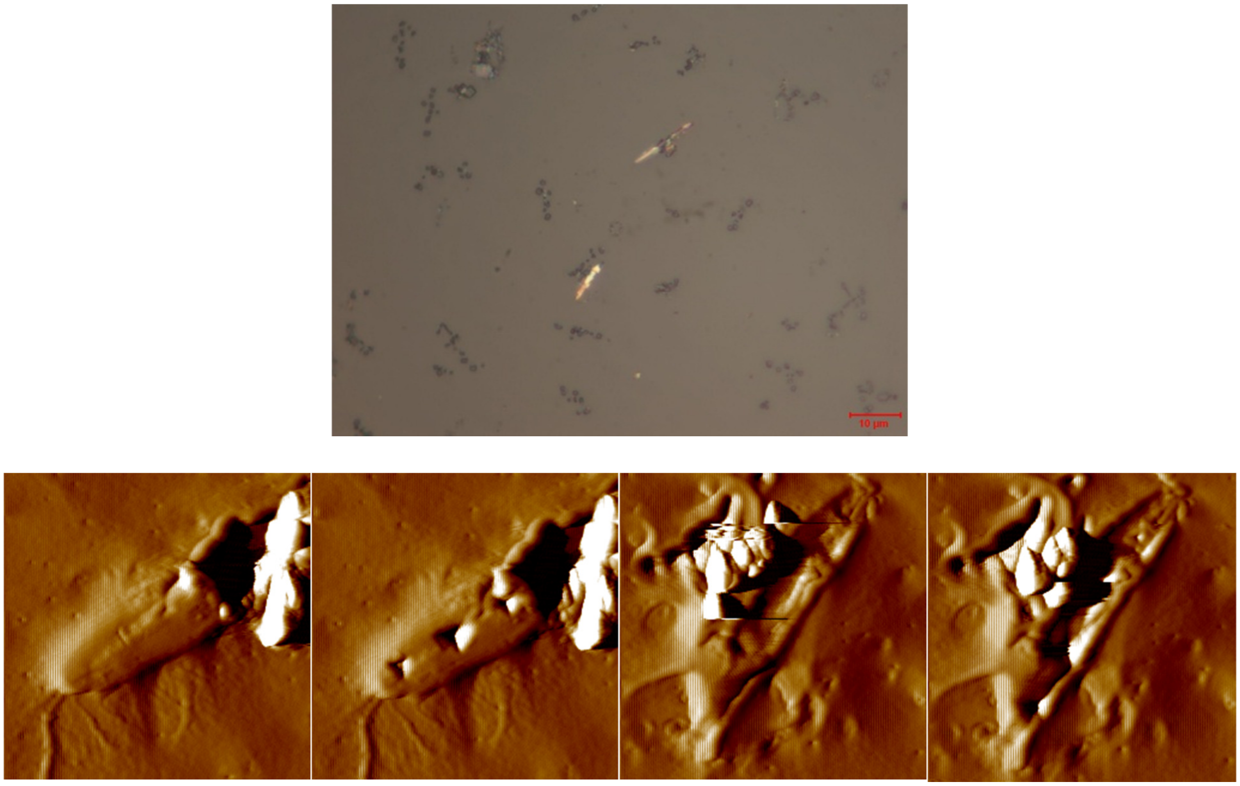

Figure A-7. Rods 6-7, optical microscope image and gradient SPM images before and after indentations.

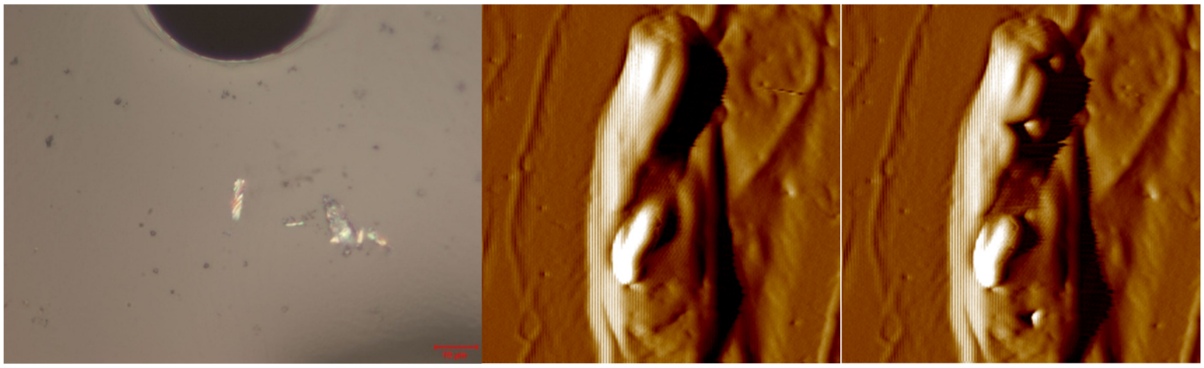

Figure A-8. Rod 8, optical microscope image and gradient SPM images before and after indentations.

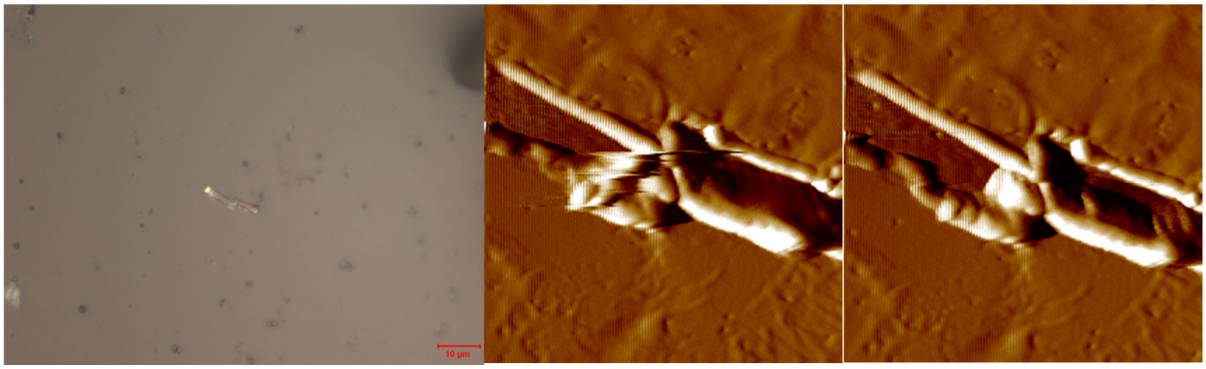

Figure A-9. Rod 9, optical microscope image and gradient SPM images before and after indentations.

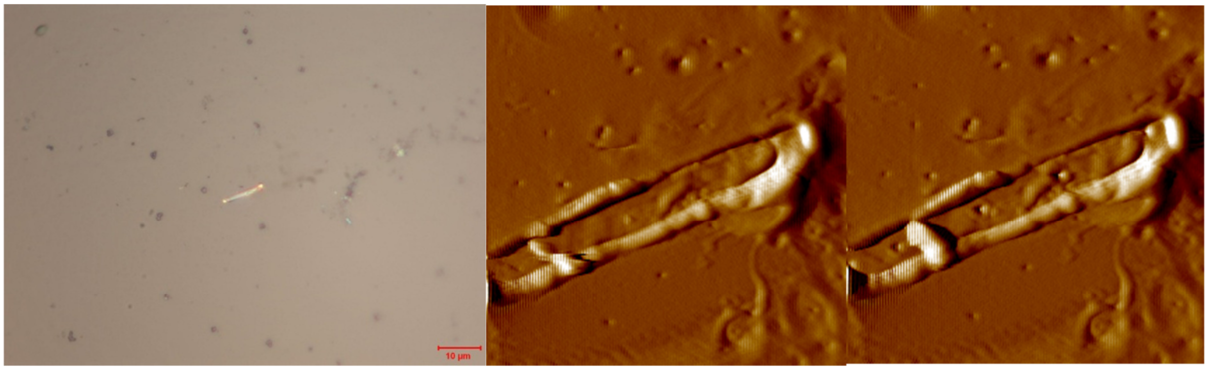

Figure A-10. Rod 10, optical microscope image and gradient SPM images before and after indentations.

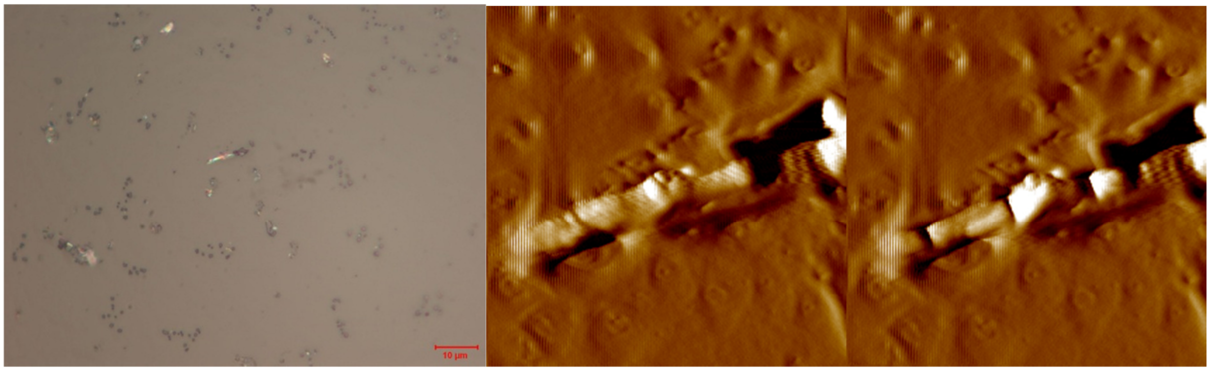

Figure A-11. Rod 11, optical microscope image and gradient SPM images before and after indentations.

It is evident from the SPM images above that even though all of the rods looked exposed under the microscope, some remained obscured by epoxy. For example, rods 1, 5, and 8 have no clear flat surfaces present in their SPM images. By inspecting their mechanical properties, it is clear that the lower values are likely the result of influence from the epoxy substrate. This can be thought of as the epoxy resin seeping underneath the rod during hardening. Since the epoxy is transparent, the rod surface is still shown clearly on the microscope images since they exist very close to the surface. Rods 3, 4, 9, and 10 have at least a portion of their surfaces exposed and indentations were performed on those areas. The indentation results from these rods indicate a much higher modulus that ranges from 6 - 10.6 GPa. While the range of moduli is larger than desired, it demonstrates that the ACOF structure has a modulus of at least 6 GPa which surpasses the benchmark for low-κ semiconductor materials (International Roadmap Committee, 2013).

A.4 Experimental results for Crystalbond fixation

The Crystalbond fixation technique yielded rods that were much more exposed than with the epoxy technique. This is demonstrated by the SPM images in Figure A-12 and Figure A-13 where the sides of each rod and the flat top surface can be easily discerned. Despite appearing to rest on top of the Crystalbond surface, the rods were well embedded and did not move during SPM imaging or indentation tests. However, suitable rods for testing were difficult to find since many sank too deep into the substrate or were removed by scanning. Ultimately, two long rods with ideal conditions were found and their length was separated into several sections (a through c) for testing. The nanoindentation results, displayed in Table A-2, showed much more consistent values for these rods and confirmed the 6+ GPa elastic modulus from the prior epoxy fixation study. However, the effect of the soft viscoelastic Crystalbond substrate is unaccounted for and can potentially be lowering the extracted moduli. In the epoxy fixation results, moduli up to 10 GPa were measured therefore it is possible that the actual moduli are slightly higher than the 6.5-8 GPa values measured currently.

Table A-2. Results of nanoindentation on ACOF rods fixated by crystalbond.

Rod #	Er (GPa)	H (GPa)
Crystalbond	Too viscoelastic for accurate meas.	0.23 ± 0.08
1a	6.5 ± 0.4	0.28 ± 0.08
1b	7.6 ± 0.9	0.32 ± 0.07
2a	6.6 ± 1.1	0.28 ± 0.06
2b	7.6 ± 1.3	0.40 ± 0.02
2c	7.9 ± 0.4	0.26 ± 0.01

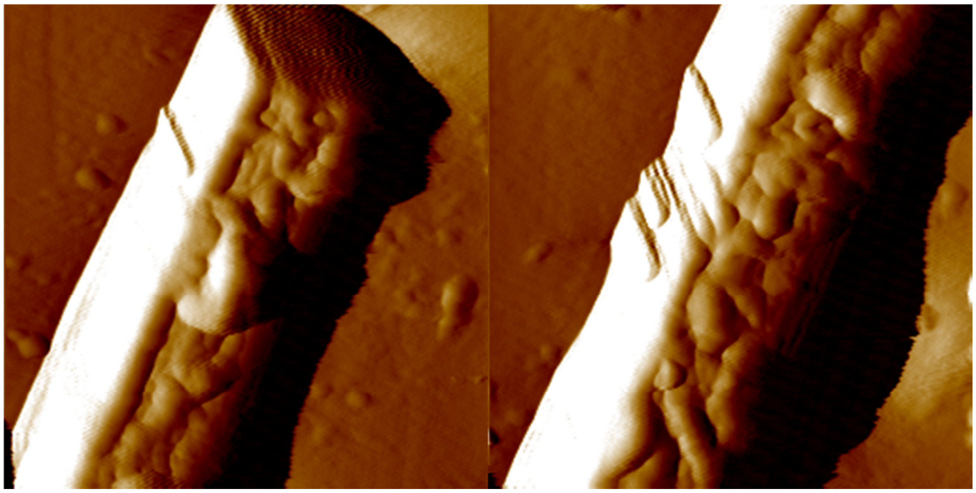

Figure A-12. Left to right, rods 1a and 1b. SPM gradient images post-indentation.

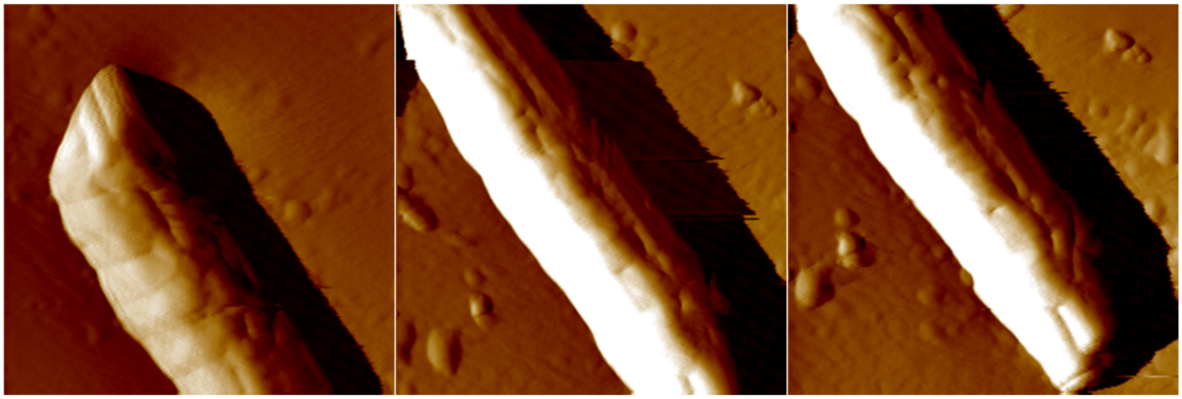

Figure A-13. Left to right, rods 2a – 2c. SPM gradient images post-indentation.

A.5 Conclusion

Nanoindentation was successfully performed on an adamantane based covalent organic framework rod structure. Sample fixation to the substrate was approached by two methods, one involving the molding of rods in epoxy resin and the other involving rod capture during Crystalbond adhesive cooling. Both types of fixation produced viable results leaving exposed areas for indentation, but the yield of suitable indentation areas was much lower for Crystalbond.

However, the few favorable rods produced through the Crystalbond method had areas with significant protrusion and full exposure therefore generating more consistent indentation results.

Indentation moduli for the epoxy fixated rods varied between 1.9 and 10.6 GPa. However, many of the rods were covered or almost fully covered by epoxy. Considering only those with exposed areas for indentation, the moduli were considerably higher ranging from 6 to 10.6 GPa. Similar results were recorded with Crystalbond fixation where moduli between 6.5 and 7.9 GPa were measured. While the results have a larger than desired distribution, the measured moduli range can only be derived from the rod structures since both substrates exhibited a moduli of 4 GPa or less. The results indicate that the ACOF rod structure has moduli greater than the 6 GPa target for low-κ dielectrics which is significant considering their substantial porosity. These mechanical tests support their use as low-κ materials in the semiconductor industry.

References for Appendix A:

FANG, Q., GU, S., LIU, Q., CHOW, G., WANG, J., MAICHEN, W., DEEM, M. W., QIU, S. & YAN, Y. 2014. Designed synthesis of 3D porous covalent organic frameworks as ultra-low-k materials. *Chemical Science,* Submitted - In Review.

FENG, X., DING, X. & JIANG, D. 2012. Covalent organic frameworks. *Chemical Society Reviews,* 41**,** 6010-6022.

INTERNATIONAL ROADMAP COMMITTEE 2013. International Technology Roadmap for Semiconductors.

Appendix B Surface skimming longitudinal waves and their potential use in LiSAW measurements

B.1 Introduction

In addition to generating Rayleigh waves, laser excitation of solids produces longitudinal and transverse waves that propagate through the material without restrictive localization to the surface. These have been very useful in other areas of research such as in quantifying the adhesion strength of thin films by compressive stress waves (Wang et al., 2002). In adhesion measurements, the compressive stress wave, or P wave, propagates perpendicular to the surface through the material. However, since P waves propagate in all directions radially from the generation point, a surface skimming longitudinal wave exists (Every, 2002). Despite having primarily longitudinal displacements, this wave contains out-of-plane motion that can be measured by typical SAW detection techniques (Sajauskas, 2004).

The surface skimming longitudinal wave (SSLW) has some important benefits for SAW testing. For uncoated samples, the residual stress can be probed by investigating the change in SSLW speed (Bescond et al., 2005). For layered samples, the SSLW can be used to fit substrate properties in order to reduce error for theoretical dispersion curves (Fourez et al., 2012). This would be especially useful for the experiments in Chapter 7 where the high doping of the silicon substrate modified its elastic parameters. For those experiments, separate SAWs were generated on bare silicon wafers prior to film deposition to account for the elastic property variations. However, using SSLWs, secondary tests may not be necessary since the SSLW and Rayleigh components can occur together.

Perhaps of greater interest are the recent simulations showing how the SSLW can exhibit reverberations based on the film thickness (Wang et al., 2007). While film thickness can be measured by profiling or focused ion beam cross-sectioning to great accuracy, elimination of extra experimental steps are always desired. The study by Wang *et al.* was based on SAW generation at the interface of a transparent film and opaque substrate. The SSLW was reported to have variable reverberations from longitudinal wave reflection between the free surface and interface. While their simulations involved much thicker films, on the order of 10's of μm, the following research study investigated whether the same phenomena could be experimentally measured on much thinner opaque films.

B.2 Experimental results

SSLWs were measured on a 230 nm aluminum film with a 380 μm thick silicon substrate, a bare 525 μm silicon substrate, and a bare 380 μm silicon substrate. It was hoped that any differences in the SAWs between the coated and uncoated substrates could be investigated for film thickness extraction. SAWs were detected at a distance of ~20 mm to allow for ample separation between the faster SSLW and the slower Rayleigh wave. The generation laser power was increased past 10 mJ in order to create larger amplitude SSLWs for detection.

SAWs detected on the bare 380 μm silicon substrate and the same substrate coated with 230 nm of aluminum are depicted in Figure B-1. The green vertical line marks the time of first displacement indicating the longitudinal wave arrival. The [100] direction SSLW was determined to have a velocity of 8360 m/s which is comparable to the theoretical value of 8430 m/s. Through inspection of the SSLW wave characteristics, it was seen that there were no discernibile wave differences between the bare substrate (red) and the coated substrate (red). Furthermore, the reverberation of the longitudinal wave was expected to be on a very short timescale within 100 ns after SSLW arrival. The high frequency displacement in the SSLW was either too small to be picked up by the detection system or not present at all. Curiously, a relatively long timescale oscllation with a period of ~160 ns was seen between the SSLW and Rayleigh wave arrivals. This was not film related since the oscillation occurred on both the bare and coated substrates. The oscillation occurs immediately after LW arrival therefore they outpace any transverse waves. It was hypothesized that this was the LW being reflected through the thickness of the substrate, thus SAWs were measured on a bare silicon substrate with larger thickness (525 μm).

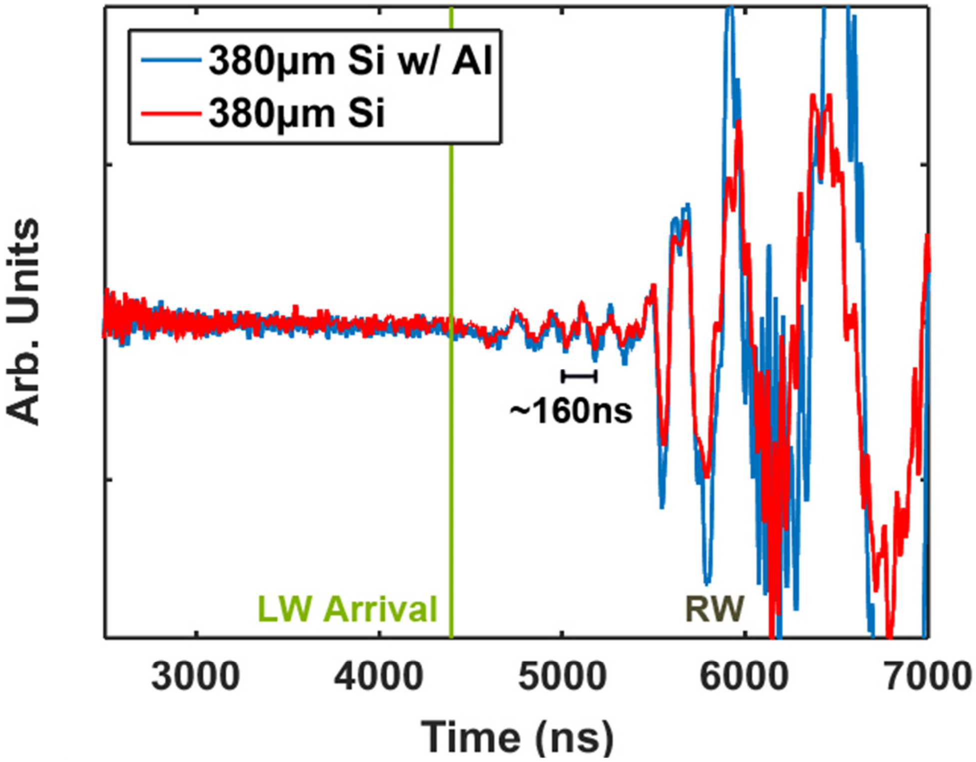

Figure B-1. Comparison of SAWs measured on a 380 μm thick silicon substrate and the same substrate with a 230 nm aluminum film. LW and RW denote the longitudinal and Rayleigh waves respectively.

Figure B-2 shows the SAWs measured on a 525 µm bare silicon substrate. The period of oscillation between the SSLW and the Rayleigh wave was observed to increase to ~220 ns and the difference is clear on the plot. While the SSLW arrived at the same time, the thinner substrate had around four periods of oscillation before larger Lamb and Rayleigh wave movement whereas the thicker substrate only exhibited three periods. Thus it was concluded that the thickness of the silicon substrate was driving the period of oscillation. However, the exact correlation between the period and substrate thickness was not determined and could be an area of future study.

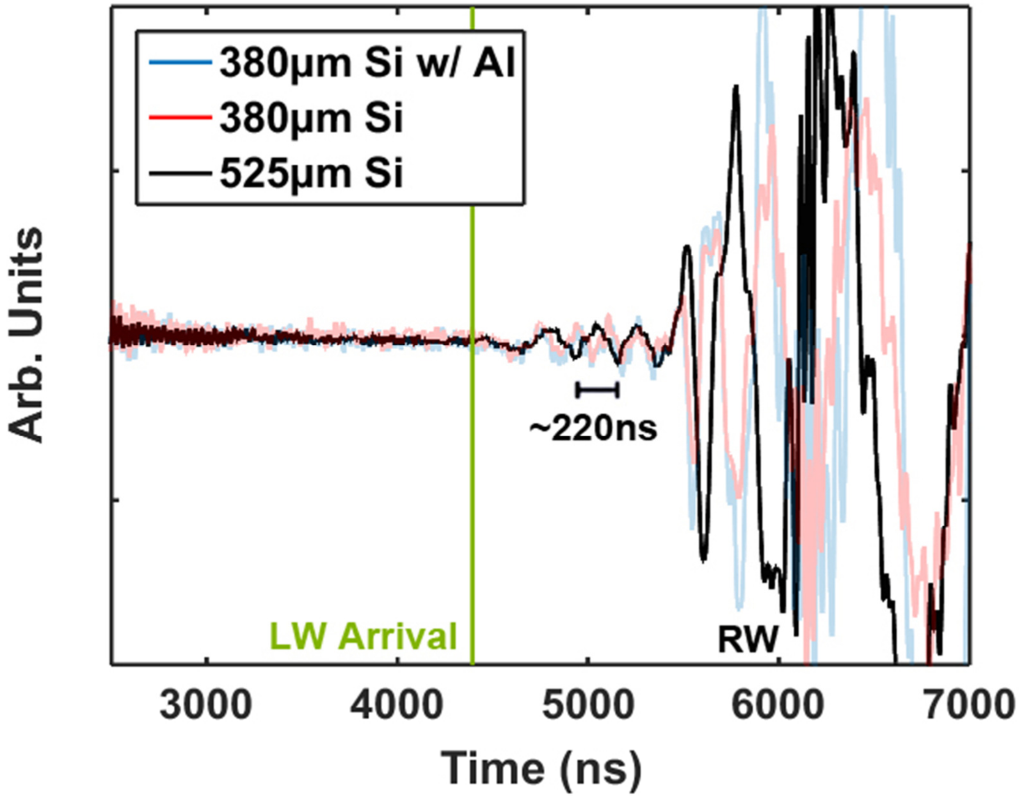

Figure B-2. SAWs measured on a 525 µm bare silicon substrate (black) compared to those from a 380 µm substrate with and without coating (red/blue). LW and RW denote the longitudinal and Rayleigh waves respectively.

B.3 Conclusion

From this brief study, it was determined that the detection system could not distinguish any SSLW differences between coated and uncoated specimens, thus additional information about the film could not be extracted from such waves currently. However, the SSLW does allow for substrate longitudinal wave speed extraction, even on coated specimens, therefore making them valuable when the substrate properties are uncertain. While investigating the SSLW, distinct oscillation was observed between the SSLW and Rayleigh wave arrivals and their periods were found to be dependent on the substrate thickness. It is believed that the phenomenon is a product of the longitudinal wave being reflected through the substrate. However, the film did not appear to modify the oscillation at all.

It should be noted that while no differences were detected between the coated and uncoated substrates, the amplitude of the SSLW and waves directly thereafter were very small. Therefore, there is a possibility that film specific information is present, but being undetected. The study by Wang *et al.* has already shown that the SSLW changes for thicker films, thus simulations for thinner films should be a logical first step in revealing a better approach for future experimental investigations.

References for Appendix B:

BESCOND, C., MONCHALIN, J.-P., LEVESQUE, D., GILBERT, A., TALBOT, R. & OCHIAI, M. Determination of residual stresses using laser-generated surface skimming longitudinal waves. 2005. 175-186.

EVERY, A. G. 2002. Measurement of the near-surface elastic properties of solids and thin supported films. *Measurement Science and Technology,* 13**,** R21.

FOUREZ, S., JENOT, F., OUAFTOUH, M., DUQUENNOY, M. & OURAK, M. 2012. Non-contact thickness gauging of a thin film using surface waves and a void effect on their propagation. *Measurement Science and Technology,* 23**,** 085608.

SAJAUSKAS, S. 2004. *Longitudinal Surface Acoustic Waves (creeping Waves)*, Technologija.

WANG, J., SHEN, Z., NI, X., XU, B., GUAN, J. & LU, J. 2007. Numerical simulation of laser-generated surface acoustic waves in the transparent coating on a substrate by the finite element method. *Optics & Laser Technology,* 39**,** 21-28.

WANG, J., WEAVER, R. & SOTTOS, N. 2002. A parametric study of laser induced thin film spallation. *Experimental Mechanics,* 42**,** 74-83.